UNIVERSITAT POLITÈCNICA DE CATALUNYA BARCELONATECH

Network-based ionospheric gradient monitoring to support ground based augmentation systems

María Caamaño Albuerne

Ph.D. Thesis
Doctoral Program in Aerospace Science and Technology

NETWORK-BASED IONOSPHERIC GRADIENT MONITORING TO SUPPORT GROUND BASED AUGMENTATION SYSTEMS

María Caamaño Albuerne

Advisors
Prof. Dr. Jaume Sanz Subirana
Prof. Dr. José Miguel Juan Zornoza

Research group of Astronomy and Geomatics
Department of Physics and Department of Mathematics
Polytechnic University of Catalonia (UPC)
Barcelona, Spain

April 2022

Committee

Dr. Sam Pullen	Stanford University, USA
Dr. Adrià Rovira García	Universitat Politècnica de Catalunya, Spain
Dr. Nadezda Sokolova	SINTEF Digital / Norwegian University of Science and Technology (NTNU), Norway

International Reviewers

Dr. Sam Pullen	Stanford University, USA
Dr. Nadezda Sokolova	SINTEF Digital / Norwegian University of Science and Technology (NTNU), Norway

Abstract

The Ground Based Augmentation System (GBAS) is a local-area, airport-based augmentation of Global Navigation Satellite Systems (GNSSs) that provides precision approach guidance for aircraft. It enhances GNSS performance in terms of integrity, continuity, accuracy, and availability by providing differential corrections and integrity information to aircraft users. Differential corrections enable the aircraft to correct spatially correlated errors, improving its position estimation. Integrity parameters enable it to bound the residual position errors, ensuring safety of the operation. Additionally, a GBAS ground station continuously monitors and excludes the satellites affected by any system failure to guarantee system integrity and safety.

Among the error sources of GNSS positioning, the ionosphere is the largest and most unpredictable. Under abnormal ionospheric conditions, large ionospheric gradients may produce a significant difference between the ionospheric delay observed by the GBAS reference station and the aircraft on approach. Such a spatially decorrelated ionosphere could lead to hazardous unbounded position errors if undetected. Conventional GBAS solutions to mitigate this threat assume that the "worst-case" ionospheric gradient ever observed in the relevant region is always present, which is a very conservative assumption. This approach, which relies on the conservative ionospheric threat models derived for GBAS, maximizes integrity, often at the expense of availability and continuity, especially in geographic areas with highly active ionosphere.

As opposed to assuming a permanent "worst-case" gradient, I propose the Network GBAS concept, in which several reference stations collaborate to monitor for actual ionospheric gradients. This concept consists of two main steps. First, the network detects the anomalous ionospheric gradients, estimates the gradient parameters, and transmits this information to the GBAS stations installed in its coverage area. Then, the GBAS stations replace the "worst-case" gradient used to mitigate the ionospheric threat in current algorithms with the gradient information provided by the network. This approach reduces conservatism and leads to an improvement of the system availability without compromising user integrity.

This thesis validated the performance of the detection and estimation al-

gorithms with simulated and real ionospheric gradients from two different locations known for their high levels of ionospheric activity. One location was Alaska, where the analyzed real anomalous gradients were small in size but fast-moving; the other location was Brazil, dominated by large-but-slow anomalous gradients. This analysis led to the adaptation of the algorithms to work in challenging scenarios.

The evaluation of the Network-GBAS concept compared in simulations the availability of a Category I (CAT I) GBAS station at the Brazil location in two cases: assuming the conservative ionospheric threat model, and using the gradient information provided by the network. On a selected nominal day (i.e., with no significant ionospheric activity), availability improved from 79.5% to 94.6% during the nighttime. On a selected active day, availability improved from 68.7% to 89.5% during the nighttime. During the daytime, availability achieved 100% on both days.

Results demonstrate that the Network-GBAS concept can significantly enhance CAT I GBAS availability in active ionospheric regions without compromising user integrity. Furthermore, by incorporating the information provided by the network into existing solutions, the Network-GBAS is compatible with existing algorithms and hardware, and thus should be certifiable if adapted to the characteristics of each region where GBAS is fielded.

Resumen

El Sistema de Aumentación Basado en Tierra (GBAS por sus siglas en inglés) en un sistema de área local que se instala en los aeropuertos. GBAS aumenta las señales de los Sistemas Globales de Navegación por Satélite (GNSSs) y proporciona a las aeronaves la información necesaria para realizar aproximaciones de precisión. Su principal objetivo es mejorar el rendimiento de GNSS en términos de integridad, continuidad, exactitud y disponibilidad, mediante la transmisión de correcciones diferenciales y parámetros de integridad. Las correcciones diferenciales le permiten a la aeronave mejorar la exactitud de su posición. Los parámetros de integridad le permiten calcular límites para los errores residuales de posición. Adicionalmente, la estación GBAS monitoriza y excluye los satélites afectados por cualquier tipo de fallo en el sistema para garantizar la integridad y la seguridad de los usuarios.

Entre las fuentes de error de GNSS, la ionosfera es la mayor y más impredecible. En condiciones ionosféricas anormales, los grandes gradientes ionosféricos pueden producir una diferencia significativa entre el error ionosférico observado por la estación GBAS y la aeronave. Si esta diferencia no se detecta y se mitiga, podría dar lugar a grandes errores en la posición de la aeronave. Las soluciones GBAS convencionales para mitigar esta amenaza asumen que el gradiente ionosférico más grande jamás observado en la región pertinente está siempre presente, lo cual es una suposición muy conservadora. Este enfoque, basado en los modelos conservadores de amenaza ionosférica derivados para GBAS, maximiza la integridad, a menudo a expensas de la disponibilidad y la continuidad del sistema, especialmente en zonas geográficas con una ionosfera muy activa.

Para solucionar este problema, esta tesis propone el concepto de "Network-GBAS", en el que varias estaciones de referencia colaboran para monitorizar los gradientes ionosféricos. Este concepto consta de dos pasos. Primero, la red detecta los gradientes ionosféricos, estima sus parámetros y transmite esta información a las estaciones GBAS instaladas en su zona de cobertura. A continuación, las estaciones GBAS sustituyen el valor del gradiente basado en el modelo de amenaza por la información del gradiente proporcionada por la red. Este enfoque reduce el conservadurismo y conduce a una mejora de la

disponibilidad del sistema sin comprometer la integridad del usuario.

Esta tesis valida el rendimiento de los algoritmos de detección y estimación con gradientes ionosféricos simulados y reales de dos lugares diferentes conocidos por sus altos niveles de actividad ionosférica. Uno de los lugares es Alaska, en dónde los gradientes anómalos reales analizados son de pequeño tamaño, pero se mueven a altas velocidades; el otro lugar es Brasil, en dónde los gradientes característicos son de gran tamaño, pero lentos.

La evaluación del concepto de "Network-GBAS" compara en simulaciones la disponibilidad de una estación GBAS de Categoría I (CAT I) situada en la ubicación de Brasil en dos casos: asumiendo el modelo conservador de amenaza ionosférica, y utilizando la información del gradiente proporcionada por la red. En un día nominal, seleccionado para este estudio, la disponibilidad del sistema mejoró del $79,5\%$ al $94,6\%$ durante la noche. En un día activo, la disponibilidad mejoró del $68,7\%$ al $89,5\%$ durante la noche. Durante el día, la disponibilidad alcanzó el 100% en ambos días.

Los resultados demuestran que el concepto de "Network-GBAS" mejora significativamente la disponibilidad de una estación GBAS CAT I en regiones ionosféricas activas sin comprometer la integridad del usuario. Además, al incorporar la información proporcionada por la red en las soluciones existentes, el "Network-GBAS" es compatible con los algoritmos y el *hardware* existentes, por lo que sería certificable si se adapta a las características de cada región en la que se instale GBAS.

Resum

El Sistema d'augmentació basat en terra (GBAS per les sigles en anglès) és un sistema d'àrea local que s'instal·la als aeroports. GBAS augmenta els senyals dels Sistemes de Navegació Globals per Satèl·lit (GNSSs) i proporciona a les aeronaus la informació necessària per fer aproximacions de precisió. El seu objectiu principal és millorar el rendiment de GNSS en termes d'integritat, continuïtat, exactitud i disponibilitat, mitjançant la transmissió de correccions diferencials i paràmetres d'integritat. Les correccions diferencials permeten a l'aeronau millorar la exactitud de la seva posició. Els paràmetres d'integritat permeten calcular límits per als errors residuals de la posició. Addicionalment, l'estació GBAS monitoritza i exclou els satèl·lits afectats per qualsevol tipus de fallida del sistema per tal de garantir la integritat i la seguretat dels usuaris.

Entre les fonts d'error de GNSS, la ionosfera és la més important i més impredictible. En condicions ionosfèriques anormals, grans gradients ionosfèrics poden produir una diferència significativa entre l'error ionosfèric observat per l'estació GBAS i l'aeronau. Si aquesta diferència no es detecta i mitiga, pot provocar grans errors en la posició de l'aeronau. Les solucions GBAS convencionals per mitigar aquesta amenaça assumeixen que sempre és present el gradient ionosfèric més gran mai observat a la regió pertinent, la qual cosa constitueix una suposició molt conservadora. Aquest enfocament, basat en els models conservadors d'amenaça ionosfèrica derivats per a GBAS, maximitza la integritat, sovint a costa de la disponibilitat i la continuïtat del sistema, especialment en zones geogràfiques amb una ionosfera molt activa.

Per solucionar aquest problema, aquesta tesi proposa el concepte de "Network-GBAS", en què diverses estacions de referència col·laboren per monitoritzar els gradients ionosfèrics. Aquest concepte consta de dos passos. Primer, la xarxa detecta els gradients ionosfèrics, estima els seus paràmetres i transmet aquesta informació a les estacions GBAS instal·lades a la seva zona de cobertura. Tot seguit, les estacions GBAS substitueixen el valor del gradient basat en el model d'amenaça per la informació del gradient proporcionada per la xarxa. Aquest enfocament redueix el conservadorisme i condueix a una millora de la disponibilitat del sistema sense comprometre la integritat de l'usuari.

Aquesta tesi valida el rendiment dels algorismes de detecció i estimació amb

gradients ionosfèrics simulats i reals de dos llocs diferents coneguts pels alts nivells d'activitat ionosfèrica. Un dels llocs és Alaska, on els gradients anòmals reals analitzats són de petit tamany, però es mouen a altes velocitats; l'altre lloc és Brasil, on els gradients característics són de grans dimensions, però lents.

L'avaluació del concepte de "Network-GBAS" compara en simulacions la disponibilitat d'una estació GBAS de categoria I (CAT I) situada a la ubicació del Brasil en dos casos: assumint el model conservador d'amenaça ionosfèrica, i utilitzant la informació del gradient proporcionada per la xarxa. En un dia nominal, seleccionat per a aquest estudi, la disponibilitat del sistema va millorar del $79,5\%$ al $94,6\%$ durant la nit. En un dia actiu, la disponibilitat va millorar del $68,7\%$ al $89,5\%$ durant la nit. Durant el dia, la disponibilitat va assolir el 100% en tots dos dies.

Els resultats demostren que el concepte de "Network-GBAS" millora significativament la disponibilitat d'una estació GBAS CAT I en regions ionosfèriques actives sense comprometre la integritat de l'usuari. A més, en incorporar la informació proporcionada per la xarxa en les solucions existents, el "Network-GBAS" és compatible amb els algorismes i el *hardware* existents, per la qual cosa seria certificable si s'adapta a les característiques de cada regió on s'instal·li GBAS.

Acknowledgments

This PhD has been a very important experience in my career and I would like to thank the people who have accompanied me on this long journey.

First of all, I would like to thank Prof. Jaume Sanz and Prof. José Miguel Juan for their continuous support and encouragement. Although I was not working at the Polytechnic University of Catalonia (UPC), they were always available for technical discussions and kept supporting my efforts. Their expertise and advice have steered my research into the right direction and I appreciate all their involvement, contributions, and new ideas that helped to improve and finalize this work. I would also like to thank Prof. Guillermo González, and the colleagues from UPC, Dr. Adrià Rovira and Deimos Ibañez, for their direct help and support in carrying out this work.

I conducted the research and produced this thesis as part of my work at the Institute of Communications and Navigation of the German Aerospace Center. I would like to thank the head of the Institute, Prof. Christoph Günther, as well as the head of the Navigation Department, Prof. Michael Meurer, and the head of the Visual and Terrestrial Augmentation Systems group, Dr. Chen Zhu, for giving me the opportunity to conduct the research presented in this thesis and to combine my research with project work. I would like to give special thanks to Dr. Michael Felux, who was my mentor throughout all these years both technically and personally and became a very good friend. He introduced me to the world of GBAS and taught me not to be afraid of presenting in public. I would also like to thank Dr. Simona Circiu and Dr. Okuary Osechas, my mentors in the second half of my PhD. Their support, guidance and encouragement helped me to go the long way to the completion of this thesis. I am also very grateful to my colleague Daniel Gerbeth, office mate and friend, who has always been willing to discuss technical problems and help in solving any kind of issue. This thesis would not have been possible without his expertise on various programming languages. Many thanks also to the rest of my DLR colleagues, many of them now friends, with whom I have shared many discussions and worked together: Dr. Omar García, Anja Grosch, Dr. Santiago Perea, Dr. Marion Gödel, Dr. Friederike Fohlmeister, Shrivatsan Naranayan, Gianluca Zampieri, Markus Rippl, Dr. Stefano Caizzone, and a long etcetera.

I would like to extend my sincere thanks to my friends for being by my side during these years, motivating and supporting me.

Finalmente, pero no por eso menos importante, me gustaría expresar mi profunda gratitud a mis padres y al resto de mi familia. A pesar de estar a miles de kilómetros de distancia, siempre han encontrado la manera de darme la fuerza que necesitaba en épocas de altibajos con sus llamadas, visitas y mensajes. También me gustaría darle las gracias, muy especialmente, a Alberto, que ha permanecido a mi lado durante todo este proceso. Sin su apoyo, su paciencia y sus ánimos, que me han dado la fuerza y la motivación hasta el final, esta tesis no habría sido posible.

Contents

List of Figures

List of Tables

Acronyms

AADs Airborne Accuracy Designators
AAD A Airborne Accuracy Designator A
AAD B Airborne Accuracy Designator B
AAIM Aircraft Autonomous Integrity Monitoring
ABAS Aircraft Based Augmentation System
ALs Alert Limits
APV-I Approach with Vertical Guidance I
APV-II Approach with Vertical Guidance II
ARAIM Advanced Receiver Autonomous Integrity Monitoring
AATR Along Arc TEC Rate
CAT I Category I
CAT II Category II
CAT III Category III
CAT IIIa Category IIIa
CAT IIIb Category IIIb
CAT IIIc Category IIIc
CCD Code Carrier Divergence
CDF Cumulative Distribution Function
CONUS Conterminous United States
CORS Continuously Operating Reference Stations
DH Decision Height
DLL Delay Lock Loop
DSIGMA Dual-Solution Ionospheric Gradient Monitor
ECEF Earth-Centered Earth-Fixed
EGNOS European Geostationary Navigation Overlay Service
EPB Equatorial Plasma Bubble
GAD Ground Accuracy Designator
GAD A Ground Accuracy Designator A
GAD B Ground Accuracy Designator B
GAD C Ground Accuracy Designator C
GASTs GBAS Approach Service Types
GAST A GBAS Approach Service Type A
GAST B GBAS Approach Service Type B

GAST C GBAS Approach Service Type C
GAST D GBAS Approach Service Type D
GAST F GBAS Approach Service Type F
GAST X GBAS Approach Service Type X
GBAS Ground Based Augmentation System
GDOP Geometry Dilution Of Precision
GI Geometry Index
GLONASS Global Navigation Satellite System
GNSS Global Navigation Satellite System
GPS Global Positioning System
HMI Hazardously Misleading Information
ICAO International Civil Aviation Organization
IEV Ionosphere-induced Error in Vertical
IGM Ionospheric Gradient Monitor
ILS Instrument Landing System
IPP Ionospheric Pierce Point
LAL Lateral Alert Limit
LOI Loss of Integrity
LPL Lateral Protection Level
LPV Localizer Performance with Vertical guidance
LSTIDs Large Scale Travelling Ionospheric Disturbances
MAP Missed Approach Point
MDA Minimum Descent Altitude
MDE Minimum Detectable Error
MDG Minimum Detectable Gradient
MIEV Maximum Ionosphere-induced Error in Vertical
MMR Multi-Mode Receiver
MLAs Multipath Limiting Antennas
MODIP Modified Dip Latitude
MRCC Multiple Receiver Consistency Check
MW Melbourne-Wübbena
PDF Probability Distribution Function
PDGS Position Domain Geometry Screening
PFA Probability of False Alert
PHMI Probability of Hazardously Misleading Information
PLL Phase Lock Loop
PLs Protection Levels
PMD Probability of Missed Detection
PNE Probability of Non-bounded Errors
PRN Pseudorandom noise
RAIM Receiver Autonomous Integrity Monitoring
RBMC Brazilian Network for Continuous Monitoring of GPS
RFI Radio Frequency Interference

RNAV Area Navigation
RVR Runway Visual Range
SARPS Standards and Recommended Practices
SBAS Satellite Based Augmentation System
SESAR Single European Sky ATM Research
SiS Signal-in-Space
TEC Total Electron Content
TECU TEC Unit
TEL Tolerable Error Limit
TTA Time to Alert
VAL Vertical Alert Limit
VDB Very High Frequency Data Broadcast
VHF Very High Frequency
VPL Vertical Protection Level
WAAS Wide Area Augmentation System

Nomenclature

Measurements and measurement errors

Symbol	Description	Unit
ρ	Pseudorange (referred also as code) measurement	m
ϕ	Carrier-phase measurement	m
R	Geometric range	m
δt_r	User clock bias	s
δt^j	Satellite clock bias	s
T	Tropospheric error	m
I	Ionospheric error	m
MP_ρ	Pseudorange multipath error	m
η_ρ	Pseudorange receiver thermal noise error	m
MP_ϕ	Carrier-phase multipath error	m
η_ϕ	Carrier-phase noise error	m
N	Carrier-phase ambiguity	cycles
θ	Satellite elevation angle	deg
ψ	Satellite azimuth angle	deg
λ	Wavelength	m
τ	Smoothing time constant	s
ΔT	Measurement sampling rate	s
c	Speed of light in vacuum	m/s
θ_{GPA}	Glidepath angle	deg
t	Measurement epoch	unitless
$\mathcal{J}$	Number of satellites used	unitless
$\mathcal{R}_\mathcal{G}$	Number of GBAS reference receivers	unitless

For a given measurement, e.g. $\rho^j_{i,r}(t)$, the indexes refer to the satellite j, recorded by receiver r on frequency band i at time t. An overline ($\bar{\rho}$) indicates that the measurements have been smoothed.

GBAS ground subsystem parameters

Symbol	Description	Unit
PRC_{CSC}	Smoothed pseudorange correction	m
PRC_{SCA}	Smoothed receiver clock adjusted pseudorange correction	m
PRC_{TX}	Transmitted pseudorange correction	m
RRC_{TX}	Transmitted range rate correction	m/s

Aircraft position solution

Symbol	Description	Unit
Δh	Height of the aircraft above the GBAS reference station	m
$\boldsymbol{x_{air}}$	Aircraft position vector in ECEF	m
$\boldsymbol{x}^j$	Satellite position vector in ECEF	m
$\tilde{\varepsilon}_\rho$	Residual pseudorange error	m
$\bar{\rho}_{air,corr}$	Corrected pseudorange measurement	m
$\Delta\rho$	Difference between the smoothed corrected pseudorange measurement and the geometric range	m
$\boldsymbol{\Delta x_{air}}$	Vector containing the increment of position in ECEF and the increment of the clock offset	[m,m,m,s]
$\boldsymbol{G}$	Geometry matrix	unitless
$\boldsymbol{S}$	Weighted least-squares projection matrix	unitless
$\boldsymbol{W}$	Weighting matrix	$1/m^2$

For a given parameter, e.g. $\widehat{I}$, a hat indicates that it is an estimation.

Integrity parameters and requirements

Symbol	Description	Unit
TC	Differential tropospheric correction	m
N_r	Refractivity index of the atmosphere	unitless
h_0	Tropospheric scale height	m
σ_{GBAS}	Standard deviation of the total GBAS fault-free error	m
σ_{pr_gnd}	Standard deviation of the ground pseudorange error	m
σ_{pr_air}	Standard deviation of the airborne residual error	m

σ_{iono}	Standard deviation of the residual ionospheric error	m
σ_{tropo}	Standard deviation of the residual tropospheric error	m
σ_{vig}	One-sigma variation in the vertical ionospheric delay per user-to-reference separation	mm/km
$\sigma_{anomalous\_tropo}$	One-sigma bound for anomalous tropospheric gradients	mm/km
σ_{ref}	Standard deviation of the refractivity uncertainty	m
σ_n	Standard deviation of code receiver noise	m
σ_{mp}	Standard deviation of code multipath error	m
s_{apr_vert}	Projection factor from pseudorange domain into vertical position domain in approach coordinates	unitless
VPL_{H_0}	Fault-free vertical protection level	m
VPB	Vertical ephemeris protection level	m
x_{Air}	Horizontal distance from the airplane to the GBAS reference point	m
v_{Air}	Aircraft speed	m/s
P	Ephemeris decorrelation parameter	unitless
D_v	Difference in vertical position between 30 seconds smoothed and 100 second smoothed position solution	m
P_{md}	Probability of missed-detection	unitless
P_{fa}	Probability of false alert	unitless
$P_{LOI,abnormal\_iono}$	Probability of Loss of Integrity (LOI) due to anomalous ionosphere	unitless
$P_{md,abnormal\_iono}$	Probability of missed detection given the existence of abnormal ionospheric activity	unitless
$P_{prior,abnormal\_iono}$	Prior probability of an anomalous ionospheric gradient occurring	unitless
P_{ne}	Probability of non-bounded errors	unitless
k_{ffmd}	Fault-free missed detection multiplier	unitless
k_{md}	Missed detection multiplier to meet the required probability of missed detection	unitless
k_{md_e}	Sigma multiplier for the missed detection probability needed to cover ephemeris faults	unitless
k_{fa}	False alert multiplier to meet the required probability of false alert	unitless
$k_{md,abnormal\_iono}$	One-sigma multiplier to meet the required probability of missed detection given the existence of abnormal ionospheric activity	unitless

k_{ne}	One-sigma multiplier to meet the required probability of non-bounded errors	unitless

Ionosphere and ionospheric gradient parameters

Symbol	Description	Unit
F_{pp}	Vertical-to-slant obliquity factor	unitless
R_e	Radius of the Earth	m
h_I	Ionospheric thin shell height	m
g_{iono}	Slant slope of the ionospheric gradient	mm/km
w_{iono}	Width of the ionospheric gradient	km
v_{iono}	Speed of the ionospheric gradient	m/s
d_{iono}	Direction of the ionospheric gradient	deg
D_{iono}	Maximum differential delay	m
$g_{iono,vert}$	Vertical slope of the ionospheric gradient	mm/km
zl_{iono}	Zonal length	km

Integrity monitoring

Symbol	Description	Unit
MDE	Minimum detectable error	varies
Thr	Monitor threshold	varies
$I_{monitor}$	Inflation factor to overbound non-Gaussian tails for monitoring	unitless
$\sigma_{monitor}$	Standard deviation of the test statistic distribution for monitoring	varies
$MDDR_{ccd}$	Minimum detectable error of the CCD monitor	m/s
ε	Ionosphere-induce range error	m
Δv	Relative speed between the ionospheric gradient and the IPP	varies
IEV	Ionosphere-induced error in vertical	m
I_{vig}	Inflation factor for σ_{vig}	unitless
I_{gnd}	Inflation factor for σ_{pr_gnd}	unitless
$Tcsd_{GF}$	Threshold for the geometry-free cycle slip detector	m
$Itest$	Test statistic of the network-based ionospheric gradient monitor	mm/s
$\mathcal{R}$	Number of receivers of the network	unitless
μ_{Itest}	Mean of $Itest$ in nominal conditions	mm/s
σ_{Itest}	Standard deviation of $Itest$ in nominal conditions	mm/s

$\boldsymbol{B_{Itest_r}}$	Buffer containing a history of test statistic values	mm/s
κ_r	Time delay between detection at station r and the station of reference	s
$t_{d,r}$	Time of detection at station r	s
N_B	Size of the buffers for the cross-correlation process	unitless
α	Cross-correlation coefficient	unitless
ζ	Planar wave phase	rad
ω	Angular frequency	rad/s
$\boldsymbol{x}$	IPP position vector	m
$\boldsymbol{k}$	Wave propagation vector	rad/m
$\boldsymbol{v}$	Vector of the speed of the gradient	m/s
$\boldsymbol{s}$	Slowness vector	s/m
$\boldsymbol{\Delta x}$	Difference of IPP position vectors	m
$\boldsymbol{X}$	Matrix containing the difference of IPP position vectors	m
$\boldsymbol{z}$	Vector containing time delays	s
$\boldsymbol{W_\alpha}$	Weighting matrix	unitless
$\boldsymbol{v_{IPP}}$	IPP speed vector	m/s
T_W	Time width of the gradient	s
GI	Geometry index	1/m
$I_{g_{iono}}$	Inflation factor for overbounding the slope estimation errors	unitless
$\sigma_{g_{iono}}$	Standard deviation of slope estimation errors	mm/km

Vectors are expressed in bold lowercase letters and matrices are expressed in bold uppercase letters. The product between two scalars is expressed with a dot ($\cdot$). The scalar product between two vectors is expressed with a dot ($\cdot$). The product between two matrices is expressed without a dot and without a space.

1 Introduction

1.1 GNSS and its use in aviation

Air transport is considered one of the greatest contributors to the advancement of modern society, as it provides a rapid and reliable means of transport for millions of people and goods around the world [1, 2]. Due to its importance for society and the economy, different studies worldwide have predicted a significant increase in world air traffic in the coming years [3, 4, 5]. However, the capacity of busy airports and airspace surrounding those airports is not increasing at the same rate [6, 7].

In this scenario, Global Navigation Satellite Systems (GNSSs) play an important role in aeronautical navigation, which was supported only by on-board inertial navigation systems and ground-based radio navigation aids in the past. The reason is that they provide global coverage and significantly enhanced navigation performance that enable more efficient use of airspace and airport capacity. However, standalone GNSS positioning is not able to meet the stringent requirements demanded by the International Civil Aviation Organization (ICAO) for all phases of flight [8] because in addition to a high level of accuracy, different levels of integrity, continuity, and availability are required.

Therefore, the use of additional methods to achieve the required level of performance is needed. GNSS augmentation systems provide integrity information for the primary GNSS satellite core constellations as, for example, the US Global Positioning System (GPS), and improve the accuracy of the user position solution with respect to unaugmented use of the primary GNSS constellations. According to the origin of the augmentation information and how the performance of the navigation signals is monitored, these systems can be classified in three different groups: Aircraft Based Augmentation Systems (ABASs), Satellite Based Augmentation Systems (SBASs), and Ground Based Augmentation Systems (GBASs).

In ABAS, GNSS augmentation is fully performed on the aircraft, which is fully responsible for integrity monitoring. Unlike the remaining augmentation

systems, ABAS focuses on integrity only and not on improving position solution accuracy (i.e. no corrections are provided). Typically, augmentation is achieved by two methods: the inclusion of additional sensors and the leveraging of redundant GNSS measurements. The first type of ABAS, so-called Aircraft Autonomous Integrity Monitoring (AAIM), combines GNSS signals with additional measurements coming from altimetry systems or inertial sensors and can provide horizontal and vertical navigation down to 350-ft Minimum Descent Altitude (MDA) for a Non-Precision Approach [9] (one foot (ft) is equivalent to 0.3048 meters (m)). The second type of ABAS, so-called Receiver Autonomous Integrity Monitoring (RAIM) [10, 11], detects and excludes potentially corrupted ranging signals on the aircraft by leveraging redundant GNSS measurements. However, current RAIM supports only Non-Precision Approaches using a single-frequency single-constellation architecture (GPS L1). The Advanced Receiver Autonomous Integrity Monitoring (ARAIM), which is an extension of the "traditional" RAIM, is still under development. It uses signals from two frequencies and multiple constellations to detect and mitigate independent and correlated GNSS signal faults, which will make it possible to support applications such as aviation precision approaches [12, 13].

SBAS is a form of wide area differential GNSS. It uses a network of accurately located ground reference stations spread over continental regions to compute integrity and correction information for one or more primary GNSS constellations. This information is then broadcast to the covered area using geostationary (GEO) satellites. The differential corrections enable an aircraft approaching an airport to correct the navigation satellite measurements by removing the spatially correlated errors between the ground stations and the aircraft. Thus, the aircraft is able to improve the accuracy of its position estimation. Additionally, the integrity parameters enable the airborne system to calculate bounds on the residual position errors and ensure safety of the operation. In SBAS coverage areas, GNSS-based precision approaches are already established today. The Wide Area Augmentation System (WAAS) and the European Geostationary Navigation Overlay Service (EGNOS), the United States and the European systems respectively, are certified as precision approach guidance systems for approaches with Localizer Performance with Vertical guidance (LPV) down to a decision height of 200 ft (LPV-200) [14, 15]. However, for precision approach guidance under visibility conditions lower than the Category I (CAT I) minima (i.e. a cloud ceiling lower than 200 ft or a visibility of less than 800 m or a runway visual range of less than 500 m), local augmentation provided by GBAS is necessary to meet the stringent performance requirements.

GBAS is a local area, airport-based differential GNSS that also supports one or more primary GNSS constellations. It is the only system based on GNSS that can support approaches under Category III (CAT III) weather conditions

including automatic landings. The principle of GBAS is not significantly different from SBAS. A GBAS reference station broadcasts differential corrections along with integrity parameters. As in SBAS, the aircraft uses the differential corrections to improve its position estimation and the integrity parameters to calculate reliable bounds on the residual position errors. The main difference between the two is that GBAS corrections to satellite pseudoranges are computed using only the ground infrastructure installed inside the protected area of an airport. Therefore, GBAS is more accurate than SBAS, since pseudorange error characteristics are more similar the closer the ground receivers are located from the aircraft. Furthermore, GBAS provides scalar corrections (i.e., one value for each satellite) while SBAS provides vector corrections (i.e., satellite orbit correction, satellite clock correction, and ionospheric correction). GBAS pseudorange corrections and integrity parameters are broadcast to users through Very High Frequency Data Broadcast (VDB) antennas located at an airport to provide optimal coverage of its runways and approach paths. The currently certified GBAS augments GPS L1 service supporting only CAT I precision approach operations. The standards to support approaches under CAT III weather conditions were published at the end of 2018 [8], and ground stations meeting this standard are expected to be operational in the near future.

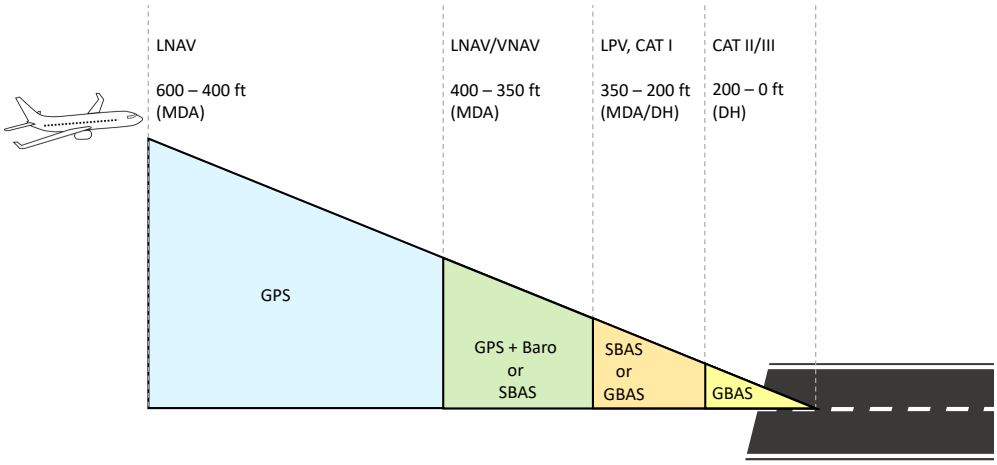

Figure 1.1: Aircraft approach procedures based on GNSS augmentation systems.

Figure 1.1 illustrates the application of each GNSS augmentation system attending to the requirements of each phase of flight in terms of MDA and/or Decision Height (DH) expressed in feet (information taken from [9]). Note that the MDA and the DH refer to different requirements. The MDA is a specified altitude or height in a Non-Precision Approach below which the aircraft must not descend without the required visual reference [16]. Therefore, an aircraft flying a Non-Precision Approach remains at the MDA until the pilot can see

the runway and continues the descent to land. If the aircraft reaches the Missed Approach Point (MAP) and the pilot still cannot see the runway, the Missed Approach procedure must be initiated. The DH is a specified altitude in the Precision Approach (approach with vertical guidance) at which a Missed Approach must be initiated if the required visual reference to continue the approach has not been established [16].

1.2 State of the art and motivation

For more than 50 years, airports have relied on the Instrument Landing System (ILS) to provide pilots with approach and landing guidance in low-visibility conditions. Although the system has proved to be reliable and functional, ILS is costly to maintain and has operational limitations that reduce runway capacity in certain conditions. In contrast to the conventional ILS in use today, GBAS can provide approach guidance to multiple runway ends at an airport and thus can significantly reduce the required amount of infrastructure and the associated costs. Furthermore, it provides a steadier approach guidance signal than ILS [17] and could reduce environmental impacts due to shorter routes and noise abatement.

A GBAS station can offer two types of services: the Positioning Service and the Approach Service [18]. The GBAS Positioning Service provides horizontal position information with integrity and supports Area Navigation (RNAV) operations. The GBAS Approach Service provides guidance on the final approach segment by outputting ILS-like deviation information relative to a defined reference path. Currently, only the GBAS Approach Service is operational. GBAS Approach Service Type C (GAST C) stations, which support operations under CAT I weather conditions, have been certified and are fully operational. In the last years, an increasing number of stations are used on a regular basis for approach guidance in Newark, Houston, Sydney, Malaga, Frankfurt, and Zurich [19]. Standards for GBAS Approach Service Type D (GAST D) stations, which are designed to support precision approaches and automatic landings under CAT III weather conditions, have been agreed upon by ICAO at the end of 2016 [20] and are in effect since November 2018. However, the ground stations and the avionics equipment are still under development.

The current GBAS architecture for both GAST C and GAST D is based on the use of a single constellation (GPS) and single frequency (L1 C/A code). The GBAS reference station broadcasts differential corrections that enable airborne users to correct most of the spatially correlated GPS ranging errors, including the ones caused by the ionospheric delay, which is typically the largest source of error. Nevertheless, residual errors still remain for which models are derived at the range domain. At the position domain, so-called Protection Levels

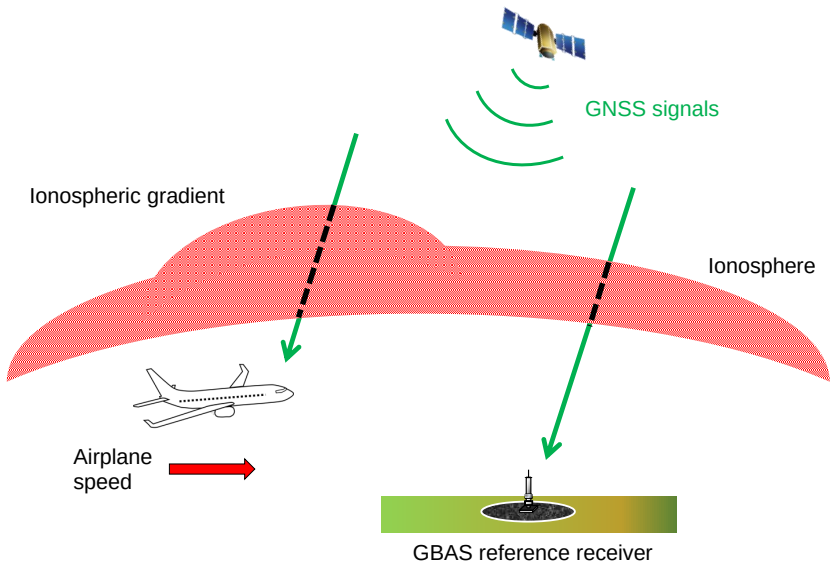

Figure 1.2: Ionospheric gradient threat in GBAS.

(PLs) are calculated by the avionics using these error models and the integrity parameters received from the GBAS ground station. Then, they are compared to the Alert Limits (ALs), the maximum allowable bounds, to determine safety of the operation for each user. If any of the PLs exceed the corresponding ALs, GBAS is unavailable.

The component of the PLs that describes the remaining residual errors due to the nominal ionospheric decorrelation between the reference station and the user is called σ_{vig}. This integrity parameter, explained in more detail in Section 2.3.3.5, is broadcast by the ground station and derived based on historical data collected in the relevant regions [21, 22, 23]. However, under abnormal ionospheric activity such as large ionospheric gradients, there could be a large difference between the ionospheric error experienced by the GBAS reference station and the aircraft, as shown with the black dashed lines in Figure 1.2. Since this error is not corrected through the use of the differential corrections and is also not overbounded by the PLs, the presence of spatial abnormal ionospheric gradients may lead to non-differentially-corrected and insufficiently bounded position errors [24].

Protection of airborne users against the ionospheric gradient threat has already been tackled in GAST C and GAST D. In GAST C, it is the sole responsibility of the ground subsystem to ensure mitigation of anomalous ionospheric errors. The GAST C station implements a monitor called Code Carrier Di-

vergence (CCD) that allows the detection of abnormally large gradients in the experienced ionospheric delay [25]. However, this monitor alone is not sufficient to mitigate all hazardous ionospheric errors. For this reason, a GAST C ground station verifies by simulation that each satellite geometry potentially usable at the aircraft (PLs $\leq$ ALs) is safe in the presence of the ionosphere-anomaly threat applicable in the region in a process called "Position Domain Geometry Screening (PDGS)" ([26, 27, 28]). In case a simulated satellite geometry is not safe, the ground station inflates the integrity parameters so that the PLs exceed the ALs when an arriving aircraft aims to use this satellite geometry, making GBAS unavailable. These ionosphere-anomaly threats form the so-called "ionospheric threat model", which is based on the worst-ever-experienced ionospheric gradients measured in the relevant regions and defines a range of values for the gradient parameters that could harm GBAS ([29, 23, 30, 31]). The main problem in this case is that the PDGS methodology assumes that the "worst-case" or largest gradient is always present. This is a very conservative assumption since large ionospheric gradients typically occur around solar maximums, which are linked to the phase of the 11-year solar cycle and also depend on the geomagnetic latitude, the time of the day, and the season within a year [32]. Despite this conservative assumption, the PDGS method has been shown to meet the CAT I availability requirements in the Conterminous United States (CONUS), which is representative of the mid-latitudes [26]. Nevertheless, the assessment of the Brazilian and Asia-Pacific GBAS ionospheric threat models performed by Yoon et al. in [30] and Saito et al. in [31] respectively showed the existence of much larger spatial gradients (produced by so-called Equatorial Plasma Bubbles (EPBs)) than those of the mid-latitudes (e.g. CONUS [29] or German [23] threat models). The very severe ionospheric threat models developed for the equatorial regions together with the assumption of an "always present ionospheric gradient" resulted in excessive inflation of the integrity parameters when using the PDGS methodology, decreasing GBAS availability to 58.3% in Brazil [28].

Therefore, recent studies have focused on reducing the above conservative assumptions in order to meet CAT I availability requirements in equatorial regions. Yoon et al. propose in [28] a probabilistic method that uses Monte Carlo simulations and a prior probability of extreme EPBs occurring to reduce the required inflation factors. However, although the system availability for CAT I precision approaches improved to 89.6%, it is not yet sufficient to achieve the required 99%. In [33], Yoon et al. propose to use the existing information about the characteristics of the EPBs to improve the stochastic approach developed in [28]. However, the lack of sufficient historical data collected during large ionospheric events in equatorial regions might limit the use of this approach. Furthermore, this method cannot predict and protect against a larger gradient that might occur at some point in time in the future.

In GAST D, new monitors implemented on the airborne and ground are responsible to mitigate these errors and their risks [34]. The new monitors implemented on the airborne are: the CCD and the Dual-Solution Ionospheric Gradient Monitor (DSIGMA). The general monitoring principle for CCD implemented at the airborne stays unchanged from the ground CCD monitor implemented in GAST C, but different time constants and different detection thresholds are used in GAST D [34]. DSIGMA is specific to the GAST D system as it compares the difference between the 30 seconds and the 100 seconds smoothed measurements [34]. However, even if most of the responsibility in mitigating the ionospheric anomaly is shifted to the airborne, the standards require also the ground to detect ionospheric gradients that are not visible to the aircraft. Thus, on the ground an Ionospheric Gradient Monitor (IGM) [35] and the CCD monitor are implemented to detect a portion of the threat space. The CCD monitor implemented on ground for GAST D also has the same monitoring principle as the one implemented for GAST C but again uses a different time constant and a different threshold. The IGM needs a very precise phase center stability (in the order of mm) and has associated siting constraints of the GBAS reference receiver antennas to ensure that all potential gradients can be detected. Especially at large, space constrained airports this causes significant problems in finding appropriate sites for the ground station. Furthermore, the baseline concept of GAST D assumes that the prior probability of occurrence of an anomalous ionospheric gradient is one. This assumption, as previously mentioned, is conservative and requires that the monitors designed to protect integrity in GAST D be very sensitive and trigger false alerts. Recent studies [36] suggest reducing this prior probability of occurrence to 10^{-3}, which would significantly relax the monitoring thresholds making the implementation of GAST D easier in regions where its availability is degraded. However, the derivation of the prior probabilities of occurrence of an anomalous ionospheric gradient relies on a statistical approach that uses historical data. Therefore, again, the lack of sufficient historical data collected under active ionospheric conditions could limit the use of this statistical approach. Due to the these issues, it is expected that the current version of GAST D will not meet the operational requirements (especially continuity and availability) in regions with more severe ionospheric conditions than those present in mid-latitudes [8].

All the methodologies mentioned above for ionospheric threat mitigation in GBAS have one characteristic in common: they consider only the ionospheric information obtained from ground infrastructure installed inside the protected area of the airport or from the aircraft itself. This implies poor observability of certain gradients and forces the GBAS ground station to make conservative assumptions to protect integrity, which impacts the availability of the system. For that reason, Lee et al. propose in [37] a methodology for real-time ionospheric threat adaptation using predicted values of space weather indices. Since

space weather prediction itself is unreliable due to prediction errors, the authors also develop an uncertainty model derived from historical data in order to feed this external information into GBAS. However, even if such an uncertainty model is developed, these indices come from an external source not controlled by the service provider, which could lead not only to integrity issues but also to security threats. Furthermore, the methodology in [37] was only tested with data from mid-latitudes, which are significantly less active than the equatorial regions.

In recent years, with the launch of new satellites that transmit signals in the L5/E5a frequency band (a second frequency band that can be used for air navigation), the use of dual-frequency and multi-constellation algorithms has become a promising solution to mitigate the ionospheric gradient threat (especially in equatorial regions). Dual-frequency methods allow better detection of ionospheric gradients or forming an ionosphere-free combination of the navigation signals for positioning. The use of more than one constellation makes the system less vulnerable to signal loss due to ionospheric scintillations. However, until today, no clear concept for future dual-frequency multi-constellation GBAS that provides improved performance compared to the current single-frequency single-constellation systems has been established. Two different options for the future GBAS system, which will support CAT III precision approaches and automatic landings, are under discussion: the GBAS Approach Service Type F (GAST F) concept being developed primarily through the Single European Sky ATM Research (SESAR) program in Europe [38, 39], and the GBAS Approach Service Type X (GAST X) concept being developed primarily in the United States [40, 41]. Both concepts propose to shift all responsibility for anomalous ionospheric gradient monitoring to the aircraft. This has the advantage of allowing more realistic error bounding because the actual real-time navigation and aircraft performances can be exploited and less conservative assumptions have to be made. Another approach ([42]) proposes the use of a dual-frequency carrier-phase based ionospheric gradient monitor installed at the ground station to support future GBAS. This monitor, as its single-frequency version for GAST D (IGM), assumes a prior probability of occurrence of anomalous ionospheric gradients of 10^{-3}, which is a conservative value for CONUS but not for equatorial regions like Brazil during nighttime. Furthermore, the baseline between the two GBAS receivers performing the monitoring is expected to be at least 1 km, which is unusual, thus maintaining some of the siting constraints of the single-frequency version. Validation of this monitor has been carried out only in simple simulations, using a cut-off satellite elevation angle of 15°. However, the signals from satellites at elevations between 5° and 15°, which are used in GBAS, experience most of the cycle slips and scintillation. This could seriously impair the false alert probability and carrier phase ambiguity resolution on which this monitor depends. The

next generation of dual-frequency multi-constellation GBAS brings with it new technical, regulatory, and political challenges that must be resolved before it can become operational. In fact, standards for future GBAS are not expected to be finalized before 2030.

Therefore, it is clear that increasing GBAS availability in equatorial regions remains a challenge nowadays that needs to be solved so that GBAS can become the primary guidance system for precision approaches and landings worldwide.

1.3 Research questions and objectives

The main objective of this thesis is to support the development of GBAS worldwide by proposing a methodology to increase its availability in geographic areas with highly active ionosphere without compromising user integrity. This thesis focuses on increasing the system availability in active ionospheric regions for the currently operational system (GAST C). The motivation is to provide a solution for all aircraft on which GBAS is to be installed until the date when the new GAST F/X stations are operational, which is expected to be not earlier than 2037.

To this end, this thesis develops a real-time ionospheric gradient monitoring concept that reduces the existing excess of conservatism in the current GBAS assumptions adopted to mitigate the ionospheric threat. The concept is based on the use of a dual-frequency, multi-constellation wide-area network that monitors for ionospheric gradients and transmits this information to GBAS stations installed in the coverage area.

However, the inclusion of ionospheric information external to the GBAS installation implies a high risk to the overall integrity of the system, as discussed in Section 1.2. For this reason, this thesis has two sub-objectives: i) the proposed solution must provide sufficiently reliable ionospheric information to meet the integrity requirements of GBAS, and ii) it must be certifiable with minimal additional effort and maintain compatibility with existing hardware with as few modifications as possible.

To achieve these objectives, this thesis should answer the following Research Questions (RQ):

- **RQ1:** How can the existing excess of conservatism be reduced in current GBAS solutions to mitigate the ionospheric gradient threat without compromising user integrity?
- **RQ2:** What is the interface to current GBAS solutions so that no changes to the current standards are required?

- **RQ3:** What is the performance of the proposed method under nominal and highly active ionospheric conditions?
- **RQ4:** How much does the proposed concept increase GBAS availability in geographic areas with highly active ionosphere relative to current state-of-the-art solutions?

Note that this work does not consider the secured communication link required between the network and the specific GBAS stations. This topic is left for future work to experts in these areas.

1.4 Thesis outline and contributions

This thesis proposes solutions to the research questions identified above. Each solution and the main contributions of this thesis are presented in Chapters 3 to 6. Therefore, this section gives only a brief summary of the major contributions together with an outline of the thesis.

Chapter 2 provides a detailed overview of the single-frequency single-constellation GBAS fundamentals and the main existing solutions for the ionospheric threat mitigation. The first part of the chapter focuses on explaining the generation of GBAS corrections and the calculation of the aircraft's position. It also describes the error sources and the integrity concept, including the calculation of the protection levels and a brief description of the main integrity monitors. The second part of the chapter focuses on explaining the impact and mitigation of the ionospheric threat in GBAS. Thus, it describes the main characteristics of the ionosphere in different regions of the world and the ionospheric threat models of CONUS, Germany, and Brazil. It also explains the PDGS algorithm currently adopted in CAT I GBAS.

Chapter 3 contains the main contributions of this thesis and addresses RQ1 and RQ2. It gives the complete methodology to be followed, from the detection and estimation of anomalous ionospheric gradients in real time to the integration of this information with current GBAS solutions. The main contributions of this chapter are:

- The design and development of the Network-GBAS concept, which uses an external monitoring network to detect and estimate ionospheric gradients in real time.
- The design and development of the algorithm for real-time ionospheric gradient detection, which is based on the time derivatives of the slant ionospheric delays measured by each satellite-station pair.
- The design and development of the algorithm for the estimation of the

ionospheric gradient parameters and their overbounding based on a network of stations and the cross-correlation between the slant ionospheric rates.

- The design and description of the methodology to derive the minimum detectable error for each of the stations in the network to meet the integrity requirements.
- The design and description of the methodology to integrate the information from the network in the current CAT I GBAS solutions adopted for the ionospheric threat mitigation, more specifically in the PDGS algorithm.

Chapter 4 evaluates the concept and algorithms proposed in Chapter 3 with simulated and real ionospheric perturbations from a high-latitude, active ionospheric region, namely in Alaska. Therefore, it contributes to answering RQ3 for the auroral region. The RQ3 is also addressed in Chapter 5 for the equatorial region. The main contributions of this chapter are the following:

- The design and implementation of an ionospheric gradient simulator capable of generating synthetic ionospheric perturbations with the typical characteristics of those of the auroral region.
- The evaluation of the detection algorithm with simulated ionospheric gradients and with a real ionospheric gradient experienced in Alaska by several satellites both in post-processing and in real time.
- The evaluation of the estimation algorithm with simulated ionospheric gradients and with a real ionospheric gradient experienced in Alaska by several satellites both in post-processing and in real time.
- The adaptation of the estimation algorithm proposed in Chapter 3 for the automatic selection of the reference station considering the characteristics of the real measurements in Alaska.

Chapter 5 evaluates the concept and algorithms proposed in Chapter 3 with simulated and real ionospheric perturbations from a low-latitude, active ionospheric region, specifically in Brazil. Therefore, it addresses RQ3 for the equatorial region. Chapter 5 follows a structure analogous to Chapter 4 to facilitate the comparison of the results between the two regions. The contributions of this chapter are the following:

- The design and implementation of an ionospheric gradient simulator capable of generating synthetic equatorial plasma bubbles.
- The evaluation of the detection algorithm with simulated ionospheric gradients and with a real ionospheric gradient experienced in Brazil by several satellites both in post-processing and in real time.

- The evaluation of the estimation algorithm with simulated ionospheric gradients and with a real ionospheric gradient experienced in Brazil by several satellites both in post-processing and in real time.
- The adaptation of the estimation algorithm proposed in Chapter 3 to cope with the equatorial plasma bubbles, which are composed of two single gradients, one downward and one upward.

Chapter 6 addresses RQ4. The main contributions of this chapter are:

- The design and development of the methodology to derive the minimum detectable gradient for a real airport and a simulated GBAS station protected by the network in Brazil.
- A first evaluation of CAT I GBAS availability using the methodology proposed in this thesis and its comparison with the system availability obtained using the current solutions in Brazil.

Chapter 7 contains the conclusion of this thesis. It concludes with suggestions for further research.

1.5 Thesis publications

This section presents the publications that resulted from the work accomplished in this thesis.

The Network-GBAS concept and the algorithms for detection and estimation of ionospheric gradients together with their evaluation in Alaska (Chapters 3 and 4) have been published in:

- M. Caamano, M. Felux, D. Gerbeth, J.M. Juan, G. Gonzalez-Casado, and J. Sanz, "Network-Based Ionospheric Gradient Monitoring to Support GBAS", in Proceedings of the 32nd International Technical Meeting of the Satellite Division of The Institute of Navigation (ION GNSS+ 2019), 2019, pages 2888-2902.
- M. Caamano, J.M. Juan, M. Felux, D. Gerbeth, G. Gonzalez-Casado, and J. Sanz, "Network-based ionospheric gradient monitoring to support GBAS" in NAVIGATION, Journal of the Institute of Navigation, 2021, 68(1), pages 135-156. This article is an extension of the paper presented at ION GNSS 2019+ and therefore was published with the same title.

Furthermore, preliminary studies on the design of the methodology for the "Network GBAS" were published in:

- M. Caamano, D. Gerbeth, M. Felux, and M.S. Circiu,"Using a Wide Area Receiver Network to Support GBAS Ionospheric Monitoring", in

Proceedings of the 30th International Technical Meeting of the Satellite Division of The Institute of Navigation (ION GNSS+ 2017), 2017, pages 1418-1428.

The methodologies to derive the minimum detectable gradient by the network and to overbound the estimated gradient parameters (explained in Chapter 3) together with the results of Chapters 5 and 6 will be published in two journal papers that are, at the moment of writing this thesis, under preparation.

2
Background

This chapter provides an overview of the Ground Based Augmentation System (GBAS) and describes the architecture and integrity concept of the existing state-of-the-art single-frequency system. The scope of the chapter focuses on the GBAS Approach Service Type (GAST) that is as of April 2022 operational, which offers approach guidance under CAT I weather conditions (GAST C). In addition, it includes a detailed description of the ionospheric error mitigation strategy in GAST C. Particularly, it describes the Position Domain Geometry Screening (PDGS) methodology, which is used in Chapter 6.

2.1 GBAS architecture

The Ground Based Augmentation System (GBAS) is a development of local-area differential GNSS whose main purpose is to provide precision approach guidance for aircraft.

The system consists of three elements shown in Figure 2.1:

1. The GNSS Space Segment provides ranging signals and broadcasts navigation data (orbit and clock parameters, satellite health status, and other complementary information) to the ground facility and users. Current GBAS is based on GPS C/A signals transmitted on the L1 frequency band (1575.42 MHz).

2. The GBAS Ground Subsystem provides aircraft within its coverage volume with approach path data and, for each satellite in view, pseudorange differential corrections and integrity information. Initially, GBAS coverage was defined through the Maximum Use Distance (Dmax) parameter, which was set to 43 km. However, according to current standards [8], pilots can use GBAS pseudorange corrections beyond this limit to facilitate the transition to the approach phase. The ground system includes typically four reference receivers and antennas installed in carefully surveyed and protected locations inside the area of an airport. These antennas

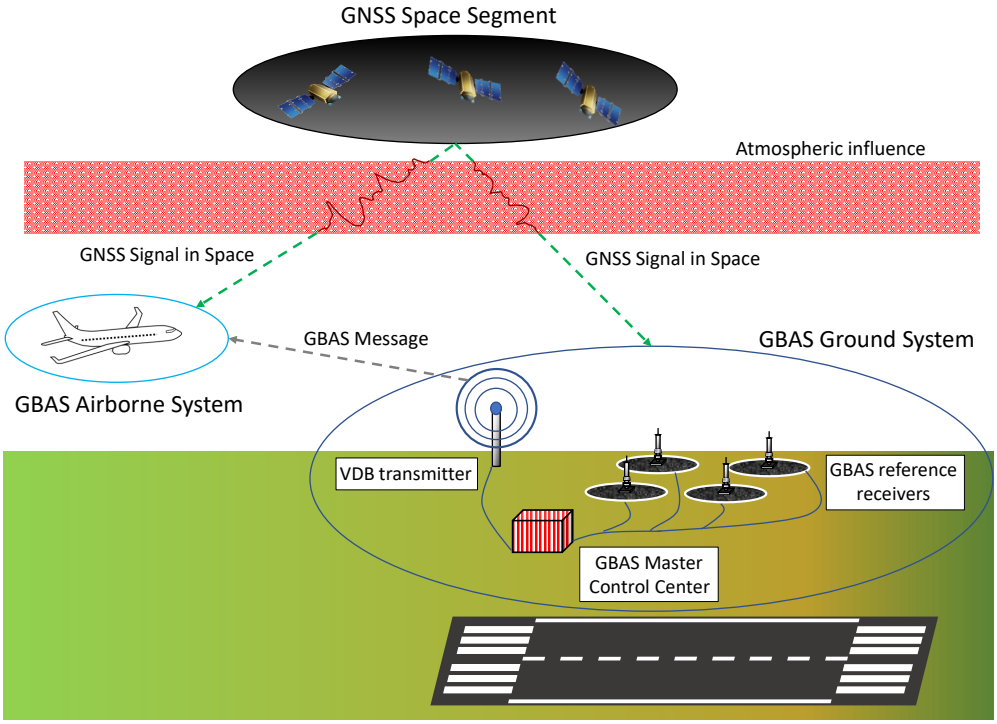

Figure 2.1: GBAS architecture.

are specially developed for GBAS to minimize multipath errors affecting each reference receiver and are commonly known as Multipath Limiting Antennas (MLAs). The GBAS master control center collects all the measurements from the reference receivers and generates differential corrections and integrity parameters. Furthermore, it constantly monitors the GPS signals and, in case it detects any system failure, it excludes the affected measurements (e.g. satellites) from the correction and integrity messages. Differential corrections and integrity information are broadcast to users in different messages types via Very High Frequency Data Broadcast (VDB) transmitters.

3. The Airborne Subsystem uses the GPS signals collected by the GNSS receivers on board the aircraft and the differential pseudorange corrections transmitted by the GBAS ground station to determine its position relative to the approach path very accurately. Furthermore, it uses the integrity parameters received from the ground station to calculate conservative bounds of the residual position errors and ensure safety of the operation.

2.1.1 GNSS Space Segment

The GNSS Space Segment is the responsible of providing the ranging signals and navigation data to the ground facility and users.

As of April 2022, three GNSS core constellations are fully deployed and operational: the NAVSTAR Global Positioning System (GPS) from the United States of America, the Global Navigation Satellite System (GLONASS) from the Russian Federation, and BeiDou from the People's Republic of China. The European Galileo constellation is expected to be completed in 2022 with a total of 30 satellites (24 active and 6 spares)[43]. In spite of the existence of all these satellite constellations, current operational GBAS is based on an architecture designed in the 1990s, which was a single-constellation architecture (GPS) only. GPS consists of at least 24 satellites that are distributed in six orbital planes. The satellites operate in near-circular orbits at an altitude of about 20,200 km above the Earth's surface. The orbital planes are inclined by an angle of 55 degrees to the equator, and each satellite completes an orbit in approximately 11 hours and 58 minutes (twice a day) [44]. Furthermore, since the start of GPS operation, the GPS satellites transmit signals at two frequencies, designated L1 and L2. The main GPS carrier signal L1 is transmitted at 1575.42 MHz and is modulated by two codes: the coarse/acquisition (C/A) code, which is the one used by civilian users, and the precision/secure (P/Y) code, which is encrypted and reserved for military and authorized civilian users. The second signal, GPS L2, is centered at 1227.6 MHz and was established to provide a second frequency for ionospheric group delay correction. More recently, since the launch of the Block IIF satellites on May 2010, GPS introduced signals on a third frequency designated L5 and centered at 1176.45 MHz. In contrast to GPS L2, GPS L5 is usable for aviation safety-of-life applications, and these two signals, L1 and L5, are compatible with their equivalents in the Galileo constellation, E1 and E5a.

2.1.1.1 GNSS observables and potential influences

Two different types of measurements are used in GBAS: pseudorange or code measurements and carrier-phase measurements. The basic process of generating the pseudorange measurements is as follows: first, the receiver generates a replica of the Pseudorandom noise (PRN) code for each satellite and correlates the replicas with the actual PRN codes transmitted by each of the satellites in view. When the maximum of the correlation is reached, the difference between the signal transmission time on the satellite and the reception time on the receiver is calculated. This time difference or transit time is then multiplied with the speed of light to obtain the pseudorange. This process of aligning the PRN code replicas with the received signals is known as code lock

and is done continuously through a Delay Lock Loop (DLL).

The carrier-phase measurement is the difference between the phase of the carrier received from the satellite and the phase generated internally by the receiver's oscillator. The receiver continuously tracks the carrier modulated by the navigation data with a Phase Lock Loop (PLL) and records these phase measurements in equal intervals of receiver time. Note that the receiver can measure only a partial number of cycles and not the number of whole cycles between the receiver and the satellite. When combining these partial cycles with an initial unknown number of whole cycles, the apparent distance or range between the satellite and the receiver is obtained. This unknown number of cycles is the so-called integer ambiguity [44], which changes arbitrarily every time the receiver loses the lock on the signal, producing jumps or discontinuities in the carrier-phase measurement.

Equation 2.1 describes in a simplified form the pseudorange ($\rho^j_{i,r}$) and carrier-phase measurements ($\phi^j_{i,r}$) in meters for frequency i, a single satellite j, and a single receiver r as:

$$\begin{aligned} \rho^j_{i,r} &= R^j_r + c \cdot (\delta t_r - \delta t^j) + T^j_r + I^j_{i,r} + MP_{\rho}{}^j_{,i,r} + \eta_{\rho}{}^j_{,i,r}, \\ \phi^j_{i,r} &= R^j_r + c \cdot (\delta t_r - \delta t^j) + T^j_r - I^j_{i,r} + \lambda_i \cdot N^j_{i,r} + MP_{\phi}{}^j_{,i,r} + \eta_{\phi}{}^j_{,i,r}. \end{aligned} \tag{2.1}$$

Here, R^j_r is the geometrical satellite-user range in meters, c is the speed of light in meters per second, δt_r and δt^j are the receiver and the satellite clock biases respectively both expressed in seconds, $I^j_{i,r}$ is the ionospheric delay for frequency i in meters, T^j_r is the tropospheric delay in meters, and $N^j_{i,r}$ and λ_i are the integer ambiguity in cycles and the corresponding wavelength of the frequency i. Finally, $MP_{\rho}{}^j_{,i,r}$ and $MP_{\phi}{}^j_{,i,r}$ represent the code multipath and the phase multipath errors on frequency i, and $\eta_{\rho}{}^j_{,i,r}$ and $\eta_{\phi}{}^j_{,i,r}$ the thermal noise and other code and phase measurement errors all in meters.

As can be seen in Equation 2.1, both the pseudorange and carrier-phase measurements are affected by a number of common errors that prevent the user from obtaining the true range R: (i) the user clock offset because the user receiver is not synchronized to the satellite clocks, (ii) errors introduced by the propagation of the signal through the ionosphere and troposphere, and (iii) errors coming from the user side such as multipath and noise. However, some of these errors have a different behavior for the code and the carrier-phase measurements, a fact that is used in GBAS to improve position accuracy as explained in the following sections. Note that in Equation 2.1, terms referring to the receiver and satellite code and carrier-phase hardware biases and carrier-phase wind-up have not been considered as they are not used throughout this thesis. For a more detailed description of the errors in the pseudorange and the carrier-phase measurements refer to Section 4 of [45].

2.1.2 GBAS Ground Subsystem

GBAS is a code-based differential system. The GBAS Ground Subsystem is responsible for generating and broadcasting carrier-smoothed pseudorange differential corrections and integrity information for each satellite in view. Furthermore, it also includes fault detection monitoring to ensure integrity in non-nominal conditions by excluding the affected measurements from the correction and integrity messages.

The differential pseudorange corrections are calculated based on the known (pre-surveyed) position of the reference receivers and the satellite position broadcast in the navigation message. Inside the GBAS coverage area, the aircraft applies the approved pseudorange corrections, and errors common to both the ground and the airborne are removed from each airborne measurement, improving the accuracy of its position estimation. Common errors include those due to the satellite (clock offset, ephemeris, hardware delays) or those introduced by the propagation medium (ionosphere, troposphere), which are assumed to be similar because they are correlated over short distances. The processing algorithms, including carrier-phase smoothing and the computation of differential corrections, are explained in Section 2.1.2.1.

The broadcast integrity parameters enable the overbounding of the residual remaining errors on the aircraft after the application of the corrections. Since the description of the integrity assurance in nominal and non-nominal conditions by the GBAS Ground Subsystem requires a lengthy explanation, these methods will be presented separately in Section 2.3.

2.1.2.1 Generation of pseudorange corrections

As explained in Section 2.1.1.1, the code and carrier-phase measurements experience common errors. Since the carrier-phase measurements are less noisy than the code measurements but ambiguous, the difference between carrier-phase measurements recorded in two consecutive epochs can be used to reduce high frequency noise and multipath in code measurements. This process is called carrier-phase smoothing in the literature and is done by using a Hatch filter [46]. Note that, by using the difference between two consecutive epochs or rate of change of the carrier-phase measurements, the integer ambiguity is automatically removed if no cycle slip has occurred. However, the time-varying ionosphere induces a bias called “Code-Carrier Divergence” in the single-frequency smoothed pseudorange when it is averaged in the smoothing filter. In Section 4.2.3.1 of [45], this effect is analyzed.

To build the carrier-smoothed code measurements, the carrier-phase difference between the current and the previous epoch is added to the previous

smoothed pseudorange, and that value (a projection of the current smoothed pseudorange) is weighted and added to the weighted current raw pseudorange measurement. The expression of the smoothed pseudorange at epoch t (according to section 3.7.1.2.8.3.3 of [47] and section 3.2.1.2.8.5.1 of [48]) is:

$$\bar{\rho}^j_{i,r}(t) = \frac{\Delta T}{\tau} \cdot \rho^j_{i,r}(t) + \left(1 - \frac{\Delta T}{\tau}\right) \cdot \left[\bar{\rho}^j_{i,r}(t-1) + \phi^j_{i,r}(t) - \phi^j_{i,r}(t-1)\right], \quad (2.2)$$

where $\bar{\rho}^j_{i,r}(t)$ is the current carrier-smoothed pseudorange, $\bar{\rho}^j_{i,r}(t-1)$ is the previous carrier-smoothed pseudorange, $\rho^j_{i,r}(t)$ is the current raw pseudorange measurement, $\phi^j_{i,r}(t)$ is the current carrier-phase measurement, and $\phi^j_{i,r}(t-1)$ is the previous carrier-phase measurement, all expressed in meters. Here, ΔT represents the sample interval, and τ is the filter time constant, both expressed in seconds. The time interval or sampling rate of the measurements for GBAS is 0.5 seconds, and the smoothing time constant (τ) depends on the active service type of the station (e.g., 100 seconds for GAST C). Note that the definition of the weights on the current pseudorange and the projection from the carrier phase difference in Equation 2.2 heavily emphasizes the latter compared to the former.

After the carrier-smoothing process, the ground subsystem computes carrier-smoothed pseudorange corrections for satellites in view and above the minimum elevation angle (5°). A pseudorange correction candidate (denoted as $PRC_{CSC}{}^j_r$) for each reference receiver r and satellite j is initially obtained by subtracting the smoothed pseudorange and the satellite clock bias from the geometric range as described in Equation 2.3 (see sections 3.7.1.2.8.3.1 of [47] and 3.2.1.2.8.5.4 of [48]):

$$PRC_{CSC}{}^j_r = R^j_r - \bar{\rho}^j_r - c \cdot \delta t^j, \quad (2.3)$$

where R^j_r is the geometric range from the receiver r to the satellite j calculated from the precisely known position of the reference antennas and the position of the satellite, $\bar{\rho}^j_r$ is the smoothed pseudorange, and δt^j represents the clock error for satellite j relative to GPS time. Both the satellite position and the satellite clock error are computed from information included in the broadcast navigation message encoded on the carrier-phase measurements. Note that all equations in this chapter refer to the measurements on the L1 frequency band at time epoch t. Thus, the indices for the frequency and time are omitted for simplicity and are included only if necessary.

The candidate pseudorange corrections (PRC_{CSC}) contain the receiver clock error that is common to all satellites tracked by that receiver, which is removed by subtracting a weighted average of all candidate pseudorange corrections for a given receiver in a process called smoothed clock adjustment (SCA). This

process also removes the common part of all other errors contained in all visible satellites, including a fraction of the atmospheric errors. However, this does not impact the position solution estimation in the aircraft. This is because any bias common to all satellites that would be introduced when applying the corrections projects into the user receiver's clock estimate but leaves the position estimate unaffected. In this process, only the satellites common to all ground reference receivers (the so-called "common set") are used.

The correction for a receiver r and a satellite j after the smoothed clock adjustment is:

$$PRC_{SCA}{}_r^j = PRC_{CSC}{}_r^j - \sum_{j=1}^{\mathcal{J}} w_r^j \cdot PRC_{CSC}{}_r^j, \tag{2.4}$$

where $\mathcal{J}$ represents the total number of used satellites and w_r^j represents the weights given to each satellite. The existing methods to compute these weights are not specified in this thesis, but the requirement is that $\sum w_r^j = 1$. Commonly used methods are either equal weights [48] or a weighting that is dependent on satellite elevation [47].

Finally, the broadcast correction for satellite j is computed as an average of all candidate pseudorange corrections over all receivers for that particular satellite $\mathcal{R}_\mathcal{G}(j)$:

$$PRC^j_{TX} = \frac{1}{\mathcal{R}_\mathcal{G}(j)} \cdot \sum_{r=1}^{\mathcal{R}_\mathcal{G}(j)} PRC_{SCA}{}_r^j. \tag{2.5}$$

In addition to the pseudorange corrections, the ground also broadcasts range rate corrections (RRC_{TX}) to enable the airborne system to extrapolate during the interval following the last received message. The reason behind is that the airborne update rate is specified to be at least 5 Hz [49] and thus faster than the update rate of the GBAS message from the ground (2 Hz). The range rate corrections at current epoch t are computed as the rate of change of the current and previous transmitted pseudorange corrections as:

$$RRC^j_{TX}(t) = \frac{PRC^j_{TX}(t) - PRC^j_{TX}(t-1)}{\Delta T}. \tag{2.6}$$

2.1.3 Airborne Subsystem

The Airborne Subsystem receives the pseudorange and range rate corrections broadcast by the GBAS ground station and applies them to its own smoothed pseudorange measurements in order to compute its position. The

processing algorithms, including carrier-phase smoothing and the computation of the position, are explained in Section 2.1.3.1.

Additionally, it receives the broadcast integrity parameters, which allow it to compute safety bounds of the residual position errors that remain after the application of the differential corrections. The explanation of the integrity assurance and protection level computation will be presented in Section 2.3.

2.1.3.1 Airborne processing

GBAS avionics typically consist of a Multi-Mode Receiver (MMR) capable of receiving the GBAS messages from the ground system and the GNSS ranging signals from the satellites.

The smoothed pseudorange measurements are computed in the aircraft by processing the raw pseudorange and carrier-phase measurements using the same smoothing filter [46] and time constant (100 seconds for GAST C) as for the generation of the corrections on the ground (see Equation 2.2). This is done to avoid introducing different time-varying errors due to mismatched filters. Then, the pseudorange corrections broadcast by the ground station are applied to the airborne smoothed pseudoranges, $\bar{\rho}^j_{air}(t)$. This process is described in Section 2.3.8.2 of [49]. The corrected smoothed pseudorange at the airborne receiver for a satellite j at airborne epoch t, $\bar{\rho}^j_{air,corr}(t)$, is then:

$$\bar{\rho}^j_{air,corr}(t) = \bar{\rho}^j_{air}(t) + PRC^j_{TX}(t_{PRC_{TX}}) + RRC^j_{TX}(t - t_{PRC_{TX}}) + TC^j_{air}(t) + c \cdot \delta t^j(t), \tag{2.7}$$

where $\bar{\rho}^j_{air}(t)$ is the airborne smoothed pseudorange for satellite j, PRC^j_{TX} is the broadcast correction at time $t_{PRC_{TX}}$, RRC^j_{TX} is the range rate correction broadcast at time $t_{PRC_{TX}}$, TC^j_{air} is the differential tropospheric correction, and δt^j is the satellite clock bias for satellite j computed by the airborne receiver. The $t_{PRC_{TX}}$ is the time at which the corrections and the range rate corrections were generated. The user computes the time difference between its current epoch t and the time of transmission of the corrections from the ground station $t_{PRC_{TX}}$. If this time difference is within the time of applicability of the pseudorange corrections (Section 2.3.11.5.2.1.1 of [20]), it is multiplied with the range rate corrections to account for the temporal variation of the errors during this time difference.

The difference in tropospheric delay between the GBAS reference station and the aircraft arises in part due to the altitude difference between the two [50]. Therefore, a differential tropospheric correction is computed according

to the formula of Section 2.3.8.3 in [49]:

$$TC_{air}^{j} = N_r \cdot h_0 \cdot \frac{10^{-6}}{\sqrt{0.002 + \sin^2(\theta_{air}^{j})}} \cdot \left(1 - e^{\frac{-\Delta h}{h_0}}\right), \tag{2.8}$$

where Δh is the height of the aircraft above the GBAS reference station, θ_{air}^{j} is the elevation angle of satellite j computed by the airborne receiver and N_r and h_0 are the refractivity index and the troposphere scale height, which are parameters specific to the ground station and broadcast in the GBAS message that will be explained in Section 2.3.3.4. There is also a tropospheric delay difference due to spatial decorrelation between ground and air, but since this difference is small and unknown, no correction can be made for it.

2.1.3.2 Airborne position determination

After the application of the corrections, atmospheric errors and errors due to the satellite are largely removed, but the corrected pseudorange measurements, $\bar{\rho}_{air,corr}^{j}$, still contain the receiver clock offset, $c \cdot \delta t_r$, and a residual error, $\tilde{\varepsilon}_{\rho}^{j}$, in addition to the geometric range.

Based on the smoothed and corrected pseudorange measurements, the airborne receiver can calculate its position coordinates in an Earth-Centered Earth-Fixed (ECEF) coordinate system ($\boldsymbol{x_{air}} = [x_{air}, y_{air}, z_{air}]$) and its receiver clock bias error ($c \cdot \delta t_r$) for $\mathcal{J} \geq 4$ by solving the following system of equations:

$$\bar{\rho}_{air,corr}^{j} = \left\| \boldsymbol{x}^{j} - \boldsymbol{x_{air}} \right\| + c \cdot \delta t_r + \tilde{\varepsilon}_{\rho}^{j}, \quad j = 1, ..., \mathcal{J}, \tag{2.9}$$

where $\boldsymbol{x}^{j}$ represents the position of satellite j at the time of the signal transmission, $\boldsymbol{x}^{j} = [x^{j}, y^{j}, z^{j}]$.

Equation 2.9 defines a nonlinear system whose usual resolution technique consists of determining the position of the aircraft and the receiver clock bias iteratively by starting with an initial approximate position, $\boldsymbol{x_{air,0}}$ (typically the estimated position of the previous epoch or the center of the Earth if no prior knowledge is available), and an initial clock offset estimate, $c \cdot \delta t_{r,0}$ (initial value typically used is 0).

Thus, after linearising the geometrical range of Equation 2.9 in the neighborhood of a point ($\boldsymbol{x_{air,0}}$) corresponding to the approximate position of the aircraft's receiver, and rewriting it for all visible satellites ($\mathcal{J} \geq 4$) in a matrix form, this equation can be expressed as:

$$\Delta\rho = \bar{\rho}_{air,corr}^{j} - R_r^{j} = \boldsymbol{G}\boldsymbol{\Delta}\boldsymbol{x_{air}} + \tilde{\varepsilon}_{\rho}^{j}, \tag{2.10}$$

where $\Delta\rho$ represents the difference between the smoothed corrected airborne measurements, $\bar{\rho}^j_{air,corr}$, and the estimated geometric range between the estimated aircraft position at each time and the satellite position, R^j_r, $\boldsymbol{\Delta x_{air}} = [\delta x_{air}, \delta y_{air}, \delta z_{air}, \delta t_{air}]$ contains the increment of position and the increment of the clock offset, and the so-called "geometry matrix", $\boldsymbol{G}$, has a dimension of $\mathcal{J} \times 4$. It contains on the j^{th} row the unit vectors from the user to satellite j described as:

$$g^j := [-cos(\theta^j) \cdot cos(\psi^j), -cos(\theta^j) \cdot sin(\psi^j), -sin(\theta^j), 1], \tag{2.11}$$

with θ^j being the elevation and ψ^j the azimuth angles (relative to the horizon in the ECEF coordinate system) of the satellite j. The last column of 1 represents the receiver clock offset.

Then, Equation 2.10 is solved for $\boldsymbol{\Delta\widehat{x}_{air}}$ using the weighted least squares method as described in Equation 2.12:

$$\boldsymbol{\Delta\widehat{x}_{air}} = \boldsymbol{S}\Delta\rho. \tag{2.12}$$

The $\boldsymbol{S}$ matrix is the weighted pseudo-inverse of the geometry matrix $\boldsymbol{G}$, which relates the measurements from the pseudorange domain to the position domain and is defined as:

$$\boldsymbol{S} = (\boldsymbol{G}'\boldsymbol{W}\boldsymbol{G})^{-1}\boldsymbol{G}'\boldsymbol{W}. \tag{2.13}$$

The weighting matrix, $\boldsymbol{W}$, is introduced to give more weight to the satellites where less measurement error is expected. $\boldsymbol{W}$ can be defined as a $\mathcal{J}$ x $\mathcal{J}$ diagonal matrix containing the inverse of the expected uncertainty associated with each pseudorange measurement as entries. It is defined as:

$$\boldsymbol{W} = \begin{pmatrix} \frac{1}{(\sigma^1_{GBAS,x})^2} & 0 & \cdots & 0 \\ 0 & \frac{1}{(\sigma^2_{GBAS,x})^2} & \cdots & 0 \\ \vdots & \vdots & \ddots & \vdots \\ 0 & 0 & \cdots & \frac{1}{(\sigma^j_{GBAS,x})^2} \end{pmatrix}, \tag{2.14}$$

where the $(\sigma^j_{GBAS,x})^2$ terms represent the overbounding variances of the differential corrected pseudorange measurements for satellite j and GBAS Approach Service Type "x", e.g. C or D, that will be explained in Section 2.3.3. This matrix is defined assuming that the measurement errors from different satellites are uncorrelated and can be described by a zero-mean Gaussian distribution.

Once the increment $\boldsymbol{\Delta\widehat{x}_{air}}$ is computed, it is added to the previous position and user clock estimate to obtain a new position and clock estimate. The process is repeated until the increment is small enough to remain below

a predefined threshold. This is a standard method of GNSS-based position determination, and it is fully described in Chapter 6 of [44].

Note that, all previous equations are valid only for a single constellation. In the case where measurements from a second GNSS constellation are used, the rows of $\boldsymbol{G}$ would be the same for the first three terms (columns) as in Equation 2.11 but, instead of a single column with "1" for the clock offset, two columns with either "1 or 0" or "0 or 1" depending on the constellation per row would be added. This is done to select the specific constellation to which each of the satellites belongs to. Thus, $\boldsymbol{G}$ would have a dimension of $\mathcal{J}$ x 5.

In GBAS Approach services, the aircraft computes its lateral and vertical position deviations from a reference approach track. The computation of the deviations is out of scope and is not explained in this thesis, but a detailed description of their calculation can be found in Section 2.3.11.5.1 of [20].

2.2 GBAS performance requirements

GBAS provides precision approach service for three different categories of operation: Category I (CAT I), II, and III. The different categories refer to the requirements in terms of Decision Height (DH) and Runway Visual Range (RVR) that have to be met in order to proceed with the intended operation. For example, in case of CAT I, the aircraft can be guided to a minimum altitude, the DH, below which it can only continue if the runway is visible. The requirements for Category II (CAT II) and CAT III are more stringent because they allow operations for lower DHs, which means that the pilot has less time to react if an unexpected problem occurs (such as being out of position when the runway becomes visible) and the operation has to be aborted, leading to a missed approach. Table 2.1 specifies the limits on the RVR and DH for the different precision landing categories [16]. For CAT I the requirement is either a RVR no lower than 550 m or a visibility not less than 800 m. The difference between these two terms is the following: RVR refers to the distance over which a pilot of an aircraft on the centerline of the runway can see the runway surface markings delineating the runway or identifying its center line, whereas visibility is a general metric applicable to an area, and is normally measured by a person from the tower.

Moreover, in each intended operation, different levels of accuracy, integrity, continuity, and availability have to be achieved. These four performance evaluation parameters are defined in [8, 51] as follows:

- **Accuracy:** *"GNSS position accuracy is defined as the difference between a computed and a true position"* [51]. The probability that the position

error is within the accuracy requirements under nominal fault-free conditions should be at least 95%.

- **Integrity:** *"Integrity is a measure of the trust that can be placed in the correctness of the information supplied by the total system"* [51]. It is defined through three quantitative elements: (i) the integrity risk, or the Probability of Hazardously Misleading Information (PHMI), (ii) the Time to Alert (TTA), and (iii) Alert Limits (ALs). PHMI represents the probability that the true aircraft position lies outside the confidence position error bounds and above the ALs due to an erroneous output, and this condition has not been notified to the pilot (or autopilot) within the specified Time to Alert (TTA). Thus, TTA represents the maximum time that the system has to warn the user in case GBAS should not be used for the intended operation. The Alert Limits (ALs) are the maximum position errors that are acceptable in the lateral and vertical domain. As an example, if Hazardously Misleading Information (HMI) causes a vertical error greater than 10 meters to a CAT I user, the GBAS ground station must detect this event and alert the users within a 6-second TTA if the affected measurements cannot be reliably excluded. The probability of HMI occurring should be less than 2×10^{-7} per approach to guarantee the system's safety (see Table 2.2).
- **Continuity:** *"Continuity is the capability of the system to perform its function without unscheduled interruptions during the intended operation, expressed as a probability. For example, there should be a high probability that guidance will remain available throughout an entire instrument approach procedure" [51].*
- **Availability** is the percentage of time that the system simultaneously meets the Accuracy, Integrity and Continuity requirements.

Category	DH	RVR	Visibility
CAT I	DH $\geq$ 60 m	RVR $\geq$ 550 m	Visibility $\geq$ 800 m
CAT II	30 m $\leq$ DH $<$ 60 m	RVR $\geq$ 300 m	-
CAT IIIa	0 m $\leq$ DH $<$ 30 m	RVR $\geq$ 175 m	-
CAT IIIb	0 m $\leq$ DH $<$ 15 m	50 m $\leq$ RVR $<$ 175 m	-
CAT IIIc	0 m	RVR $\geq$ 0 m	-

Table 2.1: Precision Approach Categories.

The navigation performance requirements and the ALs (Vertical Alert Limit (VAL) and Lateral Alert Limit (LAL)) for each category of operation and specific GBAS Approach Service Types (GASTs) are summarized in Table 2.2. Here, "lateral" refers to "cross-track" or perpendicular to the approach direction of the aircraft. Furthermore, all types of operation require the availability

Oper. type & GAST	Accuracy		Integrity				Cont.
	Lat.	Vert.	Integrity Risk	TTA	LAL	VAL	
APV-I (GAST A)	16 m	20 m	2×10^{-7} per 150 s	10 s	40 m	50 m	8×10^{-6} per 15 s
APV-II (GAST B)	16 m	8 m	2×10^{-7} per 150s	6 s	40 m	20 m	8×10^{-6} per 15 s
CAT I (GAST C)	16 m	4 m	2×10^{-7} per 150s	6 s	40 m	10 m	8×10^{-6} per 15 s
CAT II (GAST D)	5.0 m	2.9 m	1×10^{-9} per 15 s vert. and 30 s lat.	2 s	17 m	10 m	4×10^{-6} per 15 s
CAT III (GAST D)	5.0 m	2.9 m	1×10^{-9} per 15 s vert. and 30 s lat.	2 s	17 m	10 m	2×10^{-6} per 15 s vert. and 30 s lat.

Table 2.2: Performance requirements.

to be above 99%. This information has been extracted from [8, 52].

As can be seen in Table 2.2, civil aviation demands high levels of availability and continuity, but also high integrity, especially for precision approach and automatic landings under CAT III weather conditions. However, ensuring integrity might produce a loss of continuity and availability in certain conditions. As an example, during an approach, sensitive integrity monitors designed to meet the stringent integrity requirements could trigger excessive false alerts, and therefore produce a loss of continuity. Furthermore, prior to an approach, protection against the ionospheric gradient threat in equatorial regions could cause a loss of availability due to the high values of the threat model [28, 53, 54]. Therefore, there is a trade-off between these requirements that represents a challenge for GBAS development: integrity must be protected without making too many conservative assumptions that might degrade the system's availability and continuity.

2.3 Integrity assurance in GBAS

Depending on the rate of occurrence and the size of the impact of the different errors that might affect GBAS positioning, the integrity of the system can be achieved in two complementary ways. As a first step, however, it is important to define the integrity risk requirement of each of the potential errors (see Section 2.3.1) and to bound their probability of occurrence. Any

error that is known to occur at a rate below the allocated integrity risk does not need to be considered.

For all the other errors, which occur with a probability higher than the defined integrity risk, two different strategies are used: (i) integrity monitoring to detect and exclude faulty measurements from the position solution, and (ii) bounding of the nominal position errors through the generation of Protection Levels (PLs).

This section provides the background information on the protection level calculation and the principles of integrity monitoring, with a focus on GAST C.

2.3.1 Integrity risk allocation in GAST C

In GAST C, the ground is fully responsible for ensuring integrity of the GBAS Signal-in-Space (SiS) to support CAT I operations. This means that the ground station must detect any failure in the ground or in the space segment and prevent users from losing integrity as a result. To do this, the ground subsystem broadcasts integrity parameters which, when applied by the airborne user, bound the actual error with the given integrity risk. In addition, the ground executes several integrity monitoring algorithms that detect and exclude faulty signals that can lead to hazardous user position errors and might not be bounded by the protection levels.

The GBAS SiS integrity risk value is defined to be less than 2×10^{-7} in any one approach (see Table 2.2). From the total SiS integrity risk, 0.5×10^{-7} in any one approach is allocated to the H0 and H1 protection levels. The remaining 1.5×10^{-7} is allocated to the so-called H2 faults and includes failures that must be mitigated by the GBAS Ground Subsystem [47]. From these errors, ephemeris errors are covered by a protection level with an integrity risk allocation of 2.3×10^{-8} [55]. Protection against the remaining failures is achieved through integrity monitoring. Figure 2.2 shows an example of GBAS CAT I integrity risk allocation (information taken from [55]).

2.3.2 Protection levels

To ensure the integrity risk requirement is met, the system computes position error bounds after the application of differential corrections. These conservative error bounds are called Protection Levels (PLs) and consist of the Vertical Protection Level (VPL) and the Lateral Protection Level (LPL). They are calculated based on models of the individual error components in the pseudorange measurements (σ_{GBAS}), a given integrity risk (an allocation from the 2×10^{-7} requirement), and the current satellite geometry ($\boldsymbol{G}$). The protection levels are then compared with the Alert Limits (ALs) and the system is

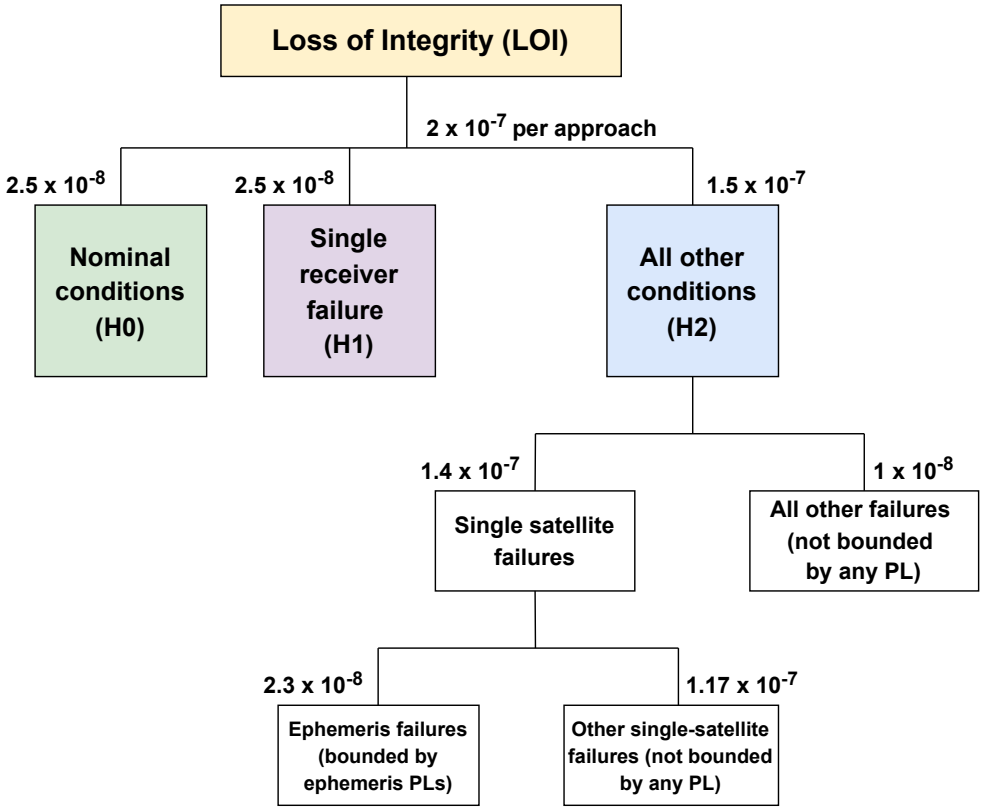

Figure 2.2: Example of GBAS CAT I integrity risk allocation ([55]).

declared unavailable if at least one of the PLs exceeds the corresponding AL. Figure 2.3 illustrates these two concepts.

The ALs are defined for the vertical and lateral domain (Vertical Alert Limit (VAL), Lateral Alert Limit (LAL)) and represent the maximum allowable errors that can be safely tolerated. They vary with the distance of the aircraft to the landing threshold point. The CAT I LAL decreases from 63.15 m to a value of 40 m on the final approach segment close to the runway threshold, where the minimum decision height is reached. The VAL decreases from 43.35 m to a maximum value of 10 m. The values mentioned here are maximum values, however tighter ALs may be used for specific approaches or specific aircraft implementations as necessary.

PLs are defined to address the fault-free condition (H0), the case of a failure in one of the reference receivers (H1), and the position errors due to errors in the ephemeris data. The aircraft computes the maximum among the three and verifies if the values are below the alert limits (in both lateral and vertical domain). As explained previously, in case any of the protection levels exceeds

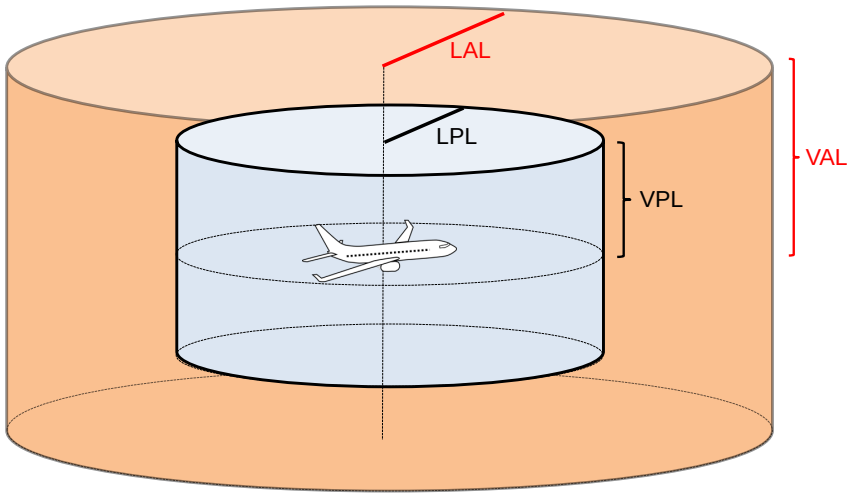

Figure 2.3: GBAS protection levels and alert limits.

the alert limits, the service becomes unavailable (or continuity is lost if an approach has already begun).

In this thesis, only the fault-free and the ephemeris protection levels are used. The explanation of the H1 protection levels is out of scope, but an explanation and calculation of them can be found in [20]. Furthermore, since the most stringent requirements while performing a precision approach are in the vertical domain, only VPL and ephemeris vertical protection level (VPB) are explained.

The fault-free vertical protection level, VPL_{H_0}, is computed as [20]:

$$VPL_{H_0} = k_{ffmd} \cdot \sqrt{\sum_{j=1}^{\mathcal{J}} (s^j_{apr\_vert})^2 \cdot (\sigma^j_{GBAS,x})^2} + D_v, \tag{2.15}$$

where $s^j_{apr\_vert}$ represents the projection factor of the vertical and the along-track components of the error from the pseudorange domain into the vertical position domain for satellite j. This projection factor is computed with the elements from the $\boldsymbol{S}$-matrix as:

$$s^j_{apr\_vert} = s_{3j} + s_{1j} \cdot \tan(\theta_{GPA}), \tag{2.16}$$

with θ_{GPA} being the glidepath angle and $\boldsymbol{S}$ the weighted pseudo-inverse of the geometry matrix $\boldsymbol{G}$ defined in Equation 2.13.

The fault-free missed detection multiplier in Equation 2.15, k_{ffmd}, represents the extrapolation of a bounding one-sigma error value to the very small required

integrity risk allocation for nominal protection levels (2.5×10^{-8} in Figure 2.2) based on the standard Gaussian distribution. It depends on the number of reference receivers, as described in Table 2.3. D_v is a service type specific term that represents the magnitude of the vertical projection of the difference between 30-second and 100-second smoothed position solutions in GAST D. In GAST C, D_v is set to 0.

Number of reference receivers	2	3	4
k_{ffmd}	5.762	5.810	5.847

Table 2.3: Fault-free Missed Detection Multiplier [20].

The $\sigma^j_{GBAS,x}$ element is the standard deviation of the uncertainty of the residual differential pseudorange error for satellite j and is described in Equation 2.17:

$$\sigma^2_{GBAS,x} = \sigma^2_{pr\_gnd,x} + \sigma^2_{pr\_air} + \sigma^2_{iono,x} + \sigma^2_{tropo}. \tag{2.17}$$

As we can see in Equation 2.17, after the application of corrections, the remaining error sources affecting the differentially corrected pseudorange measurements are ground multipath and receiver noise ($\sigma_{pr\_gnd,x}$), airborne multipath and receiver noise (σ_{pr_air}), ionospheric error ($\sigma_{iono,x}$), and residual tropospheric error (σ_{tropo}). Thus, the uncertainty of the residual error that remains in the differential pseudorange can be expressed as the root-sum-square of the uncertainties introduced by the different error sources because each error source is assumed to be statistically independent from the others. Additionally, these uncertainties are also used for weighting in the position solution as described in Equation 2.14 of Section 2.1.3.2. In the following sections, the different error models used in GBAS are described. Note that both $\sigma_{iono,x}$ and $\sigma_{pr\_gnd,x}$ depend on the active approach service type "x" because, in GAST C, both parameters ($\sigma_{iono,C}$ and $\sigma_{pr\_gnd,C}$) could be inflated to protect against the ionospheric gradient threat, which is not the case for GAST D. Furthermore, a GAST D ground station broadcasts two sets of values for $\sigma_{pr\_gnd,D}$ for 30 seconds and 100 seconds smoothing time constants. The $\sigma_{pr\_gnd,D,30}$ is used in the weighting in the position solution and the $\sigma_{pr\_gnd,D,100}$ is used in the computation of the protection levels.

Additionally, the vertical ephemeris protection level (VPB) is defined as:

$$VPB^j = |s^j_{apr\_vert}| \cdot x_{Air} \cdot P^j + k_{md\_e} \cdot \sqrt{\sum_{j=1}^{\mathcal{J}} (s^j_{apr\_vert})^2 \cdot (\sigma^j_{GBAS,x})^2}, \tag{2.18}$$

$$VPB = \max(VPB^j), \tag{2.19}$$

where x_{Air} is the distance (slant range) between the aircraft and the GBAS reference point (in meters), k_{md_e} represents the ephemeris missed detection

multiplier, and P^j represents the ephemeris decorrelation parameter for satellite j (see Section 2.3.3.2). These last two parameters are both dependent on the approach service type (see Section 2.3.11.5.2.4 of [20]).

Since this thesis focuses on GAST C, in the following sections, the subindex "x" to distinguish between different active approaches is dropped for simplicity and is only retrieved when necessary.

2.3.3 Integrity parameters and models for the error sources

The GBAS ground station broadcasts, together with the differential corrections, several integrity parameters that enable aircraft approaching an airport to bound the residual position errors remaining in the corrected measurements by means of the PLs.

One important assumption to compute the protection levels is that, in the fault-free case, the measurement errors of the ground and the airborne systems can be described by a zero-mean Gaussian distribution. As described in Equation 2.17, the standard deviation of the total uncertainty error is computed as the root-sum-square of the ground multipath and noise contribution, the troposphere residual uncertainty, the ionospheric residual uncertainty, and the airborne multipath and noise.

In the next subsections, the models for each of the components of the residual uncertainty are discussed. Additionally, the integrity parameters broadcast by the GBAS ground station, which are related to these different error sources, are also explained.

2.3.3.1 B-values

B-values are estimates of the contribution of a single reference receiver to the average pseudorange correction error under the hypothesis that a given reference receiver has failed [56]. They are computed for each satellite and reference receiver as the difference between the broadcast pseudorange corrections and the corrections obtained excluding the reference receiver measurements hypothesized to be failed. The process to calculate them can be found in Section 5.4.4 of [47]. Before a correction for a specific satellite is calculated, the corresponding B-values are compared to their respective monitoring thresholds to identify potentially faulty measurements. If all B-values are below their respective thresholds, the pseudorange correction PRC_{TX} is transmitted to the aircraft. In case one or more B-values are over the thresholds, the corresponding faulty data is excluded from the calculation of the corrections and this process is repeated continuously until all B-values are below their thresholds. These B-values are key inputs to the H1 protection levels mentioned in Section 2.3.2.

2.3.3.2 Ephemeris Decorrelation Parameter (P-value)

The P-values *"characterize the impact of residual ephemeris errors due to spatial decorrelation for each satellite"* [56]. The P-value is defined as the Minimum Detectable Error (MDE) of the ephemeris monitors implemented in the GBAS ground station divided by the minimum distance between the GBAS reference point and the satellite. P-values are used in the ephemeris protection levels as described in Equation 2.18.

2.3.3.3 Model of ground noise and multipath

The broadcast residual uncertainty of the ground noise and multipath, σ_{pr_gnd}, is defined as *"the standard deviation of a normal distribution associated with the signal-in-space contribution of the pseudorange error due to conditions on the ground"* [56]. The σ_{pr_gnd} values are obtained based on ground receiver error estimates and bounds derived from pre-operation siting trials and ongoing error monitoring during operation. Note that, although the σ_{pr_gnd} values provide a statistical measure of ground-based error sources (e.g., multipath, noise), they do not include other errors such as equipment failures, rare satellite signal anomalies, and ephemeris errors. In GAST C, the $\sigma_{pr\_gnd,C}$ and B-values broadcast to the aircraft are based on 100 seconds of ground receiver smoothing.

The σ_{pr_gnd} values are related to the Ground Accuracy Designators (GAD), which are standard error models that have been derived to define different performance levels of the GBAS Ground Subsystem. These GAD curves, and the example σ_{pr_gnd} values that they represent, do not represent the typical accuracy of the system but instead, are meant to be used in PL calculations to bound rare-event errors.

There are three different Ground Accuracy Designator (GAD) curves defined: Ground Accuracy Designator A (GAD A), Ground Accuracy Designator B (GAD B), and Ground Accuracy Designator C (GAD C) ([57], Section 3.4.1 of [47]). The GAD C curve represents the model for a standard GBAS ground station that uses Multipath Limiting Antennas (MLAs) and a narrow correlator receiver. The GAD B model defines the performance that can be achieved with receiver technologies similar to GAD C, but using conventional survey antennas instead of MLAs. The GAD A represents a level of performance that can be achieved with low-cost receivers and antenna installations. These models are described in Equation 2.20:

$$\sigma_{pr\_gnd}(\theta^j) = \sqrt{\frac{(a_0 + a_1 \cdot e^{-\theta^j/\theta_0)^2}}{\mathcal{R}_\mathcal{G}} + (a_2)^2}, \tag{2.20}$$

where $\mathcal{R}_\mathcal{G}$ represents the number of receivers, and θ^j the elevation of the satellite j. The parameters a_0, a_1, a_2 and θ_0, which depend of the ground accuracy designator type, are defined in Table 2.4.

GAD	**Elevation** [°]	a_0 **[m]**	a_1 **[m]**	a_2 **[m]**	θ_0 [°]
GAD A	≥ 5	0.5	1.65	0.08	14.3
GAD B	≥ 5	0.16	1.07	0.08	15.5
GAD C	≥ 35	0.15	0.84	0.04	15.5
	5 to 35	0.24	0	0.04	-

Table 2.4: GBAS - GPS Accuracy requirement parameters [47].

Figure 2.4 shows the GAD curves as a function of satellite elevation for $\mathcal{R}_\mathcal{G} = 4$.

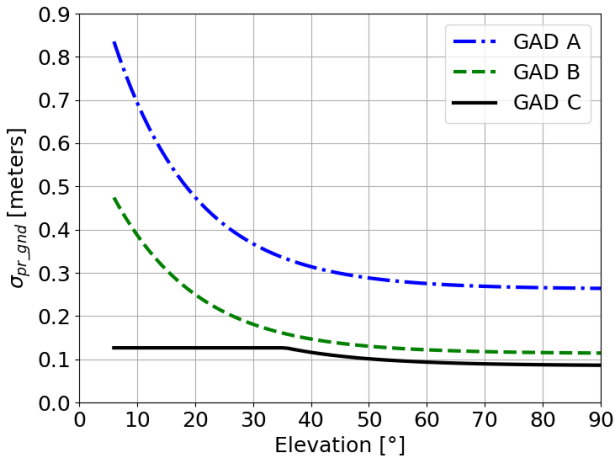

Figure 2.4: Ground accuracy models as a function of satellite elevation.

2.3.3.4 Model of tropospheric residual uncertainty

The troposphere introduces a delay in the GNSS signal propagation. In comparison with the ionosphere, the troposphere is not dispersive, which means that this delay does not cause a code and carrier phase divergence and it also does not depend on signal frequency. Since the troposphere is a ranging error source that is not common to the ground station and the aircraft, the aircraft must calculate a differential tropospheric correction and a bound of the residual troposheric error [58]. For that purpose, the ground transmits three different parameters. The first parameter is the refractivity index of the atmosphere at the GBAS location, N_r. It consists of dry and a wet components and can be calculated based on locally measured weather data (temperature, air pressure

and humidity) at a particular location. σ_{ref} is the standard deviation of this parameter and represents a conservative assessment of the one-sigma variation of daily values from the broadcast one. The last parameter is the tropospheric scale height, h_0, which is calculated based on the Earth surface height at the GBAS location, the user height, and its dry and wet components [50].

Based on the aforementioned tropospheric parameters, the standard deviation of the residual tropospheric error after the application of ground corrections, σ_{tropo}, can be calculated. The model used for σ_{tropo} as defined in Section 2.3.12.2 of the DO-253D [20] document is described in Equation 2.21:

$$\sigma_{tropo} = \sigma_{ref} \cdot h_0 \cdot \frac{10^{-6}}{\sqrt{0.002 + \sin^2(\theta^j)}} \cdot (1 - e^{\frac{-\Delta h}{h_0}}), \tag{2.21}$$

where Δh is the altitude of the aircraft above the GBAS station and θ^j represents the satellite elevation angle.

The small variation of N_r between user and ground locations is included within the ionospheric parameter σ_{vig} introduced below.

2.3.3.5 Model of the residual nominal ionospheric error

After GBAS pseudorange corrections are applied in the aircraft, residual ionospheric errors remain due to ionospheric spatial decorrelation between the GBAS reference station and the aircraft. This spatial decorrelation is taken into account by the aircraft system when computing protection levels.

Under fault-free conditions, the residual ionospheric error, σ_{iono}, is defined as in Section 2.3.12.3 of [20] and is computed as described in Equation 2.22:

$$\sigma_{iono} = F_{pp} \cdot \sigma_{vig} \cdot (x_{Air} + 2 \cdot \tau \cdot v_{Air}). \tag{2.22}$$

Here, F_{pp} is the so-called obliquity factor, which is used to convert vertical ionospheric delays (i.e. zenith direction) into the slant domain (i.e. across the path of the satellite pseudorange through the ionosphere) and assumes that the ionosphere can be approximated as a thin shell layer situated at a specific height, h_I, above the Earth's surface. The term F_{pp} is described in Equation 2.23 (Section 2.3.12.3 of [20]):

$$F_{pp}^j = \left[1 - \left(\frac{R_e \cdot \cos(\theta^j)}{R_e + h_I}\right)^2\right]^{-1/2}, \tag{2.23}$$

where R_e represents the equatorial radius of the Earth (6378.1363 km), h_I the ionospheric shell height (typically assumed to be 350 km above the Earth's surface), and θ^j the elevation angle of the satellite. In Equation 2.22, x_{Air} is

the distance (slant range) between the aircraft and the GBAS reference point (in meters), τ is the smoothing time constant, and v_{Air} is the horizontal speed of the aircraft (in meters/second). The term $2 \cdot \tau \cdot v_{Air}$ represents code-carrier divergence due to the ionosphere that occurs when the aircraft traverses the ionospheric gradient over one smoothing time constant.

Additionally, in order to enable the aircraft to calculate the bound for nominal ionospheric decorrelation, GBAS ground stations broadcast the so-called σ_{vig} parameter, where "vig" stands for Vertical Ionospheric Gradient. The σ_{vig} parameter expresses a conservative bound on typical one-sigma variation in the vertical ionospheric delay per user-to-reference separation. It is calculated per region/country, as it depends on local nominal ionospheric conditions, and it is based on measurements recorded by separated monitoring stations.

Several values for the σ_{vig} parameter have been proposed in the literature. In the Conterminous United States (CONUS) region, the typical one-sigma variation of the nominal ionospheric spatial decorrelation for GPS L1 frequency was found to be around 1 mm/km [59]. However, a conservative bound of 4 mm/km was finally selected for the σ_{vig} in CONUS [21] to add margin for small ionospheric irregularities that can be considered "nominal" and also for non-Gaussian tail behavior. In further studies ([60]), the authors suggested to include a bound for anomalous tropospheric errors in the σ_{vig} as:

$$\sigma_{vig} = \sqrt{\sigma_{vig}^2 + \sigma_{anomalous\_tropo}^2}. \tag{2.24}$$

Thus, the use of a σ_{vig} value of 6.4 mm/km, including a 5 mm/km bound for worst-case anomalous troposphere and 4 mm/km bound for nominal ionospheric decorrelation along the vector between ground facility and user, was finally proposed in the CONUS region [60]. The σ_{vig} for the CONUS region is considered to be representative for all mid-latitude regions, but each region in which GBAS is installed must calculate its own value. Other mid-latitude regions use their own σ_{vig} values, as is the case of Germany, where 2.07 mm/km is utilized [23].

In equatorial regions, where the nominal behavior of the ionosphere is more active than in mid-latitudes, higher values for the σ_{vig} parameter have been proposed. As an example, in Brazil, a value for σ_{vig} of 14 mm/km for daytime operations (between 6 am and 6 pm local time) [22] has been derived. In this case, this value also includes an anomalous tropospheric component of 5 mm/km. Work to assess σ_{vig} in Brazil to extend GBAS operations into the early morning and early evening periods while maintaining integrity against more severe ionospheric conditions is ongoing.

The σ_{vig} parameter that is actually broadcast may also depend on the active service type of the GBAS ground station. In GAST C, this parameter might be

inflated to protect users against large gradients that might be present between the GBAS ground station and the aircraft on approach. More details about this process are given in Section 2.4.3.

2.3.3.6 Model of the airborne multipath and receiver noise

The residual uncertainty attributed to the airborne multipath and noise (σ_{pr_air}) is computed based on a standardized error model. The model is designed and applied to all aircraft types in order to avoid individual testing and certification for each installation and each aircraft. Figure 2.5 shows the airborne multipath models as a function of satellite elevation.

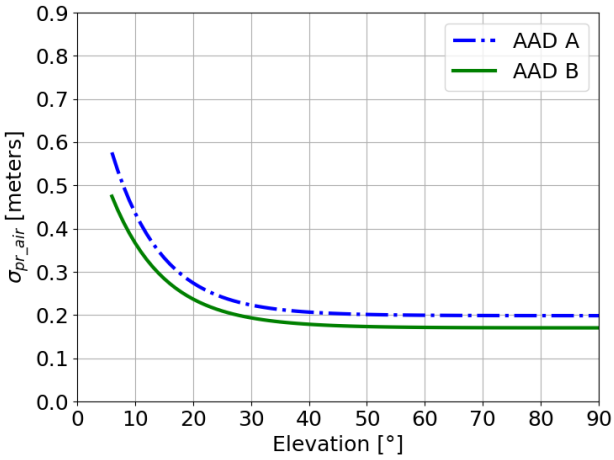

Figure 2.5: Airborne multipath models as a function of satellite elevation.

The airborne error model is composed of receiver thermal noise, σ_n, and multipath noise, σ_{mp} (Section 2.3.12.1 of [20]). Both errors are parameterized as zero-mean Gaussian overbounds, and the total error distribution is computed as the root-sum-square of the two components as shown in Equation 2.25, where θ^j represents the satellite elevation angle relative to the horizon:

$$\sigma_{pr\_air}(\theta^j) = \sqrt{(\sigma_n(\theta^j))^2 + (\sigma_{mp})^2}. \tag{2.25}$$

The model describes the distribution of the airborne error for 100 second smoothed measurements. The GPS L1 C/A standard models called Airborne Accuracy Designators (AADs) provide parameters for the noise and multipath functions for two performance classes of receiver/antenna combinations (see Section 3.6.8.2 of [8]): Airborne Accuracy Designator A (AAD A) reflects the performance of "standard" receiver technologies with wide-correlator sampling,

and Airborne Accuracy Designator B (AAD B) reflects the performance of "advanced" receiver technologies with narrow-correlator sampling. The following equations describe these models:

$$\sigma_{mp}(\theta) = 0.13 + 0.53 \cdot e^{-\theta/10}, \tag{2.26}$$

$$\sigma_n(\theta) = \begin{cases} 0.15 + 0.43 \cdot e^{-\theta/6.9} & \text{for AAD A,} \\ 0.11 + 0.13 \cdot e^{-\theta/4.0} & \text{for AAD B.} \end{cases} \tag{2.27}$$

2.3.4 Integrity monitoring

The purpose of the integrity monitors is to detect and exclude anomalous measurements before they become hazardous to the users so that the nominal protection levels given by Equation 2.15 cover all remaining error sources [55].

Typically, integrity monitors are defined as a statistical hypothesis test where there are two hypotheses: the null hypothesis (H0), which assumes no anomalies, and the alternative hypothesis (H1), for the anomalous (or faulty) case. The test observables or "test statistics" are compared with a certain significance level or "monitoring threshold". When the test statistic exceeds the threshold, the monitor triggers an alert to indicate that there is a failure.

Figure 2.6 depicts the Probability Distribution Function (PDF) of the nominal and the faulty cases. Here, two possible issues might occur. On the one hand, it can happen that an error has occurred but the test statistic has remained below the threshold, and thus the fault has not been detected. This case is depicted with the blue area in Figure 2.6 and is defined by the Probability of Missed Detection (PMD) or P_{md}. On the other hand, it may be the case that no fault has occurred but an alert has been triggered. This case is represented by the red area in Figure 2.6 and is defined by the Probability of False Alert (PFA) or P_{fa}. Note that the design of the integrity monitors is challenging because the detection thresholds have to be low enough to detect all potential hazardous errors and meet the integrity requirement but also high enough so that the monitors do not trigger excessive false alerts, allowing the continuity requirement to be met.

Integrity monitors are designed considering that the nominal test statistic follows a zero-mean Gaussian distribution with a standard deviation, $\sigma_{nominal}$. However, in practice, actual pseudorange error distributions are non-Gaussian since, typically, they are thicker in the tails. Since the stringent integrity risk requirements in GBAS demand that the tails of the error distributions be covered up to a very small probability, the nominal standard deviation must be inflated to bound the actual test statistic at these small probabilities. This is achieved by multiplying the nominal standard deviation, $\sigma_{nominal}$, by an

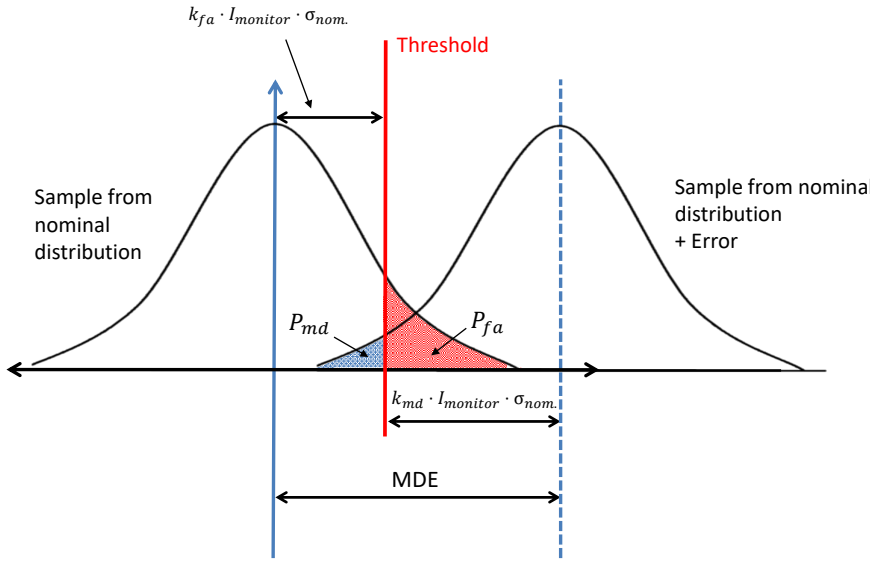

Figure 2.6: Threshold and minimum detectable error.

inflation factor, $I_{monitor}$. More details on how to calculate the inflation factors can be found in [61]. Based on a given P_{fa}, a threshold, Thr, is derived as:

$$Thr = k_{fa} \cdot I_{monitor} \cdot \sigma_{nominal}, \tag{2.28}$$

where k_{fa} is the false alert multiplier needed to meet the required P_{fa}. The k_{fa} depends on the continuity requirement and is computed from the inverse of the standard normal cumulative distribution, $Q^{-1}\left(\frac{P_{fa}}{2}\right)$.

Furthermore, the error that is detected with a missed-detection probability (P_{md}) sufficiently low to meet the integrity risk requirement is "*one whose mean impact on the test statistic is known as the minimum detectable error (MDE)*" [55] and is defined as:

$$MDE = Thr + k_{md} \cdot I_{monitor} \cdot \sigma_{nominal}, \tag{2.29}$$

where k_{md} is the scalar multiplier needed to meet the required P_{md} and is computed from the inverse of the standard normal cumulative distribution, $Q^{-1}(P_{md})$. Figure 2.6 represents the MDE as a fixed bias added to the nominal test statistic, which is depicted as a zero-mean Gaussian. More details on the relationship between MDE, which is expressed in the test statistic units, and the worst-case error impact of a fault in the range domain (meters) can be found in [55].

2.3.5 Integrity monitors in GAST C

From the ground subsystem SiS integrity risk of 2×10^{-7}, 1.5×10^{-7} is allocated to all the other errors that are not covered by the H0 and H1 protection levels. Ephemeris faults within this grouping are covered by the ephemeris protection level (see Section 2.3.2), but all other faults must be mitigated through integrity monitoring without the additional defense of a purpose-built protection level. Different types of monitoring implemented in the GBAS ground station protect against different types of faults or anomalies that can occur on the ground, at the aircraft, on the satellites, and/or in between the ground, the aircraft, and the satellites. These faults can be classified considering their origin [8]: (i) errors due to a faulty ground subsystem, (ii) errors due to faults in the ranging sources, (iii) errors due to environmental faults, and (iv) Radio Frequency Interference (RFI).

This thesis focuses only on errors due to environmental conditions, and more specifically, on errors produced by anomalous ionosphere. All other monitors are considered to be out of scope of this thesis. Therefore, only a brief description of the other potential faults and the associated integrity monitors, based on the description in [62], is given in the following. A detailed description of some of these integrity monitors can be found in [63].

Errors due to a *faulty ground subsystem* can occur due to a hardware or software error on the ground equipment, a failure on the VDB link or anomalous large multipath due to e.g. obstacles in the vicinity of the GBAS reference antennas. Two methods to protect against a faulty ground station are the ground mean and sigma monitors explained in [64]. Both methods use the B-values introduced in Section 2.3.3.1 as input, which are monitored by the Multiple Receiver Consistency Check (MRCC) (refer to Chapter 31 of [65] for an explanation of this monitor).

Errors due to *faults in ranging sources* include different types of threats. Some of these threats are: signal deformation of the transmitted C/A code (Section 5.12.1 of [47]), excessive acceleration of code and carrier phase measurements due to unpredictable satellite clock behavior [8, 66] or low power conditions that lead to transmission of the signals with power below the minimum required level (Section 5.12.2 of [47]). Furthermore, code and carrier divergence due to a failure on the satellite causes code and carrier phase signals to drift apart from each other. To detect this fault, a monitor working in the range domain, the Code Carrier Divergence (CCD) monitor, was designed [25]. Originally, the purpose of the CCD monitor was to allow for detection of satellite hardware failures causing code and carrier to diverge. However, this monitor is also used in the detection of abnormally large temporal gradients in ionospheric delay which also cause the code and carrier of the broadcast signal to diverge significantly. “Measurement quality monitoring” is also in-

cluded due to undetected cycle slips that make carrier phase measurements jump excessively. Some examples are given in Section 2.3.6.7 of DO-253D [20], but a more detailed description of the cycle slip detectors used in this work are given in Section 3.3.1.1 of Chapter 3.

Errors due to *environmental faults* are caused by: anomalous ionosphere and anomalous troposphere. In the case of anomalous troposphere, a weather front between the reference station and the aircraft can cause significant differential measurement error, up to 0.41 m over a 5 km baseline [67]. However, the work in [58] investigated the inclusion of a non-nominal troposphere model in the protection levels calculation. This was done by adding this contribution into the σ_{vig} parameter, as discussed in Section 2.3.3.5. In the case of anomalous ionosphere, anomalously large spatial ionospheric gradients well beyond nominal ionospheric spatial decorrelation can occur. This is an issue because these gradients are not removed through the application of pseudorange corrections and are also not considered by the protection levels. Therefore, they can lead to hazardous position errors if they are not detected by the GBAS ground station [24]. Furthermore, the rapid variations of GNSS signals due to small scale ionospheric irregularities, so-called ionospheric scintillations, occur often in ionospherically active regions around the geomagnetic equator and at high latitudes. These scintillation effects might cause the receiver to lose track of affected satellites [68].

Lastly, the effect of the radio-frequency interference can lead to signal tracking degradation or even to outages of the service. Thus, it is important to monitor and detect the presence of RFI (Appendix D of [20]).

In the next section, a detailed description of the existing methods to mitigate the ionospheric gradient threat in GAST C, which is the main focus of this thesis, is given.

2.4 Impact and mitigation of anomalous ionosphere on GBAS

The ionosphere is a region of the upper atmosphere of Earth ionized primarily by solar ultraviolet (UV) radiation. It has no fixed boundaries, but it is typically considered to exist within about 80 km and up to more than 2000 km altitude [69, 44]. Due to the free electrons in this region, GNSS signals are refracted as they pass through the ionosphere causing variations of the signals' time of arrival with respect to an identical signal traveling through free space. This refraction has a different effect on the pseudorange and on the carrier-phase measurements; the pseudorange measurements are delayed while the phase measurements are advanced.

The speed of propagation of radio signals in the ionosphere depends upon the number of free electrons in the path of a signal, defined as the Total Electron Content (TEC). It is defined as the number of electrons in a cylinder of 1 m^2 cross section extending from the receiver to the satellite (see Equation 5.20 from [44]). The TEC can be derived from dual-frequency code and carrier-phase measurements. Note that, in case of estimating the TEC with carrier-phase measurements, this estimate contains the carrier-phase ambiguities of both frequencies. In many GNSS applications, the ionosphere is modeled as a thin-shell layer. This model assumes that the ionosphere has all its TEC concentrated in a layer infinitely thin located at a certain height from the surface of the Earth (typically 350 km). Therefore, the ionospheric delay experienced by a signal is assumed to be concentrated in a single point, the so-called Ionospheric Pierce Point (IPP). The IPP is defined as the intersection of the line of sight satellite-receiver with the ionosphere, modeled as a spherical layer situated at a constant height of 350 km above the Earth's surface (see Figure 2.7). The specific equations to calculate IPP locations and velocities can be found in [70].

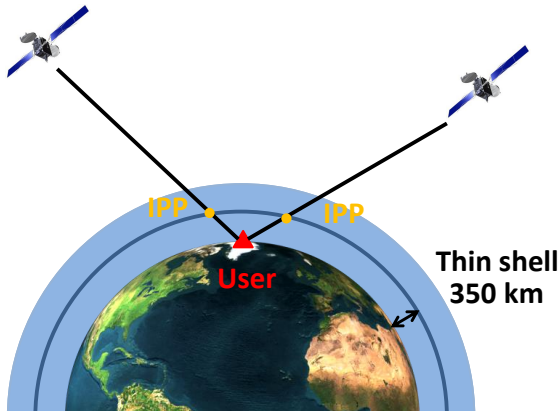

Figure 2.7: Thin shell model and Ionospheric Pierce Points (IPPs).

As mentioned in previous sections, one of the residual errors that can build up for the user of a differential GNSS system like GBAS is the ionospheric spatial decorrelation error. This error is caused by the distance between the user and the GBAS reference station, which makes that the signals received pass through the ionosphere in different regions. Therefore, the ionospheric delays experienced by the aircraft and the GBAS ground subsystem are not the same. These errors are not completely removed after the application of the differential corrections and should be overbounded in the protection levels by using the σ_{iono} term as described in Equation 2.22. However, previous studies ([59]) have shown that ionospheric anomalies can grow during severe ionospheric storms and create large spatial gradients that exceed the nominal

one-sigma error bound (σ_{vig}). If these gradients are not detected and mitigated, they can lead to unacceptably high differential position errors exceeding the 10-meter VAL [24]. Thus, considerable effort was invested in GBAS to mitigate the impact of the ionospheric gradient threat.

This chapter describes, first, the different types of ionospheric anomalies studied in the literature and the GBAS ionospheric threat models, and after, the current methods to mitigate the ionospheric gradient threat in GAST C.

2.4.1 Description of ionospheric anomalies

Prior to the investigation of the different mitigation techniques, exhaustive research analyzed data from ionospheric storms to understand and parameterize the ionospheric threat [59, 71, 72, 73]. Several studies showed that the ionospheric behavior is different depending on the geomagnetic latitude, the time of the day, and the season within a year (e.g, [74, 32]). Furthermore, the occurrence of solar events are linked to the phase of the 11-year solar cycle and the temporal and seasonal variations are linked to the geographical coordinates.

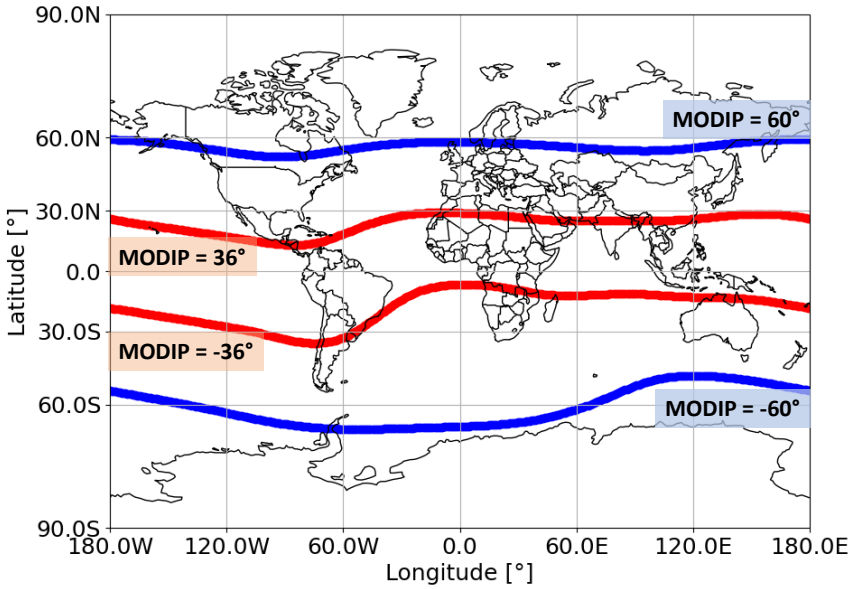

Figure 2.8: Ionospheric activity regions associated to MODIP bounds ([75]).

Regarding the geographic variability, three primary zones, represented in Figure 2.8 can be distinguished according to [75]: (i) the polar region, (ii) the mid-latitude region, and (iii) the equatorial region. Here, the authors define the different ionospheric activity regions as a function of the Modified Dip

Latitude (MODIP) angle, which is defined as:

$$MODIP = \frac{DIP}{\cos\left(lat_r\right)}, \tag{2.30}$$

where DIP is the so-called geomagnetic DIP angle, that is, the angle made with the horizontal by the Earth's magnetic field lines, and lat_r is the geographic latitude of the receiver. More details about the calculation of the MODIP lines (i.e., lines with constant MODIP) are given in [75].

The polar region ($|MODIP| > 60°$) includes the auroral band around 67° latitude. Typically, daytime ionospheric delays are low in this region due to lower solar UV ionizing flux. However, energetic events such as geomagnetic storms can feed particles into the auroral zone, causing it to extend towards the equator. The ionospheric perturbations originating in the auroral region typically propagate following the magnetic field lines and are often the source of Large Scale Travelling Ionospheric Disturbances (LSTIDs) at mid-latitudes ([76], [77]).

The ionosphere in geomagnetic mid-latitude regions ($36° \leq |MODIP| \leq 60°$) includes the US, Europe, south of South America, south of Africa, most of Asia and Australia. It is usually "calm" and varies smoothly with time and location. This smooth variation allows for the GBAS assumption of highly correlated ionospheric delays between the aircraft and the GBAS ground station. However, during the worst solar-induced geomagnetic storms, an increase in the TEC values occurs, causing large ionospheric gradients. These large gradients have been extensively studied in the literature, and an ionospheric threat model has been developed for mid-latitudes. More details are given in Section 2.4.2.1.

The equatorial region ($|MODIP| < 36°$) covers part of South America, central Africa, and part of Asia. It is characterized by the equatorial or Appleton anomaly. The Appleton anomaly describes regions of enhanced ionospheric delay occurring from pre-noon to midnight hours that are offset by $15° - 30°$ in geographic latitude north and south from the magnetic equator. In addition to the equatorial anomaly, the equatorial region is known for often experiencing scintillation phenomena. Scintillations occur in the propagation of the GNSS signals through plasma density irregularities in the ionosphere leading to observed power fades of up to 30 dB. Most common GNSS receivers are not able to track these signals resulting in loss of lock of the affected satellites [68, 78]. Scintillations are mostly observed in two bands north and south of the geomagnetic equator and in the auroral regions, and are rarely seen in mid-latitudes. Furthermore, the observed presence of scintillation is another warning sign that large anomalous ionospheric gradients may be nearby. The scintillation topic is beyond the scope of this thesis and therefore it is not further discussed.

In low latitudes, scintillation usually occurs around so-called Equatorial

Plasma Bubbles (EPBs). The term plasma bubble is used to describe a region in the nighttime ionosphere within which the plasma density is significantly reduced, causing large ionospheric gradients. Characteristics of these bubbles such as temporal evolutions and vertical, latitudinal and longitudinal development have been studied extensively in the literature, and a threat model has been developed for the equatorial regions. More details are given in Section 2.4.2.2.

In the following sections, the different threat models are described.

2.4.2 Ionospheric gradient threat models

The ionospheric threat mitigation strategies rely on the use of ionospheric threat models. As commented previously, since the ionosphere behaves differently in the different regions, the ionospheric threat model must be derived and validated per region in which GBAS is to be installed. This thesis focuses on two main threat models: the threat model for mid-latitudes and the threat model developed for the equatorial regions.

2.4.2.1 Mid-latitudes

The ionospheric threat model for mid-latitudes was firstly determined for Conterminous United States (CONUS) by analyzing historical data of days with severe abnormal ionospheric behavior during the peak of Solar Cycle 23. For this purpose, data containing unusual behavior during ionospheric storms observed by both the U.S. Wide Area Augmentation System (WAAS) and the network of Continuously Operating Reference Stations (CORS) was used. This data was analyzed since April 2000 by exhaustive automated and also manual processes. The details of these processes can be found in [71, 59, 24]. In these works, the ionospheric spatial gradients were calculated automatically for all satellites tracked by "clusters" of CORS stations within close proximity (several tens of kilometers) of each other in regions known to be affected by ionospheric storms. All apparent gradients of large anomalous magnitude were computed by dividing the difference in slant ionospheric delay (i.e., along the actual path between the satellite and receiver) between two CORS stations by the distance between the two stations by using the so-called station-pair method [29]. Finally, the selected gradients were passed through a series of automated screening algorithms and, lastly, they also underwent a manual check. Among all the gradients that were analyzed, the largest one was an extremely steep gradient that had a magnitude of up to 412 mm/km of spatial decorrelation, which is more than 100 times larger than the conservative one-sigma bound on vertical (zenith) gradient considered in the US, 4 mm/km (see

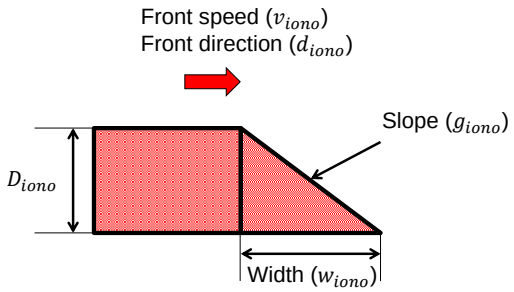

Figure 2.9: GBAS ionospheric threat model for mid-latitudes.

Section 2.3.3.5). This gradient was observed during the geomagnetic storm of November 20, 2003 [29].

As a result of the largest gradients identified in the CONUS region, a parameterization of the ionospheric threat was defined in [29]. An anomalous ionospheric spatial gradient is modeled as a simplified linear semi-infinite wave front (wedge model) moving with constant speed, as shown in Figure 2.9. The main five parameters in the GBAS ionospheric threat model are: the slope of the gradient (g_{iono}) in slant delay measured in mm/km, the width of the wedge (w_{iono}) in km, the forward propagation speed of the wave front relative to a fixed point on the ground (v_{iono}) in m/s, the direction (d_{iono}) in degrees, and the maximum delay (D_{iono}) in meters. The slant ionospheric delay is measured across the path of the satellite pseudorange through the ionosphere and not in the zenith direction. Thus, it is dependent on the satellite elevation. The behavior of the ionospheric anomalies outside the model is considered to have negligible probability.

However, as the ionosphere varies significantly with location, ionospheric threat models for each region intended to use GBAS have to be developed. Previous studies published results from the ionospheric threat models for Germany ([23]), South Korea ([79]), and Europe ([80]), which have shown that the gradients observed are within the bounds of the ionospheric threat model for CONUS. Therefore, the CONUS threat model is considered to be representative for mid-latitude regions under the condition that no significant penalty exists on system availability.

The upper bounds of the threat model parameters for the CONUS region and Germany are summarized in Table 2.5 ([29, 23]).

Threat Model Param.	**CONUS threat model**	**German threat model**
Max. slope [mm/km]	$375; \quad 5° < \theta \leq 15°$ $375 + 50 \cdot (\theta - 15)/50; \quad 15° < \theta \leq 65°$ $425; \quad 65° < \theta \leq 90°$	$40; \quad 5° < \theta \leq 30°$ $40 + 2.5 \cdot (\theta - 30); \quad 30° < \theta \leq 70°$ $140; \quad 70° < \theta \leq 90°$
Speed [m/s]	$0 - 750$	$0 - 1200$
Approach direction [°]	Any direction	Any direction
Width [km]	$25 - 200$	$20 - 200$
Max. delay [m]	50	50
Time of day	Any time	Any time

Table 2.5: GBAS ionospheric threat model parameters for CONUS and Germany.

2.4.2.2 Equatorial regions

In the equatorial regions, the CONUS threat model previously described cannot be directly applied because the ionospheric activity is significantly more variable and unpredictable compared to mid-latitude regions. Therefore, a new threat model valid for low-latitude ionospheric conditions was developed for Brazil [30], and for the Asia Pacific region [31].

An assessment of the Brazilian GBAS ionospheric spatial gradient was carried out using dual-frequency GNSS measurements collected on 123 active ionospheric days during the peak of Solar Cycle 24 (from April 2011 to March 2014) [30]. Here, almost all of the largest gradients were discovered in the presence of an Equatorial Plasma Bubble (EPB). This ionospheric phenomenon occurs during nighttime, specially after sunset, and has a band-like spatial structure elongated in the north-south direction and moving eastward. Inside an EPB region, the density of ions is significantly lower compared to the surrounding ionosphere, causing the so-called plasma deplections. These deplections can be described as two steep side walls in the east-west direction of the deplection within which there are also plasma density irregularities [81]. The largest observed slant gradient in Brazil occurred on March 1, 2014, was caused by one of these “walls”, and had a magnitude of 850.7 mm/km [30], which is almost double the upper bound of the CONUS threat model (425 mm/km).

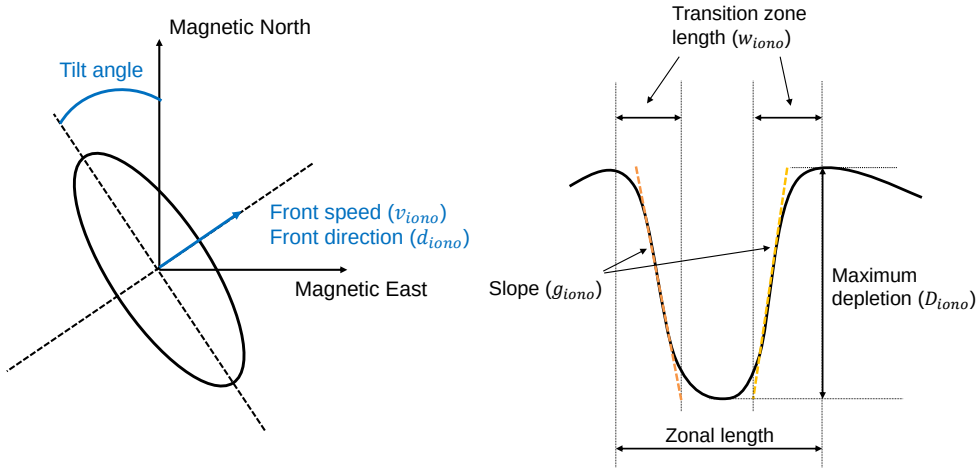

(a) Propagation parameters of an EPB. **(b)** Depletion parameters of an EPB.

Figure 2.10: GBAS ionospheric threat model for Brazil.

Threat Model Parameter	**Brazilian threat model**
Maximum slope [mm/km]	860
Speed [m/s]	40 - 246
Approach direction [°]	Within ±30° of magnetic equator (from West to East)
Width or Transition zone length [km]	22 - 454
Zonal length [km]	96 - 752
Maximum delay [m]	35
Occurrence time of day	Local nighttime

Table 2.6: GBAS ionospheric threat model parameters for Brazil [30].

Furthermore, in the Asia Pacific region, ionospheric gradients as large as 518 mm/km were observed from the analysis of GNSS data in Ishigaki (near +19.6° geomagnetic latitude) during April 3, 2008, which were also caused by an EPB event [31].

However, since not only the magnitude of the gradients induced by EPBs but also their characteristics are different than the storms occurring in mid-latitudes, a new threat model was developed in Brazil including more parameters to describe the EPBs. In Figure 2.10, the threat model parameters describing the three-dimensional geometry of a plasma bubble are shown. The first change with respect to the mid-latitude's threat model is the shape; in this case, the EPB is modeled as a double-sided linear wedge (parameterized by the gradient of the ramp and its transition zone length) with a depletion region in the middle, traveling eastward with constant propagation speed [30, 54].

These parameters include the same as for the single wedge model: gradient slope (g_{iono}), width of transition zone length (w_{iono}), maximum delay or maximum depletion (D_{iono}), and propagation speed (v_{iono}) and direction (d_{iono}). However, two other parameters were included: the tilt angle and the occurrence time. As previously mentioned, the occurrence time of the plasma bubbles is typically during the nighttime (from 6 pm to 6 am local time), especially after sunset. The tilt angle describes the orientation of the EPB relative to geomagnetic north. This is a simplification for Brazil because the EPBs are known to travel following the MODIP lines and therefore have a latitudinal variation [82].

The current set of bounding parameter values that form the EPB threat model is summarized in Table 2.6.

2.4.3 Ionospheric threat mitigation in GAST C

As mentioned previously, a GAST C ground station is responsible for ensuring integrity at the output of the airborne receiver against all threats emanating from the GBAS signal in space (i.e., not from aircraft equipment or structure). This means that the worst-case aircraft differential range error induced by an ionospheric anomaly has to be determined considering also the limitations of GBAS ground station monitoring. Typically, the ground monitor considered for determining the ionosphere-induced range errors is the Code Carrier Divergence (CCD) monitor [25] (see Section 2.3.5).

The CCD monitor detectability depends highly on the relative speed, Δv, between the ionospheric front and the projected IPP velocity over the propagation direction of the front. If the front velocity and the projected IPP velocity are the same or very similar in direction and magnitude, the ionospheric delay observed by the ground station does not change in time fast enough to be detected by the CCD monitor. Therefore, for a GBAS user, two worst-case scenarios are typically considered: (i) the gradient is seen to be almost stationary from the fixed ground station due to the motion of the satellite and the gradient, and (ii) the gradient approaches from behind the aircraft and therefore impacts it before it is visible to the ground station. The first scenario results in small variations of the ionospheric delay over time and thus, the ionospheric gradient would not be detected by the CCD monitor. In the second case, large position errors might built up at the aircraft before the gradient impacts the ground station and the CCD monitor is able to detect it. Therefore, the CCD monitor alone cannot mitigate the potential integrity failure in case ionospheric anomalies occur under specific worst-case satellite geometries.

For this reason, different approaches to mitigate the ionospheric gradient threat in CAT I GBAS have been proposed in the literature, which are described in the following subsections.

2.4.3.1 Position domain geometry screening

One possible way to mitigate this integrity threat for CAT I GBAS users is to assume that the worst possible ionospheric anomaly is always present. In this way, a GAST C ground station verifies by simulation that each satellite geometry potentially usable at the aircraft (PLs $\leq$ ALs) is safe in the presence of the "worst-case" ionosphere-anomaly threat applicable in the region in a process called Position Domain Geometry Screening (PDGS). This methodology was first proposed in [83] and adapted in [26, 84, 27]. In case a simulated satellite geometry is not safe, the ground station inflates the integrity parameters so that the PLs exceed the ALs when an arriving aircraft aims to use this satellite geometry, making GBAS unavailable. From the PLs, only the VPL is taken into account for simplicity, because the most stringent requirements are defined for the vertical domain. Furthermore, due to the satellite geometry, the navigation performance is generally worse in the vertical than in the horizontal domain.

The PDGS algorithm comprises mainly three parts: (i) simulation of the worst-case ionosphere-induced range errors based on the established ionospheric threat model, (ii) computation of the maximum vertical ionospheric-induced position errors, and (iii) the inflation of the broadcast integrity parameters.

2.4.3.1.1 Ionosphere-induced range error simulation

This step determines the worst-case differential ionospheric-induced range errors that could occur in the airborne in the presence of an ionospheric anomaly. For that purpose, exhaustive simulations are conducted to consider all possible combinations of gradient slopes and widths together with aircraft positions and relative speeds between the IPP and the ionospheric front [83]. The maximum differential range errors (ε) that build up in the aircraft before the CCD monitor triggers are included in a look-up table as a function of the ionospheric gradient slope (g_{iono}) and front velocity relative to the IPP (Δv).

Closed-form expressions derived based on the exhaustive simulations described in [83] were presented in [84, 26, 27] in order to calculate the ionosphere-induced range errors in a more straightforward manner. However, in [53], the authors argue that the previously derived formulas cannot be applied when the magnitude of a gradient gets larger than the values covered by the CONUS threat model, as it does in Brazil. Therefore, Kim et al. derived in [85] improved and more general closed-form expressions considering the Brazilian threat model to calculate the ionosphere-induced range errors. These updated formulas are summarized in the following.

Case 1: Very small relative speed of the ionospheric front and IPP

When Δv is close to zero, the CCD monitor cannot detect anomalous ionospheric gradients. Moreover, the ionosphere-induced range errors increase as the effective separation between the GBAS ground facility and an approaching airplane increases. This effective separation includes a physical separation, x_{Air}, between ground facility and airplane and a synthetic separation, $2 \cdot \tau \cdot v_{Air}$, due to the memory of the single-frequency carrier-smoothing filter used in both ground and airborne GBAS processings [25]. In this case, the ionosphere-induced differential range error in meters, ε, is calculated using Equation 2.31:

$$\varepsilon = \min\left(\frac{D_{iono}}{w_{iono}}, g_{iono}\right) \cdot \left(x_{Air} + 2 \cdot \tau \cdot v_{Air}\right), \quad \text{if} \quad \Delta v \leq a, \tag{2.31}$$

where a is:

$$a = \frac{MDDR_{ccd}}{2 \cdot \min\left(\frac{D_{iono}}{w_{iono}}, g_{iono}\right)}, \tag{2.32}$$

and $MDDR_{ccd}$ is the minimum detectable divergence rate of the CCD monitor, D_{iono} is the maximum ionospheric delay considered in the threat model (in meters), w_{iono} is the ionospheric front width (kilometers), g_{iono} is the ionospheric gradient (m/km), x_{Air} is the physical separation between the GBAS ground facility and an approaching airplane (kilometers), τ is the time constant of the single-frequency GBAS carrier-smoothing filter, which is 100 s for CAT I GBAS, v_{Air} is the velocity of the aircraft on approach (km/s), Δv is the relative speed between the ionospheric front velocity and the projected velocity of a satellite IPP (km/s), and a is a value of the relative speed Δv at which the CCD monitor starts to detect the anomalous ionospheric gradient.

Case 2: Moderate relative speed of the ionospheric front and IPP

In this case, the CCD monitor begins to detect anomalous ionospheric gradients and the ionosphere-induced differential range errors are calculated as in Equation 2.33:

$$\varepsilon = \frac{2 \cdot \tau \cdot v_{Air} \cdot g_{iono}}{a - b} \cdot (\Delta v - b) + g_{iono} \cdot x_{Air}, \quad \text{if} \quad a < \Delta v \leq b, \tag{2.33}$$

where b is a point of Δv at which the differential range error calculated from the exhaustive simulations is at a minimum (see Figure 10 of [85]) and is calculated as:

$$b = \frac{0.0165}{g_{iono}} + 0.113. \tag{2.34}$$

Case 3: Large relative speed of the ionospheric front and IPP

In this case, the CCD monitor alerts with a very small probability of missed-detection and the potential ionosphere-induced differential errors do not grow over the value calculated with Equation 2.35:

$$\varepsilon = g_{iono} \cdot x_{Air}, \quad \text{if} \quad \Delta v > b. \tag{2.35}$$

2.4.3.1.2 Maximum ionospheric vertical position errors

The first step provides the ionospheric-induced range error per satellite (ε) as a function of the relative speed either in the form of a look-up table or using the closed-form expressions. Based on this output, ionospheric-induced position errors can be computed considering potential satellite geometries.

First, the GBAS ground station generates all possible subsets of geometries from an all-in-view set of $\mathcal{J}$ usable satellites down to $\mathcal{J}-2$. This assumes that the airborne might not use up to two satellites from the ones visible to and approved by the ground station due to, e.g., maneuvering, filter convergence, etc.

Then, the ionosphere-induced position errors are computed assuming that two satellites are simultaneously affected by the ionospheric front [26, 27]. In this case, the so-called two satellites affected scenario, it is also assumed that the IPP velocity of one satellite projected into the direction of propagation of the ionospheric front is approximately the same as the velocity of the ionospheric front. This means that the relative velocity between the front and the first satellite is considered to be approximately zero. Since, in general, the IPP velocities of two satellites are always different, the relative velocity between the front and the second impacted satellite will not be zero and thus, that error will likely be detected by the CCD monitor.

Since the worst possible satellite pair in terms of position error cannot be predicted *a-priori*, all possible independent satellite pairs (j_1, j_2) must be considered for each subset geometry [26, 27]. Once all possible satellite subsets are identified, the ionosphere-induced vertical position error (denoted as Ionosphere-induced Error in Vertical (IEV)) for each of these subsets and each pair of satellites (j_1, j_2) is calculated as:

$$IEV^{j_1,j_2} = \max\left\{\left|s^{j_1}_{apr\_vert} \cdot \varepsilon^{j_1} + s^{j_2}_{apr\_vert} \cdot \varepsilon^{j_2}\right|, \left|s^{j_1}_{apr\_vert} \cdot \varepsilon^{j_1} - \gamma \cdot s^{j_2}_{apr\_vert} \cdot \varepsilon^{j_2}\right|, \left|s^{j_2}_{apr\_vert} \cdot \varepsilon^{j_2} - \gamma \cdot s^{j_1}_{apr\_vert} \cdot \varepsilon^{j_1}\right|\right\}, \tag{2.36}$$

where s_{apr_vert} is the vertical position component of the weighted-least-squares projection matrix $\boldsymbol{S}$ for satellite j_1 or j_2 (see Section 2.3.2, Equation 2.16), ε is the ionosphere-induced range error for satellite j_1 or j_2 (computed from the look-up tables or using the closed-form equations), and γ is a dimensionless constant between 0 and 1 used to overbound the errors introduced by

any observed ionosphere anomaly. When γ is equal to 1, IEV reaches its most conservative value [27]. The IEV for both satellites is computed and the largest IEV is selected to be the value of that satellite pair. After the IEV is computed for all the satellite pairs from a subset geometry, the Maximum Ionosphere-induced Error in Vertical (MIEV) for this subset is calculated as the maximum of the IEVs.

The previously described methodology can be applied to all regions in the world. However, in Brazil, where the threat model specifies certain limits for the direction of propagation of the EPBs, the selection of satellite pairs is specified within the orientation angle constraint given by the limit on the EPB tilt angle [28]. Thus, some cases where the front affects specific satellite pairs are physically very unlikely, and therefore these satellite pairs are discarded. In this case, the satellites are individually simulated as single-satellite impact scenarios [28].

The MIEV for each satellite subset that might be used by the airborne user is compared with the CAT I Tolerable Error Limit (TEL) in the vertical direction, which is 28.78 meters at the minimum DH of 200 ft [86]. If the MIEV value of a subset exceeds the TEL, the geometry must be excluded in order to mitigate the potential integrity risk. This is done by inflating the broadcast integrity parameters.

2.4.3.1.3 Inflation of the integrity parameters

The goal of this step is to inflate the broadcast integrity parameters such that the potentially hazardous satellite geometries that generate MIEVs exceeding the TEL are excluded. The reason behind is that when the ground station inflates the integrity parameters, the VPLs computed in the aircraft increase accordingly. However, depending on which integrity parameters are decided to be inflated, satellite geometries that are not hazardous (MIEV $<$ TEL) might be discarded as well, leading to an unnecessarily loss of availability.

Therefore, several possibilities have been studied in the literature for the inflation of the integrity parameters: σ_{vig} inflation in [83, 26, 27, 28], and σ_{pr_gnd} and P-value inflation in [84, 83, 27, 28]. From these possibilities, the inflation of σ_{vig} is the method that is more commonly used.

Inflation of the σ_{vig} parameter

The inflation process in this case starts with an uninflated σ_{vig} value, which is the nominal and corresponds to an inflation factor I_{vig} of 1 ($\sigma_{vig,nom}$). Then, the I_{vig} is incremented by small amounts (e.g. 0.01 [26]), and σ_{vig} is:

$$\sigma_{vig} = I_{vig} \cdot \sigma_{vig,nom}. \tag{2.37}$$

After each inflation, VPLs are computed and the process stops when all hazardous geometries are excluded. This inflation process is repeated for different decision height distances (horizontal distance between the ground facility and the aircraft when it reaches 200 ft decision height in CAT I precision approaches) [26, 27, 28]. In addition, the inflation process simulates as well aircraft distances up to 7 km from the decision height in order to guarantee integrity in the whole region [26, 27, 28]. Note that the further away the aircraft is from the decision height distance, the larger are the values of VAL and TEL [86]. Thus, σ_{vig} inflation gets usually more stringent when the distance between the aircraft and the runway threshold decreases. Finally, the inflation factor is the minimum value that eliminates all hazardous geometries.

However, since the σ_{vig} parameter does not vary across satellites, it increases the VPLs of all potentially usable geometries, including also the safe ones. This typically leads to an undesirable loss of availability.

Combined inflation

Several studies [53, 28] that apply the geometry screening algorithm together with the Brazilian threat model have suggested that when this threat model is utilized, σ_{vig} can occasionally reach its maximum value. The σ_{vig} maximum value is limited by the number of bits that can be transmitted due to space in the message [87] and it is equal to 25.5 mm/km.

Therefore, in this case, the σ_{vig} parameter is inflated until it reaches the maximum value of 25.5 mm/km and then, σ_{pr_gnd} is inflated as needed until all the potential hazardous satellite geometries are screened out [53, 28].

3
Methodology

As addressed in Chapter 2, mitigation of large ionospheric gradients remains as an issue in GBAS because the existing solutions degrade the availability of the system in geographic areas that have a highly active ionosphere.

The problem is that integrity monitoring relies on the use of "worst-case" conservative threat models, which leads to an excessive inflation of the integrity parameters in GAST C. Therefore, the main objective of this chapter is to provide a solution to reduce the excessive conservatism currently taken in GBAS assumptions in order to increase availability. The solution proposed is the use of a wide-area network of stations that monitor for ionospheric gradients in real time, which serves two purposes: (i) to distinguish abnormal from nominal ionospheric conditions, avoiding the conservative assumption of an always present "worst-case" gradient, and (ii) to estimate the actual gradient parameters when there is an anomalous ionospheric gradient present, avoiding the use of the largest values ever found in history.

In [88], I and other authors performed preliminary studies on the design of the methodology for "Network GBAS" based on the calculation of the ionospheric gradients between IPPs for each station and each satellite. This methodology relied on the accuracy of the mapping functions (see Equation 2.23) when transferring slant ionospheric delays to vertical delays. However, the mapping function employed might create large errors when there are anomalous ionospheric gradients [89, 90, 91]. Furthermore, the methodology presented in [88] depends highly on the baselines between stations and, if stations are not sufficiently close, the gradients might be underestimated. Therefore, I adapted the methodology to overcome these issues and describe it throughout this chapter. The work included in this chapter was published in [92, 93] as stated in Section 1.5.

This chapter is structured as follows: Section 3.1 reviews current GBAS standards in order to find a solution that reduces current conservatism without having to change them, Section 3.2 introduces the "Network GBAS" concept in general terms, Section 3.3 provides the methods developed in this thesis to

detect anomalous ionospheric gradients, estimate the gradient parameters and ensure integrity, and Section 3.4 describes the interface between the information provided by the network and a GBAS station.

3.1 Feasibility of reducing conservative assumptions in GBAS

As noted in Section 1.2, the availability of GBAS is determined mainly through the probability of protection levels exceeding the required alert limits, and this value increases with the assumption of an always-present "worst-case" ionospheric gradient. This means that the highest values of the ionospheric gradient threat model applied in the relevant region (see Section 2.4.2) are always used in the inflation of the integrity parameters and in the validation of the integrity monitors. In the first case, PLs will occasionally exceed ALs even in nominal conditions while, in the second case, the design of the integrity monitors may be excessively complicated or difficult to deploy.

However, although conservative, this worst-case assumption is needed to guarantee the integrity of the system because GBAS ground stations operate completely autonomously and do not receive any external information about the state of the ionosphere.

Since this assumption is the principal reason why GBAS cannot be deployed in geographic areas with a highly active ionosphere (e.g. auroral and equatorial regions), in the new version of the Standards and Recommended Practices (SARPS), provisions are explicitly made to leverage external ionospheric information (Section 7.5.6.1.7 of [8]): *"The service provider may elect to: [...] Introduce additional monitoring (internal or external to the GBAS), [...]. Another mitigation strategy is monitoring of space weather (external to the GBAS system)"*.

Thus, including external information in GBAS is possible without the need to modify the current standards, as long as the integrity of the system is guaranteed. For this reason, this thesis proposes a concept for monitoring the state of the ionosphere in real time and including this information in GBAS. As a result, a relaxation of the current conservative assumptions is possible with a consequent increase in the availability of GBAS in regions where it is degraded.

3.2 Dual-frequency ionospheric monitoring concept

As previously mentioned, integrity parameters in GBAS are typically computed under "worst-case" conservative assumptions. For this reason, this thesis

proposes a concept capable of adjusting the integrity parameters transmitted to the aircraft based on the real-time state of the ionosphere.

For this purpose, first, the concept defines a methodology that detects and estimates ionospheric gradients using a wide area network of dual-frequency and multi-constellation GNSS stations situated in carefully surveyed locations. In this way, the state of the ionosphere can be monitored in real time. Then, it defines a methodology for adjusting the integrity parameters based on the performance of the monitor. These adjusted parameters would be used in the same manner as the current conservative (unadjusted) integrity parameters in existing algorithms for mitigating the ionospheric threat at GBAS ground stations. This process is therefore transparent to aircraft, which receive the integrity parameters from the GBAS stations and use them to ensure the integrity of precision approaches and landings. Thus, the overall concept of GBAS integrity remains unchanged, facilitating the use of existing standards.

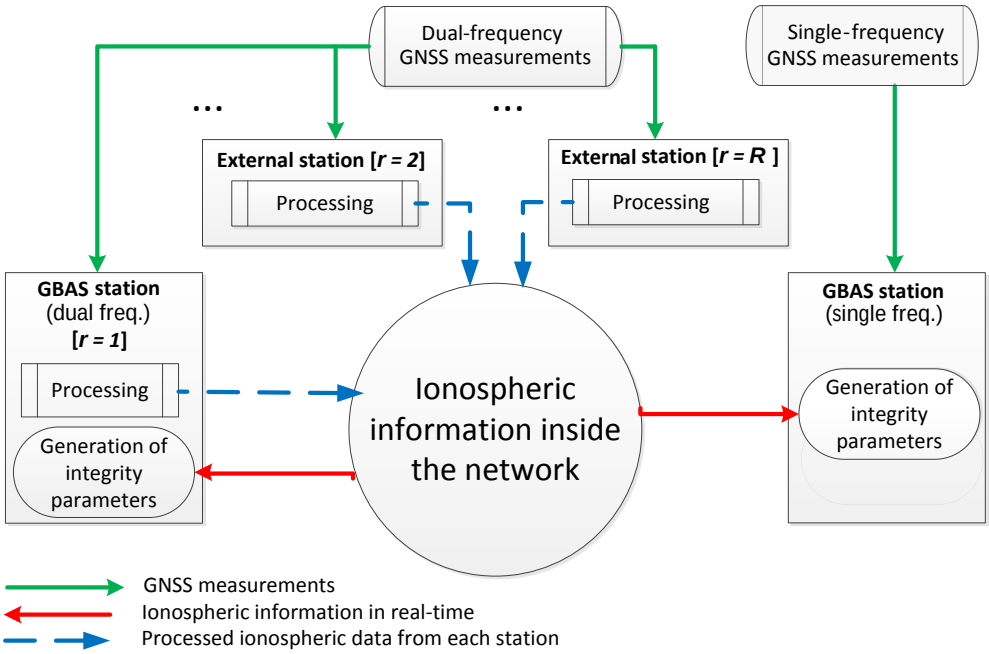

Figure 3.1: Simplified diagram of the network.

The network of stations would consist of mainly the GBAS stations installed in the relevant region that would need dual-frequency capable receivers or have a second dual-frequency receiver installed for monitoring purposes only. Since it is foreseen that GBAS stations will be installed principally at important airports, the network might need other external dual-frequency monitoring stations to enhance the coverage of the GBAS stations while monitoring for

gradients. These external monitoring stations could be newly installed and/or already existing dual-frequency reference stations like (e.g.) SBAS stations. Note that the quality of the measurements provided by existing reference stations must be sufficient to guarantee integrity in order to be considered as part of the network. The dual-frequency measurements coming from both types of stations (GBAS and external) would be used to estimate the ionospheric delay reliably in order to detect ionospheric anomalies in real-time. Furthermore, the utilization of multiple constellations would provide improved sampling of the ionosphere. Additional ionospheric measurements coming from other constellations could also be used to support the single-frequency and single-constellation GBAS by extending its knowledge of the ionospheric state beyond what would be available from a single constellation. Therefore, the stations that are part of the network must be dual-frequency capable, while the use of several constellations is optional.

The functionality of the proposed monitoring network is described in the following and depicted in Figure 3.1:

1. The processing component of each of the stations receives GNSS dual-frequency (mandatory) and multi-constellation (optional) code and carrier phase measurements and calculates the geometry-free combination of the carrier-phase measurements at current epoch t as in Equation 3.1 (Equation 5.33 of [44]):

$$\widehat{I}^{j}_{f_1,r}(t) = \frac{(f_2)^2}{(f_1)^2 - (f_2)^2} \cdot \left(\phi^{j}_{f_1,r}(t) - \phi^{j}_{f_2,r}(t) \right), \tag{3.1}$$

   where $\phi^{j}_{f_1,r}(t)$ is the carrier-phase measurement in meters for frequency f_1 (e.g., L1/E1), and $\phi^{j}_{f_2,r}(t)$ the carrier-phase measurement in meters for frequency f_2 (e.g., L5/E5a). A single satellite from the GPS or other satellite constellations is represented by j and identified with its system name and its number within its system (e.g., G03 is satellite number 3 in the GPS constellation). The station that calculates the geometry-free combination is r, which is identified with a certain station name. Moreover, each station r belongs to the set of the monitoring network of stations denoted as $\mathcal{R}$. Note that, the geometry-free combination of the carrier-phases contains the carrier-phase ambiguities of both frequencies and the hardware biases. Therefore, it is not exactly a direct estimate of the ionospheric delay. Nevertheless, this work refers to the result of Equation 3.1 as an estimate of the slant ionospheric delay (with errors). The reason is that this value is not used directly but its first derivative is used instead, and thus, the errors mentioned above cancel out because they are constant over time. Moreover, the slant ionospheric delay is calculated at the IPPs, considering the ionosphere modeled as a “thin shell”

located at 350 km above the Earth's surface [70]. Since this work considers only the slant ionospheric delay calculated for frequency (L1/E1), frequency subscripts are omitted in the following.

2. The rate of change of the estimated ionospheric delay corresponding to each satellite j and each station r is compared with a predefined threshold derived with real measurements from this station r and integrity requirements. This threshold decides whether there is a significant perturbation affecting this satellite-station pair in real time. In Sections 3.3.1 and 3.3.3, more details about the threshold derivation and the detection algorithm are given, respectively.

3. The detection information from each of the stations observing a given satellite is shared within the network in real time. Here, the network distinguishes between three possible cases: (i) several monitoring stations have detected the same ionospheric gradient, (ii) none of the monitoring stations have detected anomalous ionospheric gradients, and (iii) several monitoring stations have detected anomalous gradients, but the network is not able to ensure that this gradient is the same for all of them. In the case that several monitoring stations have detected the same ionospheric gradient, a central processor estimates its parameters. This gradient parameter estimation process is done per satellite, and it requires that at least 3 stations have detected the gradient (see Section 3.3.4). Furthermore, the estimated gradient parameters are overbounded to consider the potential "worst-case" estimation errors. If fewer than 3 stations have detected the gradient, the network is not able to estimate the actual gradient parameters, and it triggers a "Warning" to indicate that the GBAS stations should use "worst-case" assumptions. If none of the monitoring stations have detected any anomalous ionospheric gradients, the network transmits the largest gradient that could be affecting the supported GBAS stations without being detected, or the "Minimum Detectable Gradient (MDG)". The calculation of the MDG is addressed in Section 3.3.2. If several stations have detected a gradient, but the network is not able to ensure that the gradient detected is the same for all the stations, it triggers a "Warning" to indicate that the GBAS stations should use "worst-case" assumptions. Figure 3.2 describes the network decision logic.

4. Each GBAS station would be then responsible of using the network information to adjust the integrity parameters and support the already existing equipment in covering the GBAS approaches at each airport. The applicability of the dual-frequency monitoring concept to GAST C is further discussed in Section 3.4.

Note that the Network-GBAS concept would also support single-frequency

GBAS stations that are not nodes of the network but are located in the network coverage area. This could not be done if the different nodes of the network were not connected. For instance, dual-frequency GBAS reference receivers (as in [42]) or additional dual-frequency receivers installed within the airport area could be used, but this would only protect a single GBAS station. Furthermore, in both of these cases, it would be necessary to ensure that the distance between the dual-frequency receivers installed within the airport area is sufficient to detect gradients before they become harmful for GBAS. This is more difficult in the case of not using a network, because the observability of gradients is lower and, in addition, airports often have restrictions on the areas in which these receivers can be installed.

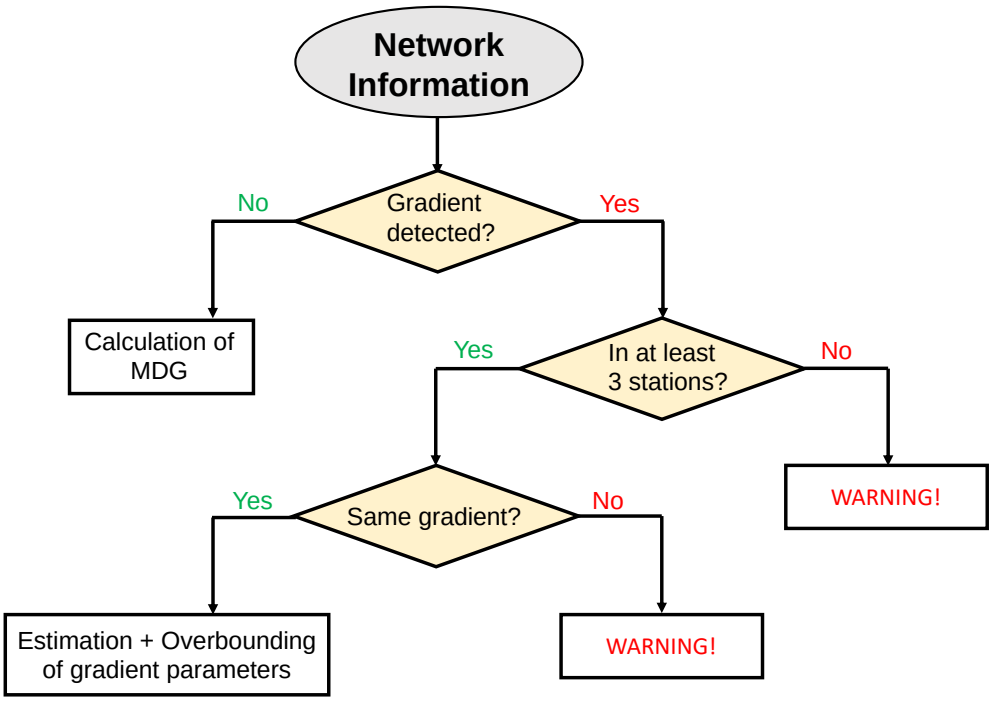

Figure 3.2: Flow chart of the network decision logic.

3.3 Methods

This section describes the algorithms to detect anomalous ionospheric gradients in real time and estimate gradient parameters like slope, width, speed, and direction in near real time. However, before the real-time operation of the algorithms, pre-processing is needed in order to derive detection thresholds while taking into account the characteristics of each of the stations in

the monitoring network. Furthermore, the process to calculate the Minimum Detectable Gradient (MDG) is described.

3.3.1 Derivation of the monitoring thresholds

An appropriate monitoring threshold derivation is the key part in the algorithmic chain, since this threshold determines whether an anomalous ionospheric gradient is measured or not. Therefore, it is important to study the expected performance of each of the monitoring stations inside the network in days when the state of the ionosphere was considered nominal. For that purpose, for each of the monitoring stations, several days of dual-frequency GNSS measurements recorded under nominal ionospheric conditions were selected manually. To select nominal days, an ionospheric index called "Along Arc TEC Rate (AATR)" defined in [32] was used. Section 4.1.2 of Chapter 4 and Section 5.1.2 of Chapter 5 give more details about this index and the selection of nominal days with real data.

Furthermore, the amount of nominal data that is selected for monitoring threshold derivation should be large enough to cover all possible satellite geometries used while avoiding false alerts due to environmental features (e.g. multipath). Note that, in the "Network GBAS" concept, a false alert in a certain station of the network does not automatically lead to a loss of continuity, but instead, requires assuming the "worst-case" ionospheric threat model parameters for that specific satellite on that area of the network.

Once the nominal data is selected, several processing steps have to be performed in order to compute the detection thresholds. These steps are: (i) data processing, (ii) definition of the test statistic, and (iii) threshold derivation.

3.3.1.1 Data processing

Even in nominal conditions, the carrier-phase measurements might contain cycle slips (discontinuities in the phase measurements due to the receiver losses of lock) that could result in false gradient detections; thus it is necessary to process the data before calculating the threshold. This data processing consists of the following two stages: (i) detection of cycle slips, and (ii) visual check to remove possible cycle slips that might be left after step (i).

Figure 3.3a shows an example of a cycle slip that occurred on the L2 carrier-phase measurements of satellite G07 during the day 73 of year 2015 at station "av17", located in Alaska (one of the stations used in Chapter 4).

3.3.1.1.1 Detection of cycle slips

In this thesis, two different cycle slip detectors that can run in real time and are based on dual-frequency measurements are implemented.

Cycle slip detector based on the geometry-free combination of carrier-phases

This cycle slip detector is based on the one explained in Section 4.3.1.1 of [45]. It searches for jumps in the slant ionospheric delay estimation ($\widehat{I}_r^j$) computed as in Equation 3.1.

The geometry-free combination from carrier-phase measurements in two different frequencies (f_1 and f_2) removes the geometry, including clocks and all non-dispersive effects. In nominal conditions (i.e., without scintillation or large gradients), slant ionospheric delays experience smooth changes between consecutive epochs, even if the receivers have a sampling rate of 30 s. This fact is taken advantage of by the detector, which predicts $\widehat{I}_r^j(t)$ by performing a second-degree polynomial fitting over a sliding window of the last N_I samples (e.g. 10 samples in Section 4.3.1.1 of [45]). The predicted value from this polynomial is subtracted from the observed value (at the current epoch) to detect cycle slips.

The threshold for this cycle slip detector depends on the sampling rate of the data. Following the explanation given in Section 4.3.1.1 of [45], the threshold used in this thesis is:

$$Tcsd_{GF} = \frac{(f_2)^2}{(f_1)^2 - (f_2)^2} \cdot \left(a_0 - \frac{a_0}{2} \cdot e^{\left(\frac{-\Delta T}{T_0}\right)} \right), \tag{3.2}$$

with $a_0 = \frac{3}{2} \cdot (\lambda_{f_2} - \lambda_{f_1})$ and $T_0 = 60$ s. Figure 3.3b shows that this detector was able to detect the cycle slip depicted in the example of Figure 3.3a.

Cycle slip detector based on code and carrier-phase data: the Melbourne-Wübbena (MW) combination

This cycle slip detector, explained in Section 4.3.1.2 of [45], uses the "Wide-lane" combination of the carrier-phase measurements in two frequencies and the "Narrow-lane" combination of the code measurements in two frequencies to compute the Melbourne-Wübbena (MW) combination (B_W). This combination has a double benefit. On one hand, the "Wide-lane" combination has a larger wavelength than each signal individually. On the other hand, the measurement noise is reduced by the "Narrow-lane" combination of code measurements. These two facts together lead to an easier detection of the cycle slips.

The detection is based on the real-time computation of mean (m_{B_W}) and standard deviation (σ_{B_W}) values of the B_W measurement test data computed

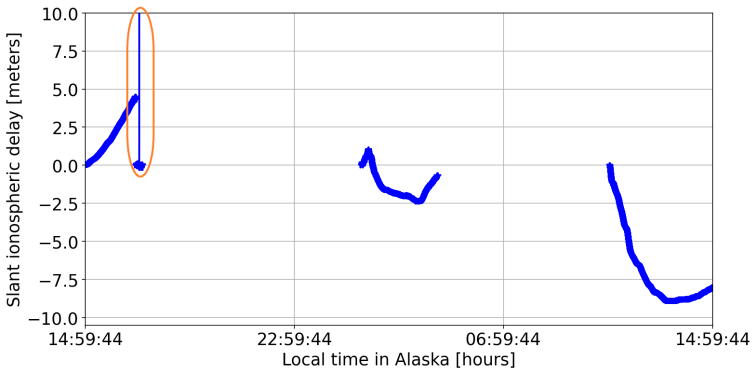

(a) Slant ionospheric delay for satellite G07 and station "av17".

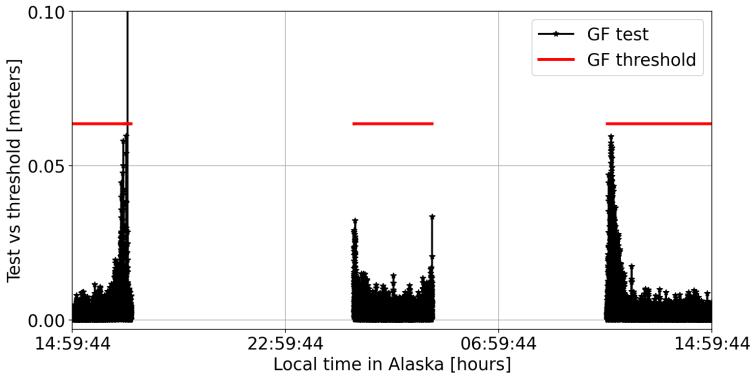

(b) Cycle slip detector based on the geometry-free combination.

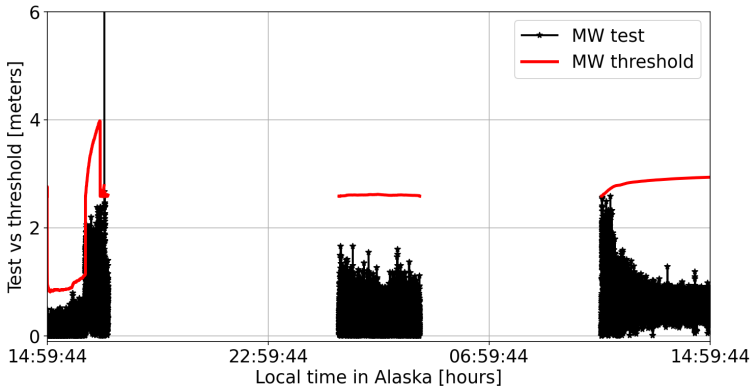

(c) Cycle slip detector based on the MW combination.

Figure 3.3: Example of cycle slip detection with two different detectors: (b) based on the geometry-free combination of carrier-phases and (c) based on the Melbourne-Wübbena (MW) combination. The measurements used to calculate the slant ionospheric delay (a) and the tests correspond to satellite G07, day 73 of the year 2015, and station "av17", located in Alaska. The orange oval highlights the effect of the cycle slip in the slant ionospheric delay estimation.

as in Equation 4.39 of [45]. A cycle slip is declared when a B_W measurement differs from the mean bias value by more than a predefined number of standard deviations (e.g., $6 \cdot \sigma_{B_W}$ in [45]), which is the threshold. Figure 3.3c shows that this detector was able to detect the cycle slip depicted inside the orange oval in the example of Figure 3.3a, where a jump in slant ionospheric delay of more than ten meters is observed.

For a more detailed explanation of the algorithm for this cycle slip detector refer to Section 4.3.1.2 of [45].

3.3.1.1.2 Visual check

However, since the test signals used to detect the cycle slips are still driven by frequency-dependent effects in regions where "nominal conditions" include some activity in the ionosphere, some less evident cycle slips could remain undetected. Examples of this problem can be found in [94] and [95]. As a consequence, the computed thresholds using only the previously described cycle slip detectors could suffer from an increase of their values, degrading the detection performance of the monitoring network.

For this reason, in this work, a manual check is applied after the cycle slip detectors to remove possible remaining cycle slips and outliers. Another possibility in this step could be to use a third more complex and sensitive cycle slip detector, which would be preferable when working with greater amounts of data. One example of these more sensitive cycle slip detectors can be found in [95], where the authors propose a method similar to the GBAS acceleration-ramp-step monitor applied to the ionospheric-free combination of carrier-phases (i.e. unaffected by ionosphere). Using the knowledge of the precise coordinates of the receivers on the ground, the precise orbits, and the clock corrections, they remove most of the physical effects present on the ionospheric-free combination. The resulting values are completely independent of the ionospheric effects, are very accurate, and can be used to detect these smaller cycle slips.

3.3.1.2 Test statistic

After data processing, the algorithm computes the test statistic $Itest_r^j(t)$ for each epoch t, each satellite j, and each station r, as the first derivative or rate of the processed slant ionospheric delay in order to remove the unresolved ambiguities in the carrier-phase measurements:

$$Itest_r^j(t) = \frac{\widehat{I}_r^j(t) - \widehat{I}_r^j(t-1)}{\Delta T}. \tag{3.3}$$

Here, $\widehat{I}_r^j(t)$ is the slant ionospheric delay estimation calculated with Equation 3.1 for station r, satellite j, and epoch t, $\widehat{I}_r^j(t-1)$ is the slant ionospheric

delay estimation for station r, satellite j, and the previous epoch, and ΔT is the time difference between two consecutive epochs. Note that any cycle slip would produce a high rate value if it is not detected and removed from the slant ionospheric delay estimation.

3.3.1.3 Threshold derivation

The values of the test statistics, $Itest_r^j(t)$, for a given station r, computed for all the satellites with elevations $\theta_r^j(t)$, and all epochs t during the selected nominal days, are sorted in bins of satellite elevation angle. The size of these elevation bins depends on the elevation angle. This different binning size is used to account for the fewer number of samples available from high elevation satellites and for the faster movement of the satellites at lower elevations in comparison to their slow movement at high elevations (see Section 4.2.2.1 of [62]). This thesis applied two different binning strategies for the two networks of stations studied, one situated in Alaska and the other one in Brazil, due to the different characteristics of the data. The sizes of the elevation bins used in Alaska were: 2° between 5° and 25° of elevation, 5° between 25° and 50° of elevation, and 10° between 50° and 90° of elevation. The sizes of the elevation bins used in Brazil were: 2° between 5° and 55° of elevation, 5° between 55° and 70° of elevation, and 10° between 70° and 90° of elevation.

Then, given an acceptable false alert probability, P_{fa}, a threshold for each station can be defined as:

$$Thr_r(\theta_m) = k_{fa} \cdot \sigma_{Itestr}(\theta_m), \tag{3.4}$$

where $\sigma_{Itestr}(\theta_m)$ is the standard deviation of the $Itest_r(\theta_m)$ distribution composed of the $Itest_r^j(t)$ samples for all satellites and epochs arranged into elevation bins, with θ_m and $m = 1, 2, .., \mathcal{M}$ representing the elevation bins. Moreover, k_{fa} is the false alert multiplier computed from the inverse of the standard normal cumulative distribution, $Q^{-1}\left(\frac{P_{fa}}{2}\right)$. However, this methodology only applies if $Itest_r(\theta_m)$ is Gaussian. In the case this probability distribution presents non-Gaussian behavior, a Gaussian overbound of the tails of $Itest_r(\theta_m)$ distribution is calculated.

For that purpose, first, the data is normalized by subtracting from each $Itest_r^j(t)$ sample the mean computed with the samples inside each elevation bin, $\mu_{Itest_r}(\theta_m)$, and dividing the result by the standard deviation of each bin, $\sigma_{Itest_r}(\theta_m)$. The probability distribution composed of these normalized data samples is denoted as $Itest_{r,norm}(\theta_m)$. Figure 3.4a shows an example of the normalized distribution for one of the stations of the network located in Alaska used in Chapter 4, and Figure 3.4b shows an example of the normalized distribution for one of the stations of the network located in Brazil used in Chapter 5.

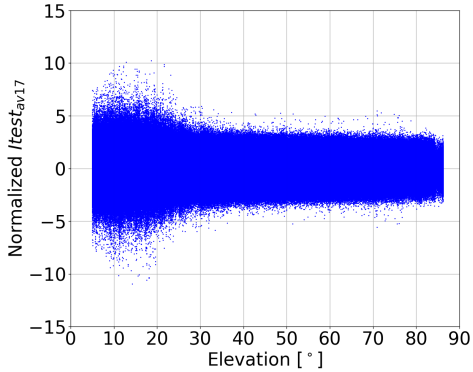

(a) Normalized test statistic distribution for station "av17". All elevation bins contain more than 242,000 samples with the exception of the 80° to 90° bin, which contains 121,493.

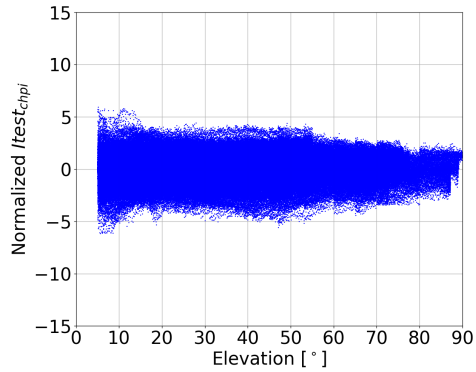

(b) Normalized test statistic distribution for station "chpi". All elevation bins contain more than 43,000 samples with the exception of the 80° to 90° bin, which contains 10,135.

Figure 3.4: Two examples of the normalized test statistic distributions for: (a) one of the stations of the network used in Chapter 4,"av17", and (b) one of the stations of the network used in Chapter 5, "chpi".

Typically, the distribution obtained after normalizing the samples of the original distribution is homogeneous throughout all the elevation bins. In these cases, a global inflation factor is used for overbounding the tails of the entire normalized distribution (see Section 2.2 of [63]). However, Figure 3.4 shows that in both cases, Alaska and Brazil, even after normalizing, the distributions are not homogeneous throughout all the elevation bins but instead, they present higher values for the low elevation bins.

In Figure 3.4a, it can be observed that below 30° of elevation the normalized distribution is thicker, presents more outliers, and is generally noisier than above 30° of elevation. In Figure 3.4b, it can be observed that below 20° of elevation the normalized distribution is also thicker and presents curved patterns. In both cases, this increase in the values of the normalized distributions at low elevations is due to the fact that the Gaussian model is less applicable because the tails of the distributions are thicker. The reason is that satellites at low elevations experience higher nominal ionosphere due to the longer path that the signals have to travel. Furthermore, the IPPs move faster at low elevations and thus, they are farther apart than at high elevations when computing the first derivative over time. This higher effect of the nominal ionosphere at low elevations is more visible in the case of Brazil (Figure 3.4b) since the curved patterns in the normalized test statistics come from IPPs that moved across the Appleton anomaly, which is quite far from the network under study (see Figure 5.1 of Chapter 5) and therefore does not affect high elevation satellites.

In addition, it can be observed that, in high elevation bins, the lack of samples impairs the calculation of statistics. This is more visible in Figure 3.4b (Brazil) because there are fewer samples available per bin than in Figure 3.4a (Alaska) due to the different data sampling rate (15 seconds in Brazil versus 1 second in Alaska). A more detailed description of the data used can be found in Sections 4.1.1 and 5.1.1.

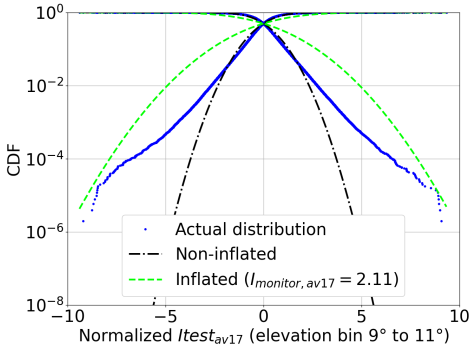

(a) Elevation bin corresponding to satellite elevations between 9° and 11°.

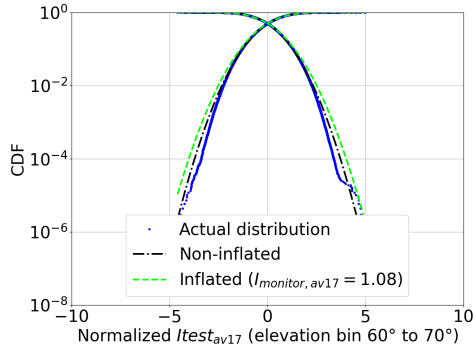

(b) Elevation bin corresponding to satellite elevations between 60° and 70°.

Figure 3.5: Example of the tail overbounding process for two different elevation bins and station "av17". The blue dots show the normalized test statistics, the black dot-dashed line represents the non-inflated Gaussian distribution and the dashed green line represents the inflated Gaussian distribution.

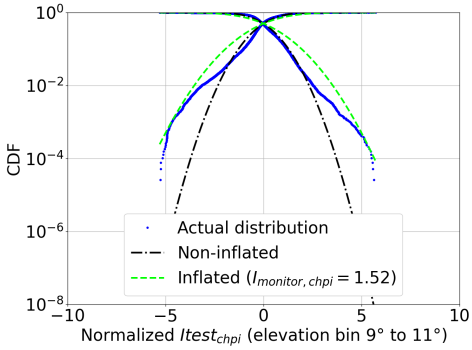

(a) Elevation bin corresponding to satellite elevations between 9° and 11°.

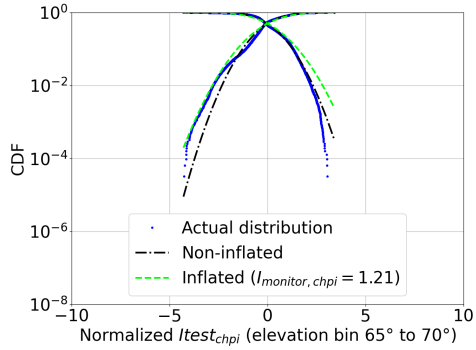

(b) Elevation bin corresponding to satellite elevations between 65° and 70°.

Figure 3.6: Example of the tail overbounding process for two different elevation bins and station "chpi". The blue dots show the normalized test statistics, the black dot-dashed line represents the non-inflated Gaussian distribution and the dashed green line represents the inflated Gaussian distribution.

To consider the particularities of the data mentioned above, this work followed the approach in [96] and a different inflation factor was calculated for each elevation bin instead of using a global inflation factor. In this way, the necessary inflation factors to overbound the tails of the distribution in each elevation bin are applied. To compute the inflation factor per elevation bin, first, the Cumulative Distribution Function (CDF) of $Itest_{r,norm}(\theta_m)$ and its complement (1-CDF) are computed for each elevation bin. Also, the CDF and its complement are calculated for a zero-mean Gaussian distribution with an inflated standard deviation $I_{monitor,r}(\theta_m)$ and $m = 1, 2, .., \mathcal{M}$ representing the elevation bins, $G_m \sim \mathcal{N}(0, I^2_{monitor,r}(\theta_m))$. These two functions are used to overbound the tails of $Itest_{r,norm}(\theta_m)$ per bin. Therefore, the standard deviation inflation factor $I_{monitor,r}(\theta_m)$ is calculated such as the following conditions are fulfilled per elevation bin: $CDF(Itest_{r,norm}(\theta_m)) < CDF(G_m)$ and $1 - CDF(Itest_{r,norm}(\theta_m)) < 1 - CDF(G_m)$.

Figure 3.5 depicts an example of the tail overbounding process for two different elevation bins and station "av17". In the example of the bin for low elevations, the actual distribution of the normalized test statistics, $Itest_{r,norm}(\theta_m)$ represented in blue dots, is above the normal distribution $\mathcal{N}(0, 1)$ in the tails, represented by the black dot-dashed line. Therefore, inflation is needed in order to protect the tails of the distribution. This inflation is represented by the green dashed line, which corresponds to a $\mathcal{N}(0, I^2_{monitor,r}(\theta_m))$. In the example of the bin for high elevations, the actual distribution of the normalized test statistics, $Itest_{r,norm}(\theta_m)$ represented in blue dots, is only exceeding slightly the normal distribution $\mathcal{N}(0, 1)$ in the tails, represented by the black dot-dashed line. Therefore, the inflation factor needed in this case ($I_{monitor,av17}(\theta_{17}) = 1.08$) was much lower than in the case for lower elevations ($I_{monitor,av17}(\theta_3) = 2.11$). The same effects were observed for the case of Brazil, where the distribution at high elevations required less inflation than the distribution at low elevations (see Figure 3.6).

Figure 3.7a provides all the inflation factors needed to overbound the distribution for $Itest_{av17,norm}(\theta_m)$ with $m = 1, 2, .., \mathcal{M}$. Here, the inflation factors are above 1.5 for satellite elevations below 25° but below 1.2 for satellite elevations above 35° due to the higher effects of noise and multipath and higher nominal ionosphere present on low elevation satellites as mentioned previously. Figure 3.7b provides all the inflation factors needed to overbound $Itest_{chpi,norm}(\theta_m)$ distribution with $m = 1, 2, .., \mathcal{M}$. In this case, the inflation factors are also higher at lower elevations than at higher elevations, but have higher values at higher elevations than in the case of Alaska (Figure 3.7a) due to the characteristics of the data: lower numbers of available samples recorded in nominal conditions due to the sampling rate and higher ionospheric activity.

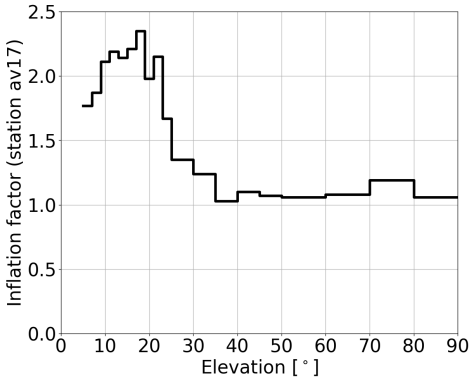

(a) Inflation factors calculated for station "av17".

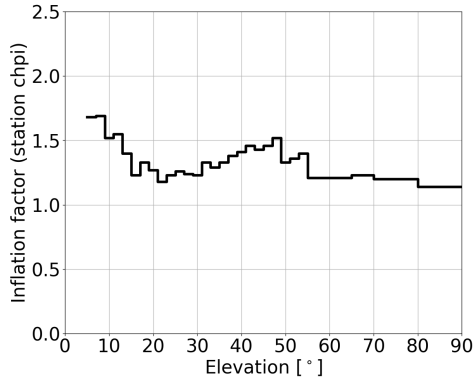

(b) Inflation factors calculated for station "chpi".

Figure 3.7: Inflation factors needed to overbound the tails of the test statistic distributions per elevation bin.

Finally, the detection threshold for each elevation bin at station r is defined following Section 2.3.4 as:

$$Thr_r\left(\theta_m\right) = \mu_{Itest_r}(\theta_m) \pm k_{fa} \cdot I_{monitor,r}\left(\theta_m\right) \cdot \sigma_{Itest\,r}\left(\theta_m\right). \tag{3.5}$$

Figure 3.8 shows an example of different test statistic values (in blue) and different values for the detection threshold depending on different probabilities of false alert considered. The data used in this example corresponds to all visible GPS satellites for the nominal days specified for station "av17" in Section 4.1.2 and station "chpi" in Section 5.1.2. In this case, the probability that a certain $Itest_r^j(t)$ value exceeds the threshold is smaller than the P_{fa} utilized to calculate the k_{fa} multiplier due to the overbounding performed, which means that the requirement of false alert probability of the monitor is satisfied. Furthermore, it can be observed that the threshold values depend greatly on satellite elevation due to the higher effects of noise, multipath, and nominal ionosphere on low elevation satellites, which also make the inflation factors required for overbounding larger. Comparing Figures 3.8a and 3.8b with each other, it can be observed that the $Itest_{chpi}^j(t)$ are lower than those of $Itest_{av17}^j(t)$. This is due to the different sampling rate of the measurements (15 seconds in "chpi" versus 1 second in "av17"). This causes the ionosphere variation to be divided by a larger number in the case of "chpi", which also smooths the effects of noise and multipath.

Concerning the different probabilities of false alert, when a larger number of false alerts is allowed, the threshold gets more restrictive, and when fewer false alerts are allowed, the threshold is relaxed, but then some anomalous

ionospheric gradients could be missed. The false alert probability values selected in Figures 3.8a and 3.8b were chosen taking into account the power of 10 immediately below and immediately above the number of samples in each elevation bin, which are considered to be statistically independent in this work. Figures 3.9a and 3.9b show the number of samples in each of the bins for stations, "av17" and "chpi", respectively. Sections 4.3.1 and 5.3.1 explain in more detail the selection of the P_{fa} for each of the considered networks.

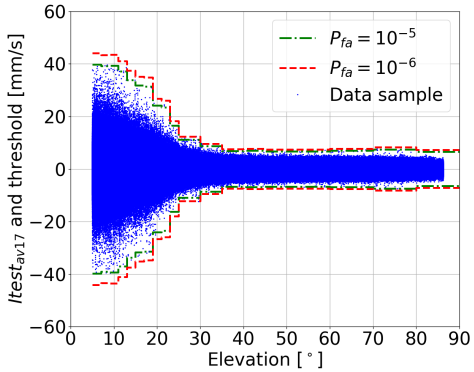

(a) Detection thresholds for station "av17".

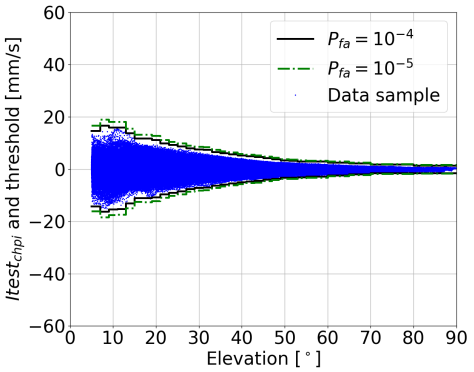

(b) Detection thresholds for station "chpi".

Figure 3.8: Example of different detection thresholds for different P_{fa} considered. The blue dots show the test statistic distributions calculated for all visible GPS satellites and the nominal days selected in Chapters 4 and 5.

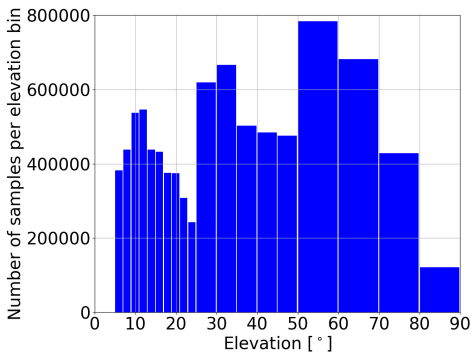

(a) Number of samples in each elevation bin for station "av17".

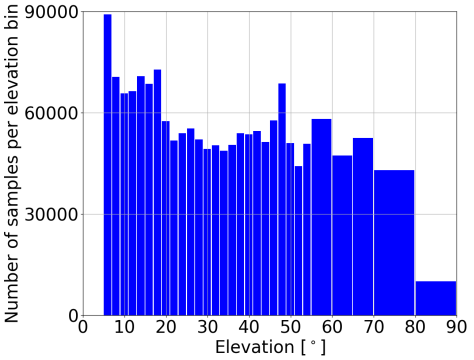

(b) Number of samples in each elevation bin for station "chpi".

Figure 3.9: Number of samples in each elevation bin for stations "av17" and "chpi".

Note that calculating a different inflation factor for each elevation bin has the disadvantage that the number of samples in each bin is significantly lower than if the entire normalized distribution were used. Therefore, deriving mean-

ingful threshold values for each station requires a larger number of statistically independent samples than the corresponding P_{fa} used (e.g., above 10^6 to cover $P_{fa} = 10^{-6}$). In this thesis, a simplification has been made to show how the methodology works with a limited data set. However, in a real "Network GBAS", the detection thresholds would be obtained with a much larger number of samples that would have to be ensured to be statistically independent. Additionally, the thresholds would be updated every some time (e.g., every month) to consider significant changes in satellite geometry, different values of nominal ionosphere due to the different seasons of the year, etc.

3.3.2 Derivation of the Minimum Detectable Gradient by the network

The detection threshold derived for each of the monitoring stations in Section 3.3.1 considers a certain probability of false alert, but these thresholds do not consider any probability of missed detection.

However, since the goal of this work is to substitute the current conservative threat model for the output of the network, the network itself must cover the integrity budget allocated to the threat model. Although the ionospheric threat model is considered to always be true and, in principle, it does not have a fixed integrity budget associated, in Section D.3 of [47] ("GBAS integrity risk not covered by protection levels"), it is stated that: *"The GBAS Ground Subsystem integrity risk is less than* 1.5×10^{-7} *in any one approach. [...] The integrity risk due to Ground Subsystem failures can be divided into risks associated with undetected events of environmental anomalies (Note 1) and Ground Subsystem failures resulting in erroneous GBAS messages. [...] Anomalous ionosphere, anomalous troposphere, excessive RFI and excessive multipath are notably considered as environmental anomalies".* This description corresponds to the probability of Loss of Integrity (LOI) allocated to faults different from individual satellite failures not bounded by any PLs, which is 1×10^{-8} in Figure 2.2. A part of this integrity budget should be sub-allocated to anomalous ionosphere. The GBAS manufacturer selects these allocations according to the characteristics of the GBAS station (e.g., detectability of the implemented monitors). As a simplification, this work considers a sub-allocated probability of loss of integrity per 150-second approach for abnormal ionospheric activity ($P_{LOI,abnormal\_iono}$) of 1×10^{-8} from the total of 1.5×10^{-7} (integrity risk allocation for H2 conditions in Figure 2.2) as in [28]. Sub-allocation for other anomalous conditions, such as anomalous troposphere, has not been considered. Therefore, the following condition must be fulfilled [28]:

$$P_{LOI,abnormal\_iono} \geq P_{md,abnormal\_iono} \cdot P_{prior,abnormal\_iono}, \tag{3.6}$$

where $P_{md,abnormal\_iono}$ is the probability of missed detection given the existence

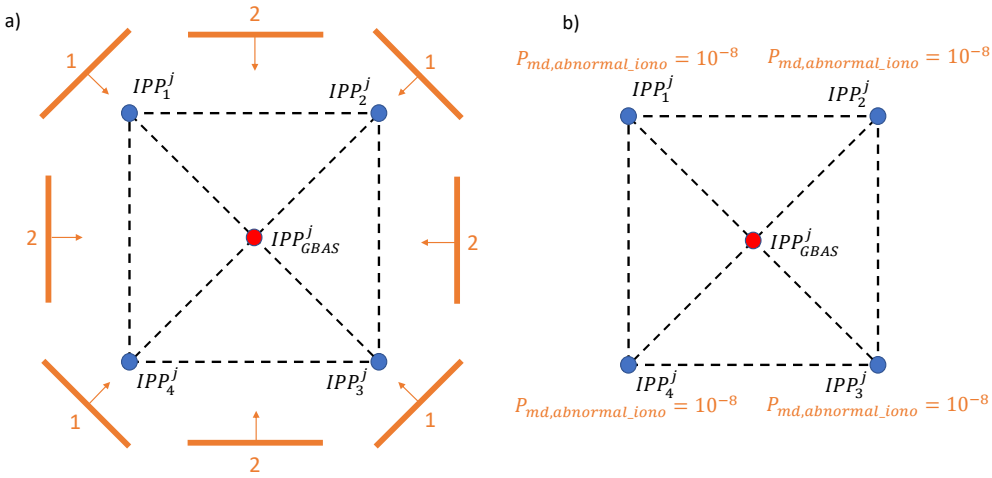

Figure 3.10: Example of a square-shaped network, where the GBAS station to be protected is located in the center. The four blue circles represent four IPPs belonging to the same satellite and four different stations, and the red circle represents the IPP belonging to the same satellite and the GBAS station. In Figure 3.10a, the orange lines represent the gradient fronts moving towards the IPPs from different directions, and the numbers near each front represent the number of stations that might detect the gradient before it arrives at the IPP belonging to the GBAS station. In Figure 3.10b, the associated probabilities of missed detection that must be covered by each station are shown.

of abnormal ionospheric activity, and $P_{prior,abnormal\_iono}$ is the prior probability of an anomalous ionospheric gradient occurring. Typically, $P_{prior,abnormal\_iono}$ is assumed to be 1 and, $P_{md,abnormal\_iono} = P_{LOI,abnormal\_iono}$, but recent studies have also assumed this prior probability to be $P_{prior,abnormal\_iono} = 10^{-3}$ [28, 36].

Furthermore, the amount that each of the stations of the network must cover from this integrity budget depends on the characteristics of the ionospheric gradients in the specific region, the number of stations composing the network, and the location of the GBAS station(s) within the protected area of the network. In the following, we present several examples of the calculation of $P_{md,abnormal\_iono}$ that each of the monitoring stations would need to cover, conservatively assuming $P_{prior,abnormal\_iono} = 1$. Note that, once the network is operational, it could compute a $P_{prior,abnormal\_iono}$ based on the data it processes.

Figure 3.10 shows one example of a square-shaped network configuration, where the single-protected GBAS station is located in the center. Here, the four blue circles represent four IPPs belonging to the same satellite and four different stations, and the red circle represents the IPP belonging to the same satellite and the GBAS station. Note that this is a simplification since the

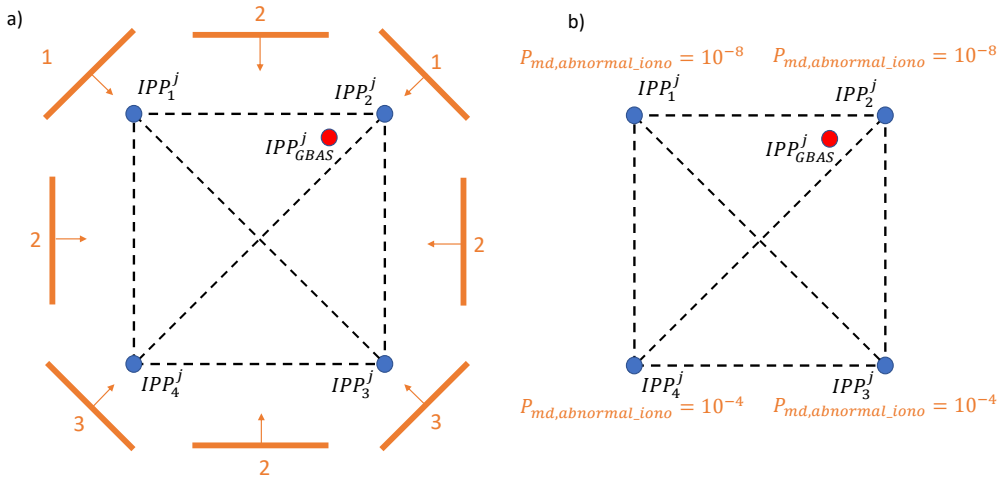

Figure 3.11: Example of a square-shaped network, where the GBAS station to be protected is located near one of the corners. The four blue circles represent four IPPs belonging to the same satellite and four different stations, and the red circle represents the IPP belonging to the same satellite and the GBAS station. In Figure 3.11a, the orange lines represent the gradient fronts moving towards the IPPs from different directions, and the numbers near each front represent the number of stations that might detect the gradient before it arrives to the IPP belonging to the GBAS station. In Figure 3.11b, the associated probabilities of missed detection that must be covered by each station are shown.

geometry of the stations on ground can be considered similar to that of the IPPs only when the satellites are at medium and high elevations [97]. Assuming that the probability of a gradient moving in any direction is the same, the most representative directions of it moving towards the network are represented as arrows perpendicular to the ionospheric front. As can be observed in Figure 3.10a, a gradient moving from north to south could be detected by two stations before impacting the IPP of the GBAS station. This situation is represented with a "2" written above this direction. However, a gradient moving from northeast to southwest could only be detected by one station before impacting the GBAS, since the other two stations are aligned with it. This situation is represented with a "1" written above this direction. This process is repeated for all directions of the gradient. Then, for each of the directions, the probability of missed detection that each of the stations would need to cover is calculated assuming that the probability of missed detection for these two stations are statistically independent. As an example, when the gradient comes from north to south, the total of 1×10^{-8} can be shared between the two stations situated in the upper part of the square because both can detect the gradient before it reaches the GBAS station. Therefore, in this case, the two top stations would need to cover a $P_{md,abnormal\_iono}$ of 1×10^{-4} each and the two bottom stations

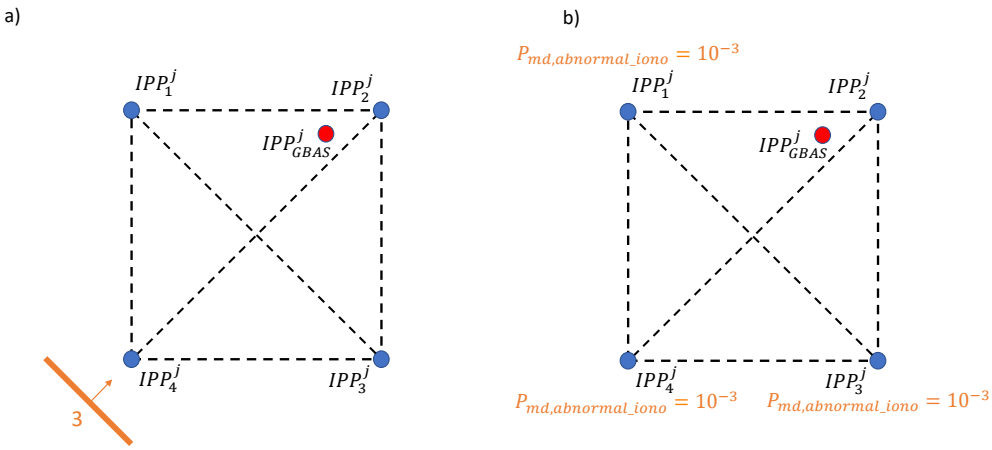

Figure 3.12: Example of a square-shaped network, where the GBAS station to be protected is located near one of the corners. The four blue circles represent four IPPs belonging to the same satellite and four different stations, and the red circle represents the IPP belonging to the same satellite and the GBAS station. In Figure 3.12a, the orange line represents the gradient front moving towards the IPPs from a single direction, and the number below the front represents the number of stations that might detect the gradient before it arrives to the IPP belonging to the GBAS station. In Figure 3.12b, the associated probabilities of missed detection that must be covered by each station are shown.

are not considered since they are located after the GBAS station. In the case of the gradient moving from northeast to southwest, only one station can detect and therefore it would need to assume the whole budget of 1×10^{-8}, while the others are not considered. Once this study has been carried out with all the possible directions, the "worst case" for each station is selected, which is the lowest $P_{md,abnormal\_iono}$. As can be observed in Figure 3.10b, the "worst case" in all corners is that only one station can detect, and therefore all corners need to cover a $P_{md,abnormal\_iono}$ of 1×10^{-8}.

However, the situation changes if the GBAS station is not situated in the center of the square. This is the case of the example depicted in Figure 3.11. Here, only the two stations located in the upper part of the square have to cover the total integrity budget while the stations located in the lower part of the square only have to cover 1×10^{-4}. Considering that most networks will have more stations available in more complex configurations, the $P_{md,abnormal\_iono}$ that will need to be covered by each station will likely be less restrictive.

Furthermore, there are ionospheric threat models that do not consider all directions of the ionospheric gradient as, e.g., the threat model in Brazil (see Table 2.6). This case is exemplified in Figure 3.12a with a single direction rep-

resenting the very limited range of directions that need to be considered. Here, the integrity budget is distributed among all stations that could be impacted before the gradient reaches the GBAS, but only one direction is considered. This differs from the previous examples in that there is no "worst case" for the rest of the corners that is more conservative, and therefore the integrity budget can be distributed equally among these stations.

Assuming that all satellites present similar behavior, the $P_{md,abnormal\_iono,r}$ for each of the stations of the network can be computed only once. Next, the Minimum Detectable Error (MDE) is calculated for each of the stations composing the network. The MDE has the same units as the threshold, mm/s in this case, and is computed following the approach explained in Section 2.3.4 as:

$$MDE_r(\theta_m) = Thr_r(\theta_m) + k_{md,abnormal\_iono,r} \cdot I_{monitor,r}(\theta_m) \cdot \sigma_{Itestr}(\theta_m), \tag{3.7}$$

where $k_{md,abnormal\_iono,r}$ is the scalar multiplier needed to meet the required $P_{md,abnormal\_iono,r}$ previously calculated and computed from the inverse of the standard normal cumulative distribution, $Q^{-1}(P_{md,abnormal\_iono,r})$.

However, in order to include the network information in GBAS, the MDEs of each of the stations that compose the network need to be translated into the Minimum Detectable Gradient (MDG) by the network at the location of the GBAS station(s) it protects. This is achieved by means of Monte Carlo simulations (explained in Chapter 6), in which the different parameters of the GBAS ionospheric threat model are varied until a representative number of samples is achieved. In addition, these simulations also allow to take into account those cases where the locations of the stations on ground are not similar to that of the IPPs due to the low elevation of the satellites. The result of this simulation is a MDG expressed in mm/km that can serve as an input to the protected GBAS stations. In Chapter 6, more information on this process is given with examples of application on a real network located in Brazil.

Note that, in the case of including additional constellations, other satellites could be used for monitoring, achieving a lower value of the MDG.

3.3.3 Detection of ionospheric gradients

The detection step is the first part of the real-time operation of the network. As previously stated in Section 3.2, the detection step is performed individually per station r, satellite j, and epoch t, monitoring for ionospheric anomalies in the rate of the estimated slant ionospheric delays. The detection algorithm receives the GNSS dual-frequency and multi-constellation carrier-phase measurements and calculates the slant ionospheric delay as in Equation 3.1. Then, these measurements undergo a processing step intended to remove

possible cycle slips in the data. Once the data is processed, the test statistic $Itest_r^j(t)$ is computed (Equation 3.3). Given a predefined threshold curve for a certain monitoring station r and considering its value for the elevation of a satellite j at a certain epoch t, $\theta_r^j(t) \in \theta_m$, the condition for detecting the ionospheric gradients is:

$$\left|Itest_r^j\,(t)\right| \geq Thr_r\,(\theta_m)\,. \tag{3.8}$$

The algorithm, presented in Algorithm 1, outputs detection information that is shared over the network in real time (i.e., at the sampling rate of the receivers in the network, which is assumed to be the same for all receivers). This detection information consists of the $Itest_r^j(t)$ values, a detection flag ($dtc_r^j(t)$) that becomes one when a gradient is detected, and a signal flag ($sgl_r^j(t)$) that indicates that valid measurements in both frequencies exist at the current epoch t. Algorithm 1 runs continuously and receives samples at every epoch t. Therefore, the GBAS station would receive and be able to act on this information at the sampling frequency of the network receivers with an additional margin for data transmission.

Note that the detection capabilities of each of the individual reference stations are just as important as those of the network. In the case that the reference stations forming the network are so far apart that the use of multiple constellations is not sufficient to monitor the whole area, ionospheric irregularities such as small plasma bubbles might not be detected, as mentioned in [98]. This issue should be carefully investigated when assessing the detection capabilities of the network and calculating the Minimum Detectable Gradient (MDG), and a criteria for a maximum distance between monitoring stations should be established. However, the study of the "desired" value of the station separation for ideal detection of these small irregularities is not addressed in this thesis and is part of future work.

Furthermore, in the real-time operation of the algorithm, only stage 1 of the data processing presented in Section 3.3.1.1 is performed. The main reason is that both cycle slip detectors introduced in that section can be implemented in real time, whereas a manual check or another more complex cycle slip detector (such as the one proposed in [95]) are not yet real-time capable, although studies on how to adapt these more complex cycle slip detectors to real time are ongoing. Since the monitoring thresholds were designed using both stages in order to guarantee integrity, in the very rare occasions where an undetected cycle slip occurs, the monitoring thresholds will trigger false alerts. In these cases, the monitoring network tries to estimate the ionospheric gradient parameters as if the false alerts were real gradients. Section 3.3.4 explains this process and discusses the behavior of the algorithm during false alert events. Moreover, the monitoring network would consist of either GBAS stations with very high quality and reliable measurements or external stations that are also

expected to provide high-quality measurements, therefore minimizing the likelihood of this problem.

Algorithm 1 Detection algorithm for a single monitor station

Input: $\phi^j_{f_1,r}(t)$, $\phi^j_{f_2,r}(t)$, $\rho^j_{f_1,r}(t)$, $\rho^j_{f_2,r}(t)$, $\theta^j_r(t)$;
Initialization: $sgl^j_r(t) \leftarrow 0$, $dtc^j_r(t) \leftarrow 0$;
for each t **do**
  for each j **do**
    if $\phi^j_{f_1,r}(t)$ and $\phi^j_{f_2,r}(t)$ exist **then**
      $sgl^j_r(t) \leftarrow 1$
      Compute $\widehat{I}^j_{f_1,r}(t)$ ▷ according to Equation 3.1
      if cycle slip is declared **then**
        $sgl^j_r(t) \leftarrow 0$
        Delete $\widehat{I}^j_{f_1,r}(t)$
      else
        Compute $Itest^j_r(t)$ ▷ according to Equation 3.3
        if $\left|Itest^j_r(t)\right| \geq Thr_r(\theta_m)$ with $\theta^j_r(t) \in \theta_m$ **then**
          $dtc^j_r(t) \leftarrow 1$
Output: $Itest^j_r(t)$, $sgl^j_r(t)$, $dtc^j_r(t)$.

3.3.4 Estimation of ionospheric gradient parameters with an individual satellite

The estimation step of the algorithm collects in a central processor the detection information shared in the network per station r in real time (see Figure 3.13). First, this central processor groups the information coming from different stations for the same satellite. Then, it estimates the gradient parameters explained in Section 2.4.2 per satellite following a modification of the so-called "time-step method" ([59, 23]). This method has been adapted to work in real time. All the formulas in the following are therefore expressed for an individual satellite j, and thus the j superscript is omitted.

3.3.4.1 Determination of the spatial propagation of the gradient with time

For estimating the gradient parameters, the gradient's spatial evolution with time or, in other words, the time delay κ_r between detections in two stations that are spatially separated, a station r, and a station selected as reference needs to be tracked. In principle, the reference station is the first station that detects the gradient, and is distinguished by substituting the subscript r with 0. Additionally, it is assumed that the ionospheric gradient is local, maintaining its characteristics of magnitude (slope and width) and propagation (speed

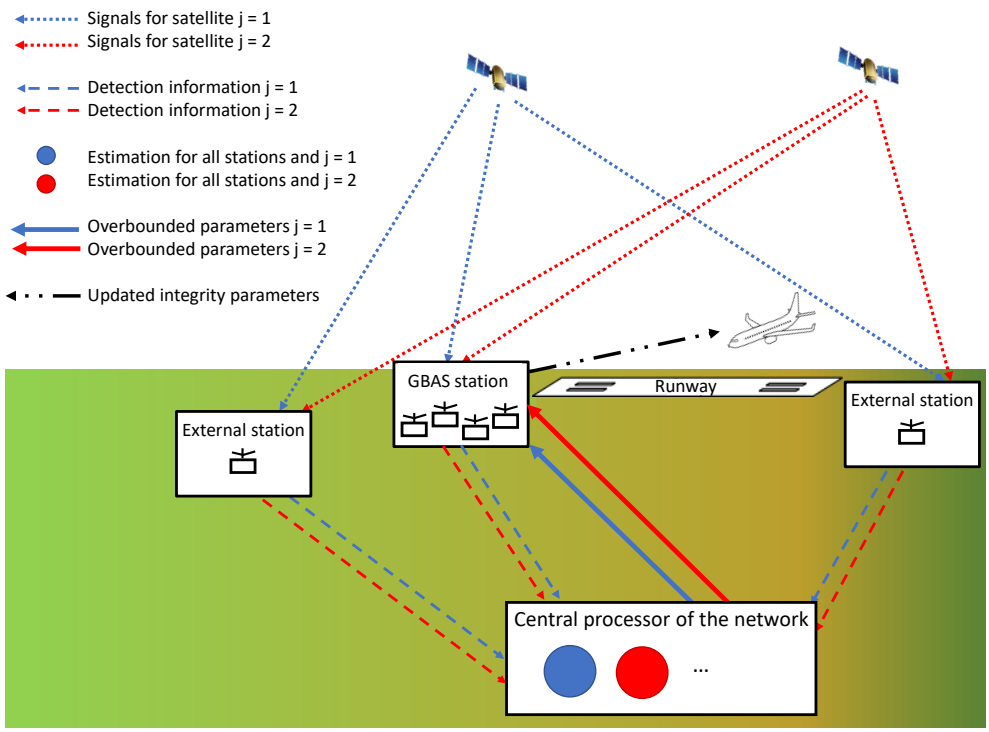

Figure 3.13: Diagram that shows where the different steps of the "Network GBAS" methodology occur for two different satellites (one depicted in blue and one in red). The dotted arrows represent the signals transmitted by each of the satellites and the dashed arrows represent the detection information shared by each of the monitoring stations for each of the satellites. The circles represent the information grouped for each satellite by the central processor: the blue circle represents the detection information for satellite $j = 1$ and all stations and the red circle represents the detection information for satellite $j = 2$ and all stations. The solid arrows represent the information transmitted by the network to the GBAS ground station and the dotted-dashed arrow the updated integrity parameters broadcast to the aircraft.

and direction) constant only over a certain time and distance. This assumption, referred to as the "locality principle" in this work, is verified at the end of the following subsection. Furthermore, it is also assumed that the ionospheric disturbance propagates as a planar wave that moves with a certain speed and impacts the different IPPs corresponding to the same satellite and different stations r at different times. Note that the assumption of an approximately planar wave propagation is used to simplify the analysis of the problem. This assumption is reasonable when the spatial size of the ionospheric perturbation is orders of magnitude larger than the station baselines. The longer the baselines and the smaller the size of the ionospheric perturbations, the more limitations this method has. The applicability of this assumption to real gra-

dients and its limitations are presented in the results in Chapters 4 and 5.

However, since several ionospheric perturbations can occur in a short period of time at each ground station, it is necessary to identify the same ionospheric perturbation occurring at different ground stations. This is achieved through the computation of the cross-correlation between the different test statistics in real time.

3.3.4.1.1 Real-time cross correlation

Under the assumption that the ionospheric perturbation maintains its characteristics of magnitude during a certain period of time, identifying the same ionospheric perturbation means identifying the perturbations with the same shape at different stations. To this end, the cross-correlation between the test statistic values calculated in different stations for the same satellite is computed.

Nevertheless, due to the real-time constraint in GBAS, it is necessary to perform the cross-correlation between the test statistics as fast as possible instead of using the complete set of measurements over a day. Thus, the cross-correlation between $\boldsymbol{B_{Itest_r}}$, a sliding window buffer containing a history of test statistic values until current epoch t for any of the stations $r \neq 0 \in \mathcal{R}$, and $\boldsymbol{B_{Itest_0}}$, the buffer for the station of reference is computed.

The two buffers involved in the cross-correlation process are defined as:

$$\left.\begin{aligned} \boldsymbol{B_{Itest_0}} &= \left[Itest_0(t_B)\right]_{1\times N_B} \\ \boldsymbol{B_{Itest_r}} &= \left[Itest_r(t_B)\right]_{1\times N_B} \end{aligned}\right\} \text{ with } t_B = t_{d,0} - N_W, \ldots, t \tag{3.9}$$

where $t_{d,0}$ is the epoch when the station of reference detected the anomalous ionospheric gradient for the first time, N_B is the size of both buffers, and N_W is a window of time designed to capture the part of the test statistic that starts to increase when a gradient begins but is still not sufficiently large to trigger the detection thresholds. Note that the size of N_W is a design parameter that depends on the characteristics of the data.

As can be observed in Equation 3.9, the buffers belonging to all non-reference stations begin to fill at the same moment the station of reference detected an anomalous gradient, $t_{d,0}$. Therefore, all buffers are initialized with the test statistic values from the stations to which they belong from time $t_{d,0} - N_W$ to $t_{d,0}$ and continue to receive and store the test statistic values until current epoch t. Thus, all buffers have the same length. The maximum length of these buffers is another design parameter, and its determination should take into account the range of values of the expected anomalous gradient parame-

ters. A more detailed description of the selection of N_W and N_B is given in Chapters 4 and 5, where the data used in this thesis is introduced.

Algorithm 2 describes the cross-correlation process in more detail. For the times when $dtc_r(t)$ is equal to 1, the algorithm checks if there is any sample of the test statistics missing in any of the two buffers involved in the cross-correlation process. These missing data are often due to a cycle slip, a data gap or when the satellite is no longer visible. Since integrity cannot be ensured if there is a gap in the data, if this occurs, a "Warning" is declared to indicate to the network that there has been a detection, but the gradient parameters cannot be determined. In this case, the network should use the "worst-case" threat model parameters on that area. After this initial check, Algorithm 2 computes the cross-correlation between the two buffers, $\boldsymbol{B_{Itest_0}}$ of the reference station and $\boldsymbol{B_{Itest_r}}$, as:

$$cc(p) = \sum_{l=0}^{N_B-1} \boldsymbol{B_{Itest_r}}(l) \cdot \boldsymbol{B_{Itest_0}}(l - p + N_B - 1). \tag{3.10}$$

For each epoch t in which the cross-correlation is computed, the maximum of the cross-correlation and the index of the cross-correlation vector where the maximum occurs $p_{max}(t)$ are found. Then, the time delay between the two stations at epoch t is computed as:

$$\kappa_r(t) = (p_{max}(t) - (N_B - 1)) \cdot \Delta T. \tag{3.11}$$

Once the time delay is found, the cross-correlation coefficient, $\alpha_r(t)$, is calculated between $\boldsymbol{B_0}$ and $\boldsymbol{B_r}$, two buffers containing the relevant parts of the signal from $\boldsymbol{B_{Itest_0}}$ and $\boldsymbol{B_{Itest_r}}$. This cross-correlation coefficient, also known as the Pearson correlation coefficient, is determined by:

$$\alpha_r(t) = \frac{\mathrm{cov}(\boldsymbol{B_0}, \boldsymbol{B_r})}{\sigma_{B_0} \cdot \sigma_{B_r}} \quad \text{with} \quad \begin{cases} \boldsymbol{B_0} = \boldsymbol{B_{Itest_0}}\{0, \ldots, t - \kappa_r(t)\} \\ \boldsymbol{B_r} = \boldsymbol{B_{Itest_r}}\{\kappa_r(t), \ldots, t\} \end{cases} \tag{3.12}$$

where "cov" represents the covariance of the two buffers, and σ the standard deviation.

A cross-correlation coefficient of 1 between the test statistics computed at two different stations means that the perturbation is the same, but delayed by a certain time interval, which is used to estimate the propagation parameters. A cross-correlation coefficient of 0 means that the perturbations at these two stations appear to be unrelated. Therefore, these cross-correlation coefficients $\alpha_r(t)$ are compared in each epoch with a minimum value α_{min}, below which the perturbation occurring at the station r is not considered to be the same as the one occurring at the station of reference. This work uses for α_{min} a value of 0.5, which is a common value used in signal processing. Until $\alpha_r(t)$ reaches the value chosen for α_{min}, the network does not know if both stations

detected the same anomalous ionospheric gradient. Therefore, it declares a "Warning" to indicate to the GBAS stations in that area that they should use the "worst-case" threat model parameters.

When $\alpha_r(t)$ is above α_{min}, the network considers that the anomalous gradient measured at both stations, r and the reference, are the same. However, when the difference between current epoch t and time of detection at a station different from the reference, $t_{d,r}$, is low, the real-time cross-correlation algorithm finds poor correlations due to the noise and multipath present in the $Itest_r(t)$ samples and the very limited amount of data corresponding to the ionospheric perturbation stored in the respective buffers. Therefore, the algorithm needs a certain time to converge. It is considered that the algorithm converges when the difference between the cross-correlation coefficients at the current epoch and at the previous epoch is below 1×10^{-2} for the last N_C samples (e.g. 3 samples). The convergence condition is summarized in Equation 3.13:

$$|\alpha_r(t_C) - \alpha_r(t_C - 1)| \leq 1 \times 10^{-2} \text{ with } t_C = t - N_C, t - (N_C - 1), \ldots, t. \tag{3.13}$$

The amount of time that the algorithm needs to converge depends on the characteristics of the ionospheric gradient and the level of noise and multipath present on the measurements, and it is further discussed in the results in Chapters 4 and 5. Until the convergence criterion is met, the two stations involved in Algorithm 2, which protect one or more GBAS stations, are treated as having detected an anomalous ionospheric gradient, but they still do not have any information of the size and propagation of the gradient. Therefore, a "Warning" is issued to warn the network that there is an anomalous ionospheric gradient in that area that cannot yet be estimated. Thus, the GBAS stations that those stations cover should use the "worst-case" threat model.

Once the algorithm converges, it outputs the cross-correlation coefficient $\alpha_r(t)$ and the time delay $\kappa_r(t)$. While the convergence criteria is fulfilled, both parameters are very similar from one epoch to the next and can be considered constant.

For the times when the cross-correlation coefficients no longer fulfill the convergence criteria but the detection flag, $dtc_r(t)$, is one, the network indicates again the use of "worst-case" assumptions. Algorithm 2 continues searching for high cross-correlations until the gradient is no longer detected ($dtc_r(t)$ changes from 1 to 0), and the buffer for station r is reset to empty to wait for another gradient to come.

As stated in Section 3.3.3, when false alerts from different stations occur, they are treated as "real alerts", and they also go through the cross-correlation

procedure. However, since the source of these alerts are not real anomalous ionospheric gradients, Algorithm 2 does not find sufficient correlation between the test statistics from the different stations and the same satellite and the estimation of the gradient parameters is not calculated. In these cases, Algorithm 2 triggers a "Warning" indicating that the GBAS stations affected by these false alerts should use more conservative approaches because the network cannot guarantee the integrity otherwise.

Note that the case that Algorithm 2 produces a high cross-correlation due to false detection is very unlikely since this algorithm requires a minimum number of samples within the buffers of Equation 3.9 to run. Moreover, it is even more unlikely that this would occur for three different stations (the reference station and two others) such that an erroneous estimate of the gradient parameters could be made. For this reason, the case of getting an erroneous estimation of the gradient due to finding large cross-correlations between false detections or detected anomalous ionospheric gradients that are not the same, has not been considered in this work because it is assumed to be highly improbable.

Algorithm 2 Real-time cross-correlation algorithm for an individual satellite

Input: $\boldsymbol{B}_{Itest_0}$, $\boldsymbol{B}_{Itest_r}$, $sgl_0(t)$, $sgl_r(t)$, $dtc_r(t)\ \forall\ r \in \mathcal{R}$;
Initialization: $\boldsymbol{B}_{Itest_0}$, $\boldsymbol{B}_{Itest_r}\ \forall\ r \in \mathcal{R}$; ▷ according to Equation 3.9
for each t **do**
  for each r **do**
    if $dtc_r(t)$ is 1 **then**
      if $sgl_r(t_B)$ is 1 and $sgl_0(t_B)$ is 1 $\forall\ t_B \in [t_{d,0} - N_W, ..., t]$ **then**
        Calculate $cc(p)$, $\kappa_r(t)$ and $\alpha_r(t)$ ▷ according to Equations 3.10, 3.11, 3.12
        if $\alpha_r(t) > \alpha_{min}$ **then**
          if $|\alpha_r(t_C) - \alpha_r(t_C - 1)| \leq 1 \times 10^{-2}$ **then** ▷ see Equation 3.13
            Output $\kappa_r(t)$, $\alpha_r(t)$
          else
            Trigger "Warning"
        else
          Trigger "Warning"
      else
        Trigger "Warning"
        Reset $\boldsymbol{B}_{Itest_r}$
    else
      Reset $\boldsymbol{B}_{Itest_r}$
Output: $\kappa_r(t)$, $\alpha_r(t)\ \forall\ r \in \mathcal{R}$.

When the ionospheric threat model is not a simple wedge (e.g. CONUS), but is more complex (e.g. Brazil), the network might be comparing two different areas of the gradient at different stations (e.g., one station observes the downward part of the gradient while another observes the upward part) due

to the movement of the satellites and the perturbation itself. In this case, this method is able to compare exactly the same parts of the gradient at different stations since it separates the test statistic values of the downward part (i.e. negative values) from the upward part (i.e. positive values) before the calculation of the cross-correlation with the absolute value of the test statistics (refer to Chapter 5 for a more detailed explanation).

3.3.4.2 Speed and direction of the gradient

When at least 3 stations are impacted by the same gradient, the speed vector of the gradient, $\boldsymbol{v}$, can be estimated by applying the work accomplished in [23] and [97]. Under the assumption that the ionospheric disturbance propagates as a planar wave, the wave phase ζ can be expressed as:

$$\zeta = \boldsymbol{x} \cdot \boldsymbol{k} - \omega \cdot t + \zeta_{in}, \tag{3.14}$$

where $\boldsymbol{k}$ is the wave propagation vector, $\boldsymbol{x}$ is the position vector, ω is the angular frequency, and ζ_{in} is the initial phase.

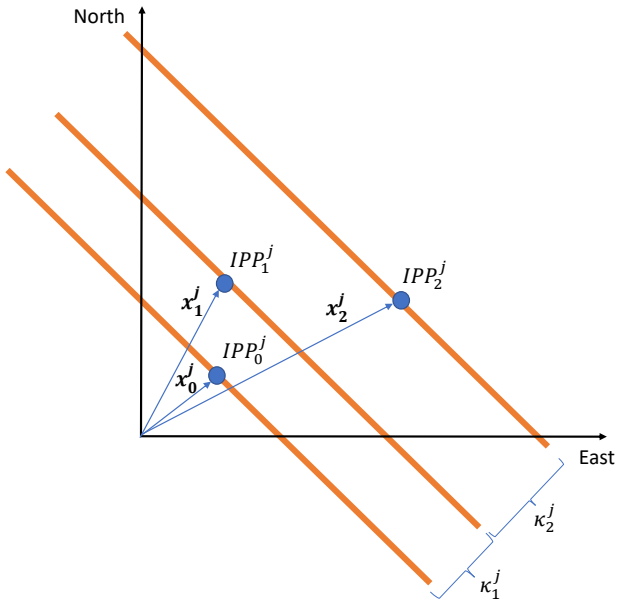

Figure 3.14: Propagation of the ionospheric gradient.

Given an ionospheric gradient affecting the observations of a certain GNSS satellite, the condition to obtain the same phase between the corresponding perturbation observed from two stations of the network (for example the ref-

erence station and another station r), can be written as:

$$(\boldsymbol{x}_r - \boldsymbol{x}_0) \cdot \boldsymbol{k} = \omega \cdot \kappa_r, \tag{3.15}$$

where $\boldsymbol{x}_r$ and $\boldsymbol{x}_0$ are the position vectors of the IPPs at the times of detection of the gradient (see Figure 3.14) expressed in a local reference coordinate system. That is, $\boldsymbol{x}_r = [x_{r,East}, x_{r,North}]$. The center of this local reference coordinate system is the average of the positions of the IPPs at the times of detection in each of the stations. Note that the variables that follow are also expressed in this coordinate system. Defining the vector slowness as $\boldsymbol{s} = \frac{\boldsymbol{k}}{\omega}$ as in [97], Equation 3.15 can be expressed in terms of the vector difference of position between IPPs, $\boldsymbol{\Delta x_r}$, and the time delay κ_r as:

$$\boldsymbol{\Delta x_r} \cdot \boldsymbol{s} = \kappa_r. \tag{3.16}$$

Now, Equation 3.16 is considered for the different stations r belonging to the network $\mathcal{R}$ that have detected the gradient until the current epoch t denoted as N_R. Thus, matrix $\boldsymbol{X}$ and vector $\boldsymbol{z}$ are defined as:

$$\boldsymbol{X} = \begin{bmatrix} \boldsymbol{\Delta x_1} \\ \boldsymbol{\Delta x_2} \\ \vdots \\ \boldsymbol{\Delta x_{N_R-1}} \end{bmatrix}_{N_R-1\times 2} \qquad \boldsymbol{z} = \begin{bmatrix} \kappa_1 \\ \kappa_2 \\ \vdots \\ \kappa_{N_R-1} \end{bmatrix}_{N_R-1\times 1} . \tag{3.17}$$

Here, $\boldsymbol{X}$ contains the IPP position vectors and $\boldsymbol{z}$ the time delays between the different stations r and the station of reference. Note that the differences of position vectors composing $\boldsymbol{X}$ and the time delays in $\boldsymbol{z}$ appear in the order in which the different stations detected the gradient. This order replaces the name of the stations represented by subscript r. The dimensions of $\boldsymbol{X}$ and $\boldsymbol{z}$ are $[N_R - 1 \times 2]$ and $[N_R - 1 \times 1]$ respectively because the first station that detects the gradient is used as reference for calculating the cross-correlation coefficients and the time delays.

Therefore, Equation 3.16 can be expressed as:

$$\boldsymbol{X}\boldsymbol{s} = \boldsymbol{z}. \tag{3.18}$$

Since $\boldsymbol{X}$ in Equation 3.18 is not invertible, the Moore-Penrose pseudoinverse is used, and thus $\boldsymbol{s}$ can be estimated as in Equation 3.19, which can be solved by Least Squares:

$$\widehat{\boldsymbol{s}} = (\boldsymbol{X}'\boldsymbol{X})^{-1}\boldsymbol{X}'\boldsymbol{X}. \tag{3.19}$$

However, since the information of the level of cross-correlation between the test statistics (α_r) is available, it is used to estimate $\widehat{\boldsymbol{s}}$. In this way, information

about the trust that can be given to the measurements coming from the different stations can be introduced in the estimation of $\widehat{\boldsymbol{s}}$. Thus, the estimation of $\widehat{\boldsymbol{s}}$ can be solved with a Weighted Least Squares as:

$$\widehat{\boldsymbol{s}} = \left(\boldsymbol{X}^{\prime}\boldsymbol{W}_{\boldsymbol{\alpha}}\boldsymbol{X}\right)^{-1}\boldsymbol{X}^{\prime}\boldsymbol{W}_{\boldsymbol{\alpha}}\boldsymbol{X}, \tag{3.20}$$

where $\boldsymbol{W}_{\boldsymbol{\alpha}}$ is a diagonal matrix containing the weights of the Weighted Least Squares (based on the cross-correlation results) as:

$$\boldsymbol{W}_{\boldsymbol{\alpha}} = \begin{bmatrix} \alpha_1 & 0 & \dots & 0 \\ 0 & \alpha_2 & \dots & 0 \\ \vdots & \vdots & \ddots & \vdots \\ 0 & 0 & \dots & \alpha_{N_R-1} \end{bmatrix}_{N_R-1 \times N_R-1} \tag{3.21}$$

Then, the speed of the gradient $\widehat{\boldsymbol{v}}$ is the Samelson inverse of the vector $\widehat{\boldsymbol{s}}$:

$$\widehat{\boldsymbol{v}} = \frac{\widehat{\boldsymbol{s}}}{\widehat{\boldsymbol{s}} \cdot \widehat{\boldsymbol{s}}}. \tag{3.22}$$

From the vector $\widehat{\boldsymbol{v}} = [\widehat{v}_{East}, \widehat{v}_{North}]$, the module of the speed of the ionospheric gradient, $\widehat{v}_{iono}$, can be calculated as:

$$\widehat{v}_{iono} = \sqrt{\widehat{v}_{East}^2 + \widehat{v}_{North}^2}, \tag{3.23}$$

and the direction of the gradient (azimuth measured from the North pole) can be computed (in degrees) as:

$$\widehat{d}_{iono} = 90^{\circ} - \operatorname{atan2}(\widehat{v}_{North}, \widehat{v}_{East}). \tag{3.24}$$

Nevertheless, as previously stated, the algorithm assumes that the perturbation (i.e. the anomalous ionospheric front) is local, which means that the result of comparing the measurements from two stations with a long distance between them (e.g. 200 km) might be inaccurate since the perturbation might change during its propagation from one station to the next. Moreover, the geometry of the IPPs in the sky should not be aligned in order to avoid singularities while calculating the speed vector.

Therefore, before the estimation of the gradient parameters, IPPs corresponding to the different stations are grouped in clusters, and these clusters are validated to check if they are suitable to calculate a reliable estimation of the speed vector. At the time of detection in each of the stations, the position vectors $\boldsymbol{x}_r$ for each of the IPPs corresponding to the satellite of interest and different stations r impacted by the same gradient in a local coordinate system are computed. Then, a cluster with these position vectors is formed, which is

validated attending to two different criteria: (i) a radius around the central point of the local coordinate system to guarantee the locality principle, and (ii) a geometry index that ensures that the geometry of the IPPs in the sky is acceptable. For the first criteria, a validation radius of 200 km is chosen. This value is based on the maximum station separation distance considered in the literature that addresses the ionospheric threat model derivation in the CONUS region [29] and in Korea [79]. For the second criteria, the Geometry Index (GI) is defined as:

$$GI = \sqrt{\text{trace}\left((\boldsymbol{X}'\boldsymbol{X})^{-1}\right)}. \tag{3.25}$$

This GI evaluates the impact of the geometry of the IPPs in the solution of Equation 3.20 and plays a similar role as the Geometry Dilution Of Precision (GDOP) in the estimation of the position solution: a high GI means a bad geometry, whereas a low GI means a good geometry from the point of view of the resolution of Equation 3.20. The values that the GI can get are further discussed in Chapters 4 and 5.

3.3.4.3 Slope and width of the gradient

Once the speed vector of the gradient is known, the slant slope of the gradient estimated by the considered satellite and station r is determined by the following geometrical relationship:

$$\widehat{g}_{iono,r}\left(t\right) = \frac{Itest_r\left(t\right)}{\Delta v_r\left(t\right)}, \tag{3.26}$$

where $\Delta v_r(t)$ is the relative speed between the gradient, $\widehat{\boldsymbol{v}}$, and the IPP, $\boldsymbol{v_{IPP_r}}(t)$, projected in the direction of propagation of the gradient calculated as:

$$\Delta v_r\left(t\right) = \left(\boldsymbol{v_{IPP_r}}(t) - \widehat{\boldsymbol{v}}\right) \cdot \frac{\widehat{\boldsymbol{v}}}{\|\widehat{\boldsymbol{v}}\|}. \tag{3.27}$$

As can be observed in Equation 3.26, the slope is calculated per epoch t and is not considered constant during the propagation of the gradient as the speed vector. The reason behind is that the algorithm looks for the "worst case" or highest slope and therefore, it needs to consider all the values of the $Itest_r(t)$ stored in the buffer ($\boldsymbol{B_{Itest_r}}$) until it finds the maximum. Once the maximum slope for this specific satellite-station pair is found, the algorithm assumes that it is constant until the perturbation is not detected any more. Since the convergence of the algorithm may have occurred later than the occurrence of the maximum slope, all slope values prior to the current epoch within the buffer are also computed to find the maximum value.

Another possibility to calculate the slope of the gradient is the "station-pair method", which calculates the difference of the slant ionospheric delay between two stations and divides it by the distance between the stations [29]. However, this methodology requires very accurate ambiguity resolution, and its estimation accuracy is often degraded by any remaining erroneous systematic offset. In contrast, the methodology used in this work, is not highly sensitive to remaining biases on ionospheric delay estimates, since the ambiguity is removed when calculating the first derivative of the ionospheric delay. Note that, as will be seen in Chapters 4 and 5, the approach used in this work to estimating the gradient slope could have a high degree of error due to (i) the uncertainty in the relative speed estimate, and (ii) the error in the thin-shell assumption under IPP calculations. However, the gradient slopes estimated by the proposed method are overbounded to consider the uncertainty in the estimations. Furthermore, these gradient slope estimates include both spatial and temporal changes in the ionospheric delay when only the spatial changes are desired, which is acceptable when searching for the "worst-case" gradient estimations in real time.

Additionally, greater observability of gradients is obtained with the proposed method than with other methods (e.g., the "station-pair method") that use slant ionospheric delay differences between stations. The reason is that the "station-pair method" could easily underestimate the gradient slope if stations with baselines comparable to the gradient width are not used (e.g., estimation of gradient widths of 20 km with stations separated by more than 100 km would lead to large underestimation errors).

The width of the gradient estimated by the considered satellite and station r is calculated as:

$$\widehat{w}_{iono,r}\left(t\right) = \Delta v_r\left(t\right) \cdot T_W\left(t\right), \tag{3.28}$$

where $T_W(t)$ is the time in seconds that has passed since the gradient was detected until current time t. Note that the total width of the gradient can only be known when the whole gradient has passed and the station r is not detecting the gradient any more.

3.3.4.4 Uncertainty model and overbound of the estimated gradient parameters

The previously described estimation process is not free from errors that cause the estimated values to deviate from true values. These errors exist due to several factors such as the presence of multipath and noise in the measurements, the approximations and simplifications in the mathematical models, and the insufficient time resolution of the measurements to name some. Chapters 4 and 5 study these errors and their causes with simulated and real data.

Therefore, in order to be able to substitute the conservative threat model by the estimated gradient parameters from the network, a statistical model of the uncertainty of the estimations is needed. To derive such a model, first, the determination of the gradient parameter estimation errors is needed. This work focuses specifically on the estimation errors of the slope of the gradient since it is the parameter that serves as the interface between the network and the GBAS stations (see Section 3.4). The estimation error of the slope for station r and satellite j can be computed as:

$$\Delta^{j}_{g_{iono,r}} = \widehat{g}^{j}_{iono,r} - g^{j}_{iono,r}, \tag{3.29}$$

where $\widehat{g}^{j}_{iono,r}$ is the maximum estimated slant slope for satellite j and station r, and $g^{j}_{iono,r}$ is the true value for the slant slope at the same epoch, for the same satellite and the same station. However, as the true values are unknown, Monte Carlo simulations are carried out by varying all the gradient parameters to calculate these errors in a controlled environment. The estimation errors for all the other gradient parameters can be determined in the same manner by subtracting the simulated value of the parameter from the estimated value of it.

The algorithm calculates these parameter estimation errors for all satellites, stations and variations of all gradient parameters in the threat model. Sections 4.2 and 5.2 (Chapters 4 and 5) describe in detail the different simulation steps and Tables 4.3 and 5.3 show the distributions used to generate variations of each parameter for Alaska and Brazil, respectively.

Then, the algorithm sorts the error values for one parameter in bins of estimated values in order to allow for variable behavior under different levels of ionospheric intensity while maintaining a sufficient number of samples per bin to obtain reliable statistics. The number of samples inside each bin and the interval of estimated values that each bin covers depend on the characteristics of the errors obtained. For example, the estimation errors could be comparable for different ranges of simulated slopes, but the length of these ranges could be different depending on the magnitude of the gradient. Section 4.3.2.2 of Chapter 4 and Section 5.3.2.2 of Chapter 5 explain with simulated data how to select the size of the bins, as it depends on the data and can be different for different data sets.

The estimation error uncertainty in each bin is modeled as a Gaussian distribution, which is commonly used in GNSS augmentation systems because of its simplicity for defining the error distribution with only two parameters (its mean and standard deviation). Therefore, once the estimation errors are divided into bins, the estimation error samples are normalized (e.g. $\Delta^{j}_{g_{iono,r}}$ with $j \in 1, ..., \mathcal{J}$ and $r \in 1, ..., \mathcal{R}$) by using the sample mean, $\mu_{g_{iono,m}}$, and the sample standard deviation, $\sigma_{g_{iono,m}}$, in each bin with $m = 1, 2, .., \mathcal{M}$ representing the bins.

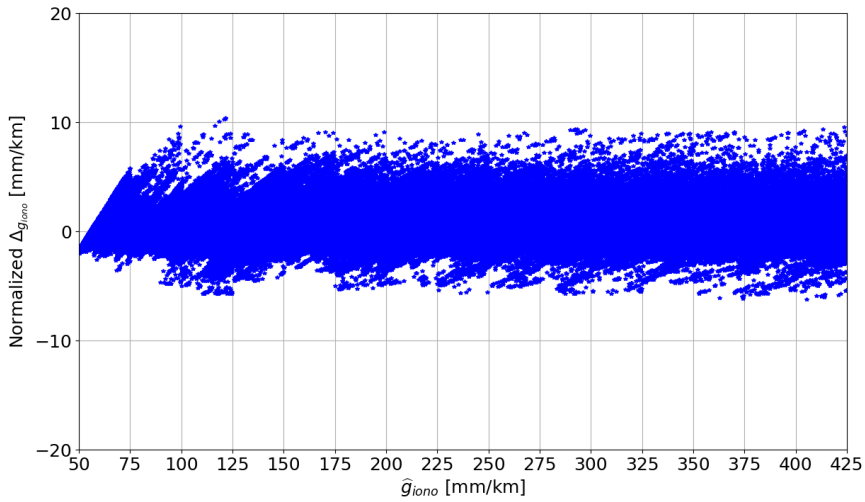

Figure 3.15: Normalized slant slope estimation errors versus slant slope estimated values for the network studied in Chapter 4 (Alaska). The data bins considered are of 25 mm/km in estimated slant slope.

Figure 3.15 shows an example of the normalized slant slope estimation errors for the network of stations studied in Chapter 4 (Alaska). As can be observed, after normalization, the distribution is practically homogeneous except for the first three bins (50 - 75 mm/km, 75 - 100 mm/km, and 100 - 125 mm/km) because they have less data due to the way the gradients are simulated. Section 4.3.2.2 explains this phenomenon. Therefore, unlike Section 3.3.1, a single inflation factor, $I_{g_{iono}}$, is calculated for the entire distribution to properly overbound the non-Gaussian tails of the normalized $\Delta_{g_{iono}}$ distribution formed by the normalized samples in all bins. Figure 3.16 shows the inflated distribution (green dashed line) for the case in Alaska, which was calculated following the method described in Section 3.3.1. Thus, the inflated standard deviation per bin can be calculated as:

$$\sigma_{g_{iono,overbound,m}} = |\mu_{g_{iono,m}}| + I_{g_{iono}} \cdot \sigma_{g_{iono,m}}. \tag{3.30}$$

Then, when the algorithm is running in real time, and the network estimates the value of a gradient parameter (e.g. the slope), the previously-determined inflation factors are applied to compute the appropriately overbounded estimated parameter as described in Equation 3.31:

$$\widehat{g}^{j}_{iono,overbound,r}(t) = \widehat{g}^{j}_{iono,r}(t) + k_{ne} \cdot \sigma_{g_{iono,overbound,m}}, \tag{3.31}$$

where k_{ne} is the scalar multiplier needed to meet the required Probability of Non-bounded Errors (PNE), P_{ne}, computed from the inverse of the standard

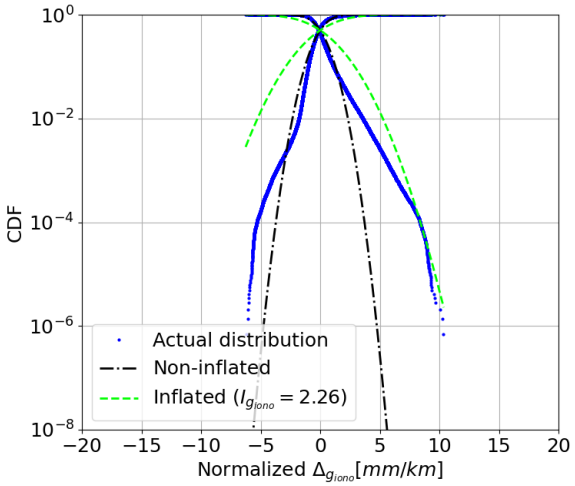

Figure 3.16: Example of the Gaussian tail overbounding process for the gradient slant slope estimation errors and the network studied in Chapter 4 (Alaska). The blue dots show the normalized slant slope estimation error distribution for all the data bins, the black dot-dashed line represents the non-inflated Gaussian distribution that would correspond to the mean and standard deviation of the normalized distribution, and the dashed green line represents the inflated Gaussian distribution.

normal cumulative distribution, $Q^{-1}(P_{ne})$. The PNE has been defined specifically for this work as the probability of estimating errors erroneously in a way that compromises GBAS integrity. Considering again the integrity tree in Figure 2.2 and following the same argumentation as in Section 3.3.2, this probability has been selected to be 1×10^{-8}. Furthermore, $\sigma_{g_{iono,overbound,m}}$ is the overbounded standard deviation corresponding to the data bin m associated to the estimated slant slope $\widehat{g}^{j}_{iono,r}(t)$.

The process of calculating the overbounded estimated gradient parameters is depicted in Figure 3.17. First, the real-time algorithm estimates the gradient slant slope ($\widehat{g}^{j}_{iono,r}(t)$). Then, it calculates the bin to which the estimated slant slope belongs (e.g., $m = 3$). This slope has an associated estimation error ($\Delta^{j}_{g_{iono,r}}$) that is unknown in the real case. Therefore, the information obtained in simulation is used to overbound the estimated slant slope. This is done by using the mean and standard deviation of the bin to which the estimate belongs ($\mu_{g_{iono,3}}$ and $\sigma_{g_{iono,3}}$ in the example of Figure 3.17, respectively) to calculate the inflated sigma ($\sigma_{g_{iono,overbound,3}}$ in Figure 3.17) (see Equation 3.30). Finally, the previous elements and P_{ne} are used to compute the overbounded slant slope of the gradient (see Equation 3.31). In Chapters 4 and 5, the process previously explained is described with simulated and real data.

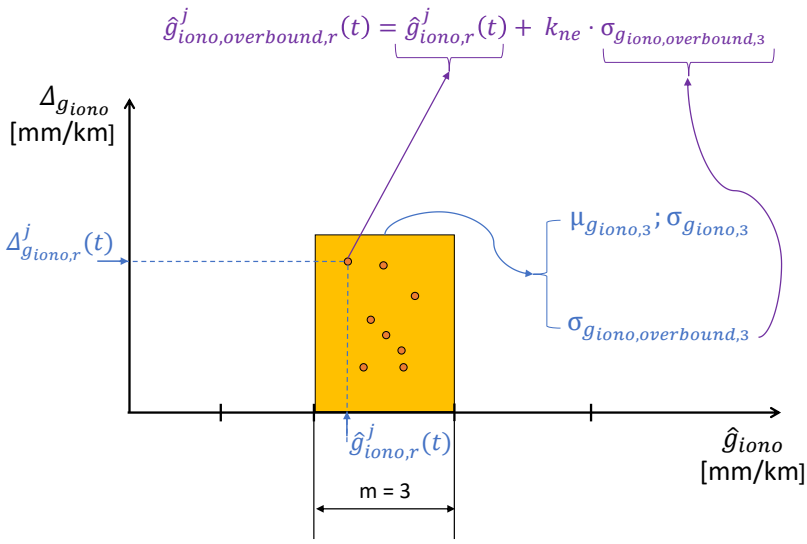

Figure 3.17: Process of calculating the overbounded estimated gradient parameters.

3.4 Interface between the network-based ionospheric gradient monitor and GBAS

The network determines the current state of the ionosphere in the monitored area by either detecting and estimating the gradients per satellite or ensuring that no gradient is present over a certain magnitude. Then, it is the task of each GBAS ground station to use this information to update the threat model to be used at a certain time epoch.

This thesis proposes a methodology that includes this information into a GAST C station inside the geometry screening algorithm explained in Section 2.4.3.1. In this way, a GAST C ground station would use a variable maximum gradient slope per satellite, g^j_{iono}, in the calculation of anomalous ionosphere-induced differential range errors within the PDGS algorithm (see from Equation 2.31 to Equation 2.35 in Section 2.4.3.1) instead of using the constant value from the threat model as done today. This variable maximum gradient slope depends on the information received from the network, which is one of the following values:

(i) The MDG calculated in Section 3.3.2 for the coverage area of the network, when the network does not detect any anomalous ionospheric activity. This value would be used as the maximum anomalous gradient that can currently be observed by each satellite instead of the maximum "worst-

case" gradient defined by the regional ionospheric threat model.

(ii) The "maximum possible slope" estimated and overbounded in real time for each satellite in the coverage area of the network calculated in 3.3.4.4, when the network detects an anomalous ionospheric gradient and the algorithms converge. This value would be larger than the minimum detectable gradient from (i) but typically smaller than the maximum "worst-case" gradient from the ionospheric threat model.

(iii) A "Warning" that implies the use of the "worst-case" ionospheric threat model applicable to GBAS for that area, when the network detects an anomalous ionospheric gradient but the algorithms are not yet able to reliably estimate the gradient parameters. The "worst-case" ionospheric threat model would also be used in case the "maximum possible slope" from point (ii) exceeds its "worst-case" bounds, as it has much less statistical uncertainty than the real-time gradient estimates.

Therefore, the integrity parameters transmitted by the GAST C station would require less inflation most of the time. Thus, availability would increase in regions where conservative ionospheric threat models have to be applied to protect integrity. The results justifying the previous statements are presented in Chapter 6. Figure 3.18 shows a diagram of the interface between GBAS and the network.

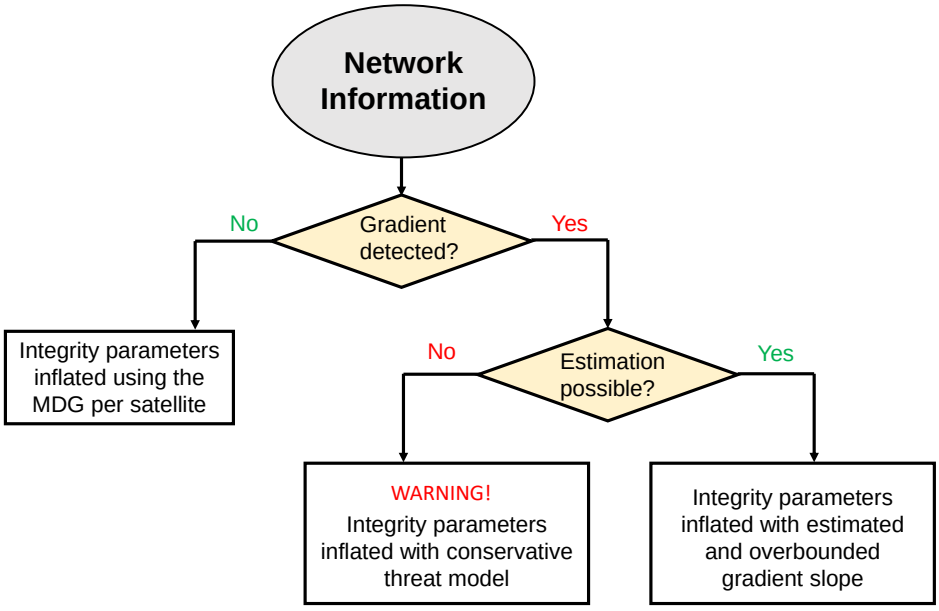

Figure 3.18: Diagram of the interface between GBAS and the network.

3.4.1 Real-time operation of the network

To be useful for ionospheric threat mitigation, the network information would have to be generated and transmitted at a frequency that would allow the GBAS stations to act in real time (send inflated integrity parameters to aircraft every 0.5 seconds or alert aircraft within 6 seconds for CAT I approaches). Therefore, assuming that PDGS could determine an inflation factor using the input from the network every 0.5 seconds, the network receivers should have a sampling rate sufficiently high to meet these requirements (i.e., below 0.5 seconds to allow certain margin for data transmission). Otherwise, if PDGS could not work in real time, an inflation factor update interval of 60 seconds could be used and the GBAS station should ensure that the inflated parameters are valid for the next 60 seconds as proposed in [26].

In the case that the sampling rate of the network receivers is lower than that of GBAS (e.g., 15 seconds versus 0.5 seconds), which is not advisable, it must be ensured that the gradient slope observable by the GBAS is not greater than the last slant slope transmitted by the network. In the nominal case, this is ensured by the calculation of the MDG, which should be calculated by means of exhaustive simulations and consider the sampling frequency of the network receivers (see Chapter 6). In the case of gradient parameter estimation, while Algorithm 2 does not converge, the network warns the GBAS station to use the current conservative threat model. After convergence of Algorithm 2, the overbounding process should consider an additional uncertainty for possible variations of the gradient parameters (e.g., slant slope) between the time when they were estimated by the network and the time when the gradient affected the GBAS station. Note that if the sampling rate of the network receivers and the baselines between them were adapted to the correlation distance of the ionospheric disturbances (i.e., distance within which the disturbances do not experience significant variations), this additional uncertainty in the overbounding process would not be necessary.

3.5 Summary

This chapter has presented the “Network-GBAS” concept, a method capable of detecting anomalous ionospheric gradients in real time (i.e., at the sampling rate of the network receivers) and estimating their parameters in near-real time (i.e., after Algorithm 2 has converged and the parameters have been estimated and overbounded). The “Network GBAS” concept is based on a wide-area network of dual-frequency (mandatory), multi-constellation (optional) GNSS monitoring stations.

This chapter has begun by analyzing whether such a concept, which includes

external information into GBAS, is possible within current GBAS standards. The next section has introduced the "Network-GBAS" concept in general.

Then, this chapter has described in detail the algorithm for detecting anomalous ionospheric gradients for each station-satellite pair, including the necessary processing of the measurements and the derivation of the detection thresholds as a function of satellite elevation. It has also explained the methodology for calculating the minimum detectable error for each station of the network to meet the integrity requirements.

Subsequently, it has described the estimation of the ionospheric gradient parameters and the methodology to overbound them considering the possible estimation errors. Here, it has introduced weighting within the equations for the estimation of the gradient parameters that takes into account the cross-correlation coefficients between the test statistics coming from different pairs of stations. In addition, it has defined a geometry index to check if the clusters formed by the IPPs for estimating the gradient parameters are adequate to limit the geometric approximation errors in the methodology.

Finally, this chapter has explained the interface between the "Network-GBAS" concept proposed in this thesis and the ionospheric threat mitigation solutions for a GBAS CAT I station.

4

Performance of the Network-Based Ionospheric Gradient Monitor in a High-latitude Region

The previous chapter has provided a methodology to reduce the current excessive conservatism in the assumptions adopted to protect GBAS against large undetected ionospheric gradients. The proposed method not only provides a solution to detect and estimate such gradients but also provides an associated integrity concept to ensure the integrity of GBAS.

The main objective of this chapter is to analyze the performance of the proposed methodology first with simulated data and then with real data from a network of stations located in the auroral region. The underlying idea is to compare the performance of the methodology with both simulated and real data to establish a relationship that ensures that the simulations are representative of the real world. Within the auroral region, I have chosen a network of stations located in Alaska for this study. The reason is that, in this region, anomalous ionospheric gradients tend to be small in magnitude but propagate with very high speeds, although they could still have a negative impact on GBAS. Because of these characteristics, these gradients present a great challenge for the methodology proposed in Chapter 3, which is based on time derivatives. Since there are no airports near the network considered, this chapter conceptually evaluates the detection, estimation and overbounding algorithms of Chapter 3, leaving the direct application to GBAS for Chapter 6 with the network studied for the equatorial region, which does have airports nearby.

This chapter is organized as follows: Section 4.1 presents the data used throughout the chapter, Section 4.2 describes the simulation setup developed to be representative of ionospheric characteristics in the auroral region, Section 4.3 evaluates the performance of the method with simulated data, and Section 4.4 evaluates the performance of the method with a real anomalous ionospheric perturbation measured by the network in Alaska. The work in this chapter

was published in [92, 93], as stated in Section 1.5.

4.1 Description of the real data used for the evaluations in the auroral region

This section describes the characteristics of the network used to evaluate the performance of the methodology proposed in Chapter 3 in the auroral region. First, Section 4.1.1 describes the network architecture and the measurements used. Then, Section 4.1.2 presents the method for selecting nominal (i.e., no abnormal ionospheric activity present) and active days.

4.1.1 Data description

As a representative monitoring network for the auroral region, five stations situated in Alaska belonging to the Geodetic Facility for the Advancement of Geosciences (GAGE) were used. The locations of these stations are depicted in Figure 4.1 and their coordinates are presented in Table 4.1. Public data is available for this network at a 1 Hz sampling rate both for L1 and L2 frequencies and GPS satellites [99].

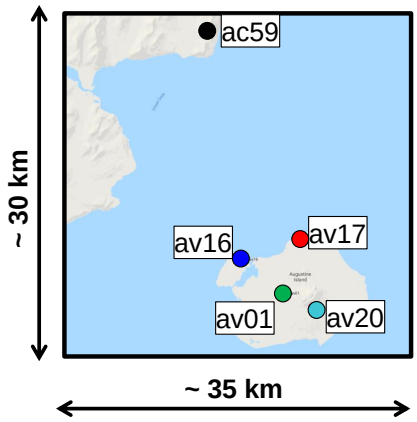

Figure 4.1: Locations of the stations in Alaska.

Note that, due to the limited availability of data recorded with L1/L5 frequencies and other constellations (e.g. Galileo) during active ionospheric conditions, real measurements on L1 and (semi-codeless) L2 frequencies and only the GPS constellation were used for this study. It is expected that the performance of the methodology evaluated with measurements from multiple satellite constellations broadcasting L1/E1 and L5/E5a will be better than the performance achieved in the present thesis with only GPS and L1/L2 frequencies.

The reason why this is expected is that measurements recorded on L5 are typically less noisy and contain fewer cycle slips than on L2, and more measurements available from more satellites will provide better sampling of the ionosphere, improving the detection capabilities of the network as discussed in Section 3.3.2 of Chapter 3.

Name	**Latitude** [°]	**Longitude** [°]
ac59	59.567	-153.585
av17	59.404	-153.451
av16	59.386	-153.535
av01	59.359	-153.461
av20	59.347	-153.428

Table 4.1: Coordinates of the stations in Alaska.

4.1.2 Date selection

The dates selected from all the data available attend to two different purposes: (i) the study of a real anomalous ionospheric gradient measured by the network depicted in Figure 4.1, and (ii) the derivation of monitoring thresholds for each of the stations in the network.

As an "active" ionospheric day, the geomagnetic storm that occurred on the 17th of March of 2015, St. Patrick's Day, which has been extensively studied in the literature [100, 101] was selected. For threshold derivation, ten "quiet" days prior to this so-called "St. Patrick's Day Storm" were manually selected.

Both active and nominal days were selected based on an ionospheric activity index, the AATR [32], calculated for one of the stations under study, "av17". Figure 4.2 shows the specific AATR values for this station. As can be observed, the AATR for the day of year 76, i.e. St. Patrick's Day, is above 1 TEC Unit (TECU) per minute, which appears to be very high activity [32]. Furthermore, this work considers that "quiet" ionospheric conditions refer to AATR values below 0.2 TECU/min, which is well below the 0.6 TECU/min proposed in [32] as some ionospheric activity. As a last step, visual inspection of the data recorded in the stations under study, "ac59", "av17", "av16", "av20", and "av01", during the days considered "nominal" was performed. During this process, days with corrupted or missing measurements were discarded.

According to these criteria, the nominal days used to derive the detection thresholds for the stations "av16", "av17", "ac59", and "av20" were: 52, 56, 57, 58, 63, 64, 68, 69, 72 and 73 of year 2015. In the case of station "av01", the measurements presented certain discontinuities on the days 63 and 64. Thus, these corrupted days were replaced with days 67 and 70 of year 2015.

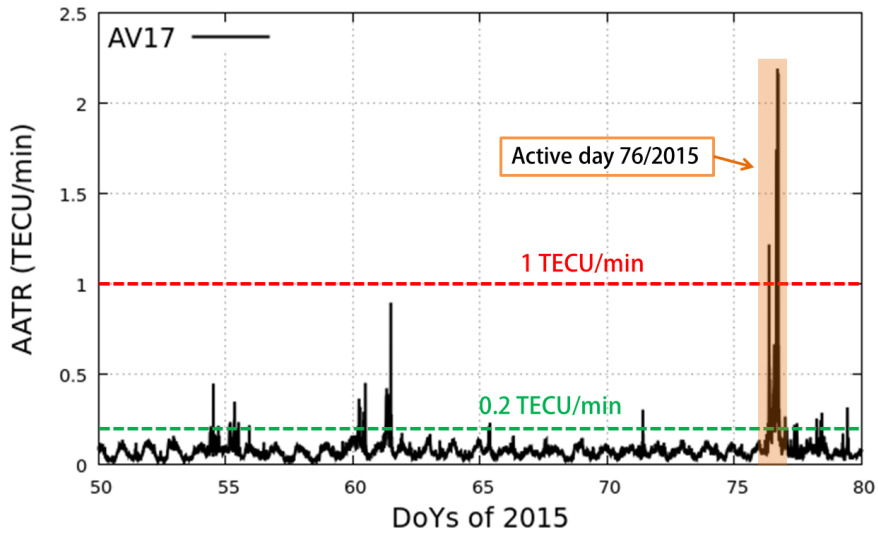

Figure 4.2: AATR values for reference station "av17" during 30 days of year 2015. The AATR values are calculated every 5 minutes. The threshold of 0.2 TECU/min represents the value below which the ionosphere is considered "quiet" or nominal and the threshold of 1 TECU/min is the value above which the ionosphere is considered very "active" or abnormal.

4.2 Simulation setup

This section presents the simulation setup designed to evaluate the detection and estimation capabilities of the network introduced in Section 4.1.

As a first step, it is necessary to calculate the nominal slant ionospheric delays present in the measurements over which the simulated gradient is to be added. For this purpose, Equation 3.1 was used with the measurements recorded by the network on one of the "quiet" days. Among the ten nominal days specified in Section 4.1, day 73 of 2015 was selected. Note that it was assumed that the information recorded on this day is representative of all nominal days in terms of multipath and noise present in the measurements, satellite geometries, and nominal slant ionospheric delays. However, this is a simplification, and more simulations with measurements from different days of the year and different years would be needed to obtain more representative results.

Then, on top of the nominal slant ionospheric delays, synthetic ionospheric perturbations designed to be representative of the GBAS threat model shown in Figure 2.9 are simulated. Since there is no established ionospheric threat model for Alaska, the single-wedge threat model was simulated, which is the threat model used in most regions of the world.

For simulating the synthetic gradient, the perturbation was defined as a

planar wave front that moves with a constant speed (meters per second) and direction (degrees) over a "thin shell" layer at a height of 350 km above the Earth's surface. Here, "speed" and "direction" of the simulated gradient refer to the magnitude (v_{iono}) and direction (d_{iono}) of the speed vector $\boldsymbol{v}$, measured in the clockwise direction from the North Pole. With these two parameters, the trajectory of the center of the ionospheric perturbation represented by its latitude ($lat_{iono}(t)$), longitude ($lon_{iono}(t)$), and time ($t_{iono}(t)$) at current epoch t was defined as:

$$\begin{aligned} lat_{iono}(t) &= lat_{iono}(t-1) + \Delta lat_{iono}, \\ lon_{iono}(t) &= lon_{iono}(t-1) + \frac{\Delta lon_{iono}}{\cos(lat_{iono}(t-1))}, \\ t_{iono}(t) &= t_{iono}(t-1) + \Delta T, \end{aligned} \tag{4.1}$$

where $lat_{iono}(t-1)$ and $lon_{iono}(t-1)$ are the latitude and longitude in radians, and $t_{iono}(t-1)$ is the time in seconds of the center of the perturbation at the previous epoch. The data sampling rate in seconds is represented by ΔT and Δlat_{iono} and Δlon_{iono} are defined as:

$$\begin{aligned} \Delta lat_{iono} &= v_{iono} \cdot \Delta T \cdot \frac{\cos(d_{iono})}{R_e + h_I}, \\ \Delta lon_{iono} &= v_{iono} \cdot \Delta T \cdot \frac{\sin(d_{iono})}{R_e + h_I}, \end{aligned} \tag{4.2}$$

where R_e is the equatorial radius of the Earth and h_I the "thin shell" layer height. The latitude, longitude, and time of the center of the ionospheric perturbation are initialized to the first latitude, longitude, and time of the perturbation, which are input parameters.

Once the gradient trajectory is known for each epoch, the ionospheric gradient in a local reference frame, where the origin ($[0, 0]$) is at the center of the perturbation $[lon_{iono}, lat_{iono}]$ and changes at each epoch, is defined. Therefore, to obtain the amount of simulated ionospheric delay experienced by each IPP, it is necessary to convert the IPPs from the global reference frame to the ionospheric perturbation reference frame. Appendix A describes this transformation. As a result of the application of these geometric transformations, the coordinates of the IPPs in the perturbation reference frame can be expressed as $\boldsymbol{x_{iono}} = [x_{iono}, y_{iono}]$. Moreover, as in GBAS, the gradient is defined only in its propagation direction while it is assumed that its dimensions in the direction perpendicular to the direction of motion are infinite. Therefore, the additional slant ionospheric delay in meters (D_{iono}) that is added to the nominal slant ionospheric delay calculated previously is expressed in Table 4.2. Here, F_{pp} is the vertical-to-slant obliquity factor explained in Equation 2.23, $g_{iono,vert}$ is the simulated gradient slope expressed in the vertical domain in mm/km, and w_{iono} is the simulated gradient width in kilometers.

Additional slant ionospheric delay [m]	**IPP coordinates in the ionospheric perturbation reference frame [m]**
$D_{iono} = 0$	$x_{iono} = (-\infty, +\infty)$; $y_{iono} > 0$
$D_{iono} = F_{pp} \cdot \frac{g_{iono,vert}}{10^6} \cdot \lvert y_{iono} \rvert$	$x_{iono} = (-\infty, +\infty)$; $-w_{iono} \cdot 10^3 \leq y_{iono} < 0$
$D_{iono} = F_{pp} \cdot \frac{g_{iono,vert} \cdot w_{iono}}{10^3}$	$x_{iono} = (-\infty, +\infty)$; $y_{iono} \leq -w_{iono} \cdot 10^3$

Table 4.2: Equations to simulate the synthetic slant ionospheric delays in Alaska.

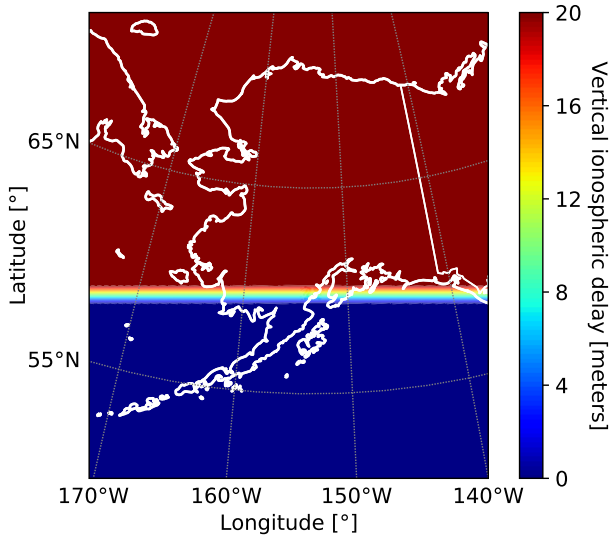

Figure 4.3: Example of one synthetic perturbation simulated with a $g_{iono,vert}$ of 200 mm/km, a w_{iono} of 100 km, and a d_{iono} of 180°.

Figure 4.3 shows an example of one simulated ionospheric gradient or change in the ionospheric delay values between the dark blue area and the dark red area, which are the areas where the ionospheric delay values are constant and no gradient is present. These ionospheric delay values are expressed in the vertical domain to be independent of the elevation of each of the satellites, which allows to simulate the same vertical ionospheric gradient for all the satellites. Moreover, these vertical ionospheric delays are simulated by the utilization of two different simulation gradient parameters: the vertical slope in millimeters per kilometer and the width in kilometers. Therefore, when an IPP corresponding to a certain satellite and station moves into the region with the gradient, the distance from the IPP to the origin of the perturbation in

meters (y_{iono}) is computed and this distance is multiplied with the vertical slope to get the vertical ionospheric delay. The multiplication of this vertical delay with the obliquity factor that depends on the elevation of the satellite translates it into the slant domain.

Note that, Table 4.2 defines the gradients only in the south-to-north direction independently of their trajectory. For this reason, Equation A.4 of Appendix A performs a rotation of the IPPs around the origin of the perturbation, which has the same effect as rotating the gradients for simulating different gradient directions. Furthermore, although the perturbation is simulated as a planetary planar wave, which is unrealistic, typically the actual front size is several times larger than the baselines of the networks used; thus, the approximation of a planar wave front is reasonably applicable to this analysis.

Parameter	Minimum	Maximum	Step
$g_{iono,vert}$ [mm/km]	50	425	25
w_{iono} [km]	20	200	30
v_{iono} [m/s]	0	1200	50
d_{iono} [°]	0	270	90
$t_{iono,0}$ [GPS seconds of day]	0	80000	2000

Table 4.3: Simulation parameters for Alaska.

For these studies, all the already defined simulation gradient parameters were varied within their ranges in the CONUS and German threat models (see Table 2.5) up to a maximum additional delay of 50 meters. Table 4.3 presents the parameter bounds for the simulation. As can be seen, the slope of the gradient was simulated in the vertical domain until the maximum value defined in slant for the CONUS threat model. The reason is that a high elevation satellite presents a similar value for the slant delay as for the vertical delay, and therefore vertical values are considered up to the maximum. Note that, in the case of low elevation satellites, much higher slant slopes than the maximum slant slopes considered in the CONUS threat model could be simulated. However, all simulation cases that produced simulated slant slopes greater than 425 mm/km or achieved additional ionospheric delays greater than 50 meters were not considered. Furthermore, the initial longitude and latitude of the center of the perturbation for each realization of the simulation represented by $lon_{iono,0}$, $lat_{iono,0}$, and $t_{iono,0}$, respectively were selected, so that the gradient trajectory crosses approximately the midpoint of the stations composing the network. This is because, in this way, the transformation errors due to the conversion of the IPP coordinates to the perturbation plane are minimized.

Figure 4.4 shows the simulated slant ionospheric delays for satellite G03, all stations of the network in Alaska, and the synthetic perturbation depicted

in Figure 4.3. As can be seen, there is a vertical offset in the estimated slant ionospheric delays. This is due to the ambiguities present in the carrier-phase measurements in Equation 2.1.

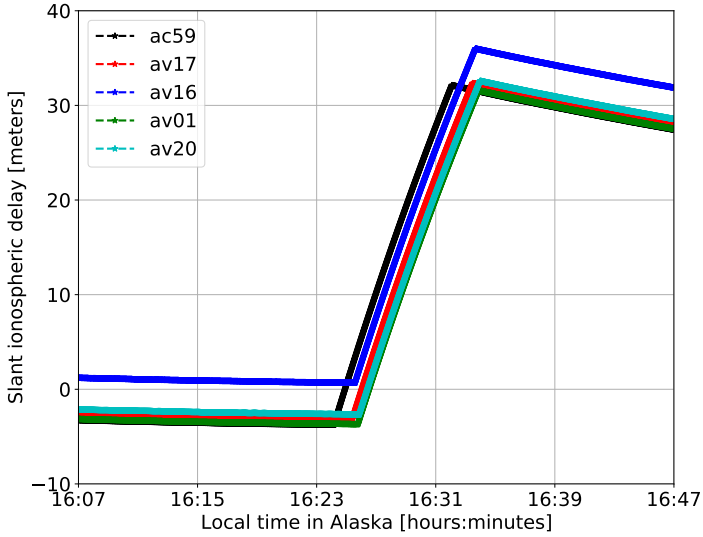

Figure 4.4: Example of simulated slant ionospheric delays for satellite G03 and the network of stations situated in Alaska. These simulated slant ionospheric delays correspond to the synthetic perturbation depicted in Figure 4.3 added to the real nominal slant ionospheric delays from satellite G03.

4.3 Evaluation of the monitor with simulated ionospheric gradients

This section analyzes the detection and estimation capabilities of the network of stations depicted in Figure 4.1.

4.3.1 Detection

To analyze the detection capabilities of the network, the performance of each of the monitoring stations inside the network was initially introduced by means of their detection thresholds (Figure 4.5). Then, the minimum ionospheric rates that each of the stations could detect were related with the minimum ionospheric rates that the simulation produced when considering ionospheric gradients with different parameters (Figure 4.6). In this way, it was possible to identify which of the simulated ionospheric gradients could be detected

depending on the performance of each of the stations.

As discussed in Section 3.3.1.3, one of the design parameters of the detection threshold is the probability of false alert. However, in the case of the network, it should be noted that a false alert at a given network station does not automatically lead to a loss of continuity but instead requires assuming the "worst-case" ionospheric threat model parameters on that area of the network. Thus, a false-alert probability (P_{fa}) of 10^{-6} was selected as an acceptable compromise for the tests with real measurements from Alaska. This value was chosen to avoid excessive false alerts due to the medium-high level of noise and multipath present in the data obtained from the network in Alaska (see Figure 3.4a of Chapter 3). Nevertheless, the selected P_{fa} is likely not optimal due to the limited data on which its selection was based, and the optimization of its value will be investigated as part of future work. Furthermore, both cycle slip detectors and the visual check explained in Section 3.3.1.1 were used to derive the detection thresholds.

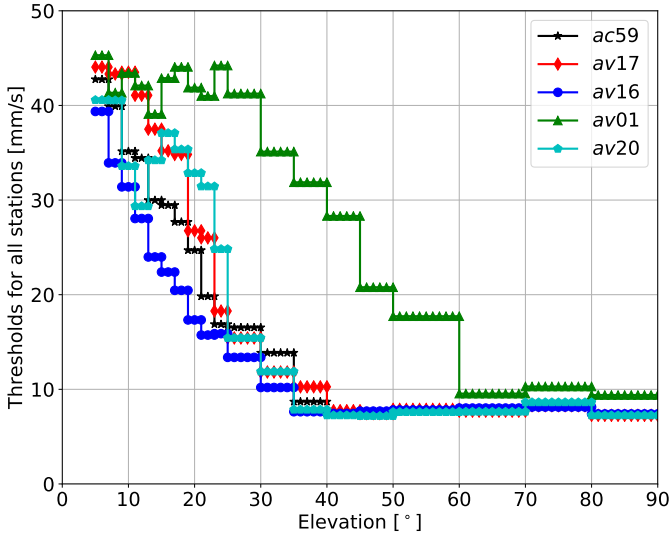

Figure 4.5: Detection thresholds for all stations considered in Alaska derived with the data specified in Section 4.1.1 and $P_{fa} = 10^{-6}$.

The detection thresholds depicted in Figure 4.5 show that all the stations of the network have similar performance with the exception of "av01", which has a higher threshold overall. This fact is translated into worse performance of station "av01" because the simulated ionospheric gradients have to generate higher ionospheric rates in order to be detected.

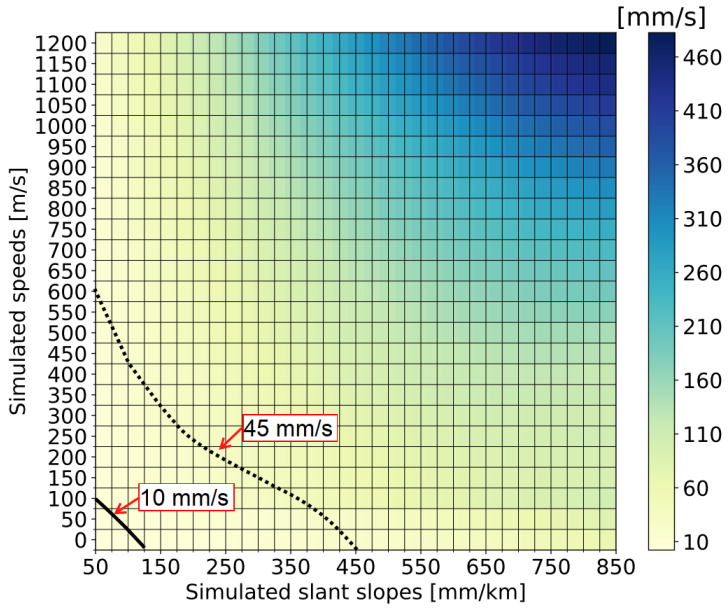

Figure 4.6: Minimum ionospheric slant rates generated by simulated ionospheric perturbations with different speeds and slant slopes that should be detected by the different stations of the network in Alaska.

However, it might happen that the characteristics of an ionospheric gradient or the propagation of the satellite being observed generates an ionospheric rate that is not high enough to trigger the detection thresholds. To illustrate this issue, Figure 4.6 shows the minimum ionospheric rate in millimeters per second that was generated by a gradient with a certain slope and a certain speed considering all GPS satellites, values of the rest of the parameters (width and direction), and times of occurrence of the gradient during the day. Note that the values shown in Figure 4.6 were calculated considering only the effects introduced by the synthetic gradients. That is, the noise, multipath, and nominal ionosphere present in the real nominal measurements on which these synthetic perturbations are simulated were not taken into account in this plot. The idea is to find the ideal performance that would be needed by the stations in order to have sufficient detectability of all simulated gradients.

Therefore, each pixel of Figure 4.6 contains the minimum ionospheric rate of the ionospheric rates generated by gradients of a certain speed (e.g. 900 m/s) and slant slopes varying between a value (e.g. 675 mm/km) and that same value plus 25 mm/km (e.g. 700 mm/km). As an example, the minimum ionospheric rate that was generated by a gradient of 900 m/s of speed and a slope between 675 mm/km and 700 mm/km was 260 mm/s (Figure 4.6).

This value is low in comparison to the rate that would be expected for such a large gradient, but it corresponds to a satellite that was moving almost perpendicularly with respect to the direction of propagation of the gradient. This means that the propagation of the satellite has also an impact on how the gradients are observed, and all velocities of satellite propagation must be taken into account to avoid integrity issues.

Hence, since the values shown in Figure 4.6 are the lowest rates (and thus test statistics) generated by the simulated gradients, if all stations in the network were able to detect these values, 100% detectability of gradients with those characteristics would be achieved. Still, from both Figures 4.5 and 4.6, it can be concluded that the detectability was not 100% for all simulated gradients.

Based on the simulations carried out, all stations presented 100% detectability for all gradients that produced ionospheric rates above 45 mm/s (see Figure 4.5) independently of the elevation of the satellite or speed and propagation characteristics of the IPPs. These were all simulated gradients above the black dashed curve in Figure 4.6. For all the other simulated gradients that fell below this curve, the probability of missed detection was larger than zero, and achieving 100% detectability depended highly on the performance of each of the stations in the network.

Thus, the following conclusion was drawn from the simulation results: there is a trade-off between the quality of the measurements of the monitoring stations and the detectability with sufficient probability of harmful gradients for GBAS. For example, all stations with exception of "av01" were able to detect 100% of the gradients that produced ionospheric rates above 10 mm/s with satellites above 35 degrees of elevation. This corresponds to all gradients above the black continuous curve in Figure 4.6. This means that if stations "ac59", "av17", "av16", and "av20" do not detect any gradients with satellites above 35 degrees of elevation, the probability that there is an anomalous ionospheric gradient above 100 mm/km of slope and 100 m/s of speed in the area that they supported is the same as the probability of missed detection of the network.

Nevertheless, as discussed in Section 3.3.2, calculating the probability of missed detection of each station in the network is complex. On the one hand, it is necessary to know the location of the GBAS station within the network coverage area. On the other hand, it is necessary to perform sufficient simulations with a representative number of parameter variations. Since there are no airports near the network used in Alaska, the study in this section has focused on finding out the performance that each station must have to detect the maximum number of gradients.

In Chapter 6, the probability of missed detection of each station and the

minimum detectable gradient for the network of stations selected for the equatorial region, which protects an area with several existing airports, are calculated.

4.3.2 Estimation

This section analyzes three different aspects of the network's estimation capability: (i) the estimation errors associated with the variation of each of the gradient parameters separately, (ii) the ability of the method to produce reliable estimates, and (iii) the real-time performance.

The results in this section are based on the simulation of the ideal threat model used in GBAS (perfectly linear fronts, constant speed, etc.). Therefore, the goal of this work is to study the possible errors due to the approximations and assumptions used for the calculation of the gradient parameters by isolating the different sources of errors. The adaptation of the method for real (actually observed) gradient measurements and its limitations due to the more complex characteristics of real gradients are explained in Section 4.4.

Future work will address the study of gradient parameter estimation errors with more complex threat models (e.g., the size and speed of the gradients change with time).

4.3.2.1 Gradient parameter estimation errors

This section presents the results corresponding to the calculation of the estimation errors with the variation of each of the gradient parameters separately.

Table 4.4 shows the summarized mean and maximum estimation errors (maximum positive and maximum negative) computed once the algorithm converged as described in Equation 3.29. Each row of Table 4.4 considers the change of one of the parameters among the values in Table 4.3 while maintaining all other parameters constant at values for which the simulation performed well. These values were: 100 m/s for the speed, 180 degrees for the direction (propagation from North to South), 100 km for the width, and 200 mm/km for the vertical slope. The idea behind is to study the impact of the change of one of the parameters on the estimation error of all the other parameters. As an example, the first row of Table 4.4 presents the mean and maximum estimation errors of all the gradient parameters when changing only the speed of the gradient from 0 m/s to 1200 m/s. However, the case of the slope is "special" since, although the fixed slope in the vertical domain is 200 mm/km, the slopes in the slant domain depend on satellite elevation and therefore also vary in each simulation. Note that, in the simulations carried out in this section, the "worst-case" parameter combination that gives the worst estimation error may not be

found. These simulations in which all gradient parameters were varied at the same time to find the "worst-case" estimation errors were carried out for the next section in order to calculate reliable bounds of the estimated parameters.

The results in Table 4.4 show that the errors in the columns "Mean" stayed with a very low value for all the gradient parameters with the exception of the slope determination. Thus, the algorithm in general appears to work well under the simulation conditions examined. The particular case of the slope is further discussed in the subsection 4.3.2.1.2.

Gradient parameters	**Estimation error**							
	Speed $[m/s]$		**Direction** [°]		**Slant slope** $[mm/km]$		**Width** $[km]$	
	Mean	**Max.**	**Mean**	**Max.**	**Mean**	**Max.**	**Mean**	**Max.**
Change of speed	-1.3	174.2 -135.6	-0.1	15.6 -20.3	14.7	139.7 -30.3	-0.3	10.5 -11.0
Change of direction	-0.5	7.6 -12.0	0.0	7.7 -6.6	33.3	122.6 -8.7	-0.5	2.1 -5.9
Change of slope	0.1	24.1 -21.3	-0.1	9.5 -9.5	30.9	134.1 -29.2	-0.2	10.0 -9.8
Change of width	-0.2	14.9 -14.7	-0.1	9.7 -17.1	32.7	138.3 -10.9	-0.3	4.7 -5.6

Table 4.4: Absolute gradient parameter estimation errors in Alaska.

Gradient parameters	**Maximum relative estimation errors**			
	Speed [%]	**Direction** [%]	**Slant slope** [%]	**Width** [%]
Change of speed	14.5 (1200 m/s) -11.3 (1200 m/s)	8.7 -11.3	37.4 (203.0 mm/km) -6.1 (425.0 mm/km)	10.5 -11.0
Change of direction	7.6 -12.0	4.3 (180°) -3.7 (180°)	28.8 (220.1 mm/km) -2.0 (425.0 mm/km)	2.1 -5.9
Change of slope	24.1 -21.3	5.3 -5.3	55.4 (125.4 mm/km) -9.8 (205.3 mm/km)	10.0 -9.8
Change of width	14.9 -14.7	5.4 -9.5	36.5 (217.8 mm/km) -1.6 (315.0 mm/km)	4.7 (100 km) -7.0 (60 km)

Table 4.5: Maximum relative gradient parameter estimation errors of the network in Alaska. The values specified in brackets represent the simulated values. For the cells where the simulated value is not specified, the simulated values were: 100 m/s for the speed, 180 degrees for the direction, and 100 km for the width.

Since the different errors in Table 4.4 are expressed in different units, Table 4.5 shows the maximum relative errors as well. In the cases where the parameters changed, the simulated value was clarified in brackets because the maximum absolute estimation errors from Table 4.4 do not necessarily correspond to the values of the maximum relative estimation errors (e.g. the 55.4% of 125.4 mm/km results in an absolute error of 69.5 mm/km instead of the 134.1 mm/km of Table 4.4).

Considering the overall results from Table 4.4 and Table 4.5, the following conclusions were drawn:

1. The greatest impact on the maximum estimation errors for all the parameters was due to the change of the speed (first row in Tables 4.4 and 4.5), and the change of the slant slope (third row in Tables 4.4 and 4.5). In the case of the change in slope, the estimation errors corresponded to cases where the generated ionospheric rates were close to the detection thresholds. In these cases, the test statistics rose above and fell below the detection thresholds several times during the duration of the gradient, resulting in only parts of the gradient being detected. This especially impacted the speed and width estimation. The case of changing the speed parameter is further discussed in the subsection 4.3.2.1.1.

2. The maximum errors for the estimation of the slope were high for the change of each of the gradient parameters (sixth column in Table 4.4 and third column in Table 4.5). This point is further discussed in the subsection 4.3.2.1.2.

3. The maximum estimation errors for the direction and the width parameters were lower than for the speed and the slope and presented comparable values for all changes of the gradient parameters.

4. The change of the direction and the width parameters did not present any impact on the estimation errors.

In the following subsections, the speed and the slope estimation errors are studied in detail.

4.3.2.1.1 Speed estimation error

As commented previously, one of the greatest impacts on the speed estimation errors was the change of the speed itself. For a direction of the gradient that is not aligned with all or most of the stations on ground, which should not occur if the network was designed for the purpose of estimating the gradient parameters, this mainly has two reasons: (i) the alignment of the IPPs due to low elevation satellites (bad geometries), and (ii) an insufficient time

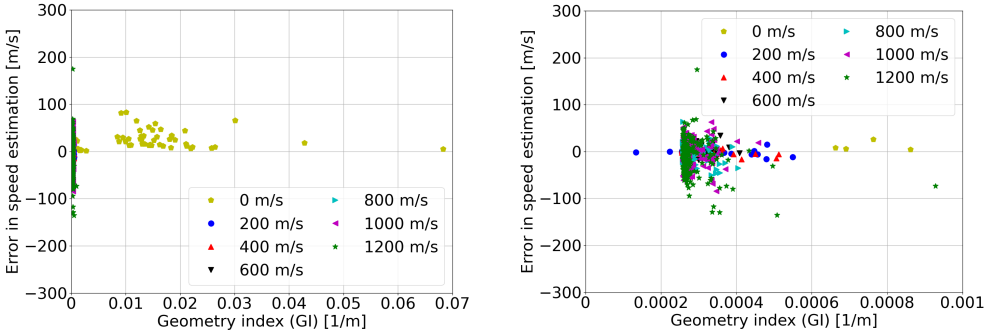

(a) Speed estimation error for all GI values (between 0 and 7×10^{-2}).

(b) Speed estimation error for GI values between 0 and 1×10^{-3}.

Figure 4.7: Absolute error in speed estimation over Geometry Index for different simulated speeds of the gradient. Each marker represents a simulated speed and each point the GI calculated at the moment of the estimation.

resolution ($\Delta T = 1$ s) that can cause appreciable errors in the detection and cross-correlation steps.

To study the impact of the IPP geometries on the estimation of the gradient parameters, the GIs introduced in Equation 3.25 are computed. As explained in Section 3.3.4, this GI can give an idea of the suitability of the IPP geometry at the moment of calculating the gradient parameters. The higher GI gets, the worse is the IPP geometry.

Figure 4.7 shows the absolute estimation error in speed versus the GI to evaluate the influence of the IPP geometry in the estimated errors. In Figure 4.7a, it can be observed that for a static gradient (i.e. speed of 0 m/s), the GI got much higher than for the rest of the speeds. This was because, when the gradient was static, all IPPs detected the gradient along the wave-front and were, therefore, aligned. Thus, in order to avoid estimation errors, IPP clusters whose GI was greater than 1×10^{-3} were excluded. Figure 4.7b shows that for the rest of the considered speeds of the gradient, the GI stayed between 2×10^{-4} and 4×10^{-4} in most cases. These values stayed within the limits for suitable IPP geometries. Moreover, the largest absolute speed estimation errors corresponded to the highest simulated speeds (green stars in Figure 4.7) while presenting average GIs. Therefore, the majority of these errors can be associated with the time resolution problem.

Regarding the impact of the time resolution, Figure 4.8a shows the mean (blue circles) and maximum speed estimation errors (up red triangles and down black triangles) when changing the simulated speeds of the gradient. As can be observed, the mean estimation errors stayed low, and only a slight change for

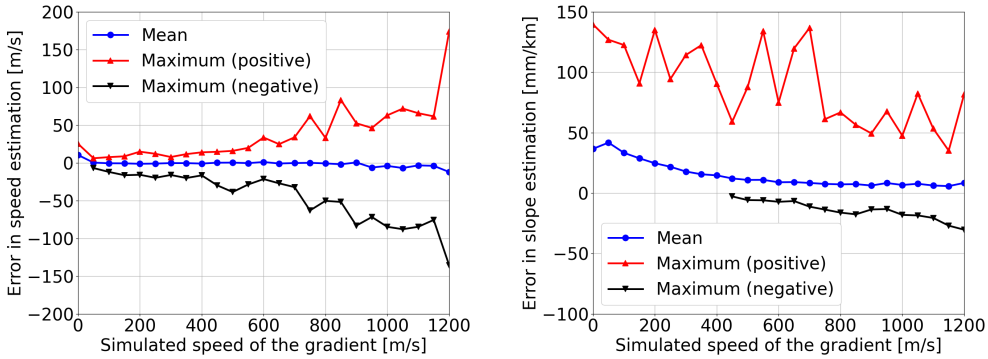

(a) Speed estimation error. **(b)** Slant slope estimation error.

Figure 4.8: Mean (blue circles), maximum positive (red up triangles) and maximum negative (black down triangles) values for absolute speed and slant slope estimation errors with respect to the simulated speed of the gradient.

speeds of 0 m/s (the gradient is not moving) and 1200 m/s are noticed. Note that, in the case that the gradient does not move, the model used in Equation 3.16 could theoretically not be used (if $\boldsymbol{v} = 0$, $\boldsymbol{s} = \infty$). However, in practice, the IPPs moved and detected the simulated ionospheric gradients, which provided the inputs to the real-time cross-correlation algorithm. Therefore, in this case, these results were obtained due to the time resolution of the measurements, which resulted in the ionospheric perturbations not being detected exactly when they occurred, and due to the geometrical approximations used: (i) to calculate the IPP locations at the perturbation plane in the simulations (see Appendix A), and (ii) to solve the Equations 3.15 to 3.22. Thus, the case of the ionospheric perturbation moving at a speed of 0 m/s was equivalent to the case of an ionospheric perturbation moving at very low speeds. In the case of the gradient moving at very high speeds, the time resolution problem became more evident. In this case, the detection was also not triggered exactly when it happened and it could have been delayed up to $\Delta T = 1$ s, which in this case could mean up to 1200 meters of error. Since some of the stations in the considered network ("av01", "av16", "av17", and "av20") are very close together (around 5 km), this can translate into large speed estimation errors. In the case of the maximum errors, this behavior was more evident, and the more the speed of the gradient was increased, the worse the estimation got. This means that in order to lower the errors in speed estimation, a sampling rate adapted to the usual speeds of the ionospheric perturbations in the area under study is needed. This improvement in speed estimation can be seen in the results with real anomalous ionospheric gradients (Sections 4.4.2.1 and 4.4.2.2), where significantly smaller errors are obtained when using interpolated data at 10 Hz than when using measurements at 1 Hz.

4.3.2.1.2 Slant slope estimation error

In the case of the slope or spatial gradient magnitude, one factor that influences both the mean and the maximum errors is that the true slope is considered to be only the one generated by the simulator (i.e. the synthetic gradient). This means that the nominal ionosphere on top of which these synthetic gradients are simulated was not considered as part of the ground truth since it was not possible to separate it from the multipath and noise coming from the real measurements. However, the "nominal" ionospheric gradients present in the measurements represented a small part of the ionospheric rates used as test statistics.

The largest impact on the slope estimation was the one caused by phase noise and multipath when calculating the ionospheric rates every second (upper part of Equation 3.26). Figure 4.8b depicts this effect with respect to the change of the speed. As can be observed, the maximum values became large due to the fact that the test statistics were noisy and the fact that their values were divided by small relative speeds between the gradient and the IPPs. However, the more the speed of the gradient was increased, the more this error was smoothed by dividing by larger relative speeds. The problem in this case was that the slope of the gradient (for speeds above 450 m/s) could be underestimated since the obtained error in slant slope got up to a -25 mm/km error (a 6.1% of the simulated value). The following section considers this issue and derives an uncertainty model for the estimated gradient parameters.

4.3.2.2 Uncertainty model of the estimated gradient parameters

Section 3.3.4.4 described a methodology to derive an uncertainty model for the estimated gradient parameters. The idea behind is to transmit to the GBAS stations an overbounded estimate of the gradient parameters using the derived uncertainty model instead of the estimate itself, which, as commented in the previous section, contains errors.

This section presents the uncertainty model derived for the gradient slant slope estimated with the measurements from the network of stations in Alaska. The derivation of the uncertainty model for the other gradient parameters would be carried out in an analogous way.

Figure 4.9 shows with blue stars the absolute slant slope estimation errors considering the variation of all gradient parameters in the ranges described in Table 4.3. As described in Section 3.3.4.4, the first step in deriving the uncertainty model is to order the estimation errors in bins to calculate the statistics. The selected bin size depends on the data; it must be large enough to contain enough samples to compute the statistics, but small enough not to mix

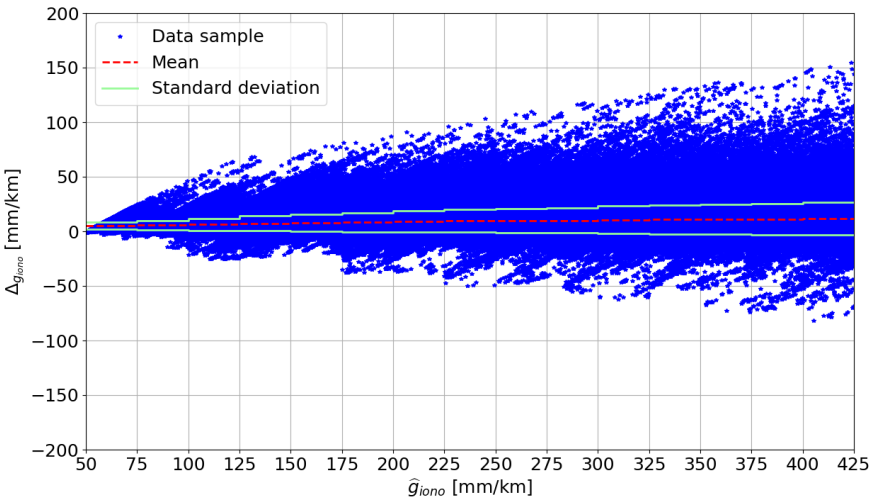

Figure 4.9: Absolute slant slope estimation errors versus estimated slant slope. The blue starts represent the slant slope estimation errors, the red dashed line represents the mean value per bin, and the solid light green lines represent the standard deviation per bin.

values that are too different from each other. Figure 4.9 suggests that a bin size of 25 mm/km in slant slope is adequate to perform these statistics since, within this bin size, the negative errors (underestimation of the gradient) were similar.

However, it should be noted that since the slopes were simulated in the vertical domain, the first bins (e.g., 50 mm/km to 75 mm/km) contained fewer samples than the rest of the bins. This was because only high elevation satellites were able to generate low slant slopes, as the low elevation satellites experienced slant slopes that were steeper than the simulated vertical ones due to the value of the obliquity factor in Equation 2.23.

In addition, Figure 4.9 shows with a dashed red line the mean value per bin and with solid light green lines the standard deviation per bin. It can be seen that, although the values of the estimation errors were high, this was only the case for few samples, as the values of the mean and standard deviation were low. Furthermore, the mean values were positive but close to zero for all bins of estimated slant slope. This means that there were slightly more samples with positive errors than with negative errors. Thus, underestimates were about as likely as overestimates.

Once the samples of the estimation errors had been sorted into their corresponding bins, they were normalized by subtracting from each sample the mean value of the bin it belonged to and by dividing the resulting value by the

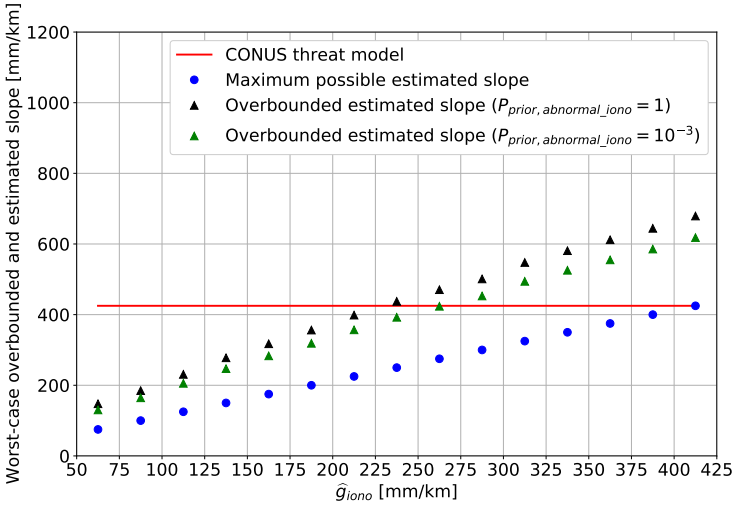

Figure 4.10: Worst case estimated and overbounded gradient slant slopes in comparison to CONUS threat model (solid red line). Blue dots (situated in a straight line) represent the maximum possible estimated slope inside each data bin, black triangles represent the worst case overbounded slope in each bin, and green triangles represent the overbounded slopes in each bin when a prior probability of occurrence of an ionospheric gradient of 1×10^{-3} is assumed.

standard deviation of the bin. Then, the tails of the entire distribution were overbounded following the process explained in Section 3.3.4.4.

Figures 3.15 and 3.16 from Chapter 3 present the normalized distribution and the Gaussian tail overbounding process for all data bins respectively. As can be observed in Figure 3.15, the number of samples in the first three data bins was lower than in the rest of the data bins as commented previously due to the way in which the gradients were simulated.

Figure 3.16 shows that the distribution was not symmetric because the gradients were typically overestimated and, in fewer cases, they were underestimated. Overestimation typically occurred when the gradients moved at low speeds and were estimated with satellites at all elevations. However, the error was always lower when high elevation satellites estimated the gradient parameters because their corresponding IPPs moved slower and their geometry was better (GI lower). Underestimation typically occurred due to fast traveling gradients that were estimated by low elevation satellites, which resulted in the combination of the two worst sources of error due to the time resolution problem. The overall inflation factor calculated was $I_{g_{iono}} = 2.26$.

Finally, Figure 4.10 shows with blue dots (situated in a straight line) the

estimated maximum value that could occur inside each bin (e.g., 75 mm/km for the bin 50 - 75 mm/km depicted in the center of the bin), and with black triangles the overbounded value considering Equation 3.31. In addition, it shows with green triangles the overbounded value if instead of assuming a Probability of Non-bounded Errors of 1×10^{-8} (see Section 3.3.4.4), a value of 1×10^{-5} is assumed considering a prior probability of occurrence of an anomalous ionospheric gradient of 1×10^{-3} as in [28, 36]. As can be seen, up to a gradient slope of 225 mm/km for the most conservative case (no prior probability considered), and 275 mm/km when assuming a prior probability, a benefit would be obtained from this methodology. Above those values, the overbounded slant slopes would be higher than the CONUS threat model, which is assumed to be valid for Alaska, and in this case, the threat model as it is would be used instead. Note that, if for a network designed for the purpose of detecting and estimating these gradients, gradient estimates higher than the threat model were obtained, the data and the threat model should be carefully reviewed. This should be done to ensure that this has occurred due to estimation errors and not due to gradients occurring that are larger than the current threat models. If this was the case, the threat model should be updated.

4.3.2.3 Real-time performance of the monitor

Finally, this section analyzes the real time capability of the methodology. Figure 4.11a shows an example of the absolute values of the $Itest_r^{G03}(t)$ calculated for all stations considered, the actual geometry of satellite G03 on day 73 of year 2015, and a gradient with the following characteristics: 200 mm/km of vertical slope, 100 m/s of speed, 100 km of width, and moving in the southward direction. Here, the test statistic values were noisy, and when the algorithm applied the cross-correlation in real-time considering the first station that detected the gradient, "ac59", as reference, at the beginning, it only found noise. Therefore, the algorithm in real time needed a certain time to converge, as explained in Section 3.3.4.1.1.

Figure 4.11b presents the cross-correlation coefficients for the example depicted in Figure 4.11a. As can be observed, the algorithm needed at least 100 seconds to satisfy the convergence condition presented in Equation 3.13. As explained in Section 3.4, these necessary waiting times for the convergence of the algorithm are considered by the network when calculating the "worst-case" real-time gradients that are transmitted to the GBAS stations; during the times when the algorithm does not converge, the network warns the protected GBAS stations to use the conservative threat model.

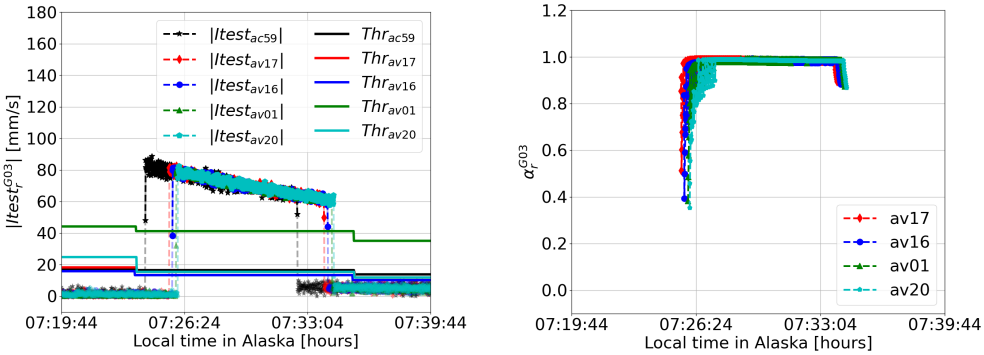

(a) Test statistics and detection thresholds.

(b) Cross-correlation coefficients.

Figure 4.11: Example of simulation test statistics and cross-correlation coefficients for satellite G03, day 73 of year 2015, and the network of stations in Alaska. The horizontal solid lines in Figure 4.11a represent the detection thresholds for the depicted epochs. The highlighted (non-transparent) markers represent the times when the simulated perturbations were detected.

4.4 Evaluation of the monitor with a real ionospheric gradient

This section evaluates the methodology with a real anomalous ionospheric gradient measured by the network in Alaska. The selected real gradient was experienced simultaneously by satellites G03, G14, and G32, and the stations in the network under study on day 76 of year 2015, i.e. during the St. Patrick's Day Storm. Figure 4.12 shows the slant ionospheric delays belonging to the anomalous ionospheric gradient studied for the different satellites and station "av17". As can be observed, it was a small ionospheric perturbation that grew quickly for all satellites.

Figure 4.13 shows the slant ionospheric delays calculated for the remaining visible satellites and one of the stations under study, "av17". From the rest of the satellites in view, only G17 experienced an anomalous ionospheric gradient detected by the network during the same time period. However, this was another gradient, different from the perturbation that affected satellites G03, G14, and G32, because the IPPs belonging to this satellite and the different stations were far from the other IPPs observing the same disturbance.

4.4.1 Detection

Figure 4.14a shows the slant ionospheric delays for all the considered stations and satellite G03, which had a mean elevation of 55° during the local times depicted. Figure 4.14b shows the absolute value of the test statistics for

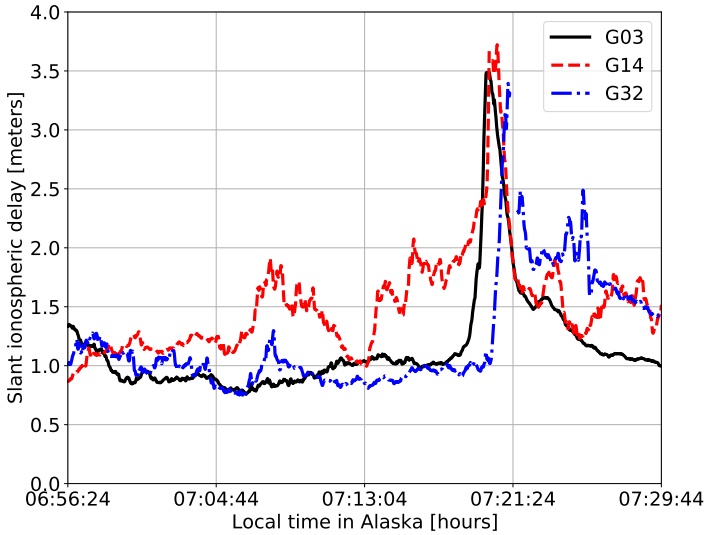

Figure 4.12: Slant ionospheric delays for the studied anomalous ionospheric real gradient experienced simultaneously by satellites G03, G14, and G32 on day 76 of year 2015 in Alaska.

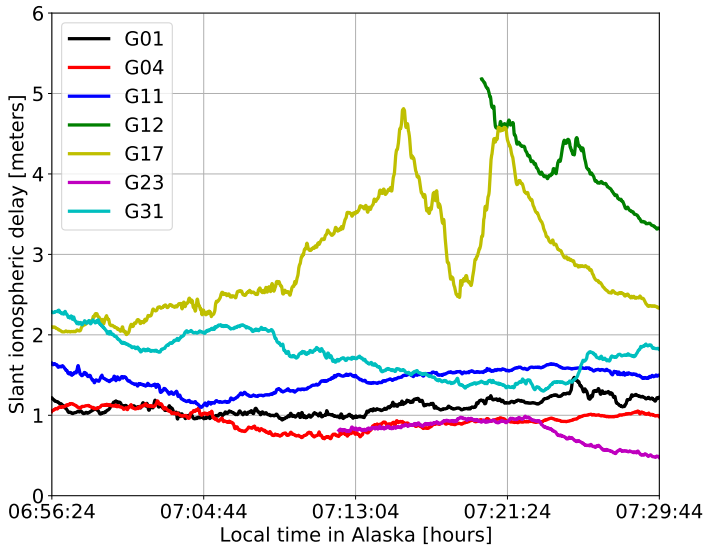

Figure 4.13: Slant ionospheric delays for the remaining visible satellites and station "av17" during the local times under study in Figure 4.12.

the same satellite, $Itest_r^{G03}(t)$, and the detection thresholds. In Figure 4.14b, Thr_{ac59}, Thr_{av17}, and Thr_{av16} have the same values as Thr_{ac20}. In both figures, the highlighted (i.e. non-transparent) respective markers represent the epochs where the gradient was detected (i.e. when the ionospheric rates are

above the detection thresholds of the corresponding stations, which are represented by separate horizontal lines). As can be observed, the detected gradients coincided with the steepest slopes in the slant ionospheric delays. Thus, the gradients were adequately detected by the algorithm. However, there were also detections prior to the steepest individual gradient slopes in Figure 4.14a, which belonged to the gradient itself. Since these first detections occurred at the beginning of the gradient, when it was still small in size, the test statistics did not continuously exceed the threshold. In fact, it can be seen that this issue broke the detected gradient into several parts.

From the detection point of view, this was not a problem since the algorithm detected the part of the signal that was not nominal. However, the estimation part of the algorithm, which was designed based on the behavior observed in the simulations, only considers continuous signal spans of more than a certain number of samples as an anomalous gradient. Since in Alaska the gradients were accompanied by rapid oscillations of the signal, their behavior was only similar to the simulation (Figure 4.11) once the gradient had grown sufficiently large. Section 4.4.2 presents in more detail the results of the estimation and the solution to this potential problem.

Figure 4.15a shows the slant ionospheric delays for all considered stations and satellite G14, which had a mean elevation of 34° during the local times depicted. Figure 4.15b shows the absolute value of the test statistics for the same satellite, $Itest_r^{G14}(t)$, and the detection thresholds. Here, the detected gradients also coincided with the steepest slopes in the slant ionospheric delays. Thus, the gradients were adequately detected by the algorithm. Moreover, there were also detections prior to the steepest individual gradient slopes in Figure 4.15a. However, in this case, this occurred at all stations except "av01". In addition, the gradient was divided into more parts than for satellite G03. This is because this satellite was at a lower elevation, and thus the thresholds were higher. This created a situation where more parts of the gradient, especially for the station with the worst performance, were not detected. Furthermore, the gradient was not measured completely, since the signals were lost at all stations after 07:20:07 local time.

Finally, Figure 4.16a shows the slant ionospheric delays for all the considered stations and satellite G32, which had a mean elevation of 72° during the local times depicted. Figure 4.16b shows the absolute values of the test statistics for the same satellite, $Itest_r^{G32}(t)$, and the detection thresholds. In this case, the algorithm detected the gradient practically continuously for all stations, since the satellite was at a higher elevation and the thresholds were lower.

It should be noted that, if the monitoring stations have poor performance and their thresholds are high, some anomalous gradients could remain undetected. However, this does not imply an integrity issue for the GBAS stations

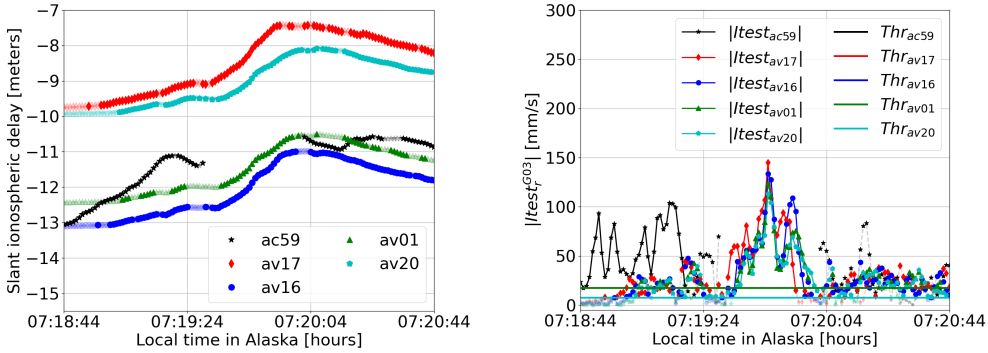

(a) Slant ionospheric delays. **(b)** Test statistics.

Figure 4.14: Slant ionospheric delays and test statistics for the studied anomalous ionospheric gradient experienced by satellite G03 (day 76 of year 2015, Alaska). The highlighted (non-transparent) markers in both figures represent the times when the ionospheric perturbation was detected. The horizontal solid lines in Figure 4.14b represent the detection thresholds for the depicted epochs. The solid lines with the markers in 4.14b represent the times when the gradient was considered for the estimation process for each station.

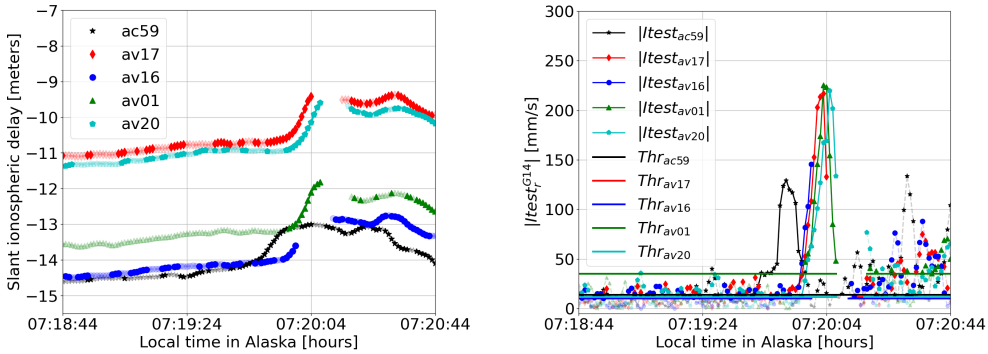

(a) Slant ionospheric delays. **(b)** Test statistics.

Figure 4.15: Slant ionospheric delays and test statistics for the studied anomalous ionospheric gradient experienced by satellite G14 (day 76 of year 2015, Alaska). The highlighted (non-transparent) markers in both figures represent the times when the ionospheric perturbation was detected. The horizontal solid lines in Figure 4.15b represent the detection thresholds for the depicted epochs. The solid lines with the markers in 4.15b represent the times when the gradient was considered for the estimation process for each station.

supported by the network. If a monitoring station does not detect any gradients, it does not automatically assume nominal conditions, but instead it considers that there might be a gradient present that is equal to its minimum detectable gradient (introduced in Section 3.3.2). In this way, the network

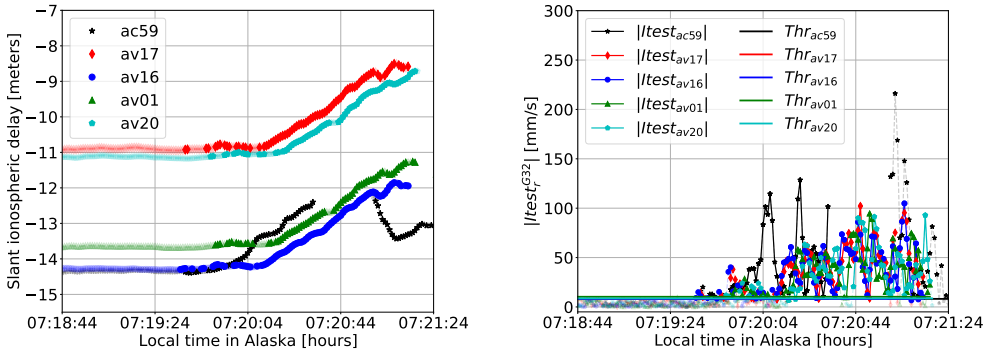

(a) Slant ionospheric delays. **(b)** Test statistics.

Figure 4.16: Slant ionospheric delays and test statistics for the studied anomalous ionospheric gradient experienced by satellite G32 (day 76 of year 2015, Alaska). The highlighted (non-transparent) markers in both figures represent the times when the ionospheric perturbation was detected. The horizontal solid lines in Figure 4.16b represent the detection thresholds for the depicted epochs. The solid lines with the markers in 4.16b represent the times when the gradient was considered for the estimation process for each station.

ensures that the supported GBAS stations are always considering the largest undetectable gradient that could be affecting them.

4.4.2 Estimation of the gradient parameters

Figures 4.14a, 4.15a, and 4.16a show that the anomalous ionospheric gradient presented a similar shape when being measured by all affected stations and the same satellite. However, the test statistics suggest that the gradient changed during its propagation; it was narrower and steeper when it reached the last stations impacted by it for satellites G03 and G14, and less steep and wider for satellite G32. This implies that the previous assumption of a non-changing ionospheric gradient held for the closest stations and did not hold only for the farthest station, which was located beyond the correlation distance of the ionospheric perturbation. As commented in Chapter 3, this assumption was used to simplify the analysis of the problem, and its applicability to real gradients is established through the cross-correlation coefficients used in Equation 3.20 (one of the steps to calculate the gradient speed). Detection information from stations where the measured gradient has changed insignificantly in its propagation from one station to another get significantly more weight in Equation 3.20 than the others, minimizing the errors due to this assumption. In addition, this methodology adds more requirements for the choice of the reference station (i.e., station with respect to which the cross-correlation coefficients are calculated) when it is applied to real gradients (refer to Section 4.4.2.1).

The algorithm was able to estimate the gradient parameters in real time for satellite G03. Section 4.4.2.1 explains in detail the results for satellite G03 in post-processing, and Section 4.4.2.2 presents the results for the same satellite in real time. Section 4.4.2.3 presents the results for satellites G14 and G32.

4.4.2.1 Estimation of the gradient parameters in post-processing with satellite G03

The first step of the algorithm searched for the station of reference. In the case of satellite G03, the algorithm assumed as the station of reference the first station impacted by the gradient ("ac59"). However, as can be observed in Figure 4.14b, the shape of $\left|Itest_{ac59}^{G03}\right|$ (black stars) was different from all the other test statistics. Thus, the cross-correlation coefficients calculated with respect to this station resulted in lower values, below 0.5 with the exception of station "av17", and quite different from the other correlation values, but they were still significantly above zero.

Reference station	α_{ac59}^{G03}	α_{av17}^{G03}	α_{av16}^{G03}	α_{av01}^{G03}	α_{av20}^{G03}
ac59	1.000	0.518	0.379	0.467	0.397
av17	0.518	1.000	0.820	0.686	0.720
av16	0.379	0.820	1.000	0.924	0.903
av01	0.467	0.686	0.924	1.000	0.926
av20	0.397	0.720	0.903	0.926	1.000

Table 4.6: Cross-correlation coefficients calculated in post-processing for satellite G03 considering the different stations in Alaska as reference.

This issue can be seen in Table 4.6, which shows the cross-correlation coefficients calculated in post-processing considering as reference each of the different stations in the network. The stations in Table 4.6 appear in the order they detected the real ionospheric gradient.

Therefore, it was necessary to adapt the requirements for better selection of the reference stations. For the case of Alaska, instead of searching only for the first impacted station, the algorithm searched for the first impacted station whose test statistic had a cross-correlation greater than 0.9 with the test statistics of at least two other stations in the network. A cross-correlation coefficient of 1 between the test statistics computed at two different stations would mean that the perturbation is the same, but delayed by a certain time interval, as stated in Section 3.3.4.1.1. However, since the actual anomalous gradients were not ideal, that value was lowered to 0.9 to allow enough margin for the algorithm to find the station considered as "reference". This strategy has been

also used for the real anomalous ionospheric gradient studied in Chapter 5.

Moreover, the values for the N_W and N_B parameters introduced in Section 3.3.4.1.1 were selected to adapt the general algorithm to this data set (Alaska). The values for these parameters adapted to the data set from Brazil (Chapter 5) are different. The first parameter, N_W, refers to the time window designed to capture the part of the test statistic that starts to increase when the gradient begins but is still below the detection threshold. The parameter N_W was selected to be 30 seconds to capture all parts of the gradient in Figure 4.14a plus margin. The second parameter, N_B, refers to the total size of the buffers considered for calculating the cross-correlation. The parameter N_B was selected to be at least 50 seconds to consider both N_W and a minimum duration of an anomalous gradient of 20 seconds. Therefore, Figures 4.14b and 4.16b present with solid lines the test statistics corresponding to the parts of the signal where the test statistics were above the threshold for at least 20 seconds. Figure 4.15b also presents with solid lines the test statistics corresponding to the anomalous gradient, but since the signal was lost and its duration was shorter than 20 seconds, these times were selected manually and not by the algorithm. Note that the value selected for N_B is the minimum and, if more samples of the gradient were available (test statistics above the threshold), the value of N_B would be higher.

According to Table 4.6, the algorithm considered station "av16" as the reference. However, it still kept the information from all past stations, since it applies weighting according to the cross-correlation coefficients (see Equation 3.20). In this process, the algorithm excluded the information coming from stations with a cross-correlation coefficient below 0.5, i.e. α_{min} in Section 3.3.4.1.1. As explained in Section 3.3.4.1.1, below this cross-correlation value, the ionospheric gradient should not be considered the same, and the inclusion of this information could make the estimation of the gradient parameters worse.

Thus, assuming station "av16" as reference, this section initially calculated the gradient parameters measured by satellite G03 in post-processing to get the best estimation possible. Then, the post-processing results were compared with the ones obtained in real-time to evaluate the feasibility of the real-time concept.

Since the gradient under study propagated with a high speed, as could be already observed in Figure 4.14, where three of the stations detected it almost at the same time, the algorithm used a spline interpolation of the data at 10 Hz. In this way, by assuming continuity of the slant ionospheric delays, a higher temporal resolution could be obtained and better accuracy was achieved in the post-processing results for a better comparison with the real-time results at 1 Hz sampling rate.

Table 4.7 summarizes the results in post-processing. The ionospheric gradient measured was a short-duration perturbation that traveled with an estimated direction of 203.3° (from northeast to southwest), a high speed, 2473.3 m/s, and not a very steep slope, up to 55.8 mm/km. These results are compatible with a propagation of the perturbation following the magnetic field lines that in this region have a declination of 15° ($180° + 15° = 195°$) and also agree with the short time delays calculated between the stations. Moreover, the slant slope and width estimations indicated that the high values of the test statistics in Figure 4.14 can be attributed more to the high speed of the gradient than to its size. These kinds of ionospheric perturbations, local and generated in the auroral region, are often the source of LSTIDs at mid-latitudes [76, 77].

Station	v_{iono}^{G03} $[m/s]$	d_{iono}^{G03} [°]	g_{iono}^{G03} $[mm/km]$	w_{iono}^{G03} $[km]$	α_r^{G03} $[-]$	κ_r^{G03} $[s]$	GI $[1/m]$
ac59 (Not used)	-	-	-	-	0.379	-36.6	-
av17	2473.3	203.3	55.8	59.4	0.820	-1.5	2.73×10^{-4}
av16 (Ref.)	2473.3	203.3	54.4	71.7	1.000	0.0	2.73×10^{-4}
av01	2473.3	203.3	49.8	69.3	0.924	0.3	2.73×10^{-4}
av20	2473.3	203.3	46.5	69.8	0.903	0.5	2.73×10^{-4}

Table 4.7: Estimated real gradient parameters in post-processing for satellite G03 and Alaska.

4.4.2.2 Estimation of the gradient parameters in real time with satellite G03

Applying the algorithm in real time with the data recorded at 1 Hz presents the same limitations as in the simulation: it is necessary to wait for convergence of the cross-correlation and to have sufficient time resolution.

Figure 4.17a shows the first limitation, where the convergence requirement (Equation 3.13) was not met until 07:19:56 (local time). Moreover, once the algorithm converged, it generated time delays of 0 seconds for two of the stations ("av01" and "av20" in Figure 4.17b) because the time resolution was insufficient. These limitations are also recognizable in the estimation of the speed in real time (Figure 4.18a), where the algorithm got high errors when it did not converge and no output when the time resolution was insufficient. Note that the algorithm would not use the values of the time delays before convergence. Therefore, Figure 4.18a shows the speed estimations before convergence of the algorithm for better understanding only.

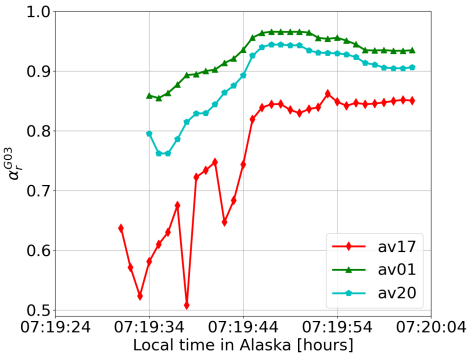

(a) Cross-correlation coefficients.

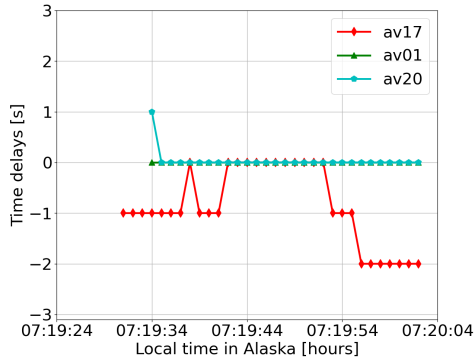

(b) Time delays.

Figure 4.17: Cross-correlation coefficients and time delays calculated in real-time for the test statistics depicted in Figure 4.14b considering as station of reference "av16".

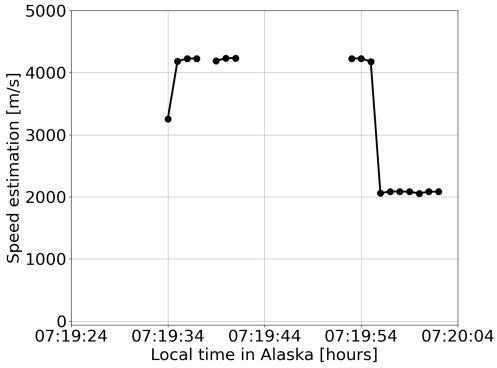

(a) Estimated speed of the gradient.

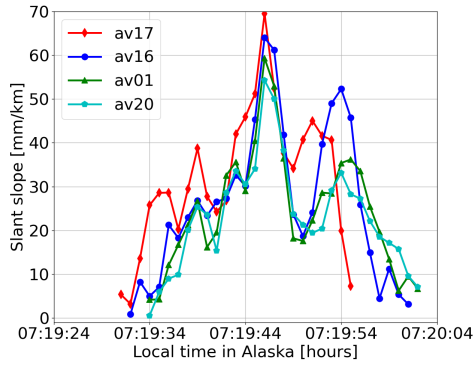

(b) Estimated slant slope of the gradient.

Figure 4.18: Estimated speed and slant slope in real time of the real gradient depicted in Figure 4.14a. The estimated slope of the gradient was estimated using the speed estimation after convergence.

After 23 seconds of continuous tracking by all stations in the network, the algorithm converged, and it had enough resolution to output results comparable to the post-processed results, 2083.9 m/s for the speed estimation and 212.9° for the direction.

Finally, the slant slope and width parameters were estimated. In the case of slope determination, two possibilities were considered. The first possibility was calculating it in real time. However, the maximum slant slope found was 34.6 mm/km, because the "worst-case" gradient occurred before the algorithm converged. The second possibility was recomputing the slope backwards to find the "worst-case" that could be transmitted to the GBAS stations. Figure 4.18b depicts this second solution. Here, the slant slope estimations were higher than

in Table 4.7 because the speed estimation used (2083.9 m/s) was lower. Thus, the same ionospheric rate was attributed to higher slopes.

The results for the estimation of the width parameter, which was determined after the gradient finished affecting all stations and based only on the continuous part of the signal considered as the gradient, were: 50.0 km for "av17", 60.4 km for "av16", 58.3 km for "av01", and 58.4 km for "av20". In this case, the width was shorter than in the post-processed results because the estimation of the speed was lower. Thus, the same time duration of the gradient T_W in Equation 3.28 was attributed to a shorter width.

4.4.2.3 Estimation of the gradient parameters with satellites G14 and G32

In the case of satellite G14, as can be seen in Figure 4.15, the signals were lost a few seconds after the start of the gradient. For this reason, the algorithm did not consider initially the gradient experienced by this satellite for the estimation process since its duration was less than 20 seconds. Therefore, in order to compare the results of the different satellites, the samples related to this gradient were introduced into the algorithm manually.

The reference station selected for satellite G14 was "av17" because the cross-correlation coefficients of stations "ac59" and "av16", the first two stations to detect the gradient, with all the other stations was less than 0.9. The parameters estimated in real time after convergence of the algorithm were: 2274.5 m/s of speed and 128.76° of direction (from northwest to southeast). The slopes of the gradient were: 143.4 mm/km, 138.1 mm/km, and 139.9 mm/km for stations "av01", "av17" and "av20" respectively. Finally, the estimated widths were 14.1 km for the three stations "av01", "av17", and "av20" because only the parts highlighted with solid lines in Figure 4.15b were taken into account. Note that stations "ac59" and "av16" were not used for the estimation process.

Therefore, the gradient experienced by this satellite had a steeper slope than the gradient experienced by satellite G03, which is consistent because satellite G14 was at a lower elevation. The speed estimation is also consistent with that estimated by the satellite G03. However, the direction parameter experienced a larger variation when estimated by the different satellites, although both satellites agreed in that the gradient moved from north to south. The error in the direction estimation was due to a combination of two factors: on the one hand, the low temporal resolution created a situation where stations "av16" and "av17" detected the gradient at practically the same time, and on the other hand, the IPP position at the time of detection was also an estimate based on geometrical approximations. These two errors combined caused the gradient for satellite G03 to be detected first at station "av17" and then at "av16", and for satellite G14, it was detected first at station "av16" and then at "av17".

In the case of satellite G32, the algorithm could not find the station of reference because none of the stations had a cross-correlation coefficient greater than 0.9 with two other stations (see Table 4.8). Therefore, the algorithm could not estimate the gradient parameters. In this case, the network would assume that the "worst-case" gradient is present for this satellite because it is detecting a gradient but is not able to estimate its parameters. Note that, the value of 0.9 could be excessively conservative and experiments with a less conservative value (e.g., 0.8) could be carried out. However, this is a trade-off and the lower this value is, the larger errors could be in the estimation of the parameters due to the change of the gradient. The optimization of the convergence criteria for different data sets was not addressed in this thesis and is part of future work.

Reference station	α_{ac59}^{G32}	α_{av16}^{G32}	α_{av17}^{G32}	α_{av01}^{G32}	α_{av20}^{G32}
ac59	1.000	0.077	0.213	0.104	0.136
av16	0.077	1.000	0.947	0.784	0.747
av17	0.213	0.947	1.000	0.757	0.693
av01	0.104	0.784	0.757	1.000	0.869
av20	0.136	0.747	0.693	0.869	1.000

Table 4.8: Cross-correlation coefficients calculated in post-processing for satellite G32 considering the different stations in Alaska as reference.

4.4.3 Overbound of the estimated slant slope in real time in Alaska

The satellites for which the algorithm was able to estimate the gradient parameters, G03 and G14, showed that the gradient moved twice as fast as considered in the simulations. This means that the assumption that was initially made for Alaska (the gradient parameters are bounded by the known threat models derived for CONUS and Germany) does not hold. This fact highlights the importance of deriving a threat model for each region in which GBAS is to be implemented. This could be done by modifying a known standard model (e.g., CONUS) as needed based on data collected in a given region, unless a new model would be needed because the characteristics of the ionosphere in this given region are more complex than those represented in the current models.

Therefore, the algorithm recomputed the inflation factor and repeated the process of Section 4.3.2.2, including the slant slope estimation errors calculated with the appropriate simulated gradient parameters. To do this, gradients propagating with a speed of 2500 m/s were simulated because this speed is slightly higher than the real estimated speeds and, as observed in the previous sections, the higher the speed is the worse the estimation gets. From all possible gradient directions, only gradient propagation from north to south

was considered, because it is the most similar direction to the estimated ones. Furthermore, all the simulated slopes, widths, and time of occurrence of the gradient were varied within their ranges in Table 4.3.

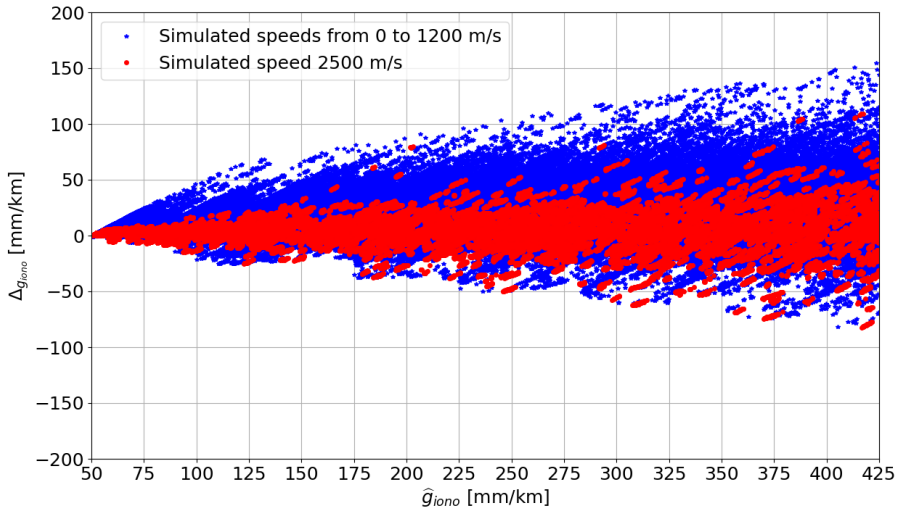

Figure 4.19: Slant slope estimation errors versus estimated slant slope. The blue starts represent the slant slope estimation errors for simulated speeds of the gradient between 0 and 1200 m/s. The red dots represent the slant slope estimation errors for a simulated speed of the gradient of 2500 m/s.

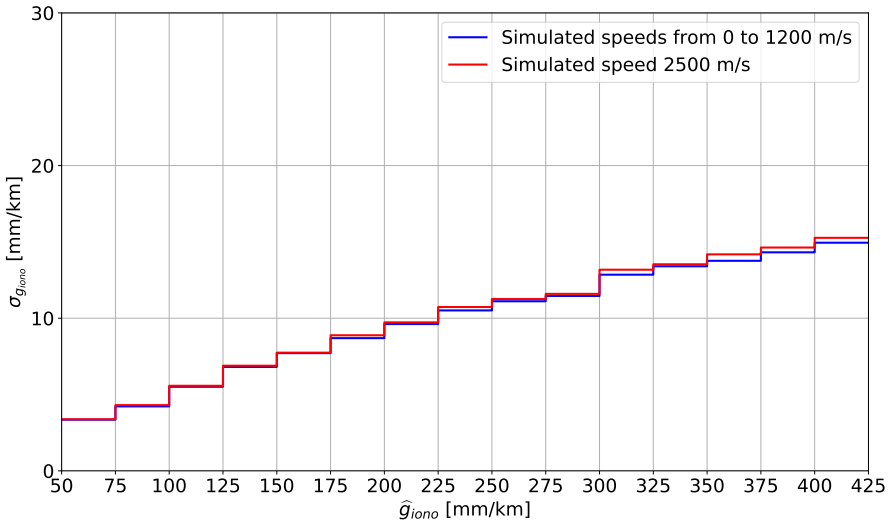

Figure 4.20: Standard deviation of the slant slope estimation error distribution calculated per bin considering the simulated data with gradient speeds from 0 to 1200 m/s only (blue line) and considering the simulated data with gradient speeds from 0 to 1200 m/s and 2500 m/s (red line).

Figure 4.19 shows the error in slant slope estimation as a function of the estimated gradient slant slope. As can be observed, the maximum negative estimation errors were due to a high gradient speed, as discussed above. However, this high speed did not lower the negative error value as much as expected, and the errors depicted with red dots were close to those already calculated previously (depicted with blue stars).

To better understand the difference, Figure 4.20 shows the standard deviation of slant slope estimation error per data bin considering the simulated gradients with speeds from 0 to 1200 m/s (in blue) and with speeds from 0 to 1200 m/s and an additional simulation with 2500 m/s (in red). As can be seen, the standard deviation for the case where the data with the gradients simulated at 2500 m/s was included was very similar to the standard deviation when the gradients were simulated between 0 and 1200 m/s only. The new inflation factor calculated with the data including the gradient speed of 2500 m/s was 2.22, which was slightly lower than previously because the overall standard deviation was slightly higher.

Finally, the overbounded gradient slant slopes for the case of the satellite G03, which was the only satellite capable of estimating the gradient parameters automatically, were: 141.3 mm/km for "av17", 136.3 mm/km for "av16", 131.3 mm/km for "av01", and 126.3 mm/km for "av20". Note that these values were calculated considering a Probability of Non-Bounded Errors of 1×10^8 and therefore, $k_{ne} = 5.61$ in Equation 3.31.

4.5 Summary

This chapter has evaluated the performance of the methodology proposed in Chapter 3 with synthetic gradients simulated to be representative of the auroral region, and a real gradient measured by a reference network in Alaska.

The detection results with simulated gradients have shown the importance of having good quality data, in terms of low noise and multipath, to detect harmful gradients for GBAS. The estimation results with simulated gradients have shown that the average estimation errors were low for all gradient parameters, which implies an overall good performance of the algorithm under the simulation conditions examined. The largest estimation errors occurred when varying the gradient speed and slope. In the case of static gradients, the error occurred due to the alignment of the IPPs when estimating the gradient speed and direction. In the case of gradients propagating at high speeds, the major influence on the estimation errors was the temporal resolution of the measurements, which resulted in the gradient not being detected exactly at the time it affected a station. In the case of the change in slope, the estima-

tion errors corresponded to cases where the generated ionospheric rates were close to the detection thresholds. This resulted in the gradient not being completely detected during all its duration impacting specifically the speed and width estimation. In addition, the simulation results of the worst-case overbounded gradient slant slopes in Section 4.3.2.2 suggest that using the concept proposed in this thesis could reduce the conservative assumptions that have to be taken to protect GBAS for gradients of up to 225 mm/km of slant slope in the auroral region. Above this value (no prior probability of occurrence of an ionospheric gradient considered), the overbounded slant slopes would be higher than the CONUS threat model, and the "worst-case" slant slope bound from the threat model would be used instead. The analysis of the real-time capability of the algorithm showed that the algorithm required a time to converge that depended on the characteristics of the ionospheric gradients and the performance of the monitoring network: the less noisy the test statistics were and the higher the cross-correlation between the different stations, the less time it took the algorithm to converge.

Finally, the results with a real anomalous ionospheric gradient have indicated the need to adapt the algorithm to the characteristics of ionospheric disturbances in the studied area, especially if they are fast traveling, of short duration, and change rapidly with their propagation. For the studied gradient, this resulted in adding minimum values for the cross-correlation coefficients used as weights in the resolution of the speed vector estimation. The cross-correlation coefficients of a given station were required to be at least 0.9 with two other stations to select it as a reference and 0.5 to determine that a station is measuring the same perturbation as the reference. The real gradient was simultaneously experienced by three satellites. Its parameters could be estimated in both post-processing and real time for satellite G03. For satellite G14, the gradient parameters could be estimated only in post-processing since the signals were lost before a sufficient number of samples were available in the buffers to perform the cross-correlation in real time. The algorithm could not estimate the gradient parameters for satellite G32 due to the poor cross-correlations between the test statistics corresponding to this satellite and the different stations. In addition, the results with the real gradient highlighted the need to derive ionospheric threat models for all areas where GBAS is to be implemented.

5

Performance of the Network-Based Ionospheric Gradient Monitor in a Low-latitude Region

In equatorial regions, ionospheric gradients have different characteristics from the gradients studied in Chapter 4. They are typically linked to so-called Equatorial Plasma Bubbles (EPBs), which propagate with slow speeds in comparison to the speeds observed in ionospheric gradients measured at mid and high latitudes (see Tables 2.5 and 2.6) and also tend to be steeper. For this reason, the threat models derived for equatorial regions (e.g. Brazil) include the highest ionospheric gradient slant slopes in the world, resulting in an excessive loss of availability. In addition, these EPBs are often accompanied by so-called scintillation phenomena, which causes strong oscillation on the signals, cycle slips, and loss of signal tracking in some cases. These well-known issues present a challenge for the methodology proposed in Chapter 3 because the algorithm needs carrier-phase signals on both L1 and L2 frequencies without scintillation for a sufficient period of time to capture the steepest part of the anomalous gradients and estimate their parameters from this information.

Therefore, the main objective of this chapter is to analyze the performance of the proposed methodology in Chapter 3 first with simulated gradients and then with a real EPB measured by a network of stations located in the equatorial region. For this study, I have chosen a network of stations located in Brazil that could provide coverage to several airports in the region.

This chapter is organized as follows: Section 5.1 presents the data used throughout the chapter, Section 5.2 describes the simulation setup developed to be representative of ionospheric characteristics in the equatorial region, Section 5.3 evaluates the performance of the method with all simulated data, and Section 5.4 evaluates the performance of the method with a real EPB measured by the network in Brazil.

5.1 Description of the real data used for the evaluations in the equatorial region

This section describes the characteristics of the network used to evaluate the performance of the methodology proposed in Chapter 3 in the equatorial region. First, Section 5.1.1 describes the network architecture and the measurements used. Then, Section 5.1.2 presents the method for selecting nominal (i.e., no abnormal ionospheric activity present) and active days.

5.1.1 Data description

As a representative monitoring network for the equatorial region, eight stations situated in the state of São Paulo, Brazil, were selected. Figure 5.1 depicts the locations of these stations and Table 5.1 shows the coordinates of each of the stations. Public data is available for this network, whose stations belong to the Brazilian Network for Continuous Monitoring of GPS (RBMC), at a 15-second sampling rate both for L1 and L2 frequencies and GPS satellites [102]. Nowadays, more stations are available in this area, and they provide data at a higher sampling rate. However, this work used the data that was available from 2014 because this year was a solar maximum and is well studied in the literature. It should be noted that, although 15 seconds is a lower sampling rate than the 1 second sampling rate used in Alaska, in this region, ionospheric perturbations (i.e., EPBs) move also at a lower speed. Therefore, this work considered a 15-second sampling rate to be sufficient for this study.

As explained in Chapter 4, due to the limited availability of data recorded with L1/L5 frequencies and other constellations (e.g. Galileo) during active ionospheric conditions, real measurements on L1 and L2 frequencies from only the GPS constellation were used for this study.

Name	**Latitude** [°]	**Longitude** [°]
poli	-23.555	-46.730
chpi	-22.489	-44.985
mgin	-22.318	-46.534
sjsp	-23.207	-45.861
uba1	-23.500	-45.118
eesc	-22.005	-47.900
neia	-25.002	-47.925
spbo	-22.850	-48.430

Table 5.1: Coordinates of the stations in Brazil.

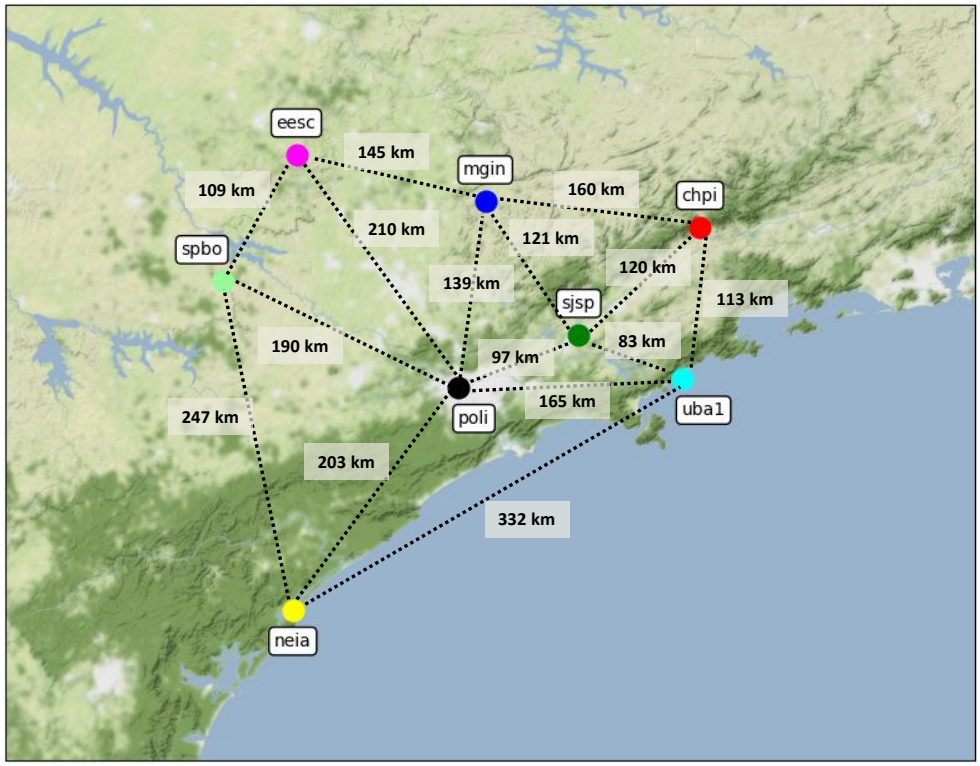

Figure 5.1: Locations of the stations in Brazil.

5.1.2 Date selection

As in Chapter 4, the dates selected from all the data available attend to two different purposes: (i) the study of a real anomalous ionospheric gradient measured by the network depicted in Figure 5.1, and (ii) the derivation of the monitoring threshold for each of the stations in the network.

Both the active and the nominal ionospheric days were determined based on the AATR [32], calculated for one of the stations under study, "chpi". Figures 5.2 and 5.3 show the specific AATR values for this station during active and nominal ionospheric periods, respectively.

As an AATR threshold to determine the "active" days, 1 TECU per minute was used, which can be considered as very high activity. From all the days in which the AATR exceeded 1 TECU/min, the day 69 of year 2014, i.e. 10th of March of 2014, was selected (see Figure 5.2). This date belongs to the time period associated with the maximum of Solar Cycle 24 when the largest anomalous ionospheric gradients were detected in Brazil [30, 33].

For the derivation of the monitoring thresholds, both nominal days (i.e.,

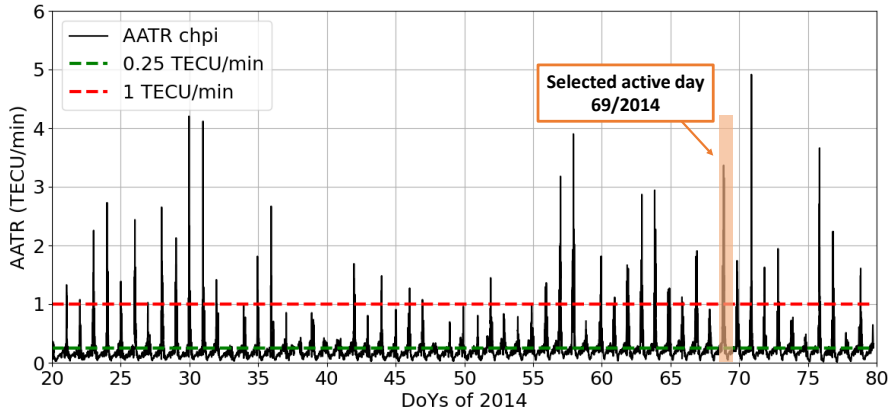

Figure 5.2: AATR values for reference station "chpi" during 60 days of year 2014. The AATR values are calculated every 5 minutes. The threshold of 0.25 TECU/min represents the value below which the ionosphere is considered "quiet" or nominal and the threshold of 1 TECU/min is the value above which the ionosphere is considered very "active".

24 hours in which no significant ionospheric activity was observed) and nominal hours of active days (i.e., 12 hours during daytime of active days) were selected. Note that the active hours of active days have not been used for the derivation of the thresholds. This is because this high ionospheric activity is considered off-nominal and is what is to be detected, even though this high activity is very frequent during nighttime of the active periods (see Figure 5.2). Therefore, first 10 "quiet" days were manually selected after the active period in March 2014. The calm period was selected after the active period and not before because the active period lasted approximately between December 2013 (see [75]) and April 2014 and, in December 2013, the measurements from some of the stations in Figure 5.1 were not available. Then, 12 nominal hours belonging to 20 "active" days were selected to account for satellite geometry variability and to obtain more measurements; in Brazil, measurements had a sampling rate of 15 seconds instead of 1 second as in Alaska, and thus, fewer measurements were available. Specifically, the hours between 6 a.m. and 6 p.m. local time were assumed to be in nominal conditions (i.e. without significant ionospheric activity) [22]. In the case of Brazil, an AATR threshold of 0.25 TECU/min was used instead of 0.2 TECU/min (the value used in Chapter 4) to distinguish nominal days/hours from days/hours with some ionospheric activity (see Figures 5.2 and 5.3). The reason is that the nominal AATR values in this region are slightly higher because some of the IPPs cross the Appleton anomaly, which is considered nominal in Brazil. The last step was to perform a visual inspection of the data recorded in the stations under study, depicted in Figure 5.1, during the days considered "nominal" and during the nominal

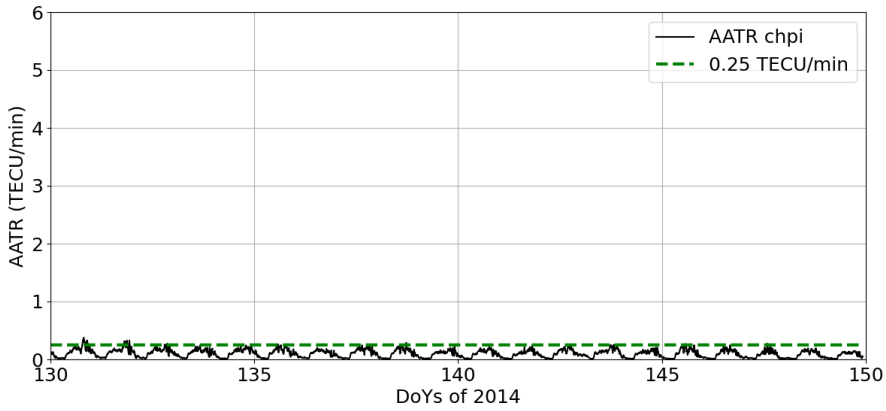

Figure 5.3: AATR values for reference station "chpi" during 20 days of year 2014. The AATR values are calculated every 5 minutes. The threshold of 0.25 TECU/min represents the value below which the ionosphere is considered "quiet" or nominal.

hours of the "active" days. During this process, the days with corrupted or missing measurements were discarded.

According to this criteria, the following nominal full days (24 hours) were selected to derive the detection thresholds for all stations: 133, 136, 139, 140, 144, 145, 146, 147, 148 and 149 of the year 2014. The selected nominal hours of the active days (12 hours, from 6 a.m. to 6 p.m. local time) from stations "chpi", "poli", "eesc", "mgin", "neia" and "uba1" belonged to the days: 23, 26, 28, 29, 31, 44, 46, 47, 56, 57, 58, 61, 62, 63, 64, 66, 67, 69, 71 and 76. For station "uba1", several active days had gaps in the data for satellite elevations between 5° and 15° and the rest of the active days during the same period had the same gaps. Therefore, fewer samples were available for this station. In the case of station "sjsp", day 26 was not available. However, sufficient samples were available from the other selected days. In the case of station "spbo", the days between 56 and 66 were not available. No more active days were available in the same period, therefore fewer measurements were used to calculate the detection threshold for this station.

5.2 Simulation setup

This section presents the simulation setup designed to evaluate the detection and estimation capabilities of the network introduced in Section 5.1.

As a first step, it is necessary to calculate the nominal slant ionospheric delays present in the measurements over which the simulated gradient is to be added. For this purpose, Equation 3.1 was used with the measurements

recorded by the network on one of the "quiet" days. Among the ten nominal days specified in Section 5.1, day 145 of 2014 was selected. As in Chapter 4, it was assumed that the information recorded on this day is representative of all nominal days in terms of multipath and noise present in the measurements, satellite geometries, and nominal slant ionospheric delays. However, this is a simplification, and more simulations with measurements from different days of the year and different years would be needed to obtain more representative results.

Then, on top of the nominal slant ionospheric delays, synthetic ionospheric perturbations designed to be representative of the GBAS threat model derived for Brazil, shown in Figure 2.10, were simulated. As introduced in Section 2.4.2.2, the EPBs, which cause most of the ionospheric gradients in Brazil, are known to travel following the Modified Dip Latitude (MODIP) isolines [82]. Therefore, simulating the EPBs travelling along the MODIP isoline of e.g., MODIP equal to $-30°$, would be sufficient. However, simulating the trajectory of the EPB in this way implies that the EPB speed is not constant since these MODIP isolines are generated by calculating the latitude of the points that create the lines from longitudes that increase in constant step lengths. As these isolines follow neither a meridian nor a parallel, but have variable latitude, the distance between points is not the same for the same time step and thus the EPB speed would change at each point.

In order to simplify this problem and keep the simulated EPB speed and direction constant over a certain period of time, a linear curve fitting of the MODIP isoline of $-30°$ was calculated in three sections for the trajectory of the EPB. Therefore, the trajectory of the center of the ionospheric perturbation can be defined with the "speed" (v_{iono}) and "direction" (d_{iono}) of the speed vector $\boldsymbol{v}$, measured in the clockwise direction from the North Pole. This definition is the same as the one explained in Section 4.2 of Chapter 4 and follows Equations 4.1 and 4.2. Note that, in spite of this simplification, the simulated trajectory is close to the actual MODIP isoline in the area of interest.

Figure 5.4 depicts with blue points the MODIP isoline of $-30°$ and with a red solid line the linear fitting in three different sections. Finally, of the three sections, only the middle section was considered because it is the only one that affects the network under study. The specific parameters of the middle section are: $d_{iono} = 58°$ measured from the North Pole, $lon_{iono,0} = -70°$, and $lat_{iono,0} = -32°$.

Once the gradient trajectory is known for each epoch, the ionospheric gradient is defined in a local reference frame, where the origin ($[0, 0]$) is at the center of the perturbation $[lon_{iono}, lat_{iono}]$ and changes at each epoch.

Therefore, to obtain the amount of simulated ionospheric delay experienced

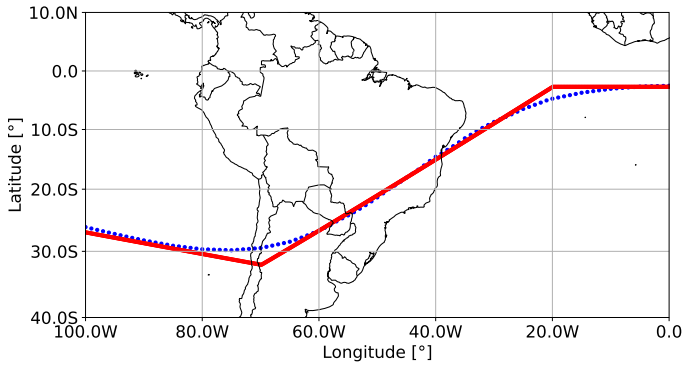

Figure 5.4: Simulated EPB trajectory. The blue dots represent the MODIP isoline of $-30°$ and the solid red line represents the linear fitting in three different sections.

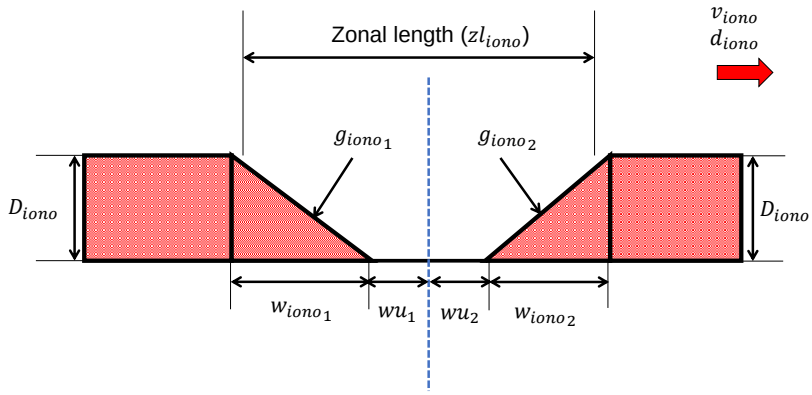

Figure 5.5: Simplified EPB model used for simulations.

by each IPP, it is necessary to convert the IPPs from the global reference frame to the ionospheric perturbation reference frame. Appendix A describes this transformation, which is the same as in Chapter 4. As a result of the application of these geometric transformations, the coordinates of the IPPs in the perturbation reference frame can be expressed as $\boldsymbol{x_{iono}} = [x_{iono}, y_{iono}]$.

EPBs can be simplified and defined as two simple gradients (one downward and one upward) that move with a constant speed (meters per second) and direction (degrees) over a "thin shell" layer at a height of 350 km above the Earth's surface [30]. Figure 5.5 shows the definition of the perturbation in its propagation direction and the parameters used for its simulation. Note that, in this case, the slopes and widths of both gradients could be different. The dimensions of the simulated EPB in the direction perpendicular to the direction of motion are considered to be infinite. The additional slant ionospheric delay in meters (D_{iono}) that is added to the nominal slant ionospheric

Additional slant ionospheric delay (D_{iono})[m]	**IPP coordinates in the ionospheric perturbation reference frame [m]**
0	$x_{iono} = (-\infty, +\infty)$; $y_{iono} \leq -(w_{iono_1} + wu_1) \cdot 10^3$
$F_{pp} \cdot \frac{-g_{iono,vert_1}}{10^6} \cdot \left(\frac{zl_{iono}}{2} \cdot 10^3 - \lvert y_{iono}\rvert\right)$	$x_{iono} = (-\infty, +\infty)$; $-(w_{iono_1} + wu_1) \cdot 10^3 < y_{iono}$; $y_{iono} \leq -wu_1 \cdot 10^3$
$F_{pp} \cdot \frac{-g_{iono,vert_1}}{10^6} \cdot w_{iono_1} \cdot 10^3$	$x_{iono} = (-\infty, +\infty)$; $-wu_1 \cdot 10^3 < y_{iono} \leq 0$
$F_{pp} \cdot \frac{-g_{iono,vert_2}}{10^6} \cdot w_{iono_2} \cdot 10^3$	$x_{iono} = (-\infty, +\infty)$; $0 < y_{iono} \leq wu_2 \cdot 10^3$
$F_{pp} \cdot \frac{g_{iono,vert_2}}{10^6} \cdot \left(\lvert y_{iono}\rvert - \frac{zl_{iono}}{2} \cdot 10^3\right)$	$x_{iono} = (-\infty, +\infty)$; $wu_2 \cdot 10^3 < y_{iono}$; $y_{iono} \leq (w_{iono_2} + wu_2) \cdot 10^3$
0	$x_{iono} = (-\infty, +\infty)$; $y_{iono} \geq (w_{iono_2} + wu_2) \cdot 10^3$

Table 5.2: Equations to simulate the synthetic slant ionospheric delays in Brazil.

delay calculated previously is described in Table 5.2, which is different from the table presented in Chapter 4 for the simple gradient (Table 4.2). Here, F_{pp} is the vertical-to-slant obliquity factor explained in Equation 2.23, $g_{iono,vert_1}$ and $g_{iono,vert_2}$ are the simulated gradient slopes expressed in the vertical domain in mm/km, and w_{iono_1} and w_{iono_2} are the simulated gradient widths in kilometers. The terms wu_1 and wu_2 are defined as:

$$\begin{aligned} wu_1 &= \frac{zl_{iono}}{2} - w_{iono_1}, \\ wu_2 &= \frac{zl_{iono}}{2} - w_{iono_2}. \end{aligned} \tag{5.1}$$

The equations in Table 5.2 define the gradients only in the south-to-north direction, independently of their trajectory. Therefore, Equation A.4 of Appendix A performs a rotation of the IPPs around the origin of the perturbation to simulate the selected direction of the gradient.

Figure 5.6 shows an example of one simulated ionospheric EPB between the two dark red areas. Note that, as discussed in Chapter 4, the assumption of the perturbation as a planetary plane wave may not be realistic if the baselines between the stations used are comparable to the typical size of the perturbations. As in the case of Alaska, the baselines of the network determine the sizes of the ionospheric perturbations that the monitor is able to estimate. In this

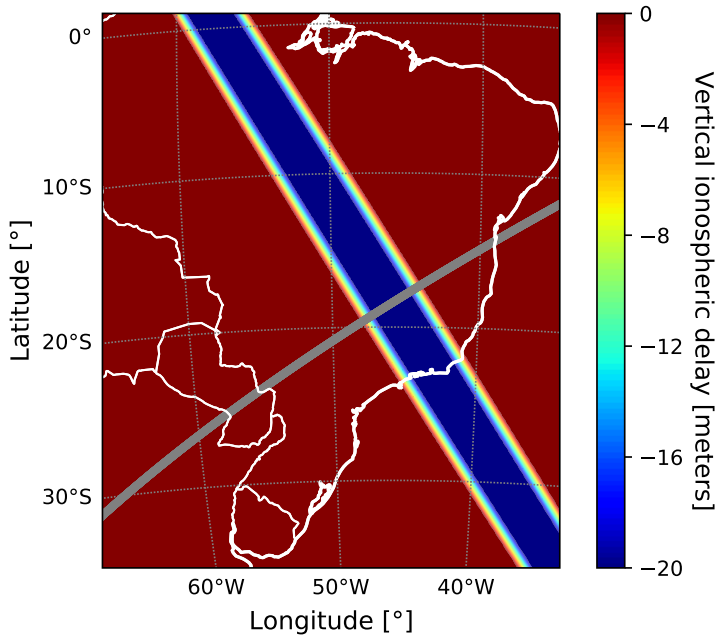

Figure 5.6: Example of one synthetic perturbation simulated with $g_{iono,vert_1} = g_{iono,vert_2}$ of 200 mm/km, $w_{iono_1} = w_{iono_2}$ of 100 km, and d_{iono} of 58°. These values are an example within the simulated ranges for each of the parameters. The grey solid line represents the trajectory of the perturbation.

way, an inadequate network would produce low correlation values, as occurred in the case of Alaska with the farthest away station. However, in the case of Brazil, high correlations were found between the real EPBs measured by some of the different stations of the network under study, separated by about 100 km. Therefore, the approximation of a planar wave front is applicable also to the work in Brazil.

The simulations varied all the already defined simulation gradient parameters within their ranges in the Brazilian threat model (see Table 2.6) up to a maximum additional slant delay of 35 meters. As can be seen, as in the case of Alaska, the slope of the gradient was simulated in the vertical domain until the maximum value defined in slant for the Brazilian threat model. Therefore, in the case of low elevation satellites, much higher slant slopes than the maximum slant slopes considered in the Brazilian threat model could be simulated. However, all simulation cases that produced simulated slant slopes greater than 860 mm/km were not considered. Table 5.3 presents the parameter bounds for this simulation. Furthermore, in this case, the initial longitude and latitude of the

center of the perturbation for each realization of the simulation represented by $lon_{iono,0}$ and $lat_{iono,0}$ respectively is always the same, and only $t_{iono,0}$ changes. Thus, the simulated trajectory is always the same (depicted in Figure 5.6) because it is considered to be representative of all the trajectories that the EPBs could follow in the region of the network under study. Note that, although the EPBs are known to occur during local nighttime (after sunset), they were simulated during the 24 hours of day 145 to have more satellite geometries available. As a simplification, $g_{iono,vert_1} = g_{iono,vert_2}$ and $w_{iono_1} = w_{iono_2}$ were considered.

Parameter	Min	Max	Step
$g_{iono,vert_1} = g_{iono,vert_2}$ [mm/km]	50	860	10
$w_{iono_1} = w_{iono_2}$ [km]	20	460	20
v_{iono} [m/s]	40	250	30
d_{iono} [°]	58	58	-
zl_{iono} [km]	90	750	220
$t_{iono,0}$ [GPS seconds of day]	0	82800	3600

Table 5.3: Simulation parameters for Brazil.

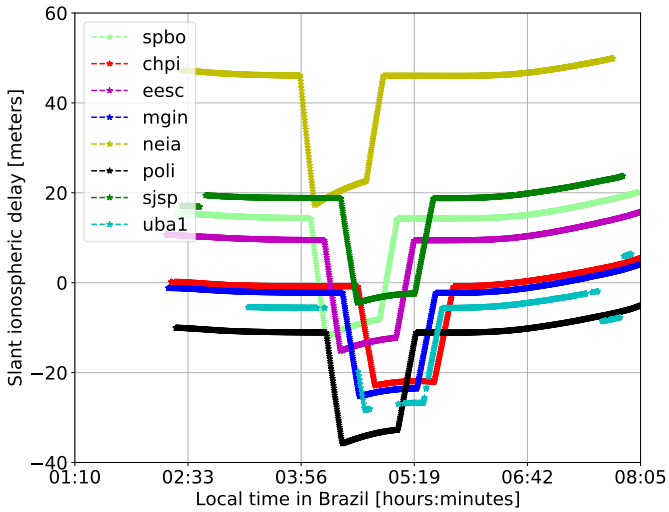

Figure 5.7: Example of simulated slant ionospheric delays for satellite G02 and the network of stations situated in Brazil. These simulated slant ionospheric delays correspond to the synthetic perturbation depicted in Figure 5.6 added to the real nominal slant ionospheric delays from satellite G02.

Figure 5.7 shows the simulated slant ionospheric delays for satellite G02, all stations of the network in Brazil, and the synthetic perturbation depicted in Figure 5.6. As can be seen, there is a vertical offset in the estimated slant

ionospheric delays. This is due to the ambiguities present in the carrier-phase measurements in Equation 2.1.

5.3 Evaluation of the monitor with simulated ionospheric gradients

This section analyzes the detection and estimation capabilities of the network of stations depicted in Figure 5.1.

5.3.1 Detection

As discussed in Section 3.3.1.3, one of the design parameters of the detection threshold is the probability of false alert.

Unlike the case of Alaska, where a P_{fa} of 10^{-6} was selected empirically, the measurements recorded by the network in Brazil presented lower levels of noise and multipath and few outliers due to the different sampling rate (15 seconds in Brazil versus 1 second in Alaska), which smooths these effects (see Figure 3.8 of Chapter 3). In addition, fewer samples, assumed to be statistically independent, were available in Brazil due to the sampling rate of the measurements recorded (see Figure 3.9). Therefore, in this case a false-alert probability (P_{fa}) of 10^{-4} was selected empirically as an acceptable compromise for the tests with real measurements from Brazil. Nevertheless, as commented in Chapter 4, this value is likely not optimal due to the limited data on which its selection was based, and optimization of its value will be investigated as part of future work. In addition, both cycle slip detectors and the visual check explained in Section 3.3.1.1 were used to derive the detection thresholds depicted in Figure 5.8.

Figure 5.8 shows that all stations in the network have similar performance for satellite elevations above 13°. Below that elevation, several satellites crossed the Appleton anomaly at different locations, causing different nominal delays. This occurred for satellite elevations between 7° and 13°, where the thresholds are higher than between 5° and 7°. In addition, the threshold for station "uba1" is slightly lower for satellite elevations below 13°. This is because, as discussed above, fewer measurements were available at these elevations for the nominal hours of the active days, and therefore the maximum values of nominal ionospheric delays could not be reached. This fact resulted in a more sensitive performance of station "uba1", which could trigger more false alerts than the others for satellites at lower elevations.

Given that, in the case of Brazil, the detectability of each of the stations is similar, the detectability of the entire network was studied directly using the

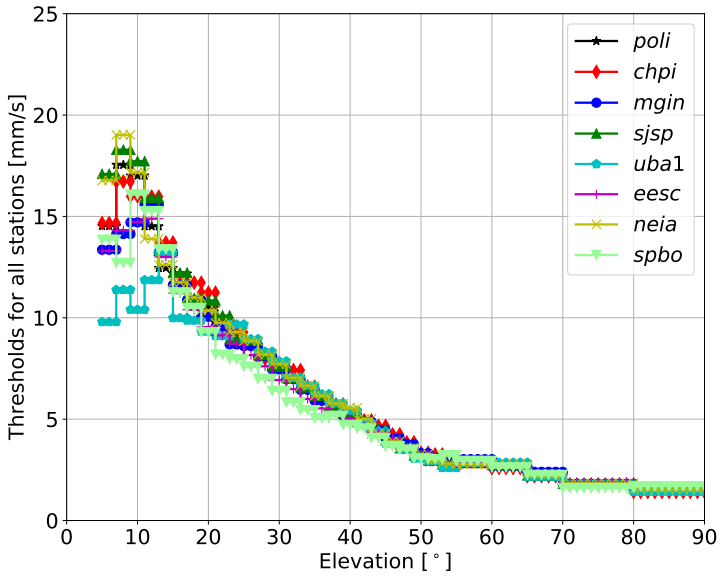

Figure 5.8: Detection thresholds for all stations considered in Brazil derived with the data specified in Section 5.1.1 and a $P_{fa} = 10^{-4}$.

Minimum Detectable Gradient (MDG) introduced in Section 3.3.2. This study is addressed in Chapter 6 since the location of the GBAS station within the network coverage area must be known in order to calculate the MDG.

5.3.2 Estimation

This section analyzes three different aspects of the network's estimation capability: (i) the estimation errors associated with the variation of each of the gradient parameters separately, (ii) the capability of the method to produce reliable estimates, and (iii) the real-time performance.

The algorithm was able to distinguish both parts of the simulated EPBs; the part corresponding to downward slopes presented negative $Itest_r^j$ values, while the part corresponding to upward slopes presented positive $Itest_r^j$ values. Therefore, the algorithm treated both parts as two different gradients to compute their parameters, following the methodology in Section 3.3.4. Since in this work EPBs were simulated following the threat model proposed for GBAS in the equatorial region [30, 103], which proposes to assume a constant ionospheric delay in the middle of both fronts, the test statistic for this intermediate part was below the detection threshold. Therefore, it was not taken into account for the estimation process in the simulations. However, when real EPBs are observed, there are often ionospheric irregularities between the two ionospheric fronts large enough to be detectable and cause hazards if not de-

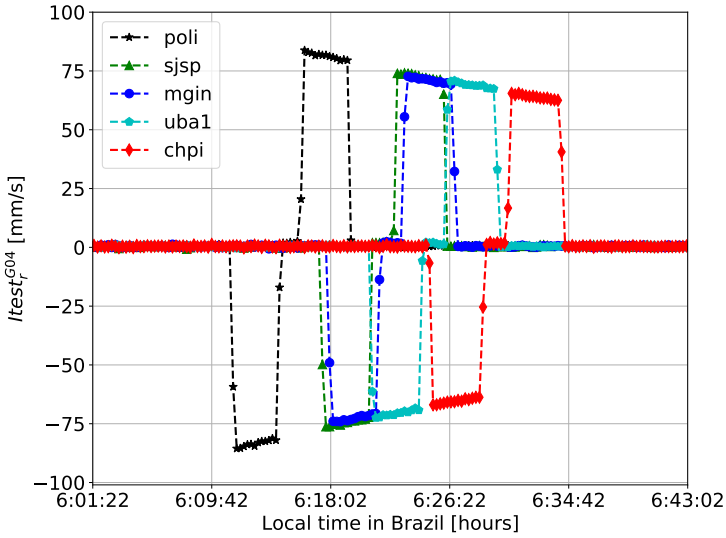

Figure 5.9: Example of simulation test statistics for satellite G04, day 145 of year 2014, and the network of stations in Brazil.

tected (see Section 5.4). As with Alaska, the goal of the work carried out in this section is to study the possible errors due to the approximations and assumptions used for the calculation of the gradient parameters by isolating the different sources of errors for the EPB case. Section 5.4 shows the limitations and adaptations of the estimation method to account for these irregularities between the two fronts in the study with real (actually observed) EPBs. Future work will address the impact of these intermediate irregularities also in simulation using more complex EPB models.

Furthermore, the algorithm used only five of the eight stations depicted in Figure 5.1: "poli", "mgin", "sjsp", "chpi", and "uba1". The reason was that the other stations ("neia", "spbo", and "eesc") were outside the radius considered for the estimation to be valid (i.e. 200 km in Section 3.3.4).

Figure 5.9 shows an example of $Itest_r^{G04}(t)$ calculated for all stations considered, satellite G04, and a simulated gradient with the following characteristics: 200 mm/km of vertical slope (downward and upward), 100 m/s of speed, 40 km of width (corresponding to each downward and upward slope), 90 km of zonal length, and moving with a direction of 58° measured from the North Pole. Here, the two gradients forming the simulated EPB are clearly distinguishable.

5.3.2.1 Gradient parameter estimation errors

This section presents the results of the estimation errors with the variation of each of the gradient parameters separately. The idea behind this study is,

as in Chapter 4, to study the impact that the change of one of the parameters has on the estimation error of the other parameters.

Table 5.4 shows the summarized mean and maximum estimation errors (maximum positive and maximum negative) computed once the algorithm converged as described in Equation 3.29. Each row of Table 5.4 considers the change of one of the parameters among the values in Table 5.3 while maintaining all other parameters constant at values for which the simulation performed well. These values were: 100 m/s for speed, 40 km for width, and 200 mm/km for vertical slope. The direction considered was 58° as mentioned above, and the zonal length was 90 km for the variation of slope and speed. In the case of width variation, the zonal length was 90 km only when possible, since it had to be increased for simulated widths greater than 40 km in order to allow for evaluation of wider gradients.

The results in Table 5.4 show that the errors in the columns "Mean" stayed within low values for all gradient parameters. This differs from the case of Alaska, which presented high error values in the "Mean" column for slope determination (see Table 4.4). The reason is that, in Brazil, the nominal measurements presented low levels of noise and multipath and, in addition, the test statistics ($Itest_r$) were calculated every 15 seconds, which also helped smooth out noise and multipath. Thus, also for the case of Brazil, the algorithm in general appears to work well under the simulation conditions examined.

Since the different errors in Table 5.4 are expressed in different units, Table 5.5 shows the maximum relative errors as well. In the cases where the parameters changed, the simulated values were clarified in brackets because the maximum absolute estimation errors from Table 5.4 do not necessarily correspond to the values of the maximum relative estimation errors (e.g. 42.0% of 110.0 mm/km results in an absolute error of 46.2 mm/km instead of 49.0 mm/km in Table 5.4).

Considering the results from Table 5.4 and Table 5.5, the following conclusions were drawn:

1. The change of the speed parameter did not present a high impact on speed determination, as occurred in Alaska. This point is further discussed in the subsection 5.3.2.1.1.

2. The maximum absolute errors for the estimation of the slope were high for the change of each of the gradient parameters (sixth column in Table 5.4). The maximum relative slant slope estimation errors were higher for the change of the slope than for the change of the rest of the parameters (third column in Table 5.5). This point is further discussed in the subsection 5.3.2.1.2.

3. The maximum estimation errors for the direction and width parameters were lower than for the slant slope and presented comparable values for all changes of the gradient parameters.

Gradient parameters	Estimation error							
	Speed $[m/s]$		Direction $[^\circ]$		Slant slope $[mm/km]$		Width $[km]$	
	Mean	Max.	Mean	Max.	Mean	Max.	Mean	Max.
Change of speed	-3.0	12.7 -17.4	-0.7	2.5 -4.0	2.0	41.7 -33.7	-0.4	4.5 -4.9
Change of slope	-1.1	10.2 -8.9	-0.8	5.3 -7.0	3.7	49.2 -38.9	-0.4	3.4 -8.1
Change of width	-1.0	14.5 -12.5	-0.5	5.0 -3.6	8.2	69.8 -34.6	-0.4	9.6 -10.0

Table 5.4: Absolute gradient parameter estimation errors of the network in Brazil with variation of one of the simulated gradient parameters.

Gradient parameters	Maximum relative estimation errors			
	Speed [%]	Direction [%]	Slant slope [%]	Width [%]
Change of speed	10.6 (70.0 m/s) -8.4 (190.0 m/s)	4.3 -6.9	11.7 (355.7 mm/km) -9.2 (363.7 mm/km)	11.2 -12.2
Change of slope	10.2 -8.9	9.1 -12.1	42.0 (110.0 mm/km) -31.5 (89.0 mm/km)	17.0 -20.2
Change of width	14.5 -12.5	8.6 -6.2	21.0 (319.6 mm/km) -10.0 (238.5 mm/km)	15.1 (60 km) -22.0 (20 km)

Table 5.5: Maximum relative gradient parameter estimation errors of the network in Brazil. The values specified in brackets represent the simulated values. For the cells where the simulated value is not specified, the simulated values were 100 m/s for the speed and 40 km for the width.

In the following subsections, the speed and the slope estimation errors are discussed in detail.

5.3.2.1.1 Speed estimation error

As commented previously, in the case of Brazil, speed estimation errors were low compared to the values obtained in Section 4.3.2.1 for the case of Alaska. The reason is that, in the EPB case, ionospheric front speeds relative to the ground (v_{iono}) of 0 m/s and above 250 m/s were not simulated because they do not belong to the threat model. Although the relative speeds between the IPPs and the gradient were occasionally close to 0 m/s for the other simulated speeds (different than 0 m/s), the positions of the IPPs when the gradient was detected

for the same satellite and different stations were not aligned. Therefore, IPP geometries were typically stronger for the lowest simulated speed in Brazil (40 m/s) than for the lowest simulated speed in Alaska (0 m/s). In the second case, the insufficient temporal resolution compared to the speed of the gradient and distance between stations, were not that significant in the case of Brazil.

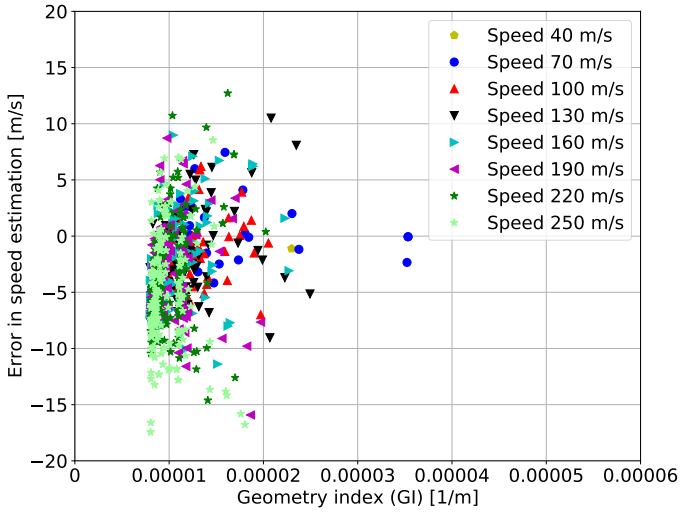

Figure 5.10: Error in speed estimation over Geometry Index for different simulated speeds of the gradient. Each marker represents a simulated speed and each point the GI calculated at the moment of the estimation.

Figure 5.10 shows the estimation error in speed versus the GI to evaluate the influence of the IPP geometry in the estimated errors. The GIs stayed below 4×10^{-5} in all cases and were thus within the limits for suitable IPP geometries. Moreover, the largest speed estimation errors corresponded to the highest simulated speeds (light green stars in Figure 5.10) while presenting average GIs. Therefore, the majority of these errors can be associated with the time resolution problem that could be solved by increasing the data sampling.

Regarding the impact of the time resolution, Figure 5.11a shows the mean (blue circles) and maximum speed estimation errors (up red triangles and down black triangles) when changing the simulated speeds of the gradient. As can be seen, the estimation errors remained low in both mean and maximum values and increased only slightly with increasing simulated speeds. This shows that, as the stations are farther apart than in the case of Alaska and the EPBs moved slower, the sampling rate did not have a large impact on the speed estimation with the simulated gradients. Moreover, the algorithm typically estimated the EPB speeds lower than their simulated value.

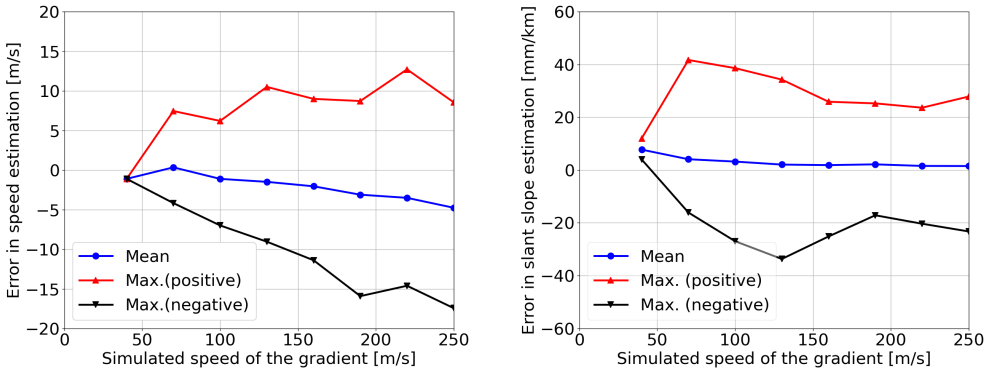

(a) Speed estimation error.

(b) Slant slope estimation error.

Figure 5.11: Mean (blue circles), maximum positive (red up triangles) and maximum negative (black down triangles) values for speed and slant slope estimation errors with respect to the simulated speed of the gradient.

5.3.2.1.2 Slope estimation error

Table 5.4 shows that the absolute slant slope estimation errors were comparable for the change of the speed, the width, and the slope itself. Therefore, the three cases were studied separately.

Figure 5.11b depicts slant slope estimation errors with the change of the simulated speed of the gradient. In contrast to Alaska, the errors were low and comparable for all the simulated speeds. Therefore, changing the speed within the threat model values did not have a large impact on slant slope estimation.

Figure 5.12a depicts slant slope estimation error with respect to change of width. Between 160 km and 460 km of width, the algorithm did not output any result because it confirmed that the multiplication of the simulated width with the selected slope gave an ionospheric delay below 35 meters before performing the simulation, and this was not the case for the parameter combinations with missing outputs. As in the case of the speed variation, the errors were low and comparable for the change of the simulated gradient widths. Therefore, changing the width within the threat model values did not have a large impact on the slant slope estimation.

Figure 5.12b depicts slope estimation error with respect to the change of slope. As can be seen, the mean error values were practically the same over the whole range of simulated slopes, and the maximum values (positive and negative) were also comparable except for the points at the beginning and at the end of the curves. Therefore, the variation of the slope parameter did not have a large impact on the slant slope estimations as long as the test statistics were well above the threshold (see second row and third column of Table 5.5).

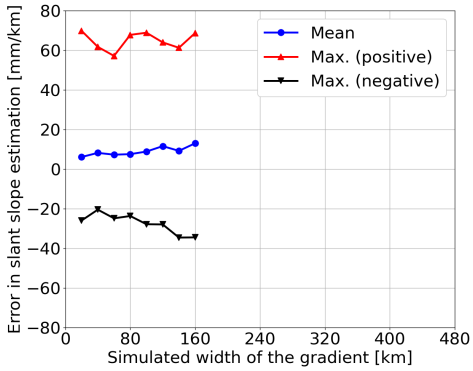

(a) Slant slope estimation errors for different simulated widths of the gradient.

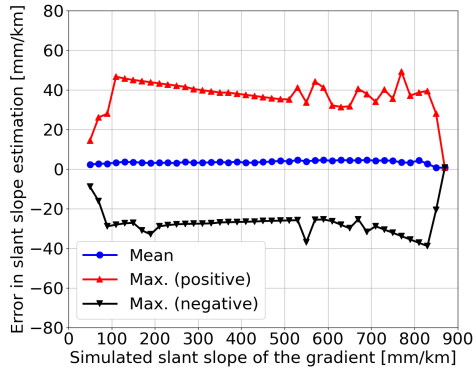

(b) Slant slope estimation errors for different simulated slant slopes of the gradient.

Figure 5.12: Mean (blue circles), maximum positive (red up triangles), and maximum negative (black down triangles) error in slant slope estimation for different simulated widths and slant slopes of the gradient.

Lower maximum error values were obtained for simulated slant slopes below 110 mm/km because the gradient slopes were simulated in the vertical domain, thus small slant slopes could only be simulated for high elevation satellites. The maximum errors in higher slopes corresponded to estimates calculated by low elevation satellites, which moved faster and had a larger impact on the error due to the 15-second sampling rate.

Since for all the changes of the gradient parameters the slope parameter can be underestimated, the following section derives an uncertainty model for the estimated gradient slant slope.

5.3.2.2 Uncertainty model of the estimated gradient parameters

This section presents the uncertainty model derived for the gradient slant slope estimated with the measurements from the network of stations in Brazil. The derivation of the uncertainty model for the other gradient parameters could be carried out in an analogous way.

Figure 5.13 shows with blue stars the slope estimation errors considering variation of all the gradient parameters in the ranges described in Table 5.3. As described in Section 3.3.4.4, the first step in deriving the uncertainty model is to order the estimation errors in bins to calculate the statistics. Figure 5.13 suggests that a bin size of 10 mm/km in slant slope is adequate to perform these statistics since, within this bin size, the negative errors (underestimation of the gradient) were similar within one bin. However, it should be noted that since the slopes were simulated in the vertical domain, the number of posi-

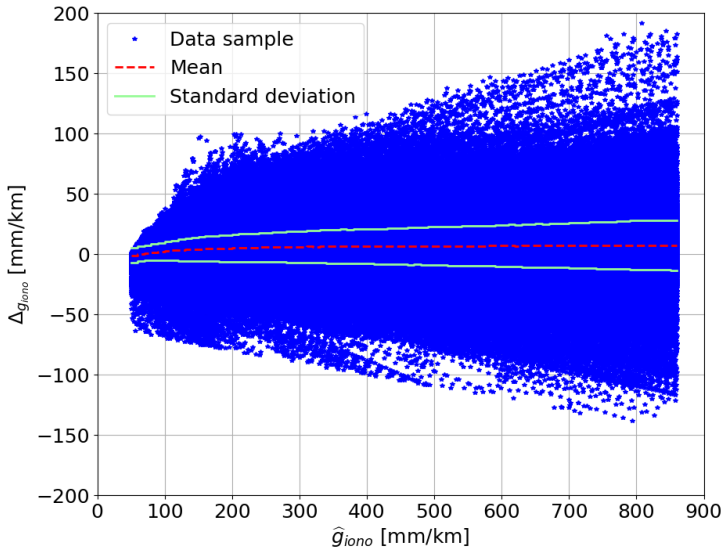

Figure 5.13: Slant slope estimation errors versus estimated slant slope. The blue starts represent the slant slope estimation errors, the red dashed line represents the mean value per bin, and the solid light green lines represent the standard deviation per bin.

tive samples in the first bins of estimated slant slope (e.g., 50 mm/km to 60 mm/km) was lower than in the rest of the bins. This occurred because only the high elevation satellites were able to observe low slant slopes, as the applied obliquity factors (Equation 2.23) caused low elevation satellites to observe steeper slant slopes than the simulated vertical slopes. Therefore, the positive samples in the first bins (e.g., 50 mm/km to 60 mm/km of estimated slant slope) belonged to simulated slant slopes between 50 mm/km and 60 mm/km that were slightly overestimated (e.g., 55 mm/km), but not enough to be sorted in other bins. The negative samples in the first bins (e.g., 50 mm/km to 60 mm/km) belonged to simulated slant slopes greater than 60 mm/km (e.g., 62 mm/km) that were underestimated (e.g., 55 mm/km). Thus, these samples were sorted into a bin of estimated slope that was different from the corresponding simulated slope. The maximum values of the negative samples were higher than that of the positive ones in the first bins because they belonged to higher simulated slant slopes that were underestimated and, the higher the simulated slope, the higher is the error to be expected in absolute value.

In addition, Figure 5.13 shows with a dashed red line the mean value per bin and with solid light green lines the standard deviation per bin. It can be seen that, although the values of the estimation errors were high, this was only the case for few samples, as the values of the mean and standard deviation were low. Furthermore, the mean values were positive but close to zero for all

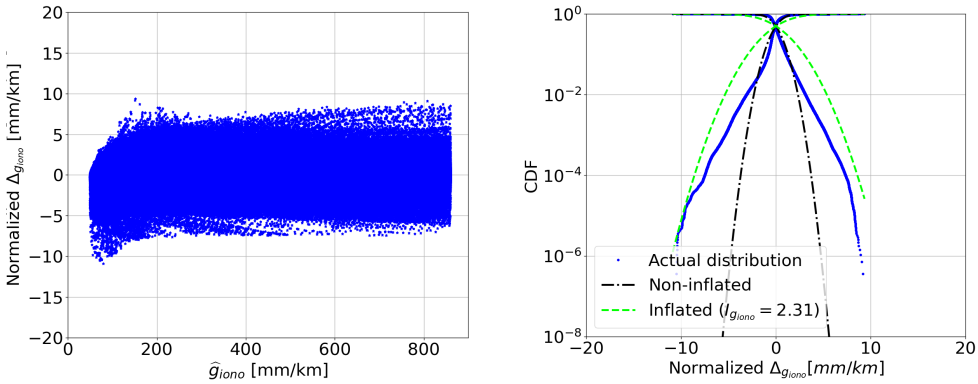

(a) Normalized slant slope estimation errors.

(b) Gaussian tail overbounding process.

Figure 5.14: Normalized slant slope estimation errors and Gaussian tail overbounding process for the gradient slant slope estimation errors for the network in Brazil. The data bins considered are of 10 mm/km in estimated slant slope. The blue dots in both figures show the normalized slant slope estimation error distribution for all the data bins, the black dot-dashed line in Figure 5.14b represents the non-inflated Gaussian distribution that would correspond to the mean and standard deviation of the normalized distribution, and the dashed green line represents the inflated Gaussian distribution.

bins of estimated slant slope except the first bin (i.e., 50 mm/km to 60 mm/km of estimated slant slope). This means that, typically, there were slightly more samples with positive errors than with negative errors. Thus, underestimates were about as likely as overestimates.

Once the samples of the estimation errors have been sorted into their corresponding bins, they are normalized by subtracting from each sample the mean value of the bin it belongs to and by dividing the resulting value by the standard deviation of the bin. Then, the tails of the entire distribution are overbounded following the process explained in Section 3.3.4.4.

Figure 5.14a presents the normalized slant slope error distribution. As can be observed, until an estimated slant slope of a 100 mm/km, the effect of having lower positive errors than negative errors due to the way in which the gradients were simulated as commented previously is clearly visible. Figure 5.14b presents the Gaussian tail overbounding process for all data bins. The overall inflation factor calculated was $I_{g_{iono}} = 2.31$.

Finally, Figure 5.15 shows with blue dots (situated in a straight line) the estimated maximum value that could occur inside each bin (e.g., 60 mm/km for the bin 50 - 60 mm/km depicted in the center of the bin), and with black triangles the overbounded value considering Equation 3.31. In addition, it

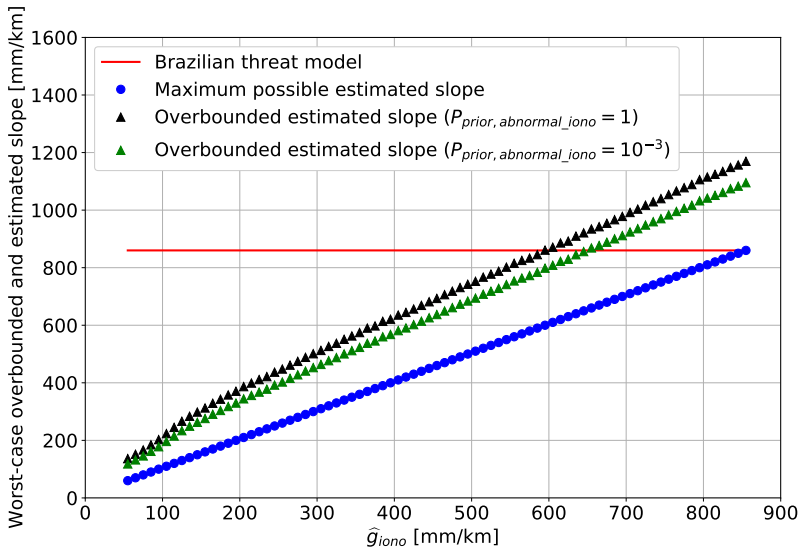

Figure 5.15: Worst case overbounded gradient slant slopes in comparison to the Brazilian threat model (solid red line). Blue dots (situated in a straight line) represent the maximum possible estimated slant slope inside each data bin, black triangles represent the worst case overbounded slant slope in each bin, and green triangles represent the overbounded slant slopes in each bin when a prior probability of occurrence of an ionospheric gradient of 1×10^{-3} is assumed.

shows with green triangles the overbounded value if instead of assuming a Probability of Non-bounded Errors of 1×10^{-8} (see Section 3.3.4.4), a value of 1×10^{-5} was assumed considering a prior probability of occurrence of an anomalous ionospheric gradient of 1×10^{-3} as in [36] for CONUS and [28] for Brazil. Note that the prior probability of 1×10^{-3} was chosen to be conservative for CONUS, but, as can be observed in Figure 5.2, it would not be conservative for Brazil at local nighttime.

As can be seen, up to an estimated gradient slope of 600 mm/km for the most conservative case (no prior probability considered), and 660 mm/km when assuming a prior probability, there would be a benefit when using this methodology in Brazil. Above those values, the overbounded slant slopes would be higher than the Brazilian threat model, and, in this case, the threat model as it is would be used instead.

5.3.2.3 Real-time performance of the monitor

Finally, this section analyzes the real time capability of the methodology. The algorithm distinguishes both parts of the gradient, the one corresponding to the downward slope and the one corresponding to the upward slope, and

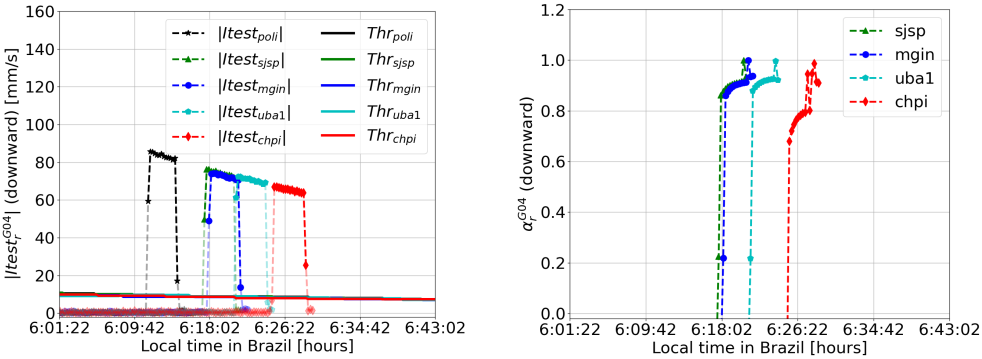

(a) Absolute value of the test statistics.

(b) Cross-correlation coefficients.

Figure 5.16: Absolute value of the test statistics and cross-correlation coefficients for the downward slope corresponding to Figure 5.9. The horizontal lines in Figure 5.16a represent the detection thresholds and the highlighted (non-transparent) markers the time epochs when the simulated ionospheric perturbation was detected.

treats them as two different gradients to compute their parameters. As commented previously, the ionospheric delay in the middle of both gradients was not considered in the simulations as a simplification but they were taken into account for the studies with real (actually observed) EPBs in Section 5.4.

Figure 5.16a presents the absolute value of the test statistics for the downward slope of the simulated gradient depicted in Figure 5.9. As can be observed, $\left|Itest_r^{G04}(t)\right|$ for the farthest away stations from "poli" (taken initially as the reference) was considerably different from $\left|Itest_{poli}^{G04}(t)\right|$. This is due to the distance between these stations (over 100 km) and the speed of the gradients (100 m/s), which meant that the elevation of the satellites had changed considerably when the gradient was detected at, e.g. "chpi". For this reason, the cross-correlation coefficients in Figure 5.16b converged to lower values than 1 after 60 seconds for stations "sjsp", "mgin", and "uba1", and 75 seconds for station "chpi". Towards the end of the curves, the cross-correlation coefficients experienced jumps, which resulted in the convergence criteria no longer being fulfilled. This is especially visible at station "chpi".

Figure 5.17a presents the absolute value of the test statistics for the upward slope of the simulated gradient depicted in Figure 5.9. As can be observed, again, the $\left|Itest_r^{G04}(t)\right|$ of the farthest away stations from "poli" were considerably different from $\left|Itest_{poli}^{G04}(t)\right|$ for the same reasons as above. The cross-correlation coefficients in Figure 5.17b converged to lower values than 1 after 45 seconds for all stations.

Note that the necessary waiting times for the convergence of the algorithm are considered by the network when calculating the "worst-case" real-time gra-

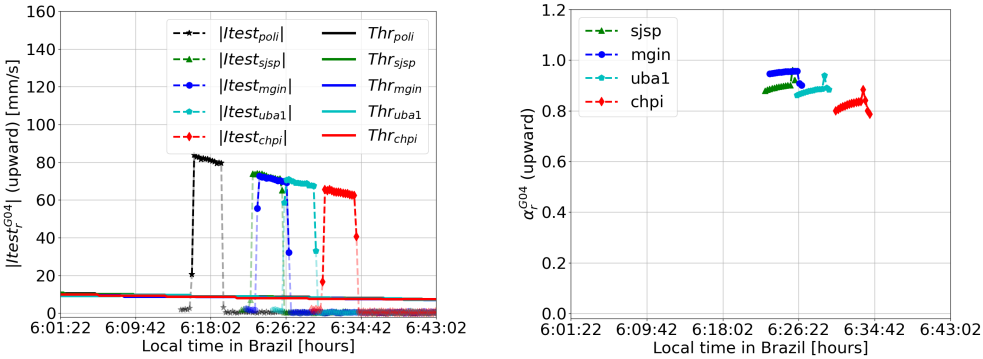

(a) Absolute value of the test statistics.

(b) Cross-correlation coefficients.

Figure 5.17: Absolute value of the test statistics and cross-correlation coefficients for the upward slope corresponding to Figure 5.9. The horizontal lines in Figure 5.17a represent the detection thresholds and the highlighted (non-transparent) markers the time epochs when the simulated ionospheric perturbation was detected.

dients that are transmitted to the GBAS stations. During the times when the algorithm has not converged, the network warns the protected GBAS stations to use the conservative threat model.

5.4 Evaluation of the monitor with a real ionospheric gradient

This section evaluates the methodology with a real anomalous ionospheric gradient measured by the network in Brazil. Unlike the simulated gradients, the real gradient was accompanied by many cycle slips that made the estimation of its parameters more difficult. However, it should be noted that, in a real implementation, receivers with a higher bandwidth which are more robust against scintillation could be installed. Furthermore, these receivers should have measurements available on the L5 frequency, which is more robust than L2 to this problem. In this case, only one of the two cycle slip detectors introduced in Section 3.3.1.1 was used for processing the measurements: the one based on the MW combination but, in this case, with a constant threshold of 4 meters. The reason is that the other cycle slip detector, based on the geometry-free combination of the carrier-phases, was very sensitive for the data in Brazil and would have discarded many parts of the signals if used. In addition, after the application of the cycle slip detector based on the MW, the cycle slips were visually inspected to avoid discarding excessive EPB measurements when the ionosphere variations were large but not due to a cycle slip.

The algorithm could estimate the selected real gradient by using the mea-

surements from satellites G01, G11, and G31, and the stations in the network under study on day 68 (local time) and 69 (GPS time) of year 2014, i.e. during the peak of Solar Cycle 24.

5.4.1 Detection

Figure 5.18a shows the slant ionospheric delays for six of the considered stations and satellite G01, which had an elevation between 60° and 70° during the local times depicted. Stations "uba1" and "neia" presented corrupted measurements during these times, thus they could not be used. Figure 5.18b shows the absolute value of the test statistics for the same satellite, $Itest_r^{G01}(t)$. In both figures, the highlighted (non-transparent) respective markers represent the epochs where the gradient was detected (i.e. the epochs when the ionospheric rates were above the detection thresholds of each station).

As can be observed, in stations "poli", "sjsp", "mgin", and "chpi", the detected ionospheric perturbations coincided with the steepest slopes in the slant ionospheric delays. Thus, the gradients were adequately detected by the algorithm. In stations "spbo" and "eesc", which are farther away from the other stations (see Figure 5.1), there were no detections during the same time as the others, but there were detections earlier, and the measurements presented many cycle slips and thus could not be used. Moreover, a few samples appear as undetected in Figure 5.18a. These samples belong to the intermediate zones between the different gradients that remained below the threshold in this case.

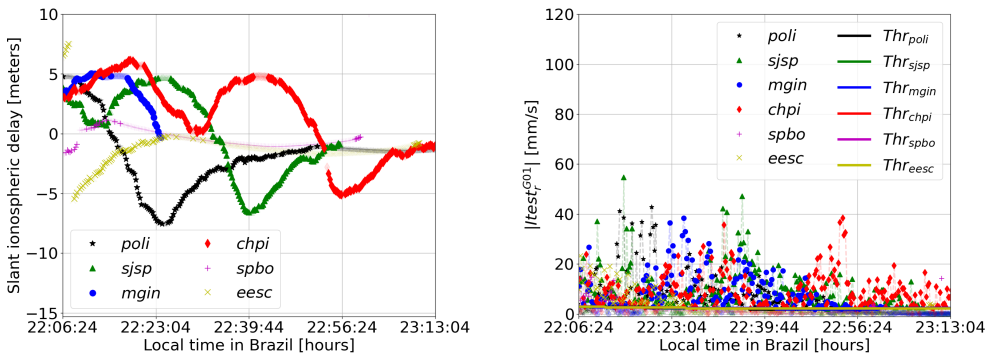

(a) Slant ionospheric delays.

(b) Absolute value of the test statistics.

Figure 5.18: Slant ionospheric delays and absolute value of the test statistics for the studied gradient experienced by satellite G01 (day 68 for local time and 69 for GPS time of year 2014, Brazil). The highlighted (non-transparent) markers of both figures represent the times when the gradient was detected. The horizontal lines in Figure 5.18b show the detection thresholds for each station.

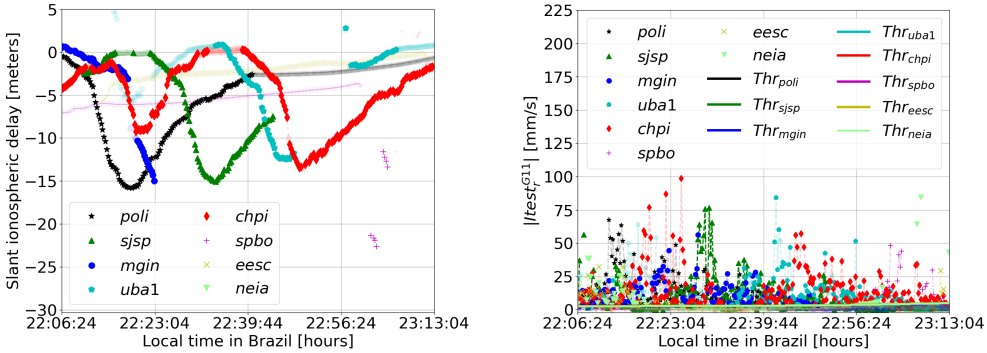

(a) Slant ionospheric delays. **(b)** Absolute value of the test statistics.

Figure 5.19: Slant ionospheric delays and absolute value of the test statistics for the studied gradient experienced by satellite G11 (day 68 for local time and 69 for GPS time of year 2014, Brazil). The highlighted (non-transparent) markers of both figures represent the times when the gradient was detected. The horizontal lines in Figure 5.19b show the detection thresholds for each station.

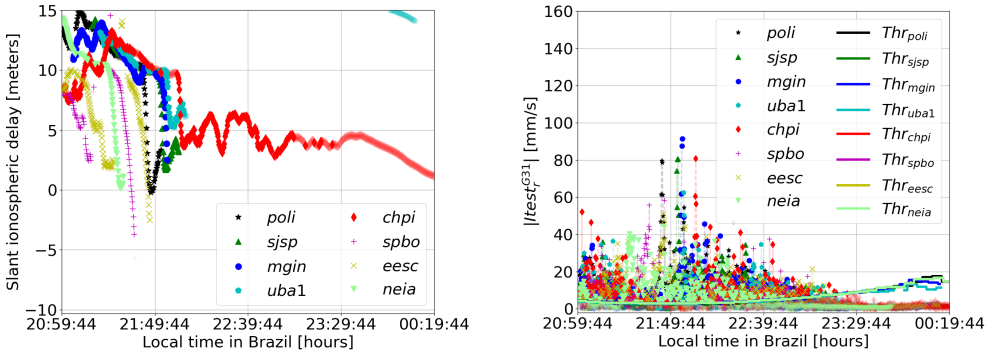

(a) Slant ionospheric delays. **(b)** Absolute value of the test statistics.

Figure 5.20: Slant ionospheric delays and absolute value of the test statistics for the studied gradient experienced by satellite G31 (day 68 for local time and 69 for GPS time of year 2014, Brazil). The highlighted (non-transparent) markers of both figures represent the times when the gradient was detected. The horizontal lines in Figure 5.20b show the detection thresholds for each station.

Figure 5.19a shows the slant ionospheric delays for all considered stations and satellite G11, which had an elevation between 65° and 45° during the local times depicted. Figure 5.19b shows the absolute value of the test statistics for the same satellite, $Itest_r^{G11}(t)$.

Here, the detected gradients also coincided with the steepest slopes in the slant ionospheric delays. Thus, the gradients were adequately detected by the algorithm. In this case, stations “poli”, “sjsp”, “mgin”, “uba1”, and “chpi”

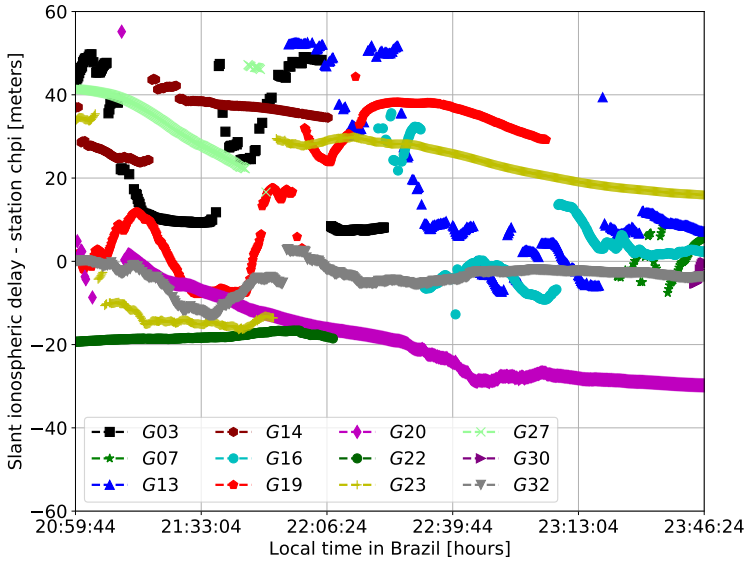

Figure 5.21: Slant ionospheric delays for the remaining visible satellites and station "chpi" during the local times under study in Figures 5.18, 5.19, and 5.20.

detected the gradient, but station "mgin" presented many cycle slips. Stations "neia", "eesc", and "spbo" detected the gradient before the others and also presented many cycle slips during the EPB passage.

Figure 5.20a shows the slant ionospheric delays for all the considered stations and satellite G31, which had an elevation between 53° and 33° during the local times depicted. Figure 5.20b shows the absolute value of the test statistics for the same satellite, $Itest_r^{G31}(t)$. In this case, the algorithm detected the gradient practically continuously for all stations.

Finally, Figure 5.21 shows the slant ionospheric delays calculated for the remaining visible satellites and one of the stations under study, "chpi". The remaining visible satellites either did not experience gradients at the same time or experienced gradients that produced excessive scintillation at "chpi" or the other stations, making it impossible to use their signals to estimate the gradient parameters.

Note that, in most satellites, the main EPBs were accompanied by earlier or later minor EPBs (e.g. satellites G01, G11, and G31 and station "chpi") or by intermediate periods between the two main EPB slopes with many oscillations (e.g. satellite G31 and station "chpi", where the upward part was not observed). For this reason, in very active periods, where the EPBs come in sequences and are accompanied by excessive scintillation, the network would be constantly alerting and the EPB parameters would be especially difficult

to estimate. In these cases, the network would indicate the use of the "worst-case" threat model for all times when the gradient parameters could not be estimated. To avoid on and off alerting under these conditions, a minimum alert period could be considered in which the network alerts would be deactivated and the conservative parameters of the current threat model would be used before recovery (normal network operation) would be allowed.

5.4.2 Estimation of the gradient parameters

Figures 5.18a, 5.19a, and 5.20a show that the slant ionospheric delays presented a similar shape when being measured by all affected stations and the same satellite. However, they also suggest that the gradient changed during its propagation; the drop in the ionospheric delay corresponding to the depletion was smaller when it reached the last stations impacted by it for satellites G01, G11, and G31. This implies that the previous assumption of a non-changing ionospheric gradient does not hold for the farthest station also in the case of Brazil. However, unlike in Alaska, where the gradient was changing in 20 km and a few minutes, in Brazil the gradient changed slowly and in distances of more than 100 km. This means that for the studies in Brazil, stations with longer baselines that the ones in Alaska could be used to estimate the gradients. Furthermore, data with a longer sampling interval can be used. As for the estimation with the simulated gradients, real data from stations "poli", "sjsp", "mgin", "uba1", and "chpi" was used for the estimation of the gradient parameters.

The algorithm was able to estimate the gradient parameters both in post-processing and in real time for satellite G31 (Section 5.4.2.1 and Section 5.4.2.2), and only in post-processing for satellites G01 and G11 (Section 5.4.2.3).

5.4.2.1 Estimation of the gradient parameters in post-processing with satellite G31

The first step of the algorithm searches for the station of reference. In the case of satellite G31, the algorithm assumed as the station of reference the first station impacted by the gradient of the subset used for the estimation ("poli").

Table 5.6 shows the cross-correlation coefficients calculated in post-processing considering as reference each of the different stations in the network. The stations in Table 5.6 appear in the order they detected the real ionospheric gradient. As can be observed, unlike Alaska, all stations presented high cross-correlations (above 0.9) with each other, which means that the gradient did not change much while on propagation from the $Itest_r^{G31}$ point of view. Therefore, the first station that detected the gradient was selected as the station

Reference station	α^{G31}_{poli}	α^{G31}_{sjsp}	α^{G31}_{mgin}	α^{G31}_{uba1}	α^{G31}_{chpi}
poli	1.000	0.952	0.950	0.950	0.960
sjsp	0.952	1.000	0.928	0.951	0.947
mgin	0.950	0.928	1.000	0.913	0.954
uba1	0.950	0.951	0.913	1.000	0.975
chpi	0.960	0.947	0.954	0.975	1.000

Table 5.6: Cross-correlation coefficients calculated in post-processing for satellite G31 considering the different stations in Brazil as reference.

of reference.

Moreover, as the sampling rate is different and also the characteristics of the gradients are different in Brazil and in Alaska, new values for the N_W and N_B parameters introduced in Section 3.3.4.1.1 were selected to adapt the general algorithm to this data set. The first parameter, N_W, refers to the time window designed to capture the part of the test statistic that starts to increase when the gradient begins but is still below the detection threshold. The second parameter, N_B, refers to the total size of the buffers considered for calculating the cross-correlation. The parameter N_W was selected to be 75 seconds to capture all parts of the gradient in Figure 5.20a plus a margin. The parameter N_B was selected to be at least 375 seconds to consider both N_W and a minimum gradient duration of 300 seconds.

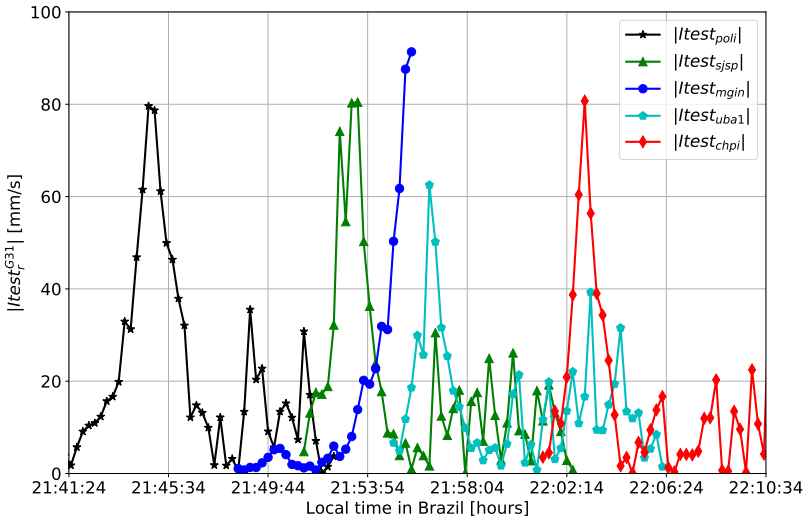

Figure 5.22: Absolute value of the test statistics corresponding to the gradient depicted in Figure 5.20a represented at the times when the gradient was considered for the estimation process for each station.

Figure 5.22 presents with solid lines the test statistics corresponding to the part of the signal that was considered for the estimation process. Note that, unlike in Alaska, the algorithm considered points of the test statistics for the estimation process after at least one of its points fell below the detection thresholds. The reason was that, in the case of Brazil, there were many oscillations of the signals, which made the test statistics much noisier than in the simulation case. These oscillations corresponded especially to the intermediate period between the EPB slopes, but were also found within the same slopes when they varied abruptly. Therefore, if the test statistic fell below the threshold for a period longer than 75 seconds, this time was considered to be the end of the current studied gradient. Otherwise, the new test statistic samples were considered to be part of the same gradient, and they were included in the same buffers for the cross-correlation process as long as there were no cycle slips or data gaps.

Initially, the gradient parameters observed by satellite G31 were calculated in post-processing using also a spline interpolation of the data at 10 Hz to get the best estimation possible and evaluate if there is a problem with time resolution in Brazil. Then, the post-processed results were compared with the ones obtained in real-time to evaluate the feasibility of the real-time concept in Brazil.

Station	v_{iono}^{G31} $[m/s]$	d_{iono}^{G31} $[^\circ]$	g_{iono}^{G31} $[mm/km]$	w_{iono}^{G31} $[km]$	α_r^{G31} $[-]$	κ_r^{G31} $[s]$	GI $[1/m]$
poli (Ref.)	165.8	44.0	-481.6	59.8	1.000	0.0	8.494×10^{-6}
sjsp	165.8	44.0	-507.6	41.8	0.952	500.4	8.494×10^{-6}
mgin	165.8	44.0	-543.7	38.2	0.950	645.0	8.494×10^{-6}
uba1	165.8	44.0	-379.1	35.8	0.950	703.4	8.494×10^{-6}
chpi	165.8	44.0	-474.6	33.5	0.960	1085.7	8.494×10^{-6}

Table 5.7: Estimated real gradient parameters in post-processing for satellite G31 and Brazil.

Table 5.7 summarizes the results in post-processing. The ionospheric gradient measured was an equatorial plasma bubble that traveled with an estimated direction of 44° (from the southwest to the northeast), a low-medium speed, 165.8 m/s, and a very steep slope, up to -543.7 mm/km. These results are compatible with the Brazilian threat model introduced in Section 2.4.2.2 and also agree with the time delays and distances calculated between the stations. Moreover, in the case of station "mgin", the signal was lost before the gradient was over, therefore the full width could not be estimated (see Figure 5.22).

5.4.2.2 Estimation of the gradient parameters in real time with satellite G31

The application of the algorithm in real time with the data recorded at a 15-second sampling rate presents the same limitations as in the simulation: it is necessary to have sufficient time for the cross-correlation estimate to converge, sufficient temporal resolution, adequate distance between stations to find sufficient correlation between the test statistics of the gradients that are the same, and test statistics that are not excessively noisy between the two slopes (downward and upward) and during the occurrence of the gradients.

Figure 5.23a shows the first limitation, where the convergence requirement (Equation 3.13) was not met until 21:54:14 for station "sjsp", 21:56:44 for station "uba1", and 22:03:29 for station "chpi" in local time. Station "mgin" did not meet the convergence criteria because the algorithm could not find cross-correlation coefficients whose difference at the current epoch and previous epochs was less than 1×10^{-2} for the last $N_C = 3$ samples. Therefore, it was not used to determine the real-time gradient propagation parameters.

Furthermore, Figure 5.23a also shows that, even once the algorithm converged, the cross-correlation coefficients did not remain constant as in the case of Alaska (see Figure 4.17). Instead, the cross-correlation coefficients experienced several jumps, and their value decreased as more samples from the test statistics were considered for their calculation and added to the buffers of Equation 3.9. This is because at the beginning of the detection at each of the stations, the samples that were included in the buffers for the cross-correlation calculation corresponded to the first of the gradient slopes (downward). As this slope is similar at almost all stations, the algorithm converged to high cross-correlation coefficients and time delays that were comparable to the post-processed results. Once the first main slope had passed, as previously explained, the test statistic samples belonging to the intermediate period between slopes (the EPB depletion part) were considered. In this period of time, the test statistics oscillated and experienced many cycle slips, resulting in the test statistics being considerably different from station to station. Although the algorithm was able to converge also in these cases, it took into account all samples within the buffer to calculate the cross-correlation coefficients, thus these were smaller than when it considered only the part corresponding to the main slope. This issue was not observable in the simulation because there both slopes were considered as two different gradients and the region between the downward and upward walls were not taken into account. Moreover, Figure 5.23b shows that although the value of the cross-correlation coefficients changed, the time delays remained practically constant during the time period under study until the signal was lost or there was a cycle slip.

Figure 5.24 shows with semi-transparent points the real-time estimates of

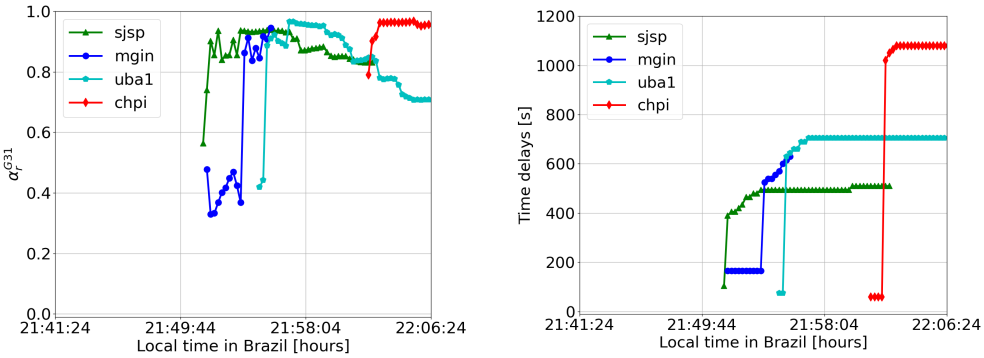

(a) Cross-correlation coefficients.

(b) Time delays.

Figure 5.23: Cross-correlation coefficients and time delays calculated in real time for the test statistics depicted in Figure 5.22 considering as station of reference "poli".

the speed and direction parameters before convergence of the algorithm and, highlighted with opaque points, the estimates that the algorithm calculated after convergence. As can be observed, the estimation errors were high for both speed and direction at the beginning, when the algorithm did not converge and the cross-correlation coefficients were low. However, the algorithm consistently estimated the speed and direction parameters after convergence. The estimated values changed smoothly when the same set of stations was used for their estimation, and there were no changes in the estimated time delays. However, this was not the case when the set of stations used changed or there was a variation in the time delay estimates. The two jumps that can be observed after the algorithm first converged in Figure 5.24 between 21:58:04 and 22:06:24 local time were due to a small variation in the time delay estimate for station "sjsp" at 22:00:04 local time and the use of stations "poli", "uba1", and "chpi" instead of "poli", "sjsp", and "uba1" for the estimation process from 22:02:44 local time. The set of stations used was different because, after 22:02:44 local time, the data from station "sjsp" had a gap during some epochs, and the algorithm concluded that the gradient had ended for this station. At the same time, the algorithm converged for station "chpi", thus it could be used in the estimation process. It can also be seen that there are points where the algorithm estimated correctly the propagation parameters, but they are not highlighted since the convergence criteria were not met. This was due to the aforementioned jumps in the cross-correlation coefficients that did not affect the estimation of the time delays between stations. This indicates that the convergence criteria used might be excessively conservative for the case of Brazil. Nevertheless, the optimization of the convergence criteria for different data sets was not addressed in this thesis and is part of future work.

The real-time speed estimates varied slightly between 114 m/s and 155 m/s,

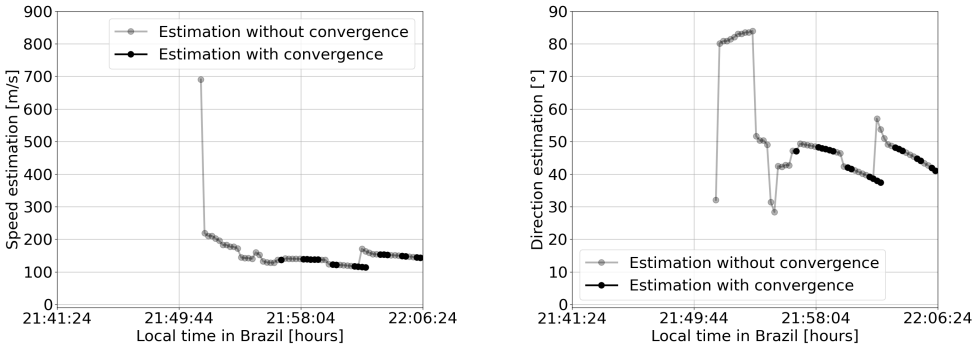

(a) Estimated speed of the gradient. **(b)** Estimated direction of the gradient.

Figure 5.24: Estimated speed and direction of the real gradient depicted in Figure 5.20a. The highlighted (non-transparent) points correspond to estimations that were calculated after the algorithm converged and the semi-transparent points correspond to estimations that were calculated before convergence.

while the direction estimates varied between 37.5° and 48.5°. These values, especially the last points of Figure 5.24 when the stations used were "poli", "uba1", and "chpi", 143.6 m/s and 41.3°, are similar to the 165 m/s speed and 44° direction obtained in post-processing with the data interpolated at 10 Hz (see Table 5.7). This means that the final real-time results converged to the post-processed values using three of the five stations that the algorithm considered to obtain the post-processed results.

The variations in the above parameters can be explained by the following reasons. Firstly, since the stations used are 100 km or more away from each other, it is possible that the EPB had slightly varied its propagation and shape, and the different stations were observing slightly different parts of the front. In addition, the elevation of the satellite G31 also changed from the time of detection at "poli" to the time of detection at "chpi", which had an impact on the IPP speed and therefore on the estimation of the gradient propagation parameters. Secondly, the algorithm used two different sets of stations for the estimation, as discussed previously. Since the center of the local coordinate system for the calculation of the estimation parameters changes depending on the position of the IPPs at the time of detection, it was different for calculations with different sets of stations. Moreover, the farther away the IPPs were from the center of the local reference coordinate system, the greater the approximation errors were at their location. Thirdly, using only three of the five available stations for real-time estimation meant that there was no redundancy since the minimum number of stations for the estimation process is three. Therefore, any errors (e.g. due to an insufficient sampling rate) on the

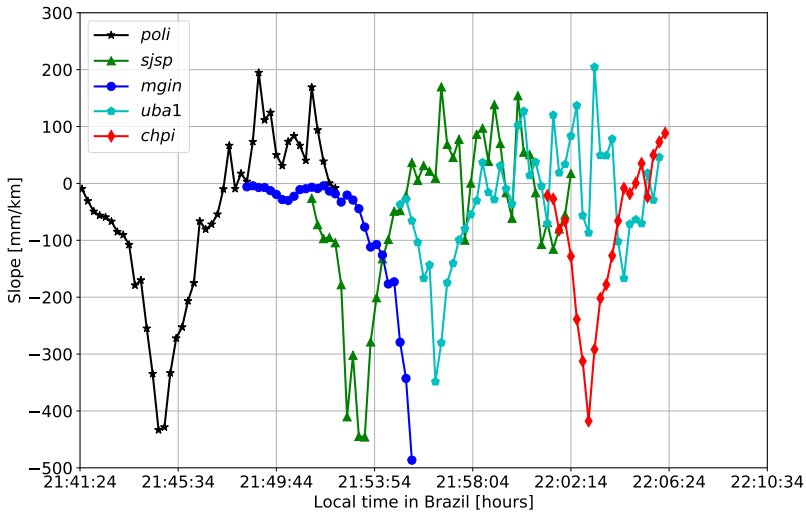

Figure 5.25: Estimated slant slope of the gradient depicted in Figure 5.20a using speed estimation after convergence.

estimation process had a greater impact in this case than when using a larger number of stations for estimation.

Finally, the real-time algorithm estimated the slant slope and width parameters. Since it was able to estimate gradient speed and direction after the maximum of the absolute value of $Itest_r^{G31}(t)$ was reached for stations "poli", "sjsp", "mgin", and "uba1", it recalculated the gradient slope backwards (as in Chapter 4) to find the "worst case" that could be transmitted to the GBAS stations. To this end, it used the first speed and direction estimates after convergence. If there were real-time estimates of speed and direction while the slope was being determined, the algorithm used these real-time estimates to calculate the slope at those times. Figure 5.25 shows the result. Here, the slant slope estimates were slightly lower but close to those calculated in post-processing (see Table 5.7) because the relative speed between the gradient and the IPPs was slightly higher. Thus, the same ionospheric delay rates resulted in lower slopes. Note that the gradient slopes are negative when the gradient is downward and are positive when it is upward, unless absolute values are taken.

The results from the width parameter estimate, which was determined after the gradient had finished affecting all stations, were: 62.7 km for "poli", 43.4 km for "sjsp", 40.7 km for "mgin", 37.8 km for "uba1", and 35.1 km for "chpi". In this case, the width was larger than in the post-processed results because the relative speed estimate between the gradient and the IPPs was larger. Thus, the same gradient duration T_W in Equation 3.28 was attributed to a larger width. Note that the determination of the width was based only

on the part of the test statistics that was continuously above the threshold, which corresponded to the downward slope. For this reason, the algorithm estimated a single width per station and satellite instead of two separate ones corresponding to the downward and upward slopes. The slopes and widths corresponding to the upward slopes could not be estimated since the carrier-phase measurements experienced many cycle slips.

5.4.2.3 Estimation of the gradient parameters with satellites G01 and G11

Figure 5.26 shows the part of the absolute value of $Itest_r^{G01}$ considered for the gradient parameter estimation process with satellite G01. As can be observed, station "uba1" was not available. Furthermore, the signal from station "mgin" was lost a few seconds after the start of the gradient and thus was also not considered for the estimation process. For this reason, the algorithm only considered stations "poli", "sjsp", and "chpi" to estimate the propagation parameters of the gradient.

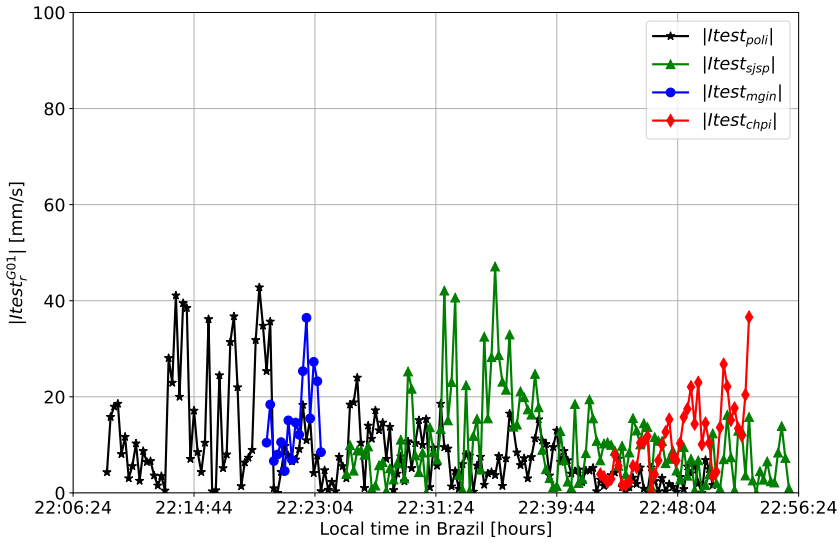

Figure 5.26: Absolute value of the test statistics corresponding to the gradient depicted in Figure 5.18a (satellite G01) represented at the times when the gradient was considered for the estimation process for each station.

The real-time algorithm could not find the station of reference because none of the stations had a cross-correlation coefficient greater than 0.9 with two other stations (see Table 5.8). Note that, the value of 0.9 could be excessively conservative and experiments with a less conservative value (e.g., 0.8) could be carried out. However, as commented previously, this is a trade-off and the lower this value is, the larger errors could be in the estimation of the

parameters due to the change of the gradient. Moreover, assuming the first impacted station ("poli") as the reference would not help in this case since the test statistics experienced cycle slips at "poli" and "sjsp" stations before the algorithm converged for station "chpi".

Reference station	α_{poli}^{G01}	α_{sjsp}^{G01}	α_{chpi}^{G01}
poli	1.000	0.637	0.634
sjsp	0.637	1.000	0.664
chpi	0.634	0.664	1.000

Table 5.8: Cross-correlation coefficients calculated in post-processing for satellite G01 considering the different stations in Brazil as reference.

In order to compare the results of the different satellites, the gradient parameters corresponding to the downward slope for satellite G01 were calculated in post-processing. The gradient propagation parameters estimated at a 15-second sampling rate were: 126.4 m/s of speed and 71.6° of direction (from southwest to northeast). The slopes of the gradient were: −447.2 mm/km, −467.2 mm/km, and −349.6 mm/km for stations "poli", "sjsp", and "chpi" respectively. Finally, the estimated widths were: 45.8 km, 53.0 km, and 42.0 km for stations "poli", "sjsp", and "chpi" respectively.

Therefore, the gradient experienced by this satellite had a less steep slant slope than the gradient experienced by satellite G31. These results were consistent with those obtained by satellite G31, as satellite G01 was at a higher elevation and thus would theoretically experience lower slant ionospheric delays. The speed estimate was also consistent with that estimated by satellite G31. However, the direction estimate experienced a larger variation when estimated from different satellites, although both satellites agreed that the gradient traveled from southwest to northeast. The reason appears to be that, in addition to the approximation errors and lack of redundancy already mentioned, satellite G01 measured the gradient relatively far away from satellite G31 and thus might have observed a different segment of the front.

Figure 5.27 shows the part of $Itest_r^{G11}$ considered for the gradient parameter estimation process with satellite G11. As can be observed, the signal from station "mgin" was also lost a few seconds after the start of the gradient for this satellite and thus was not considered for the estimation process.

Furthermore, the real-time algorithm could not find the station of reference because none of the stations had a cross-correlation coefficient greater than 0.9 with two other stations (see Table 5.9).

Therefore, the gradient parameters corresponding to the downward slope in post-processing were calculated again for comparison. The gradient para-

meters estimated in post-processing for satellite G11 at a 15-second sampling rate were: 103.2 m/s of speed and 82.3° of direction (from southwest to northeast). The gradient slopes were: −521.7 mm/km, −521.7 mm/km, −446.2 mm/km, and −479.2 mm/km for stations "poli", "sjsp", "uba1", and "chpi" respectively. Finally, the estimated widths were: 53.2 km, 29.2 km, 25.1 km, and 45.4 km for stations "poli", "sjsp", "uba1", and "chpi" respectively.

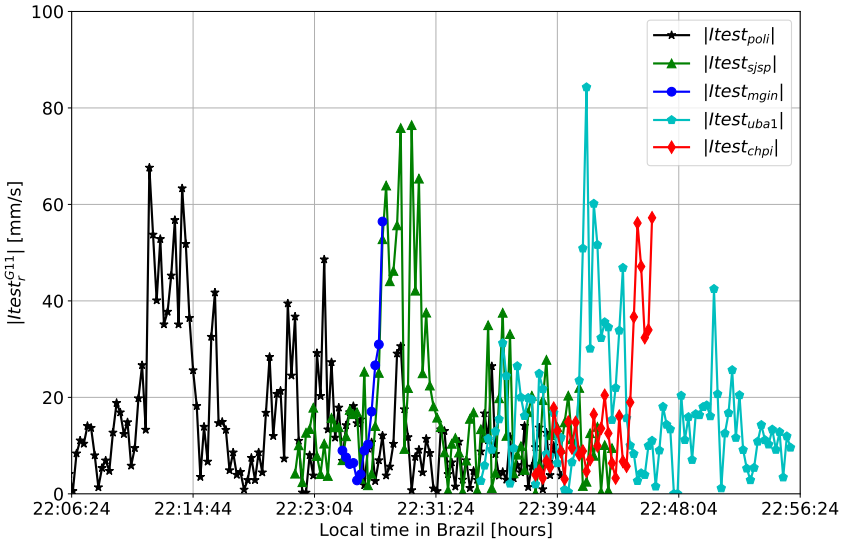

Figure 5.27: Absolute value of the test statistics corresponding to the gradient depicted in Figure 5.19a (satellite G11) represented at the times when the gradient was considered for the estimation process for each station.

Reference station	α^{G11}_{poli}	α^{G11}_{sjsp}	α^{G11}_{uba1}	α^{G11}_{chpi}
poli	1.000	0.785	0.730	0.646
sjsp	0.785	1.000	0.774	0.709
uba1	0.730	0.774	1.000	0.656
chpi	0.646	0.709	0.656	1.000

Table 5.9: Cross-correlation coefficients calculated in post-processing for satellite G11 considering the different stations in Brazil as reference.

5.4.3 Overbound of the estimated slant slope in real time in Brazil

The algorithm was able to estimate the gradient parameters for satellites G01 and G11 in post-processing, and for satellite G31 both in post-processing and in real time. The gradient parameters estimated for the three satellites were within the Brazilian threat model and thus, the uncertainty model for the slant slope estimation determined in Section 5.3.2.2 was valid.

Therefore, the estimated and overbounded gradient slant slopes for the different satellites were:

- **Satellite G31:** −662.62 mm/km for "poli", −677.89 mm/km for "sjsp", −727.71 mm/km for "mgin", −561.44 mm/km for "uba1", and −642.36 mm/km for "chpi".
- **Satellite G01:** −678.74 mm/km for "poli", −703.39 mm/km for "sjsp", and −562.38 mm/km for "chpi".
- **Satellite G11:** −769.40 mm/km for "poli", −769.40 mm/km for "sjsp", −677.74 mm/km for "uba1", and −717.49 mm/km for "chpi".

Note that these values were calculated considering a Probability of Non-bounded Errors of 1×10^{-8} and, therefore, $k_{ne} = 5.61$ in Equation 3.31.

5.5 Summary

This chapter has evaluated the performance of the methodology proposed in Chapter 3 with synthetic gradients simulated to be representative of the equatorial region and a real anomalous ionospheric gradient caused by an EPB measured by a reference network in Brazil.

The detection results with simulated gradients have shown the importance of having detection thresholds adapted to the ionospheric characteristics of the region (e.g., Appleton anomaly). Estimation results with simulated gradients have shown that average estimation errors were low for all the gradient parameters, which implies a good performance of the algorithm under the simulation conditions examined. The largest estimation errors occurred for the estimation of the slope when varying all gradient parameters. This error occurred due to the sensitivity of the test statistics to any error that produced variations of the signals every epoch such as noise and multipath. In addition, the results of the worst-case overbounded gradient slant slopes showed that using the concept proposed in this thesis could reduce the conservative assumptions that have to be taken to protect GBAS for gradients of up to 600 mm/km in Brazil. The analysis of the real-time capability of the algorithm showed that, since the stations were much more separated in Brazil than in Alaska, the cross-correlation coefficients converged to lower values for the farthest away stations in comparison to the results obtained in Chapter 4.

The results with a real gradient have indicated that, after convergence, the real-time algorithm using the data at a 15-second sampling rate was able to obtain estimation results for satellite G31 comparable to those obtained in post-processing with data interpolated at a 10 Hz sampling rate. The same ionospheric perturbation was experienced by satellites G01 and G11, but the

gradient could not be estimated with the algorithm in real time due to: (i) insufficient cross-correlation, which prevented automatic selection of the reference station, and (ii) scintillation causing excessive cycle slips, which prevented algorithm convergence at three stations at the same time. Note that, in a real implementation of the Network-GBAS concept, the network would be designed with the purpose of detecting and estimating anomalous ionospheric gradients and thus, the expected performance in real time would be higher. In the case that the detection network was based on ground stations fielded for other purposes, as with the RBMC network, only stations with adequate performance should be selected to be part of the network.

6

Performance of a Network-Supported GBAS Station in Nominal and Active Ionospheric Conditions

Chapters 4 and 5 have evaluated the performance of the methodology explained in Chapter 3 with two networks of stations located in Alaska and Brazil, respectively.

The proposed methodology not only provides a solution to detect and estimate anomalous ionospheric gradients but also provides an associated integrity concept to ensure the integrity of the GBAS stations. On the one hand, when the network does not detect any anomalous ionospheric gradients, it sets the Minimum Detectable Gradient (MDG) as the maximum gradient that can occur without being detected. Associated with this MDG, I have proposed a method to calculate, based on the integrity tree in Figure 2.2, the probability of missed detection of ionospheric anomalies that must be covered by each station in the network. On the other hand, when the network detects an anomalous ionospheric gradient, it estimates the gradient slant slope per satellite and appropriately overbounds it. In this way, the current "worst-case" threat model can be safely substituted for what is being measured and still ensure integrity. In addition, I have also given consideration to cases where the network may fail, such as when there are false alerts or the algorithm does not converge; in these cases, the network uses the current conservative threat model established prior to operations. Therefore, in the "worst-case" scenario of network operation, GBAS stations would use the same conservative threat model they use today.

The main objective of this chapter is to apply the results obtained in Chapter 5 to a simulated GBAS station situated in Brazil. The idea behind is to compare the current availability that a simulated GBAS station would have with its availability if it were protected by a network of surrounding stations in the following cases: i) 24 hours of a nominal ("calm") day, and ii) 24 hours of an active day.

This chapter is structured as follows: Section 6.1 selects the airport to locate the simulated GBAS station at, and Section 6.2 assesses the availability of the simulated CAT I GBAS station under nominal and active ionospheric conditions.

6.1 Selection of the simulated GBAS station location

Figure 6.1 shows the location of three real airports that are situated within the area of coverage of the network selected for the studies of Brazil (see Chapter 5). The blue dots are the locations of the stations of the network considered for the detection of the ionospheric perturbations. The red dot is the location of São Paulo/Guarulhos – Governor André Franco Montoro International Airport (GRU), the yellow dot is the location of Viracopos/Campinas International Airport (VCP), and the green dot is the location of Guaratinguetá Airport (GUJ).

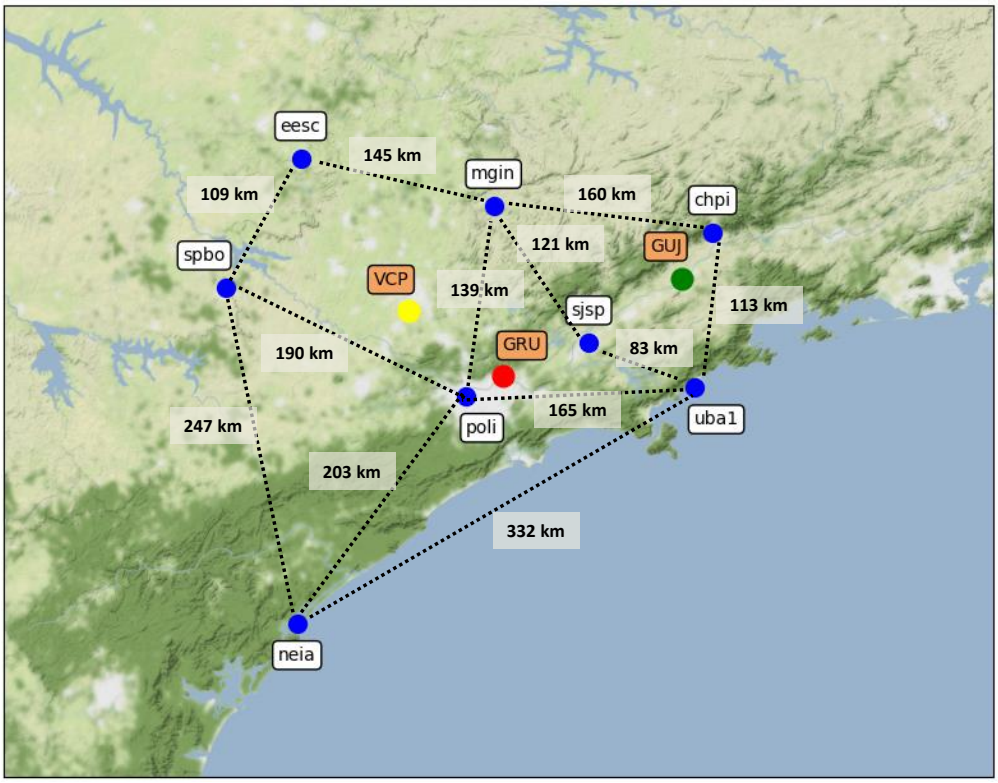

Figure 6.1: Locations of the network of monitoring stations and three airports in Brazil.

Considering EPB propagation characteristics from both the Brazilian threat model (Table 2.6) and from the real measurements of Section 5.4.2, only three

stations ("neia", "poli", and "spbo") would be able to detect anomalous ionospheric gradients before they affect "GRU" and "VCP" airports. In addition, the baselines between these stations are significantly longer than those of the stations protecting "GUJ" airport. As discussed previously, this is not optimal since the ionospheric disturbances could affect, for example, a satellite visible to "GRU" airport that was not visible at station "neia".

Therefore, in order to adequately show the benefits of the Network-GBAS methodology introduced in Section 3.3.2, Guaratinguetá Airport (GUJ) was selected as the location for the simulated GBAS station.

6.2 Availability analysis of a simulated CAT I GBAS station under nominal and active ionospheric conditions

As explained in Section 2.3.2 of Chapter 2, the availability of a GBAS station is determined through the calculation of the so-called Protection Levels (PLs). They are calculated based on models of the individual error components in the pseudorange measurements (σ_{GBAS}), a sub-allocated integrity risk, and the instantaneous satellite geometry ($\boldsymbol{G}$). The protection levels are then compared with the Alert Limits (ALs) and the system is declared unavailable if at least one of the PLs exceeds the corresponding AL.

In nominal conditions (i.e. no significant ionospheric activity is present), the PLs bound the remaining residual errors after application of the corrections, which are mainly due to the ground and aircraft noise and multipath errors, tropospheric error, and ionospheric error. However, the PLs do not bound errors produced by large ionospheric gradients acting between the GBAS stations and the aircraft on approach.

To protect airborne users against these large and undetected ionospheric gradients, CAT I GBAS ground stations (GAST C) verify by simulation that each satellite geometry potentially usable at the aircraft (PLs $\leq$ ALs) is safe in the presence of the "worst-case" ionosphere-anomaly threat applicable in the region using a process called Position Domain Geometry Screening (PDGS) ([26, 27, 28, 83, 84]). In case a simulated satellite geometry is not safe, the ground station inflates the integrity parameters (mainly the σ_{pr_gnd} and σ_{vig} components of σ_{GBAS}) so that at least one PL exceeds an AL when an arriving aircraft aims to use this satellite geometry, making GBAS unavailable. From the PLs, only the VPL is taken into account because the most stringent requirements are defined for the vertical domain.

The main problem of this methodology is that it has to assume that the

"worst-case" ionospheric gradient, which is the largest anomalous ionospheric gradient that has ever been observed in the region, is always present. This is because the integrity monitors of the GAST C ground stations are not able to observe all possible hazardous ionospheric gradients. This assumption protects GBAS users against hazardous ionospheric gradients but results in a high loss of GBAS availability in regions like Brazil, where it is well below what is required for a GBAS station to be installed at an airport (see Section 2.2). To solve this problem, the authors in [28] propose the use of the CONUS threat model during daytime hours in Brazil, since this threat model is able to bound the largest gradients that typically occur during the day in that region. However, this is not a solution for nighttime hours, where the largest threat model has to be assumed (Brazilian threat model) and GBAS availability remains extremely low (e.g. around 58.3% for Galeão International Airport (GIG) in Rio de Janeiro, [28]).

Nevertheless, the results from Chapter 5 suggested that assuming that these anomalous ionospheric gradients are always present during the nighttime hours of every day of the year is unrealistic. These large ionospheric perturbations occur during certain times of the year (see Figures 5.2 and 5.3) and generally only in years close to a solar maximum. Furthermore, within the active days, not all nighttime hours are affected by EPBs.

For this reason, this thesis proposes to replace the slope (g_{iono}) of the conservative Brazilian threat model (860 mm/km) used within the PDGS with the output of the monitoring network for each of the satellites as explained in Section 3.4 of Chapter 3. This output would be: (i) the MDG if no gradient was detected for that satellite by all the stations considered, (ii) the real-time estimated and overbounded gradient slope for that satellite if an anomalous gradient was detected and its parameters could be estimated, or (iii) the current conservative threat model if a gradient was detected for that satellite, but the network could not estimate its parameters due, for example, to false alerts. Note that the network adapts in real-time the threat model used within PDGS per satellite.

6.2.1 Computation of the Minimum Detectable Gradient for Guaratinguetá Airport (GUJ) in Brazil

The computation of the MDG requires first the calculation of the MDE for each of the stations of the network (see Section 3.3.2 of Chapter 3).

As commented previously, EPBs do not propagate in all directions but move along lines of constant MODIP (e.g. $MODIP = 58°$). Therefore, stations "neia", "spbo", "poli", "eesc", "mgin", "sjsp", and "uba1" could detect an anomalous ionospheric gradient propagating following these MODIP lines

in the area of interest before it affected GUJ airport (see Figure 6.1). For this reason, seven stations would protect a station located at GUJ airport. Therefore, the network would assign a $P_{md,abnormal\_iono,r} = 10^{-1}$ for six of the stations and a $P_{md,abnormal\_iono,r} = 10^{-2}$ for one of them that results in the $P_{md,abnormal\_iono} = 1 \times 10^{-8}$ necessary to meet the integrity requirement. Of the available stations, station "sjsp" is the closest to GUJ airport and therefore the most important for detecting ionospheric perturbations before they affect the simulated GBAS station. Additionally, this is the station whose IPPs will experience gradients most similar to those experienced by the simulated GBAS station given its proximity. Therefore, station "sjsp" should have the lowest probability of missed detection of all the monitoring stations considered. For this reason, a $P_{md,abnormal\_iono,sjsp} = 10^{-2}$ and a $P_{md,abnormal\_iono,r} = 10^{-1}$ for stations "neia", "spbo", "poli", "eesc", "mgin", and "uba1" were selected. Station "chpi" is located after GUJ airport and thus would not be able to protect the airport from undetected EPBs according to their propagation direction.

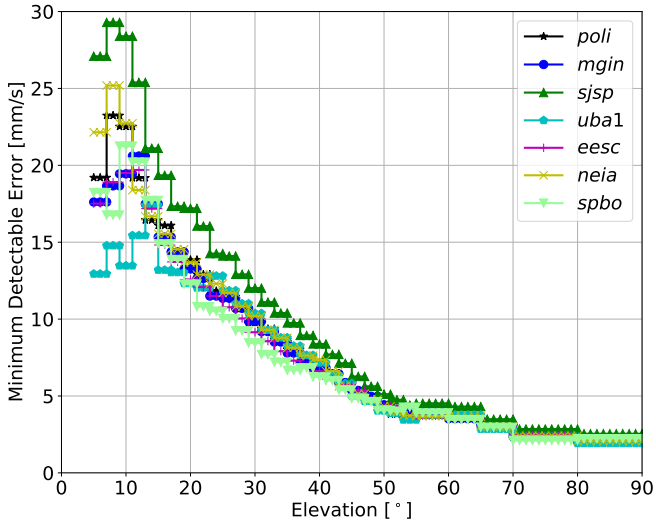

Figure 6.2: Minimum Detectable Error (MDE) for all stations considered in Brazil.

Figure 6.2 shows the MDE in mm/s (same units as the detection thresholds) calculated following Equation 3.7 for each of the stations considered. As can be observed, the MDE is similar for all stations with the exception of "sjsp" because a different $P_{md,abnormal\_iono,r}$ was selected for this station. Furthermore, there are smaller differences among the values for the other stations, especially for satellite elevations below 20°. This is because different stations have different noise and nominal ionosphere characteristics, as commented in Section 5.3.1.

Once the MDE has been calculated for each station, the MDG of the network for the particular GBAS station location can be computed, ideally, by means of exhaustive simulations. These exhaustive simulations should cover all reasonable variations of the gradient parameters, considering different values for slopes $g_{iono,vert_1}$ and $g_{iono,vert_2}$ and widths w_{iono_1} and w_{iono_2}. In addition, they should also consider all reasonable IPP motions (especially with respect to the gradient propagation) and all reasonable gradient onset times ($t_{iono,0}$). This type of simulations are computationally demanding since for each variation of each gradient parameter all reasonable variations of the other parameters must be simulated. In addition, an adequate step must be found for the variation of each of the gradient parameters that represents a significant variation of the parameter without losing important intermediate values. For this reason, in this chapter, simulations similar to those performed in Section 5.2 of Chapter 5 have been carried out to show the methodology to be followed for the MDG calculation. Therefore, although the number of simulations was large (860,706 simulations), these simulations were not exhaustive (e.g., the gradient onset time was simulated every hour, see Table 5.3). For this study, synthetic ionospheric perturbations described by the equations in Table 5.2 and depicted in Figure 5.6 were simulated. The already defined simulation gradient parameters were varied within their ranges in the Brazilian threat model (see Table 5.3) up to a maximum slant additional delay of 35 meters, and the trajectory and initial longitude and latitude for the simulated EPBs were the same as in Section 5.2. These synthetic perturbations were then added to the nominal slant ionospheric delays calculated with Equation 3.1 and the measurements recorded by the network on day 145 of 2014 (one of the "calm" days specified in Section 5.1). Note that, as in Chapter 5, it is assumed that the information recorded on this day is representative of all nominal hours and nominal days in terms of multipath and noise present in the measurements, satellite geometries, and nominal slant ionospheric delays. However, this is a simplification, and more simulations (exhaustive) with measurements from different days of the year and different years would be needed to obtain more representative results. Moreover, although the EPBs are known to occur during the nighttime (especially after sunset), they were simulated during the 24 hours of day 145 to have more satellite geometries available. As a simplification, $g_{iono,vert_1} = g_{iono,vert_2}$ and $w_{iono_1} = w_{iono_2}$ were considered as in Chapter 5.

With this data, $Itest_r^j$ was calculated for each station r and each satellite j following Equation 3.3. Next, the algorithm first computed the MDG per satellite as follows. If, at least, the absolute value of $Itest_r^j$ corresponding to one of the stations, r, and one satellite, j, exceeded its corresponding MDE_r (see Figure 6.2) before the IPP belonging to the same satellite, j, and the simulated GBAS station was affected, that simulated ionospheric perturbation was guaranteed to be detected for that satellite with the required $P_{md,abnormal\_iono,r}$.

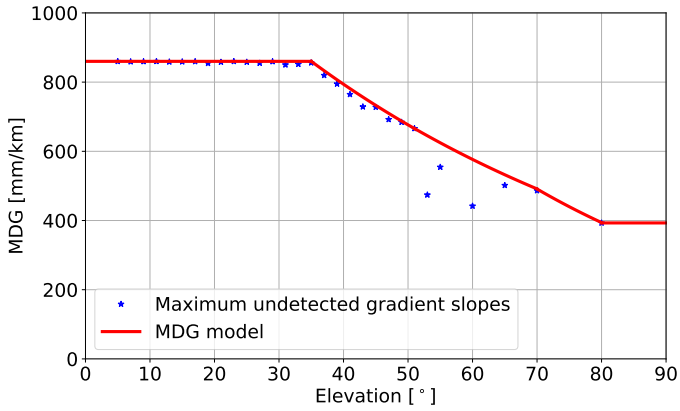

Figure 6.3: Minimum Detectable Gradient (MDG) calculated for a simulated GBAS station situated in Guaratinguetá Airport (GUJ). The blue stars show the maximum undetected (i.e., with the required probability of missed detection) gradient slant slopes per elevation bin among all the simulations. The red lines show a curve fitting to these points.

Note that for the MDG calculation the MDE values for each station were used (Figure 6.2) instead of the detection thresholds derived in Chapter 5 for this network (Figure 5.8) to take into account the probability of missed detection. Therefore, any test statistic above the MDE_r was assumed to be detected with the probability of missed detection assigned to each of the stations ($P_{md,abnormal\_iono,r}$) to meet the integrity requirement, assuming that the detection threshold for each of the stations was the one represented by the P_{fa} selected in Chapter 5 (depicted in Figure 5.8). However, it could occur that the absolute value of $Itest_r^j$ does not exceed the MDE for any of the stations before the gradient affects the IPP of the same satellite and the simulated GBAS station. This could happen if the ionospheric perturbation generated low $Itest_r^j$ because the gradient slopes were not high or because the relative speeds between the ionospheric gradient and the IPPs of the stations were low. In these cases, the network considered that this ionospheric perturbation could not be detected for that satellite with the required probability of missed detection, and the slant slope of this gradient was saved.

Once the simulation finished, the saved slant slope values measured by each of the satellites were sorted into elevation bins. The same bin sizes as for the calculation of the detection thresholds and MDEs were selected. The algorithm then selected the maximum slope value in mm/km for each bin, regardless of which satellite experienced it, as the minimum detectable gradient for each elevation bin.

Figure 6.3 shows with blue stars the maximum undetected (i.e., with the

required probability of missed detection) gradient slant slopes in mm/km per elevation bin. These points indicate that at least one gradient with that slope was not detected with the required probability of missed detection by any station for a particular satellite before affecting the IPP for the same satellite and GUJ airport. As can be seen, up to an elevation of 35°, ionospheric gradients of the same size as the conservative threat model (860 mm/km) affected at least one satellite visible at GUJ airport without being detected with the required probability of missed detection by any of the stations previously. Most of these points belonged to undetected gradient slopes produced during the simulation with the minimum front speed considered in the Brazilian threat model, 40 m/s. This occurred for several reasons. In some cases, the relative speeds between the IPPs and the simulated ionospheric perturbations were low, thus the absolute values of $Itest_r^j$ were not sufficient to exceed the corresponding MDE_r values. This was especially the case when the IPPs moved in the same direction as the simulated ionospheric perturbations. Furthermore, there were cases where a satellite rose above the elevation mask almost at the same time as the simulated ionospheric disturbance affected GUJ airport. Therefore, this ionospheric disturbance affected the IPP corresponding to GUJ airport and that specific satellite, and the other stations did not detect it because the corresponding satellite was not visible when the disturbance passed over them. This problem was aggravated by the presence of gaps in the data from the different stations, especially from the "uba1" station. These data gaps caused some ionospheric disturbances to go undetected because the measurements from the stations that would have protected GUJ airport from them were not available at these times. Moreover, it can be seen that the maximum undetected slope values for satellite elevations between 51° and 70° are lower than what would be expected given the values for the other elevation bins. The reason is that, in the cases examined during the simulations, higher relative speeds between the simulated ionospheric perturbations and the IPPs corresponding to the satellites at these elevations were found, thus perturbations with lower slopes than for lower elevations were more easily detected. In the case of carrying out exhaustive simulations considering smaller steps for the variation of gradient parameters (e.g., gradient onset time) it is possible that larger values would be found for these maximum undetected gradient slopes, especially for these satellite elevations.

Note that, for this analysis, detections from non-GPS satellites whose IPPs are close to the ones under study have not been considered. This could bring a benefit especially if other satellite constellations were available. These additional satellites could be considered for the detection of anomalous ionospheric gradients and could be used for protecting nearby GPS satellites, making the overall MDG less conservative.

Finally, in order to introduce the obtained MDG in the PDGS algorithm,

a model with the blue stars from Figure 6.3 was derived. Table 6.1 describes this model, represented by the red line in Figure 6.3.

Minimum Detectable Gradient in slant [mm/km]	**Elevation** [°]
$g_{iono} = 860$	$\theta^j \leq 35°$
$g_{iono} = 860 \cdot e^{-0.016 \cdot (\theta^j - 35°)}$	$35° < \theta^j \leq 51°$
$g_{iono} = 665.9 \cdot e^{-0.016 \cdot (\theta^j - 51°)}$	$51° < \theta^j \leq 70°$
$g_{iono} = 491 \cdot e^{-0.022 \cdot (\theta^j - 70°)}$	$70° < \theta^j \leq 80°$
$g_{iono} = 393$	$\theta^j > 80°$

Table 6.1: Model for the Minimum Detectable Gradient.

6.2.2 GBAS availability assessment for the 25th of May of 2014 (calm day) and GUJ airport

For the evaluation of the Network-GBAS performance on a nominal ("calm") day, day 145 of the year 2014 (i.e. 25th of May 2014), which is a day without significant ionospheric activity (see Section 5.1.2), was selected. Moreover, a GBAS station located at Guaratinguetá Airport (GUJ) at a latitude of −22.791° (South), a longitude of −45.205° (West), and an altitude of 537 meters, was assumed as discussed in Section 6.1.

Once a valid MDG for the network coverage area has been derived, the Network-GBAS algorithm calculates the gradient slope parameter (g_{iono}) to be used at each epoch within the PDGS considering the network's output in real time.

For this purpose, the Network-GBAS algorithm calculated the test statistics ($Itest_r^j$) with Equation 3.3 (Section 3.3.1.1) using the real measurements recorded during the 24 hours of this day for all GPS satellites. Then, it compared the absolute value of each of the $Itest_r^j$ with the respective detection thresholds depicted in Figure 5.8 (Section 5.3.1) by applying Equation 3.8 (Section 3.3.3). Note that, in this case, the objective is detecting the gradients satisfying the probability of false alert and not the calculation of the MDG. Therefore, the detection thresholds have been used here instead of the MDE.

During this day, the network did not detect any anomalous ionospheric perturbations for any of the satellites or any of the stations. Figure 6.4 shows an example of the test statistics and detection thresholds for the 24 hours of the day and six satellites. Therefore, as a result, the Network-GBAS indicated the use of the MDG at all times of the day.

As can be observed in Figure 6.4, the test statistics for satellites G12, G29, and G31 got very close to the detection thresholds. At the epochs when this

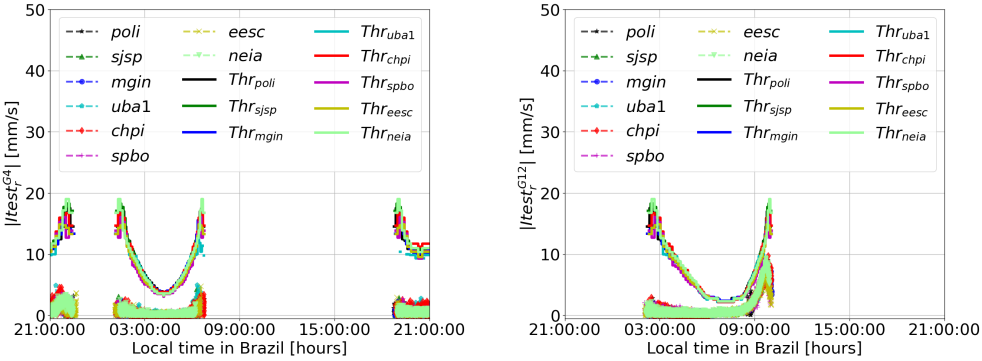

(a) Satellite G04. **(b)** Satellite G12.

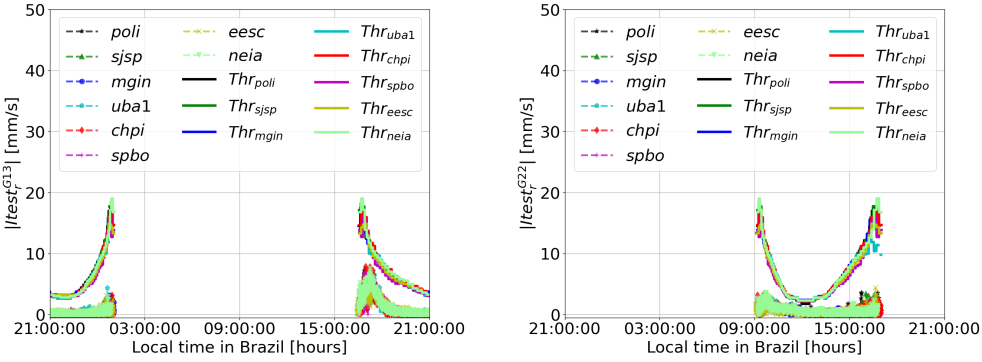

(c) Satellite G13. **(d)** Satellite G22.

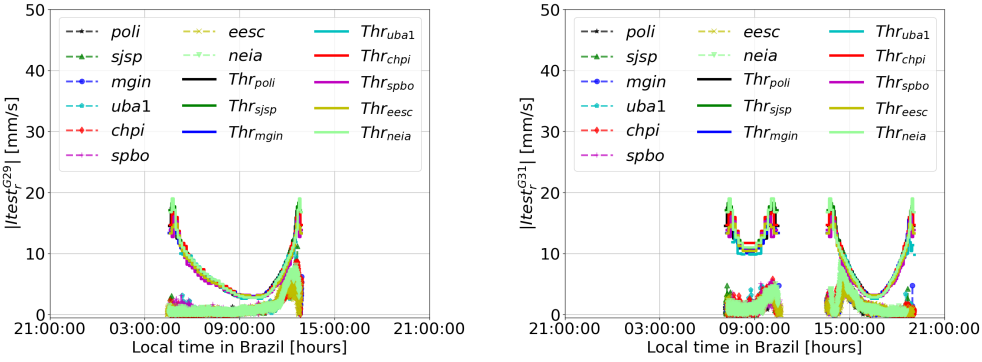

(e) Satellite G29. **(f)** Satellite G31.

Figure 6.4: Examples of test statistics and detection thresholds for different satellites during the 25th of May of 2014 (day 145 of year 2014).

occurred, these satellites were at low elevations crossing the Appleton anomaly. Therefore, these satellites experienced a raise in their slant ionospheric delay values that was also observable in the test statistics. Moreover, the detection thresholds for Brazil were derived considering a $P_{fa} = 10^{-4}$, but the number of samples in each elevation bin (considered to be statistically independent)

was, in some cases, close to 10^5 (see Figures 3.8b and 3.9b). This means that there could be cases where some samples of the test statistics were above the thresholds, even in the nominal case.

6.2.2.1 Results of EPB threat mitigation via PDGS using the Network-GBAS in a calm day

As commented previously, the network's output is the input to the PDGS algorithm. Therefore, the next step is to calculate the inflation factors for the selected day using the PDGS algorithm adapted for Brazil, as proposed in [28]. PDGS needs different parameters as input: the ground, air, tropospheric, and ionospheric residual error models, the satellite geometries to be simulated, the Decision Height (DH) distance (x_{Air}), and the values of the threat model.

For the ground error model, σ_{pr_gnd} in Equation 2.20 (Section 2.3.3.3), the Ground Accuracy Designator C (GAD C) (see Table 2.4) was selected as this is the level of noise and multipath expected in a real GBAS ground station. For the airborne error model, σ_{pr_air} in Equation 2.25 (Section 2.3.3.6), the same strategy as in [28] was followed. On one hand, the more severe airborne error model was selected for the Maximum Ionosphere-induced Error in Vertical (MIEV) calculation (i.e., airborne noise model, σ_n, with Airborne Accuracy Designator A (AAD A)). On the other hand, the theoretical minimum airborne error model (i.e., $\sigma_n = 0$) was selected for computing the VPLs. These selection, as mentioned in [28], is conservative because it maximizes the MIEV while minimizing the VPL, which makes more likely that the integrity parameters need to be inflated. The troposheric residual error was computed as described in Section 2.3.3.4 using Equation 2.21. Additionally, a broadcast $\sigma_{vig,nom}$ of 14 mm/km was used for daytime conditions as proposed in [22] and a hypothesized $\sigma_{vig,nom}$ of 15 mm/km was used for nighttime conditions as proposed in [28]. The total ionospheric error (σ_{iono}) was calculated with Equation 2.22 of Section 2.3.3.5 and the total uncertainty of the residual differential pseudorange error (σ_{GBAS}) was computed using Equation 2.17.

Also, the PDGS algorithm adapted for Brazil needs to know the possible range of EPB propagation directions to discard pairs of satellites that are physically improbable to be affected at the same time, as explained in [28]. For this purpose, an EPB direction of 58° measured in the clockwise direction from the North Pole was selected as discussed in Section 5.2. Only this direction was considered because it corresponds to the line of $MODIP = -30°$, which is close to the network under study. However, a more exhaustive study should consider a range of directions around this mean value (e.g. between 43° and 73° for the mean direction of 58°) selected from sufficient estimates of the usual directions of the EPBs in this region.

Furthermore, the almanac that describes the Standard 24 satellite GPS constellation (Section 3.2 and Table A.2-1. of [104]) was used to compute satellite geometries at selected times on the selected day. A constant speed of 70 m/s was selected for the approaching aircraft and a DH distance, x_{Air}, was assumed to be located 1 to 4 km (every 1 km) from the GBAS ground facility to obtain comparable results to the results obtained for Rio de Janeiro in [28], which is geographically close to "GUJ" airport. Unlike in [28], only the cases when the aircraft was exactly situated at the different DHs were simulated. The reason behind is that these cases are typically the ones that require the most inflation of the integrity parameters since both VAL and TEL, which increase with the distance to the DH, have the lowest values.

Three different simulations were conducted with the PDGS algorithm that generated the required inflation factors every 15 seconds for over 24 hours. In each of the simulations, the g_{iono} parameter to calculate the EPB ionosphere-induced range errors in Equations 2.31, 2.33, and 2.35 (Section 2.4.3.1 of Chapter 2) was the following: (i) the elevation-dependent maximum slope from the CONUS threat model for daytime (06:00 to 18:00 local time at GUJ), (ii) the 860 mm/km maximum slope from the Brazilian threat model for nighttime (18:00 to 06:00 local time at GUJ), and (iii) the slope that the Network-GBAS indicated as output in real-time for nighttime (18:00 to 06:00 local time at GUJ). In this case, since no gradient was detected, the output from the Network-GBAS was the elevation-dependent slope from the MDG.

Within PDGS, two VPLs were considered: the VPL under the fault-free hypothesis, VPL_{H_0}, and the vertical ephemeris protection level, VPB. PDGS uses the maximum of the two to compute inflation factors. For the calculation of VPL_{H_0} with Equation 2.15, a fault-free missed detection multiplier, k_{ffmd}, of 5.847 was used, assuming that four ground subsystem reference receivers are installed (see Table 2.3). For the calculation of VPB with Equation 2.18, an ephemeris missed detection multiplier, k_{md_e}, of 3.80 and an ephemeris decorrelation parameter for satellite j, P^j, of 0.00018 were used as in [28].

Figure 6.5 shows the maximum inflation factors for both σ_{vig}, I_{vig}, and σ_{pr_gnd}, I_{gnd}, for the three simulations at each epoch. During the daytime, σ_{pr_gnd} did not need to be inflated because the inflated σ_{vig} did not reach the maximum allowable limit of 25.5 mm/km (the maximum allowable I_{vig} is 1.82 considering $\sigma_{vig,nom}$ = 14 mm/km). This is because the CONUS ionospheric threat model, which is used during the day, is significantly less conservative than the Brazilian ionospheric threat model, therefore fewer satellite geometries had to be discarded within the PDGS algorithm.

During the nighttime, inflating only σ_{vig} was not sufficient to completely remove all potentially unsafe satellite geometries when using both the conservative Brazilian threat model (860 mm/km, blue line) and the MDG (black line).

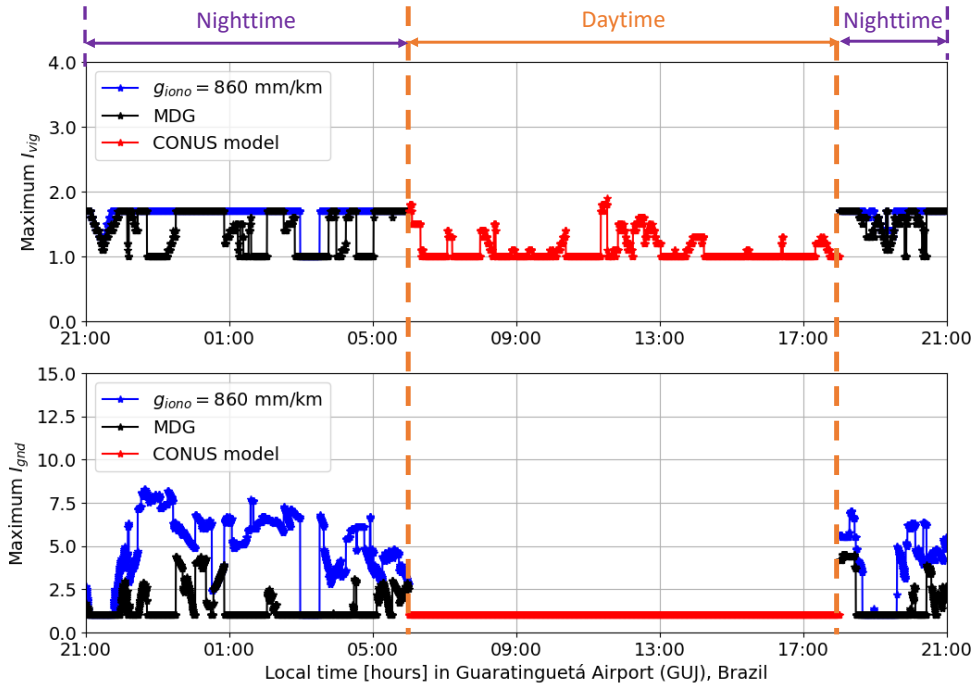

Figure 6.5: Maximum inflation factors of σ_{vig}, I_{vig}, and of σ_{pr_gnd}, I_{gnd} among the 4 simulated DH distances at each epoch (day 145 of year 2014). The CONUS threat model (red line) was used during daytime (06:00-18:00 local time), and both the Brazilian threat model (blue line) and the MDG (black line) were used during nighttime (18:00-06:00 local time).

In both cases, I_{vig} reached its maximum allowable value of 1.7 (corresponding to a $\sigma_{vig,nom}$ = 15 mm/km), thus additional inflation of σ_{pr_gnd} was required. However, the inflation factors required when using the MDG were considerably lower than when using the Brazilian threat model, especially I_{gnd}. Furthermore, both the σ_{vig} and σ_{pr_gnd} parameters needed to be inflated in far fewer epochs. These epochs, in which both the I_{vig} and I_{gnd} values calculated with the MDG were also high, corresponded to particularly weak satellite geometries. In these satellite geometries, there were cases where satellites with high S-projection factors, s_{apr_vert}, (see Equation 2.16 in Section 2.3.2) were at elevations below 35°. Since for satellite elevations below 35° the MDG values are the same as those of the Brazilian threat model, the ionosphere-induced vertical position errors (IEVs) for certain subsets of satellites within PDGS were high (see Section 2.4.3.1). This led to considerable inflation of the integrity parameters to protect against particularly weak satellite geometries. Nevertheless, even in these cases, the overall combination for the different satellite subsets within the PDGS resulted in lower inflation when using MDG than when using the conservative Brazilian threat model.

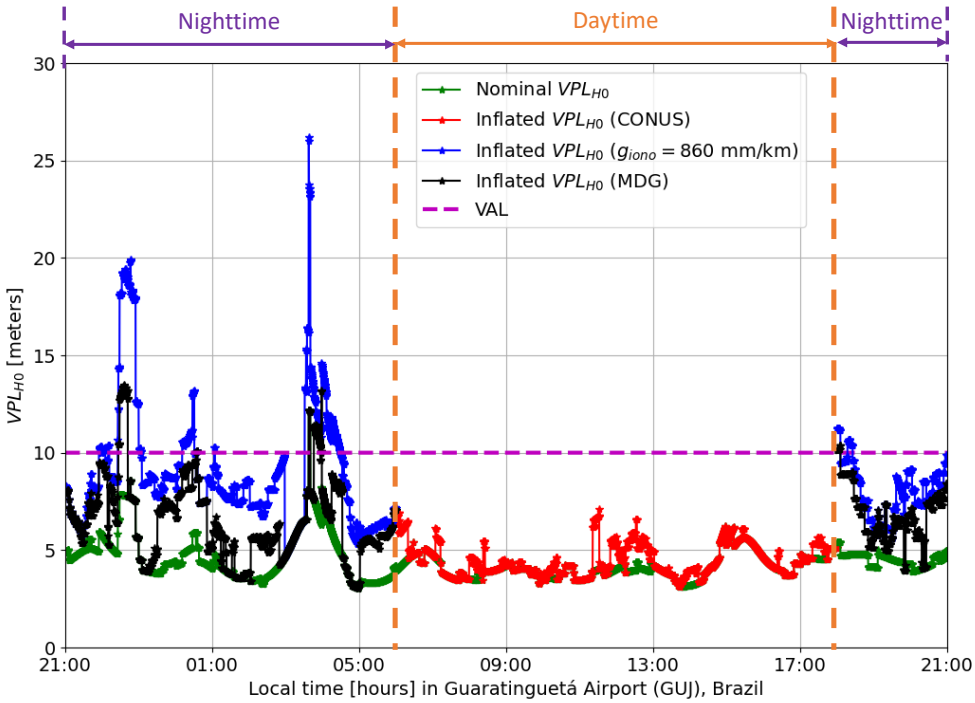

Figure 6.6: Nominal VPL_{H_0} calculated at a 4 km DH distance without inflation (in green), and inflated by applying I_{vig} and I_{gnd} from Figure 6.5 (day 145 of year 2014). The VAL is represented with a magenta dashed line.

During normal GBAS operation, the ground station broadcasts the inflated σ_{vig} and σ_{pr_gnd} integrity parameters to approaching aircraft. These aircraft calculate the VPLs with the transmitted integrity parameters, thus eliminating all potentially hazardous satellite geometries. Figure 6.6 shows the nominal VPL_{H_0} and the inflated VPL_{H_0} computed at a 4 km DH distance for the all-in-view satellite geometries during the 24 hours of the selected day. Note that, a 4 km DH distance for this evaluation was selected because it was the largest DH distance considered in the PDGS algorithm and thus the most conservative, since the value of the VPL increases with the distance to the GBAS ground station. Furthermore, only VPL_{H_0} was considered because it is typically higher than the VPB at these DH distances. This last statement was verified during the simulation with PDGS, where, for the DH distances considered, the highest VPL values were always achieved by VPL_{H_0}.

Figure 6.6 depicts with a dashed magenta line the value of the VAL at the DH distance, which is equal to 10 meters. The green line shows the nominal VPL_{H_0}, which used the uninflated σ_{vig} and σ_{pr_gnd} parameters. As can be seen, even without inflation, the nominal VPL_{H_0} grew above 7 meters, a value higher than usual, between 22:28 local time and 22:55 local time and between 03:33

local time and 03:59 local time. As explained above, this was due to the fact that at these local times, the satellite geometries were especially weak. The red line shows the inflated VPL_{H_0} during the daytime, which used the σ_{vig} and σ_{pr_gnd} parameters inflated with the CONUS threat model. In this case, the inflated VPL_{H_0} (red line) was higher than the nominal VPL_{H_0} in some epochs, especially in the cases where the satellite geometries were weak. However, all points of the red line were below the VAL, therefore GBAS availability would have been 100% during the daytime for approaching aircraft tracking all satellites in view. Note that the system availability was assessed based on the fraction of the time that the VPL was below the VAL.

The blue line of Figure 6.6 shows the "worst-case" inflated VPL_{H_0} during the nighttime, which used the σ_{vig} and σ_{pr_gnd} parameters inflated with the current Brazilian threat model (with a maximum slope of 860 mm/km). VPL grew above VAL for long periods of time during the night, causing the overall GBAS availability to drop to 79.5%. Finally, the black line shows the inflated VPL_{H_0} that used the MDG depicted in Figure 6.3 during the nighttime. Using the MDG values instead of the more conservative threat model allowed the reduction of VPL at practically all epochs. At some epochs, the inflated VPL_{H_0} with the MDG was still higher than the VAL due, again, to the combination of weak geometries with the high values of the MDG for low elevations. Nevertheless, GBAS availability increased to 94.6%.

6.2.3 GBAS availability assessment for the 10th of March of 2014 (active day) and GUJ airport

For the evaluation of Network-GBAS performance on an active ionospheric day, day 69 of the year 2014 (i.e. 10th of March 2014) was selected. This is the active day that was selected for the studies in Chapter 5 on which large EPBs were measured (see Section 5.4). Moreover, a GBAS station located at Guaratinguetá Airport (GUJ) was assumed as in Section 6.2.2.

This study followed the same process as in Section 6.2.2. First, the Network-GBAS algorithm calculated the test statistics ($Itest_r^j$) from the real measurements, then it compared them with their corresponding detection thresholds. However, in contrast to the results of Section 6.2.2, multiple satellites were affected simultaneously by large EPBs and/or scintillation during the nighttime hours of this day. Figure 6.7 shows the network output for each of the visible satellites during the active day. The network output was either "0" or "1" depending on the real-time ionospheric conditions. When the network did not detect any ionospheric disturbance at a time instant t for a specific satellite, the network output was "0" for that time and that satellite. In these cases, the network indicated the use of the MDG for that satellite as the input to PDGS.

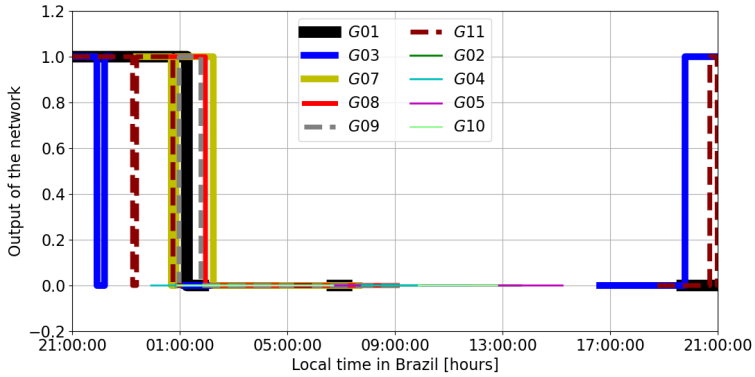

(a) Satellites G01 to G11.

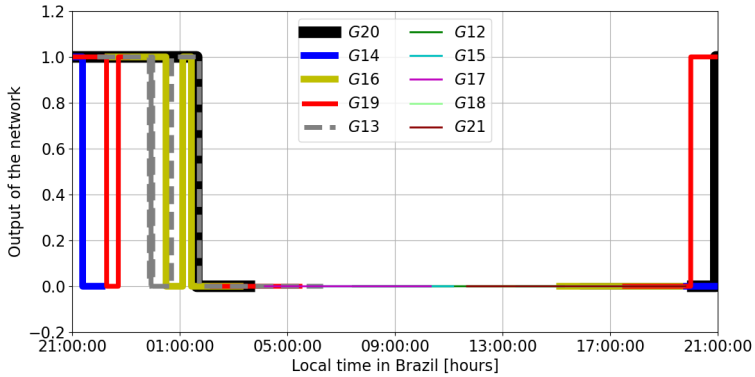

(b) Satellites G12 to G21.

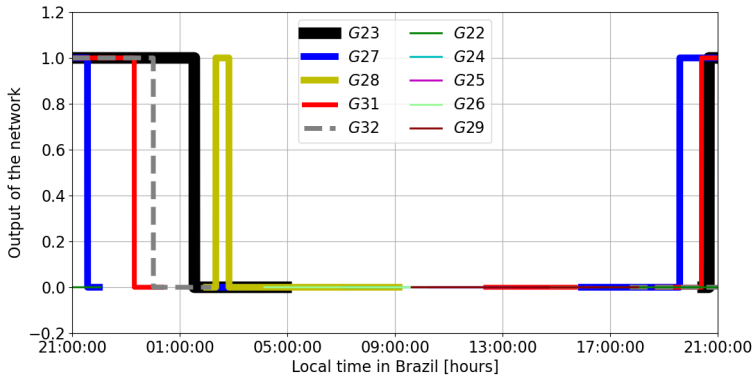

(c) Satellites G22 to G32.

Figure 6.7: Output of the Network-GBAS algorithm for all-in-view satellites (represented in different colors and types of lines) during day 69 of year 2014. When the output is "0", the network of stations did not detect any ionospheric perturbations for that specific satellite and, when it is "1", the network detected an ionospheric perturbation at least with one of its stations for that satellite.

When the network detected an ionospheric disturbance at a time instant t for a specific satellite, the network output was "1" for that time and that satellite. In these cases, the network searched in its database for the estimated and overbounded gradient slope for that particular satellite. If this value was available from multiple stations, the network indicated the use of the maximum estimated and overbounded gradient slant slope among all the stations for that satellite as the input to PDGS. This was the case for satellite G31 in Section 5.4.2.2 of Chapter 5 for which the network managed to estimate and overbound the slope of the actual detected ionospheric gradient in real time. If the value of the estimated and overbounded slope was not available for that satellite, either the algorithm had not converged yet, or it had not been able to estimate this parameter for other reasons explained in Chapter 5 (e.g. scintillation, false alerts, gaps in the data, etc.). In these cases, the network indicated the use of the current conservative Brazilian threat model as the input to PDGS.

As explained above, the work in [28] did not distinguish between nominal and active ionospheric conditions beyond using two different threat models, CONUS and Brazil, for daytime and nighttime respectively. However, Network-GBAS is able to distinguish between affected and unaffected satellites and indicates which gradient slope should be used at which time periods. As can be seen in Figure 6.7, this is an advantage with respect to the current solution given that, from about 2:48 local time to 6:00 local time and from 18:00 local time to 19:30 local time, none of the satellites detected ionospheric perturbations. Therefore, the Network-GBAS would provide at least 4.5 hours of improvement over the solution proposed in [28] in the worst-case scenario of its operation, where estimated gradient slopes may not be available.

6.2.3.1 Results of EPB threat mitigation via PDGS using the Network-GBAS in an active day

This section evaluates the performance of the PDGS algorithm when using the Network-GBAS approach during an active ionospheric day. This study conducted the same three different simulations as in Section 6.2.2.1 with the PDGS algorithm that generated the required inflation factors every 15 seconds for over 24 hours. In this case, the slope that the Network-GBAS indicated as output in real-time for nighttime (18:00 to 06:00 local time at GUJ) was different than the MDG when the network detected a gradient (see Section 6.2.3).

The rest of the parameters selected for PDGS in this section were identical to the parameters selected for Section 6.2.2.1 except for the day of the year for which to calculate the satellite geometries, which was day 69 of year 2014. The process followed in this section to calculate both the inflation factors and the VPLs were also analogous to the process followed in Section 6.2.2.1, therefore its explanation is not repeated in this section.

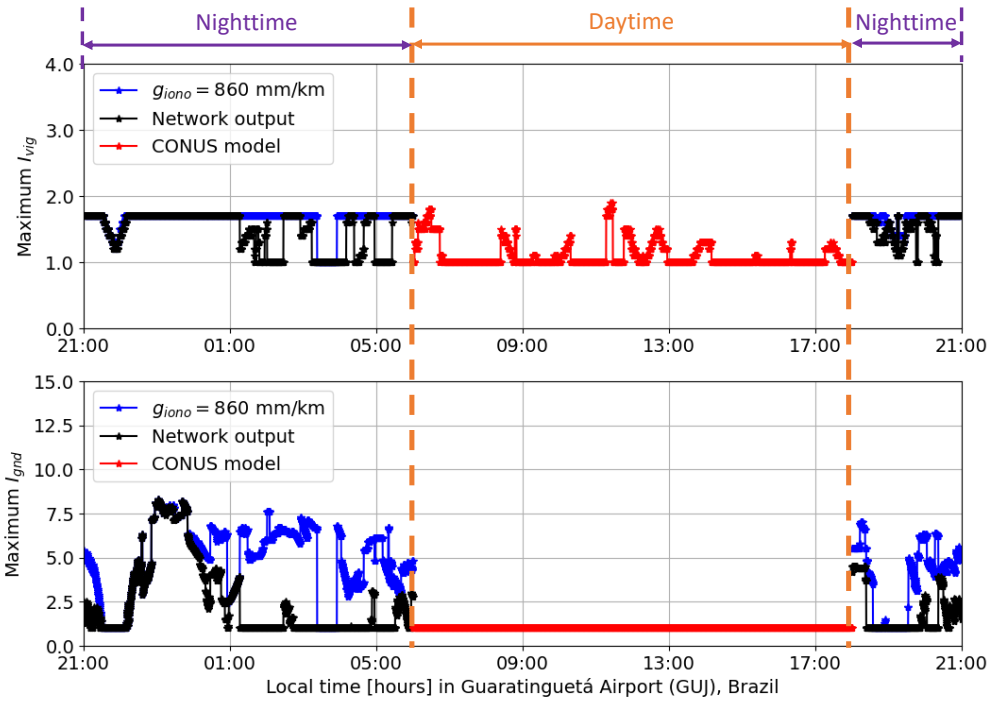

Figure 6.8: Maximum inflation factors of σ_{vig}, I_{vig}, and of σ_{pr_gnd}, I_{gnd} among the 4 simulated DH distances at each epoch (day 69 of year 2014). The CONUS threat model (red line) was used during daytime (06:00-18:00 local time), and both the Brazilian threat model (blue line) and output of the Network-GBAS (black line) were used during nighttime (18:00-06:00 local time).

Figure 6.8 shows the maximum inflation factors for both σ_{vig}, I_{vig}, and σ_{pr_gnd}, I_{gnd}, for the three simulations at each epoch. In this work, I_{gnd} had the same value for all satellites, although a less conservative approach could consider to have a separate value for each satellite. During the daytime, σ_{pr_gnd} did not need to be inflated because the inflated σ_{vig} did not reach the maximum allowable limit of 25.5 mm/km (the maximum allowable I_{vig} is 1.82 considering $\sigma_{vig,nom}$ = 14 mm/km).

During the nighttime, inflating only σ_{vig} was not sufficient to completely remove all potentially unsafe satellite geometries when using both the conservative Brazilian threat model (860 mm/km, blue line) and the network output (black line). In both cases, I_{vig} reached its maximum allowable value of 1.7 (corresponding to a $\sigma_{vig,nom}$ = 15 mm/km) thus additional inflation of σ_{pr_gnd} was required. As in the nominal day, the inflation factors required in the case of using the network output were considerably lower than in the case of using the Brazilian threat model most of the time, especially for I_{gnd}. This was especially relevant for the nighttime hours in which, in the case of using the

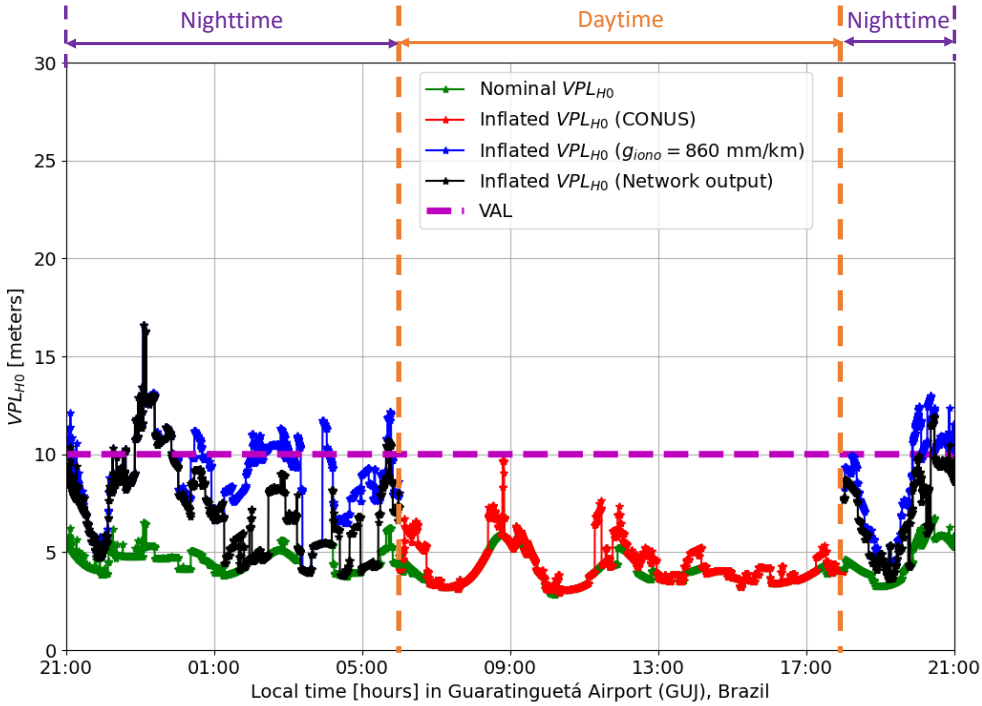

Figure 6.9: Nominal VPL_{H_0} calculated at a 4 km DH distance without inflation (in green), and inflated by applying I_{vig} and I_{gnd} from Figure 6.8 (day 69 of year 2014). The VAL is represented with a magenta dashed line.

network output, I_{gnd} did not need to be inflated, while in the case of using the Brazilian threat model, it had to be inflated up to values above 5. This occurred for nighttime hours where the network did not detect any ionospheric gradients on any satellites (see Figure 6.7). An exception occurred approximately between 21:28 local time and 23:51 local time, when the inflating factors using the network output and using the conservative Brazilian threat model were practically the same. The reason for this was that, as can be seen in Figure 6.7, between these local times, almost all satellites in view were simultaneously affected by different EPBs, therefore the network indicated the use of the conservative Brazilian threat model for all of them, obtaining the same result as the blue line.

Figure 6.9 shows the nominal VPL_{H_0} and the inflated VPL_{H_0} computed at a 4 km DH distance for the all-in-view satellite geometries during the 24 hours of the selected day. The green line shows the nominal VPL_{H_0}, which used the uninflated σ_{vig} and σ_{pr_gnd} parameters. As can be seen, the nominal VPL_{H_0} had nearly the same values throughout the day, which indicates that, during this day, the satellite geometries were "stronger" than during day 145

of 2014. The red line shows the inflated VPL_{H_0} during the daytime, which used the σ_{vig} and σ_{pr_gnd} parameters inflated with the CONUS threat model. In this case, the inflated VPL_{H_0} (red line) was higher than the nominal VPL_{H_0} (green line) at some epochs, especially in cases where the satellite geometries were weaker than for the rest of the epochs. However, all points of the red line were below VAL, therefore GBAS availability was 100% during the daytime also for the active day.

The blue line of Figure 6.9 shows the "worst-case" inflated VPL_{H_0} during the nighttime, which used the σ_{vig} and σ_{pr_gnd} parameters inflated with the current Brazilian threat model (860 mm/km). In this case, VPL grew above VAL again for long periods of time during the night, causing the overall CAT I GBAS availability to drop to 68.7%. Finally, the black line shows the inflated VPL_{H_0} that used the network output depicted in Figure 6.7 during the nighttime. Using the slope values indicated by the network instead of the more conservative threat model allowed the reduction of VPL at practically all epochs where the network output was lower than the worst-case gradient. At some epochs, VPL_{H_0} inflated with the slope indicated by the network was higher than the VAL due to the network's indication to use the more conservative threat model. This occurred when the network detected different ionospheric gradients affecting multiple satellites simultaneously. Nevertheless, the Network-GBAS increased CAT I GBAS availability to a 89.5%.

6.3 Summary

This chapter has evaluated the availability of a simulated CAT I GBAS station located at Guaratinguetá Airport (GUJ), Brazil, on two days: the 25th of May 2014 (a nominal day without significant ionospheric activity), and the 10th of March 2014 (an active ionospheric day). This evaluation has used the EPB threat mitigation strategy proposed for GBAS as an input to PDGS. Within PDGS, the value of the gradient slope used for each satellite to calculate the worst-case ionospheric induced range errors has been replaced with the value indicated by the monitoring network. The results of the MDG derived with the real data from the network of stations introduced in Chapter 5 reduced considerably the slope value of the current conservative threat model applied in Brazil while meeting the integrity requirements.

The results from the nominal day showed a CAT I GBAS availability improvement during nighttime from 79.5% with the current solution to 94.6% with the Network-GBAS approach. However, there were epochs in which no availability benefit was obtained with the Network-GBAS approach, although the network-based VPL values were lower than those obtained with the solution proposed in [28], and less inflation was needed. These cases were caused

by specific weak satellite geometries combined with the still conservative values of the derived MDG for satellite elevations below 35°.

The results from the active day showed a CAT I GBAS availability improvement during nighttime from 68.7% with the current solution to 89.5% with the Network-GBAS approach. Here, the cases where no benefit in system availability was obtained were due to the fact that, at those times, multiple satellites were affected by different EPBs simultaneously. Therefore, the network indicated the use of the conservative threat model for these epochs.

While on both days, the Network-GBAS approach provided a large improvement of the system availability compared to the "worst-case" based solution, neither of the two solutions are sufficient to achieve the 99% availability required for CAT I precision approaches. Therefore, to obtain further improvement of the system availability with the Network-GBAS approach, future work should consider the design and/or adaptation of the networks for the specific purpose of protecting certain airports. This would result in considerably lower MDG values which would automatically lead to an improvement of CAT I GBAS availability with the Network-GBAS approach.

7
Conclusion

Over the past 20 years, considerable effort has been invested in the standardization of GBAS as a primary aircraft guidance system for precision approaches and landings worldwide. However, the low availability of the system in equatorial regions, where very conservative assumptions have to be adopted to protect users against large ionospheric gradients, remains a problem to be solved.

7.1 Summary and main contributions

In this context, the work in this thesis focused on providing a method for real-time ionospheric monitoring to reduce the existing excessive conservatism in the current assumptions, thus increasing system availability in regions where it is degraded. The main contributions of this work are summarized in the following sections.

7.1.1 Network-GBAS concept

The first contribution of this thesis, addressed in Chapter 3, was the design and development of a concept that allows the reduction of the slope of the ionospheric threat model considered in current GBAS solutions. The main challenge in designing the concept was to meet the integrity requirements while being implementable within the current GBAS standards. The concept proposes the detection and estimation of anomalous ionospheric gradients in real time based on a network of external dual-frequency, multi-constellation stations, which could be other GBAS stations.

The main conclusions from this section are:

1. The Network-GBAS meets the stringent integrity requirements by assuming that:

- the largest gradient that can currently occur without being detected by the network (MDG) is present, if no gradient was detected by any of the network stations, or,
- the largest gradient within the current conservative threat model is present, if a gradient was detected, but its parameters could not be estimated, or,
- one or more gradients whose parameters have been estimated and overbounded by the network is/are present.

2. The Network-GBAS can be implemented without changing the current standards because it proposes to modify the slope of the threat model utilized within the current PDGS algorithm that already covers system integrity. Therefore, only the integrity of the network output has to be ensured.

The methodology developed in Chapter 3 is the basis for the work in Chapters 4, 5, and 6, where it is assessed with simulated and real (actually observed) ionospheric perturbations.

7.1.2 Algorithm for real-time anomalous ionospheric gradient detection based on the slant ionospheric rates

The algorithm for detecting anomalous ionospheric gradients in real time was derived and explained in Chapter 3. One of the main novelties of the proposed algorithm is that it allows detection of gradients separately by each of the stations of the network and each of the satellites in view. This avoids the issue of needing to compare the absolute value of slant ionospheric delays between different stations from other methods proposed in the literature, which requires rather short station baselines. Furthermore, this algorithm is based on the time derivatives of the slant ionospheric delays, which avoids the challenge of carrier-phase ambiguity resolution. To account for the noise present in the measurements and the nominal ionosphere, which are higher when satellites are at low elevations, the algorithm derived the detection thresholds with real measurements as a function of satellite elevation while also considering the non-Gaussian tails of the probability distributions.

Chapters 4 and 5 evaluated this algorithm with simulated gradients and with real gradients from a high-latitude area, Alaska, and from a low-latitude area, Brazil. The results with simulated gradients and real gradients in both locations showed that the algorithm adequately detected the anomalous ionospheric gradients in real time as long as the IPPs did not move in the direction of propagation of the gradients. This issue was solved by considering all potentially hazardous cases in the calculation of the MDG.

The main conclusion of this section was that it is important to find a compromise between the range of ionospheric gradient slopes to be detected and the number of false alerts that can be allowed from the network. The higher the number of false alerts, the more often the current "worst-case" threat model needs to be assumed, which leads to the loss of availability.

7.1.3 Algorithm for real-time ionospheric gradient parameter estimation and overbound based on a network of stations and the slant ionospheric rates

The algorithm for real-time ionospheric gradient parameter estimation was also developed in Chapter 3. This algorithm calculates the real-time cross-correlation of the slant ionospheric rates to find the propagation time of the gradient between stations and computes the Pearson correlation coefficient to ensure that the gradients being compared are the same. Using the information from the real-time cross-correlation, the speed and direction of the IPPs, and the slant ionospheric rates, it estimates the gradient parameters. In addition, the algorithm considers the possible errors in the estimation of the gradient slope by overbounding it in real time based on the errors studied through exhaustive simulations. In this way, reliable estimation of the anomalous ionospheric gradient slopes was achieved.

This algorithm was evaluated with simulated gradients and with real gradients observed in Alaska and Brazil in Chapters 4 and 5, respectively. These evaluations led to the following main results:

- The results with both simulated and real gradients showed that it is possible to estimate the gradient parameters in real time while fulfilling the integrity requirements.
- Estimation with the Network-GBAS approach reduced the slope of the gradients that current GBAS solutions would need to assume for detected gradients no greater than 225 mm/km in the case of Alaska and no greater than 600 mm/km in the case of Brazil. Above these values, the necessary overbounding to fulfill integrity would result in estimated gradient slopes larger than the current conservative threat models.
- In Alaska, the estimated gradients had much lower slopes but moved with much higher speeds than the gradients considered in the existing threat models. This highlighted the importance of deriving a threat model for each area where GBAS is to be installed. Estimation errors were caused mainly by the low temporal resolution of the measurements, 1 Hz, and the short baselines between stations relative to the high gradient speeds observed. In addition, it was also found that the correlation radius of the

ionospheric disturbances in this area is very low (less than 20 km), which requires very short baselines for the cross-correlation process to work.

- In Brazil, the correlation radius of the ionospheric disturbances was much larger than in the case of Alaska (more than 100 km), and the disturbances moved much slower. In this case, estimation errors were caused by excessive cycle slips in carrier-phase signals during time periods with EPBs and strong scintillation.

Considering these results, the main conclusions of this section were:

1. The estimation algorithm was adapted to the characteristics of the ionospheric perturbations in each region (Alaska and Brazil). The adapted algorithm gave reasonable parameter estimation results for both simulated and real gradients considering the challenging scenarios studied.
2. In a real implementation of a Network-GBAS, it would be recommended to design the network, or adapt the existing networks, with the target of achieving the required level of performance.

7.1.4 Derivation of the Minimum Detectable Gradient by the network

In Chapter 3, the derivation of a Minimum Detectable Gradient (MDG) was proposed to protect GBAS stations from possible anomalous gradients that went undetected by the network due to: (i) network topology (e.g. long baselines, lack of stations in certain positions, etc.) or (ii) the relative movement of the ionospheric perturbations and the IPPs. For this purpose, the Network-GBAS algorithm assigned a probability of missed detection to each of the stations in the network based on an overall probability of missed detection of ionospheric gradients of 10^{-8}.

The MDG for the network located in Brazil studied in Chapter 5 and a simulated GBAS station located within the area of coverage of this network at Guarantiguetá Airport (GUJ) was derived in Chapter 6.

The main conclusion of this section, motivated by the results, was that the Network-GBAS concept can significantly reduce the slope of the current threat model, especially for high elevation satellites, while ensuring GBAS integrity.

7.1.5 GBAS availability assessment

Chapter 6 evaluated the availability of a simulated CAT I GBAS station located at Guarantiguetá Airport (GUJ), Brazil, on two different days: a nominal day, the 25th of May 2014, and an active day, the 10th of March 2014.

This chapter compared the availability of the simulated GBAS station during the nighttime using the current conservative Brazilian threat model and the network output. The results showed that using the Network-GBAS approach greatly increased GBAS availability from 79.5% to 94.6% during the nighttime of the nominal day and from 68.7% to 89.5% during the nighttime of the active day.

The main conclusion of this section was that, while on both days, the Network-GBAS approach provided a large improvement of the system availability compared to the current "worst-case" based solution, it was not yet sufficient to achieve the 99% availability required for CAT I precision approaches. This was mainly due to the fact that the network used was not designed for this purpose.

7.2 Suggestions for future work

A number of recommendations for future research are provided in the following subsections.

7.2.1 Optimization of the Probability of False Alert to be used by each of the stations of the network

Considering the results of the detection algorithm and MDG determination, I consider that further studies to derive the optimal false alert probability according to the required performance at each airport should be performed.

Furthermore, there is a trade-off between the value used as MDG and the maximum slant slope bounds of the ionospheric threat model derived for the same region. Thus, for example, if the slopes of the ionospheric gradients are typically much lower than the assumed conservative threat models, but the characteristics of the gradients make excessively challenging the estimation of their parameters (e.g. Alaska), it might be of interest to have more gradients go "undetected" and raise the value used as MDG. In this way, avoiding many false alerts would avoid the excessive use of the "worst-case" threat models. Therefore, if the values of the MDG were still small compared to the "worst-case" threat model even after increasing the MDG values to let small gradients go undetected, the system availability would improve.

Conversely, in regions like Brazil, where the largest gradients with near maximum slopes occur at very specific times of the day and days of the year, I recommend to have more sensitive thresholds in order to reduce the MDG, even if this leads to assuming "worst-case" gradient bounds when gradients are detected.

7.2.2 Additional monitoring of anomalous ionospheric gradients based on the difference of the absolute slant ionospheric delays between the stations of the network

As previously discussed, the Network-GBAS concept was not based on the differences of the absolute slant ionospheric delays between the different stations because this would have required a great number of stations, short baselines, and the resolution of the carrier-phase ambiguities. However, I recommend to investigate this methodology as an additional monitor to support the one proposed in this thesis.

7.2.3 Derivation of a concept for integrating the information from other satellite constellations into the derivation of the MDG

As previously commented, the model of MDG derived for the case of Brazil, even though significantly reducing the current threat model, is still conservative. In this sense, I consider that the derivation of a concept that would allow the use of the IPPs from other constellations to support the IPPs from the GPS satellites could further reduce the conservative values of the MDG.

7.2.4 Design of the network to protect specific airports

As discussed in several chapters, this thesis used networks with publicly available measurements to evaluate the proposed Network-GBAS concept. However, it has been observed throughout the thesis that this is not optimal. Therefore, it would be advisable to design the network tailored to the needs of the airports to be protected based on the results and advice addressed throughout the thesis:

1. To implement the Network-GBAS concept in a geographic region with active ionosphere, I recommend to use GNSS receivers that are robust to scintillation and have an adequate sampling rate. For instance, in Alaska, a rate of at least 10 Hz would be advisable while, in Brazil, a lower rate could be used, as long as the real time capability of the GBAS stations is considered (e.g., 5 Hz).

2. The network topology should be designed in such a way that the baselines between stations are adapted to the correlation radius of the ionospheric perturbations in the region and the stations are not aligned with the expected ionospheric fronts (perpendicular to their propagation direction).

7.2.5 Adaptation of the Network-GBAS concept for CAT III GBAS (GAST D)

Finally, I recommend investigation of the use of the Network-GBAS concept to support also the implementation of GAST D stations in active ionospheric regions. In this regard, I propose to investigate the use of the network to derive a prior-probability of occurrence of anomalous ionospheric gradients, which would be useful for GAST C stations as well.

7.3 Closing

The Network-GBAS concept presented in this dissertation can significantly enhance CAT I GBAS availability in active ionospheric regions, is compatible with existing algorithms and hardware, and thus should be certifiable if adapted to the characteristics of each region where GBAS is fielded.

A

Conversion from the global reference frame to the perturbation frame

This appendix explains the steps to transform the coordinates of a given IPP, expressed in latitude (lat_{IPP}) and longitude (lon_{IPP}) in the global reference frame, to its coordinates in the perturbation local reference frame [105].

The first step is to calculate the unitary vector $\boldsymbol{u_{IPP}} = [u_{IPP_x}, u_{IPP_y}, u_{IPP_z}]$ that gives the direction from the center of the Earth to the IPP. The IPP coordinates in the ECEF coordinate system are calculated as:

$$\begin{aligned} u_{IPP_x} &= \cos(lon_{IPP}) \cdot \cos(lat_{IPP}), \\ u_{IPP_y} &= \sin(lon_{IPP}) \cdot \cos(lat_{IPP}), \\ u_{IPP_z} &= \sin(lat_{IPP}). \end{aligned} \tag{A.1}$$

Note that the distance from the center of the Earth to the IPP has been omitted from Equation A.1 to calculate the unitary vector directly.

Next, Equation A.2 calculates the unitary vector $\boldsymbol{u_c} = [u_{c_x}, u_{c_y}, u_{c_z}]$ that gives the direction from the center of the Earth to the center of the perturbation expressed in latitude (lat_{iono}) and longitude (lon_{iono}) as:

$$\begin{aligned} u_{c_x} &= \cos(lon_{iono}) \cdot \cos(lat_{iono}), \\ u_{c_y} &= \sin(lon_{iono}) \cdot \cos(lat_{iono}), \\ u_{c_z} &= \sin(lat_{iono}). \end{aligned} \tag{A.2}$$

With the two previously calculated vectors, the position vector $\boldsymbol{p_{IPP}} = [p_{IPP_x}, p_{IPP_y}, p_{IPP_z}]$ of the radial projection of the IPP onto the perturbation plane in the ECEF coordinate system can be computed as:

$$\boldsymbol{p_{IPP}} = \frac{R_e + h_I}{\boldsymbol{u_c} \cdot \boldsymbol{u_{IPP}}} \cdot \boldsymbol{u_{IPP}}. \tag{A.3}$$

Here, the perturbation plane is the tangent plane to the sphere of radius equal to the radius of the Earth plus the height of the "thin shell" layer $(R_e + h_I)$ at the point $[lon_{iono}, lat_{iono}]$, which gives the perturbation center.

Finally, several geometric transformations are applied to convert $\boldsymbol{p_{IPP}}$ to the coordinates over the perturbation plane $\boldsymbol{x_{iono}} = [x_{iono}, y_{iono}]$:

$$\begin{aligned} x_{iono} &= y_1 \cdot \cos(d_{iono}) - z_2 \cdot \sin(d_{iono}), \\ y_{iono} &= y_1 \cdot \sin(d_{iono}) + z_2 \cdot \cos(d_{iono}), \end{aligned} \tag{A.4}$$

where d_{iono} is the direction of propagation of the simulated ionospheric gradient and:

$$\begin{aligned} x_1 &= p_{IPP_x} \cdot \cos(lon_{iono}) + p_{IPP_y} \cdot \sin(lon_{iono}), \\ y_1 &= -p_{IPP_x} \cdot \sin(lon_{iono}) + p_{IPP_y} \cdot \cos(lon_{iono}), \\ z_1 &= p_{IPP_z}, \\ z_2 &= -x_1 \cdot \sin(lat_{iono}) + z_1 \cdot \cos(lat_{iono}). \end{aligned} \tag{A.5}$$

Bibliography

[1] European Commision, Directorate-General for Research and Innovation, Directorate General for Mobility and Transport, "Flightpath 2050 Europe's Vision for Aviation," 2011.

[2] Air Transport Action Group, "Aviation: Benefits Beyond Borders 2018," 2018.

[3] United States Federal Aviation Administration, "FAA Aeropace Forecast," 2019. [Online]. Available: https://www.faa.gov/data_research/aviation/aerospace_forecasts/

[4] Eurocontrol, "Eurocontrol Seven-Year Forecast, Flight Movements and Service Units 2019-2025," 2019. [Online]. Available: https://www.eurocontrol.int/publication/seven-year-forecast-flight-movements-and-service-units-february-2019

[5] International Air Transport Association. (2019) Air traffic frequency. [Online]. Available: https://www.iata.org/publications/store/Pages/20-year-passenger-forecast.aspx

[6] European Comission. (2017) Airport capacity and quality. [Online]. Available: https://ec.europa.eu/transport/modes/air/airports/airport_capacity_and_quality_en

[7] Eurocontrol, "European aviation in 2040. Challenges of Growth. Network Congestion," 2018.

[8] International Civil Aviation Organization, "International Standards and Recommended Practices (SARPs). Annex 10 to the Convention of International Civil Aviation. Volume I -Radio Navigation Aids," Tech. Rep., 2017.

[9] T. Walter, P. Enge, J. Blanch, and B. Pervan, "Worldwide Vertical Guidance of Aircraft Based on Modernized GPS and New Integrity Augmentations," in *Proceedings of the IEEE*, vol. 96, no. 12, 2008, pp. 1918–1935.

[10] Y. C. Lee, "Analysis of Range and Position Comparison Methods as a

Means to Provide GPS Integrity in the User Receiver," in *Proceedings of the 42nd Annual Meeting of the Institute of Navigation*, 1986, pp. 1–4.

[11] B. W. Parkinson and P. Axelrad, "Autonomous GPS Integrity Monitoring Using the Pseudorange Residual," *Navigation*, vol. 35, no. 2, pp. 255–274, 1988.

[12] J. Blanch, T. Walker, P. Enge, Y. Lee, B. Pervan, M. Rippl, A. Spletter, and V. Kropp, "Baseline Advanced RAIM User Algorithm and Possible Improvements," *IEEE Transactions on Aerospace and Electronic Systems*, vol. 51, no. 1, pp. 713–732, 2015.

[13] A. Katz, S. Pullen, S. Lo, J. Blanch, T. Walter, A. Katronick, M. Crews, and R. Jackson, "ARAIM for Military Users: ISM Parameters, Constellation-Check Procedure and Performance Estimates," in *Proceedings of the 2021 International Technical Meeting of The Institute of Navigation*, 2021, pp. 173–188.

[14] United States Federal Aviation Administration. WAAS Quick Facts Sheet. [Online]. Available: https://www.faa.gov/about/office_org/headquarters_offices/ato/service_units/techops/navservices/gnss/library/factsheets/media/WAAS_QFSheet.pdf

[15] European Global Navigation Satellite Systems Agency. EGNOS LPV 200 Enables Safer Aircraft Landings. [Online]. Available: https://www.gsa.europa.eu/news/egnos-lpv-200-enables-safer-aircraft-landings

[16] International Civil Aviation Organization, "ICAO Annex 6 - Operation of Aircraft," Tech. Rep., 2010.

[17] M. Felux, T. Dautermann, and H. Becker, "GBAS Landing System - Precision Approach Guidance after ILS," *Aircraft Engineering and Aerospace Technology*, vol. 85/5, pp. 382–388, 2013.

[18] International Civil Aviation Organization, "Guide for Ground Based Augmentation System implementation," Tech. Rep., May 2013.

[19] Eurocontrol. GBAS Approach & Landing Sytem. The future of precision approach. [Online]. Available: flygls.net

[20] Radio Technical Commission for Aeronautics, "DO-253D, Minimum Operational Performance Standards for GPS Local Area Augmentation System Airborne Equipment," Tech. Rep., 2017.

[21] J. Lee, S. Pullen, S. Datta-Barua, and P. Enge, "Assessment of Ionosphere Spatial Decorrelation for Global Positioning System-Based Aircraft Landing Systems," *Journal of Aircraft*, vol. 44, no. 5, pp. 1662–1669, 2007, doi: 10.2514/1.28199.

[22] H. Chang, M. Yoon, S. Pullen, L. Marini-Pereira, and J. Lee, "Ionospheric spatial decorrelation assessment for GBAS daytime operations in Brazil," *Navigation*, vol. 68, no. 2, pp. 391–404, 2021, doi: 10.1002/navi.418.

[23] C. Mayer, B. Belabbas, N. Jakowski, M. Meurer, and W. Dunkel, "Ionosphere Threat Space Model Assessment for GBAS," *Proceedings of the 22nd International Technical Meeting of the Satellite Division of the Institute of Navigation (ION GNSS 2009)*, pp. 1091–1099, 2009.

[24] S. Pullen, Y. S. Park, and P. Enge, "Impact and mitigation of ionospheric anomalies on ground-based augmentation of GNSS," *Radio Science*, vol. 44, 2009.

[25] D. V. Simili and B. Pervan, "Code-Carrier Divergence Monitoring for the GPS Local Area Augmentation System," in *Proceedings of the Position, Location, And Navigation Symposium 2006*, Apr. 2006, pp. 483–493.

[26] J. Lee, J. Seo, Y. Park, S. Pullen, and P. Enge, "Ionospheric Threat Mitigation by Geometry Screening in Ground-Based Augmentation Systems," *Journal of Aircraft*, vol. 48, no. 4, pp. 1422–1433, 2011, doi: 10.2514/1.C031309.

[27] J. Seo, J. Lee, S. Pullen, P. Enge, and S. Close, "Targeted Parameter Inflation within Ground-Based Augmentation Systems to Minimize Anomalous Ionospheric Impact," *Journal of Aircraft*, vol. 49, no. 2, pp. 587–599, 2012, doi: 10.2514/1.C031601.

[28] M. Yoon, D. Kim, S. Pullen, and J. Lee, "Assessment and mitigation of equatorial plasma bubble impacts on category I GBAS operations in the Brazilian region," *Navigation*, vol. 66, no. 3, pp. 643–659, 2019, doi: 10.1002/navi.328.

[29] S. Datta-Barua, J. Lee, S. Pullen, M. Luo, A. Ene, D. Qiu, G. Zhang, and P. Enge, "Ionospheric threat parameterization for local area Global-Positioning-System-based aircraft landing systems," *Journal of Aircraft*, vol. 47, no. 4, pp. 1141–1151, 2010, doi: 10.2514/1.46719.

[30] M. Yoon, J. Lee, S. Pullen, J. Gillespie, N. Mathur, R. Cole, J. de Souza, P. Doherty, and R. Pradipta, "Equatorial Plasma Bubble Threat Parameterization to Support GBAS Operations in the Brazilian Region," *NAVIGATION*, vol. 64, no. 3, pp. 309–321, 2017, doi: 10.1002/navi.203.

[31] S. Saito, S. Sunda, J. Lee, S. Pullen, S. Supriadi, T. Yoshihara, M. Terkildsen, F. Lecat, and I. A. I. S. T. Force, "Ionospheric delay gradient model for GBAS in the Asia-Pacific region," *GPS Solutions*, vol. 21, no. 4, pp. 1937–1947, 2017.

[32] J. M. Juan, J. Sanz, A. Rovira-Garcia, G. González-Casado, D. Ibáñez, and R. O. Perez, "AATR an ionospheric activity indicator specifically based on GNSS measurements," *Journal of Space Weather and Space Climate*, vol. 8, p. A14, 2018.

[33] M. Yoon, D. Kim, and J. Lee, "Extreme ionospheric spatial decorrelation observed during the March 1, 2014, equatorial plasma bubble event," *GPS Solutions*, vol. 24, no. 2, pp. 1–11, 2020, doi: 10.1007/s10291-020-0960-x.

[34] S. Pullen, R. Cassell, B. Johnson, M. Brenner, D. Weed, L. Cypriano, M. Topland, M. Stakkeland, B. Pervan, M. Harris, S. Saito, J. Lee, B. Clark, S. Beauchamp, and J. Dennis, "Impact of Ionospheric Anomalies on GBAS GAST D Service and Validation of Relevant ICAO SARPs Requirements," *Proceedings of the 30th International Technical Meeting of the Satellite Division of The Institute of Navigation (ION GNSS+ 2017)*, pp. 2085–2105, 2017, doi: 10.33012/2017.15135.

[35] S. Khanafseh, S. Pullen, and J. Warburton, "Carrier Phase Ionospheric Gradient Ground Monitor for GBAS with Experimental Validation," *NAVIGATION*, vol. 59, no. 1, pp. 51–60, 2012, doi: 10.1002/navi.3.

[36] M. Yoon, J. Lee, and S. Pullen, "Integrity risk evaluation of impact of ionospheric anomalies on GAST D GBAS," *NAVIGATION*, vol. 67, no. 2, pp. 223–234, 2020, doi: 10.1002/navi.339. [Online]. Available: https://onlinelibrary.wiley.com/doi/abs/10.1002/navi.339

[37] J. Lee, S. Pullen, S. Datta-Barua, and J. Lee, "Real-time Ionospheric Threat Adaptation Using a Space Weather Prediction for GNSS-Based Aircraft Landing Systems," *IEEE Transactions on Intelligent Transportation Systems*, vol. 18, no. 7, pp. 1752–1761, 2016, doi: 10.1109/TITS.2016.2627600.

[38] P. Durba, "WP27 - High level concept and modes for DFMC GBAS," ICAO NSP - Joint Working Groups, Tech. Rep., 2018.

[39] D. Gerbeth, M. Caamano, M.-S. Circiu, and M. Felux, "Airborne Ionospheric Gradient Monitoring for Dual-Frequency GBAS," in *Proceedings of the 2022 International Technical Meeting of The Institute of Navigation*, 2022, pp. 1110–1122.

[40] T. Murphy, M. Harris, G. McGraw, J. Wichgers, L. Lavik, M. Topland, M. Tuffaha, and S. Saito, "Alternative Architecture for Dual Frequency Multi-Constellation GBAS," in *Proceedings of the 34th International Technical Meeting of the Satellite Division of The Institute of Navigation (ION GNSS+ 2021)*, 2021, pp. 1334–1374.

[41] T. Murphy, M. Harris, G. Balvedi, G. McGraw, J. Wichgers, L. Lavik, M. Topland, M. Tuffaha, and S. Saito, "Ionospheric Gradient Monitoring for Dual Frequency Multi-Constellation GBAS," in *Proceedings of the 2022 International Technical Meeting of The Institute of Navigation*, 2022, pp. 1075–1097.

[42] J. Cheng, J. Li, L. Li, C. Jiang, and B. Qi, "Carrier Phase-Based Ionospheric Gradient Monitor Under the Mixed Gaussian Distribution," *Remote Sensing*, vol. 12, no. 23, p. 3915, 2020.

[43] European Union Agency for the Space Programme (EUSPA). (2022) European GNSS Service Centre: Constellation Information. [Online]. Available: https://www.gsc-europa.eu/system-service-status/constellation-information

[44] P. Misra and P. Enge, *Global Positioning System: Signals, Measurements and Performance Second Edition.* Massachusetts: Ganga-Jamuna Press, 2006.

[45] J. Sanz, J. Juan, and M. Hernández-Pajares, *GNSS data processing, Vol. I: fundamentals and algorithms. ESA communications.* ESTEC TM-23/1, Noordwijk, Netherlands, 2013.

[46] R. Hatch, "The Synergism of GPS Code and Carrier Measurements," vol. 2, 1982, pp. 1213–1231.

[47] Eurocae, *ED-114A, Minimum Operational Performance Specification for Global Navigation Satellite Ground Based Augmentation System Ground Equipment to Support Category I Operations*, Eurocae Std. ED-114A, Mar. 2013.

[48] United States Federal Aviation Administration, "Category I Local Area Augmentation System Ground Facility - NON-FED Specification," Tech. Rep. FAA-E-AJW44-2937A, 2005.

[49] Radio Technical Commission for Aeronautics, "DO-253C, Minimum Operational Performance Standards for GPS Local Area Augmentation System Airborne Equipment," Tech. Rep., 2018.

[50] T. A. Skidmore and F. van Graas, "An Investigation of Tropospheric Errors On Differential GNSS Accuracy and Integrity," in *Proceedings of the 17th international technical meeting of the satellite division of the Institute of Navigation (ION GNSS 2004)*, 2004, pp. 2752–2760.

[51] International Civil Aviation Organization, "Global Navigation Satellite System (GNSS) Manual, 2nd Edition," Tech. Rep., June 2012.

[52] W. Schuster and W. Ochieng, "Harmonisation of category-III precision

approach navigation system performance requirements," *The Journal of Navigation*, vol. 63, no. 4, p. 569, 2010.

[53] M. Yoon, D. Kim, J. Lee, S. Rungruengwajiake, and S. Pullen, "Assessment of Equatorial Plasma Bubble Impacts on Ground-Based Augmentation Systems in the Brazilian Region," *Proceedings of the 2016 International Technical Meeting of The Institute of Navigation*, pp. 368–379, Jan. 2016.

[54] M. Yoon, "Towards Worldwide GNSS-Based Landing Systems: Modeling and Probabilistic Integrity Assessment of Low-latitude Ionospheric Threat," *Dissertation, Korea Advanced Institute of Science and Technology (KAIST)*, 2018.

[55] S. Pullen and P. Enge, "An overview of GBAS integrity monitoring with a focus on ionospheric spatial anomalies," *Indian Journal of Radion & Space Physics (94.20. Vv; 94.20 B6)*, vol. 36, pp. 249–260, 2007.

[56] United States Federal Aviation Administration, "Order6884.1, Siting Criteria for Ground Based Augmentation System (GBAS)," Tech. Rep., 2010.

[57] G. A. McGraw, T. Murphy, M. Brenner, S. Pullen, and A. J. V. Dierendonck, "Development of the LAAS Accuracy Models," in *Proceedings of the 13th International Technical Meeting of the Satellite Division of The Institute of Navigation (ION GPS 2000)*, Sep. 2000, pp. 1212–1223.

[58] F. van Graas and Z. Zhen, "Tropospheric Delay Threats for the Ground Based Augmentation System," in *Proceedings of the 2011 International Technical Meeting of The Institute of Navigation*, Sep. 2011.

[59] S. Datta-Barua, T. Walter, S. Pullen, M. Luo, J. Blanch, and P. Enge, "Using WAAS Ionospheric Data to Estimate LAAS Short Baseline Gradients," in *Proceedings of the 2002 National Technical Meeting of The Institute of Navigation*, 2002, pp. 523–530.

[60] T. Murphy, M. Harris, Y. S. Park, and S. Pullen, "GBAS Differentially Corrected Positioning Service Ionospheric Anomaly Errors Evaluated in an Operational Context," *Proceedings of the 2010 International Technical Meeting of The Institute of Navigation*, pp. 25–27, 2010.

[61] C. Shively and R. Braff, "An Overbound Concept for Pseudorange Error from the LAAS Ground Facility," *Proceedings of the IAIN World Congress and the 56th Annual Meeting of The Institute of Navigation*, pp. 661–671, 2000.

[62] M.-S. Circiu, *Integrity Aspects for Dual-frequency Dual-Constellation*

Ground Based Augmentation System (GBAS). Dissertation, RWTH Aachen, 2020.

[63] G. Xie, *Optimal On-airport Monitoring of the Integrity of GPS-Based Landing Systems*. Dissertation, Stanford university, 2004.

[64] J. Lee, S. Pullen, G. Xie, and P. Enge, "LAAS Sigma-Mean Monitor Analysis and Failure-Test Verification," in *Proceedings of the 57th Annual Meeting of The Institute of Navigation (2001)*, Jun. 2001, pp. 694–704.

[65] P. Teunissen and O. Montenbruck, *Springer Handbook of Global Navigation Satellite Systems*. Springer, 2017, doi: 10.1007/978-3-319-42928-1.

[66] M. Stakkeland, Y. L. Andalsvik, and K. S. Jacobsen, "Estimating Satellite Excessive Acceleration in the Presence of Phase Scintillations," in *Proceedings of the 27th International Technical Meeting of The Satellite Division of the Institute of Navigation (ION GNSS+ 2014)*, Sep. 2014, pp. 3532–3541.

[67] J. Huang and F. van Graas, "Characterization of Tropospheric Spatial Decorrelation Errors Over a 5-km Baseline," *Navigation*, vol. 55, pp. 39–53, 2008.

[68] T. Fujiwara and T. Tsujii, "GBAS Availability Assessment and Modeling of Ionospheric Scintillation Effects," *NAVIGATION, Journal of the Institute of Navigation*, vol. 63, no. 4, pp. 403–411, 2016.

[69] Y. J. Morton, F. van Diggelen, J. J. Spilker Jr, B. W. Parkinson, S. Lo, and G. Gao, *Position, Navigation, and Timing Technologies in the 21st Century, Volumes 1 and 2: Integrated Satellite Navigation, Sensor Systems, and Civil Applications, Set*. John Wiley & Sons, 2020.

[70] J. Klobuchar, "Ionospheric Time-Delay Algorithm for Single-Frequency GPS Users," *IEEE Transactions on aerospace and electronic systems*, no. 3, pp. 325–331, 1987, doi: 10.1109/TAES.1987.310829.

[71] A. Ene, D. Qiu, M. Luo, S. Pullen, and P. Enge, "A comprehensive ionosphere storm data analysis method to support LAAS threat model development," in *Proceedings of the 2005 National Technical Meeting of the Institute of Navigation*, 2005, pp. 110–130.

[72] M. Luo, S. Pullen, S. Datta-Barua, G. Zhang, T. Walter, and P. Enge, "LAAS Study of Slow-Moving Ionosphere Anomalies and Their Potential Impacts," in *Proceedings of the 18th International Technical Meeting of the Satellite Division of The Institute of Navigation (ION GNSS 2005)*, 2005, pp. 2337–2349.

[73] M. Luo, S. Pullen, D. Akos, G. Xie, S. Datta-Barua, T. Walter, and

P. Enge, "Assessment of Ionospheric Impact on LAAS Using WAAS Supertruth Data," in *Proceedings of the 58th Annual Meeting of The Institute of Navigation and CIGTF 21st Guidance Test Symposium (2002)*, 2002, pp. 175–186.

[74] M. Hernández-Pajares, J. Juan, J. Sanz, and A. Aragón-Àngel, "Propagation of medium scale traveling ionospheric disturbances at different latitudes and solar cycle conditions," *Radio Science*, vol. 47, no. 6, 2012.

[75] J. Sanz, J. Juan, G. González-Casado, R. Prieto-Cerdeira, S. Schlueter, and R. Orús, "Novel ionospheric activity indicator specifically tailored for GNSS users," in *Proceedings of the 27th International Technical Meeting of the Satellite Division of The Institute of Navigation (ION GNSS+ 2014)*, 2014, pp. 1173–1182.

[76] C. Borries, N. Jakowski, and V. Wilken, "Storm induced large scale TIDs observed in GPS derived TEC," *Ann. Geophys*, vol. 27, no. 4, pp. 1605–1612, 2009, doi: 10.5194/angeo-27-1605-2009.

[77] M. Wang, F. Ding, W. Wan, B. Ning, and B. Zhao, "Monitoring global traveling ionospheric disturbances using the worldwide GPS network during the October 2003 storms," *Earth, planets and space*, vol. 59, no. 5, pp. 407–419, 2007, doi: 10.1186/BF03352702.

[78] V. K. Nguyen, A. Rovira-Garcia, J. M. Juan, J. Sanz, G. González-Casado, T. H. Ta *et al.*, "Measuring phase scintillation at different frequencies with conventional GNSS receivers operating at 1 Hz."

[79] M. Kim, Y. Choi, H.-S. Jun, and J. Lee, "GBAS ionospheric threat model assessment for category I operation in the Korean region," *GPS Solutions*, no. doi:10.1007/s10291-014-0404-6, Sep. 2014.

[80] E. Robert, P. Jonas, J. Vuillaume, D. Salos, L. Hecker, and P. Yaya, "Development of a European ionosphere threat model in support of GBAS deployment," in *2018 IEEE/ION Position, Location and Navigation Symposium (PLANS)*, 2018, pp. 1181–1190.

[81] R. Pradipta and P. H. Doherty, "Assessing the occurrence pattern of large ionospheric TEC gradients over the Brazilian airspace," *NAVIGATION, Journal of the Institute of Navigation*, vol. 63, no. 3, pp. 335–343, 2016.

[82] E. Blanch, D. Altadill, J. M. Juan, A. Camps, J. Barbosa, G. González-Casado, J. Riba, J. Sanz, G. Vazquez, and R. Orús-Pérez, "Improved characterization and modeling of equatorial plasma depletions," *Journal of Space Weather and Space Climate*, vol. 8, p. A38, 2018.

[83] J. Lee, M. Luo, S. Pullen, Y. S. Park, P. Enge, and M. Brenner, "Position-Domain Geometry Screening to Maximize LAAS Availability in the Pres-

ence of Ionosphere Anomalies," in *Proceedings of the 19th International Technical Meeting of the Satellite Division of The Institute of Navigation (ION GNSS 2006)*, Sep. 2006, pp. 393–408.

[84] S. Ramakrishnan, J. Lee, S. Pullen, and P. Enge, "Targeted ephemeris decorrelation parameter inflation for improved LAAS availability during severe ionosphere anomalies," in *Proceedings of the 2008 National Technical Meeting of The Institute of Navigation (ION GNSS 2008)*, Sep. 2008, pp. 28–30.

[85] D. Kim, M. Yoon, S. Pullen, and J. Lee, "Closed-form analysis of undetected range errors due to ionospheric impacts for GBAS category I operations," *Navigation*, vol. 68, no. 3, pp. 507–519, 2021, doi: 10.1002/navi.442.

[86] C. A. Shively and R. Niles, "Safety Concepts for Mitigation of Ionospheric Anomaly Errors in GBAS," in *Proceedings of the 2008 National Technical Meeting of the Institute of Navigation*, 2008, pp. 367–381.

[87] Radio Technical Commission for Aeronautics, "DO-246D, GNSS-Based Precision Approach Local Area Augmentation System (LAAS) Signal-in-Space Interface Control Document (ICD)," Tech. Rep., 2008.

[88] M. Caamano, D. Gerbeth, M. Felux, and M. Circiu, "Using a Wide Area Receiver Network to Support GBAS Ionospheric Monitoring," *Proceedings of the 30th International Technical Meeting of the Satellite Division of The Institute of Navigation (ION GNSS+ 2017)*, pp. 1418–1428, 2017, doi: 10.33012/2017.15319.

[89] M. Hoque, N. Jakowski, and J. Berdermann, "A new approach for mitigating ionospheric mapping function errors," in *Proceedings of the 27th International Technical Meeting of the Satellite Division of The Institute of Navigation (ION GNSS+ 2014)*, 2014, pp. 1183–1189.

[90] A. Komjathy, L. Sparks, J. Mannucci, and A. Coster, "The ionospheric impact of the October 2003 storm event on Wide Area Augmentation System," *GPS solutions*, vol. 9, no. 1, pp. 41–50, 2005.

[91] R. Lejeune, M. B. El-Arini, P. Doherty, J. Klobuchar, E. De Paula, F. Rodrigues, and A. Canavitsas, "Performance of SBAS ionospheric estimation in the equatorial region," in *Proceedings of the 16th International Technical Meeting of the Satellite Division of The Institute of Navigation (ION GPS/GNSS 2003)*, 2003, pp. 1658–1669.

[92] M. Caamano, M. Felux, D. Gerbeth, J. Juan, G. Gonzalez-Casado, and J. Sanz, "Network-Based Ionospheric Gradient Monitoring to Support GBAS," *Proceedings of the 32nd International Technical Meeting of the*

Satellite Division of The Institute of Navigation (ION GNSS+ 2019), pp. 2888–2902, 2019, doi: 10.33012/2019.16926.

[93] M. Caamano, J. Juan, M. Felux, D. Gerbeth, G. Gonzalez-Casado, and J. Sanz, "Network-based ionospheric gradient monitoring to support GBAS," *NAVIGATION, Journal of the Institute of Navigation*, vol. 68, no. 1, pp. 135–156, 2021, doi: 10.1002/navi.411.

[94] J. Juan, J. Sanz, G. González-Casado, A. Rovira-Garcia, A. Camps, J. Riba, J. Barbosa, E. Blanch, D. Altadill, and R. Orus, "Feasibility of precise navigation in high and low latitude regions under scintillation conditions," *Journal of Space Weather and Space Climate*, vol. 8, p. A05, 2018, doi: 10.1051/swsc/2017047.

[95] J. Juan, A. Aragon-Angel, J. Sanz, G. González-Casado, and A. Rovira-Garcia, "A method for scintillation characterization using geodetic receivers operating at 1 Hz," *Journal of Geodesy*, vol. 91, no. 11, pp. 1383–1397, 2017, doi: 10.1007/s00190-017-1031-0.

[96] S. Xiong, "Threshold Determination for Integrity Monitoring in Local Area Augmentation System," *China Satellite Navigation Conference (CSNC) 2015 Proceedings: Volume II*, pp. 293–300, 2015, doi: 10.1007/978-3-662-46635-3_24.

[97] M. Hernández-Pajares, J. Juan, and J. Sanz, "Medium-scale traveling ionospheric disturbances affecting GPS measurements: Spatial and temporal analysis," *Journal of Geophysical Research: Space Physics*, vol. 111, no. A7, 2006, doi: 10.1029/2005JA011474.

[98] M. Yoon, D. Kim, and J. Lee, "Validation of Ionospheric Spatial Decorrelation Observed During Equatorial Plasma Bubble Events," *IEEE Transactions on Geoscience and Remote Sensing*, vol. 55, no. 1, pp. 261–271, 2017, doi: 10.1109/TGRS.2016.2604861.

[99] Geodetic Facility for the Advancement of Geosciences (GAGE). UNAVCO Website. [Online]. Available: https://www.unavco.org

[100] K. Jacobsen and Y. Andalsvik, "Overview of the 2015 St. Patrick's day storm and its consequences for RTK and PPP positioning in Norway," *Journal of Space Weather and Space Climate*, vol. 6, p. A9, 2016, doi: 10.1051/swsc/2016004.

[101] Y. Béniguel, I. Cherniak, A. Garcia-Rigo, P. Hamel, M. Hernández-Pajares, R. Kameni, A. Kashcheyev, A. Krankowski, M. Monnerat, B. Nava *et al.*, "MONITOR ionospheric network: two case studies on scintillation and electron content variability," *Annales Geophysicae*, vol. 35, no. 3, pp. 377–391, 2017, doi: 10.5194/angeo-35-377-2017.

[102] Instituto Brasileiro de Geografia e Estatística (IBGE). Brazilian Network for Continuous Monitoring of GPS (RBMC) Website. [Online]. Available: ftp://geoftp.ibge.gov.br

[103] Z. Wang, T. Li, Q. Li, and K. Fang, "Impact of anomalous ionospheric gradients on GBAS in the low-latitude region of China," *GPS Solutions*, vol. 25, no. 1, pp. 1–13, 2021.

[104] U.S. Dept. of Defense, "Global Positioning System Standard Positioning Service Performance Standard, 4th Edition," September 2008.

[105] G. González-Casado, J. Juan, and J. Sanz, "Synthetic events description, generation and characterization report. Ionospheric conditions and associated scenarios for EGNOS selected from the last Solar Cycle (ICASES-2)," in *ICASES2*, 2015.